TECHNISCHE UNIVERSITÄT MÜNCHEN
PHYSIK-DEPARTMENT

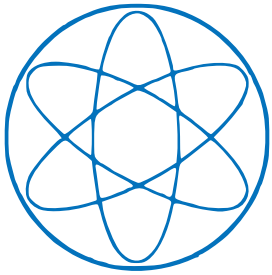

DISSERTATION

New concepts in four dimensional dose calculations

Stefan Milz

Dezember 2013

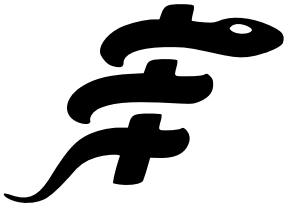

TECHNISCHE UNIVERSITÄT MÜNCHEN
Physik Department

New concepts in four dimensional dose calculations

Stefan Milz, M.Sc.

Vollständiger Abdruck der von der Fakultät für Physik der Technischen Universität München zur Erlangung des akademischen Grades eines

Doktors der Naturwissenschaften (Dr. rer. nat.)

genehmigten Dissertation.

Vorsitzender:	Univ.-Prof. Dr. Alejandro Ibarra
Prüfer der Dissertation:	
	1. Univ.-Prof. Dr. Jan J. Wilkens
	2. Univ.-Prof. Dr. Franz Pfeiffer

Die Dissertation wurde am 19.12.2013 bei der Technischen Universität München eingereicht und durch die Fakultät für Physik am 29.01.2014 angenommen.

Abstract

Radiation therapy is, together with surgery and chemotherapy, one of the most effective methods to treat cancer diseases. This approach uses ionizing radiation to treat tumor cells. Therefore, dose calculations are performed on the measured tissue data based on computer tomography (CT). In general, the treatment simulation of irradiation is performed on static geometries, but organ motions during irradiation complicate the dose calculation. Previous studies have shown that respiration induced motion is not negligible for stereotactic body radiation therapy (SBRT). The intra-fractional deformation of the organs, such as lung and abdomen, influences the delivered dose distribution on the underlying patient geometry. This leads to motion uncertainties for the dose planning process. As static methods may be insufficient, an adequate four-dimensional (4D) dose calculation approach is necessary to consider the temporal motion uncertainties. The general concept for 4D treatment planning provides a framework that is divided in several planning steps. The most important points of the approach are the deformable image registration (DIR) and the 4D dose accumulation. The aim of this thesis is to investigate on the new 4D dose planning approaches. To develop a new optimized process, DIR and 4D dose accumulation are investigated separately. With the aid of their results, a full 4D dose planning approach is developed. To prove its clinical benefit, the thesis compares the new model with established static approaches.

Respiratory correlated 4D computer tomography (4DCT) is used to record the deforming thorax geometry during respiration. The acquired data serves to define the respiratory motion, which is calculated by DIR. The thesis compares the state of the art DIR algorithms. Moreover, a new hybrid approach for DIR is introduced. Anatomical landmarks defined by medical experts are used to verify the accuracy of the mentioned algorithms. This work revealed accurate results for general DIR algorithms proven by global landmark tests. However, uncertainties for small volumes located at the surface of the lung were identified. Despite the high precision for the full 4D geometry, the new hybrid approach significantly improves the lack of accuracy at lung border areas. The clinical improvement of the hybrid approach is also confirmed by spatially optimized 4D dose distributions. Furthermore, 4D dose accumulation is investigated. A number of well known dose transformation algorithms are compared and the new divergent dose mapping model (dDMM) is introduced. For validation, an evaluation study that introduces a new error metric, which quantifies the modification of the dose mass histogram (DMH) during dose transformation, is presented. The highest accuracy was achieved for the new dDMM. The impact of an inaccurate dose transformation model is also proven by clinical investigations of 4D dose distributions. The findings of the DIR analysis and the 4D dose accumulation evaluation are used to provide a clinical solution, which is developed to compare static planning methods with 4D dose planning approaches. For this purpose, three different modalities such as tumor tracking, the concept of the internal target volume (ITV) and tumor gating are investigated. All evaluations have shown that the measured deviations are clinically not negligible.

In conclusion, this thesis presents new algorithms and techniques to optimize the entire 4D dose planning concept, where the new accurate DIR algorithm (hybrid approach) and the new precise dose transformation method (dDMM) are particularly progressive. Their advantages are proven. The new comprehensive 4D dose planning approach achieves a significant contribution as compared to established static solutions. This confirms the compelling need of a sufficient 4D dose planning model for lung SBRT.

Zusammenfassung

Die Strahlentherapie ist neben der Chirurgie und der Chemotherapie eine der effizientesten Methoden zur Behandlung von Krebs. Die grundsätzliche Idee ist die Verwendung ionisierender Strahlung zur Bekämpfung von Krebszellen. Zur Simulation der Bestrahlung werden Dosisverteilungen auf gemessenen Gewebedaten der Patienten berechnet. Im Allgemeinen wird dies auf einer statischen Geometrie durchgeführt, doch die Bewegung und Veränderung einzelner Organe während der Bestrahlung kann zu Planungsunsicherheiten führen. Studien haben ergeben, dass atmungsbedingte Veränderungen von Lunge und Abdomen für stereotaktische Körperbestrahlungen nicht zu vernachlässigen sind. Die intrafraktionelle Bewegung hat direkten Einfluss auf die lokale Dosisapplikation. Statische Planungsverfahren können hier unzureichend sein. Um zeitliche Gewebe-veränderungen zu berücksichtigen, sind genauere vierdimensionale (4D) Dosisplanungskonzepte notwendig. Das allgemeine 4D Konzept beruht auf einer sequenziellen Schrittfolge von Algorithmen, wobei die elastische Bildregistrierung und die 4D Dosisakkumulation entscheidend an der Planqualität beteiligt sind. Die Aufgabe dieser Doktorarbeit ist die Untersuchung neuer 4D Planungsverfahren. Um ein optimiertes 4D Planungsverfahren zu erarbeiten, werden zunächst die Algorithmen der elastischen Bildregistrierung und der 4D Dosisakkumulation untersucht. Mithilfe dieser Ergebnisse wird ein Gesamtkonzept zur 4D Dosisplanung entwickelt, dessen Mehrwert anhand von Vergleichsstudien gegenüber klinisch erprobten statischen Planungsverfahren bewiesen wird.

Die atemkorrelierte 4D Computer-Tomographie (4DCT) wird genutzt, um dynamische Bilddaten des Thorax zu generieren. Die Bewegungsberechnung erfolgt mithilfe der elastischen Bildregistrierung. Die vorliegende Arbeit vergleicht erprobte Verfahren der elastischen Bildfusion. Des Weiteren wird ein neuer hybrider Algorithmus vorgestellt. Die Validierung der Methoden erfolgt mittels Landmarkentests, welche von medizinischen Experten bestimmt worden sind. Mithilfe dieser Tests beweist die Arbeit die Eignung der Standardalgorithmen für 4D Dosisplanungskonzepte durch sehr präzise Ergebnisse. Im Detail wurden aber auch Ungenauigkeiten in kleinen Volumen nahe der Lungenoberfläche nachgewiesen. Durch das hybride Modell werden jene Ergebnisse jedoch deutlich verbessert. Die klinische Auswirkung des hybriden Modells wird anhand örtlich optimierter 4D Dosisverteilungen gezeigt. Außerdem werden Verfahren der 4D Dosisakkumulation untersucht. Bekannte Algorithmen der 4D Dosistransformation werden mit einem neuen Algorithmus, dem divergenten Dosis-Mapping-Modell (dDMM), verglichen. Zur Validierung dient eine Vergleichsstudie, die auf einem neuen Fehlermaß basiert, welches die Veränderung des Dosis-Massen-Histogramms (DMH) während der Dosistransformation quantifiziert. Die höchste Präzision wurde dem dDMM nachgewiesen. Die Auswirkung inakkurater Transformationsmodelle wird außerdem anhand klinischer Dosisanalysen bewiesen. Die Ergebnisse aus den beiden Teilstudien fügen sich zu einem Gesamtkonzept für die 4D Dosisplanung zusammen, welches in einem neuen Softwareprototyp implementiert wurde. Zum Vergleich von statischen und 4D-Dosisplanungskonzepten werden drei verschiedene Bestrahlungsmodalitäten verglichen. Dazu gehören Tumor Tracking, Gating und das Konzept des Internal Target Volume (ITV). In allen drei Fällen wurden deutliche Unterschiede nachgewiesen, die klinisch nicht zu vernachlässigen sind.

Zusammenfassend stellt die Arbeit neue Algorithmen und Verfahren zur Optimierung der 4D Dosisplanung vor. Wegbereitend sind vor allem das neue Modell zur elastischen Bildregistrierung (hybrider Algorithmus) und das neue akkurate Verfahren der Dosistransformation (dDMM). Ein klinisch signifikanter Mehrwert der neuen 4D Planungsmethode wurde anhand von Vergleichsstudien mit etablierten statischen Verfahren nachgewiesen. Damit beweist die Arbeit, dass ein adäquates 4D Planungsmodell für Lungenbestrahlungen zwingend notwendig ist.

Contents

Chapter 1

1 Introduction

1.1 Context

1.1.1 Radiation therapy

Cancer is the consequence of an aging society. Due to the medical progress and the accompanied increase of the life expectancy, every second resident has to expect to be affected by cancer in the course of his life. In a few years, cancer is assumed to be the leading cause of death in Germany [126]. In 2012, about 490000 new cases of cancers were diagnosed [44]. This is an incidence rate of 400 cases per 100000 inhabitants. Behind cardiovascular disease, cancer achieves the second highest mortality rate with more than 200 per 100000 residents in Germany. Thus, the disease is related to all of us. At present, it is possible to cure 45 %-50 % of all cancer patients. This can only be achieved with the aid of established therapies, which are continuously improved and developed. For oncology, the medical field of tumor disease, radiation therapy is, together with surgery and chemotherapy, one of the most effective methods to treat cancer diseases [126]. Consequently, about 50 %-60 % of all cancer patients receive one or more radiation therapies in the course of their treatment. In clinical practice, radiotherapy has become an adequate treatment for many tumor types. Such a variety of treatment options was only possible by the basic research and the steady improvement of the knowledge in physics regarding radiation therapy distributed throughout the last century.
The goal of radiation therapy is to destroy malignant tumor cells by radiation based energy deposition, while preserving healthy tissue in spatial relation to the irradiated area. Generally, this is achieved by the clinical use of different radiation types. The most common method is the use of x-rays or gamma rays known as photons. However, also neutrons, protons or heavy ion beams are suitable for clinical treatment [115]. The proportion of patients, not treated with photons, is certainly very small due to high technical effort and the enormous costs of the particle therapy. Currently, there are over 200 radiotherapy institutes in Germany, but not only a few treat patients with protons or heavy ions. Hence, this thesis presents concepts especially for the radiation therapy with photons, although major parts are equally valid for particle therapy.
To achieve the best clinical outcome after irradiation, the patient has to pass several preparation stages. For an accurate radiation application, it is necessary to simulate the irradiation before treatment (dose planning). For this purpose, the patient geometry is measured by a static computer tomograph (CT). The extracted tissue data serves for dose calculation, which is getting optimized during the dose planning progress. However, it is not guaranteed in every case that the statically measured CT for dose planning is consistent with the patient geometry during dose application. Various factors could cause significant tissue variations which falsify existing dose calculations. Such deforming tissue geometries need an adaptive dose calculation concept to incorporate motion and deformation uncertainties into the planning process.

1.1.2 Four dimensional treatment planning

The topic of this thesis is the consideration of temporal tissue changes for 4D dose calculations. As described, some indications require an adaptive dose planning approach. Those methods implement a four dimensional treatment planning concept. First research results regarding 4D planning were achieved in the early nineties [65]. Due to the computational progress at this time, the practicality of static dose algorithms was improved [48]. This led to more accurate dose calculations, e.g. Monte Carlo [21]. The technical progress enabled also more complex dose calculation strategies, such as 4D dose calculations on deforming geometries [120].
In general, 4D dose planning has to distinguish between inter-fractional motion and intra-fractional motion [38]. Inter-fractional motion describes geometrical variations between different dose applications. These are long term variations which describe tissue movements over several days or weeks. The inter-treatment movement of the rectal wall during the course of a prostate treatment is a typical example. Such organ deformations are caused by patient positioning uncertainties or physiological processes like tumor shrinking. However, the patient geometry is assumed to be static during a fractional dose application [104, 10]. In contrast, intra-fractional motion describes physiological tissue deformations that occur directly during dose delivery. Such short term variations describe tissue movements of a few seconds. Exemplary for this is the intra-fractional respiration which causes characteristic thorax or abdomen deformations of several centimeters during irradiation [90].
4D dose calculations have advanced requirements on medical imaging. To consider motion, the dose calculation needs temporal access to deforming tissue data. Inter-fraction motion is easy to record with fractional repeated static CTs or newer Cone Beam CTs [96]. However, the short term description of intra-fraction motion complicates the imaging process. Because of this, clinical research for inter-fraction has been reported earlier than comparative results based on intra-fraction motion. 4D dose calculations closely depend on 4D imaging. A milestone for intra-fraction 4D dose calculation was the invention of the respiratory correlated 4DCT [53]. This modality enabled at first a sufficient description of respiratory motion for 4D dose calculation. The present thesis exclusively deals with concepts for intra-fraction movements and 4D dose calculations that are based on breathing induced deformations of the thorax or the abdomen.

1.1.3 Stereotactic body radiation therapy (SBRT) for lung cancer

Lung cancer continues to be the leading cause of cancer death [38]. In 2008, lung cancer was the third most common cancer disease in Germany [44]. About 30000 men and 13000 women died in consequence of the disease. The five year survival probability is very low with 15 % for men and 19 % for woman. These are important reasons to improve the methods to heal the disease. Stereotactic body radiation therapy (SBRT) for lung cancer describes highly accurate radiation therapy with small numbers of radiation sessions accompanied with large single doses. Due to the complexity of this dose delivery approach, the method additionally requires a very precise 4D dose planning and motion detection.
Research results for lung cancer radiation therapy during the last decade revealed sufficient methods to describe the magnitude of breathing induced tumor motion [20, 51, 52, 62]. As mentioned before, the most important modality for imaging is the 4DCT. Its accurate motion detection led to different dose planning methods. Static dose calculations are still state of the art. Indeed, such implementations are based on the respiratory correlated 4DCT, but motion uncertainties are only considered by advanced target definition concepts. The general methods for authentic 4D dose calculations are widely accepted in research, but still rarely used on clinical practice. 4D planning for SBRT contains a general work flow [51, 33, 62, 119, 95]. Fig. 1.1 illustrates the established step sequence. The difficulty of the 4D dose calculation concept can be splitted into single problems: the deformable image registration (Fig. 1.1.b); the 4D dose transformation and accumulation

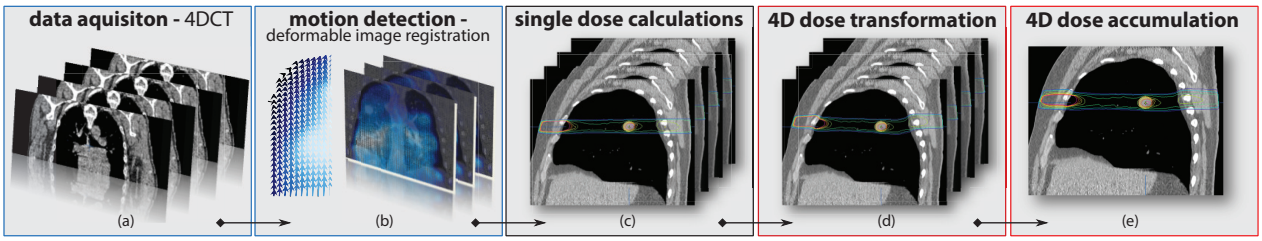

Figure 1.1 : Established work flow for 4D dose calculations: (a) 4DCT data acquisition for recording deforming tissue; (b) Elastic image fusion for determination of spatial deformation; (c) Single dose calculations for simulation of time dependent dose application; (d) 4D dose transformations to unify all dose distributions in the same coordinate system; (e) 4D dose accumulation for the determination of the final dose distribution for clinical evaluation

(Fig. 1.1.d). Both topics require very precise algorithms, but the present opportunities are not fully exploited. Hence, this thesis presents new algorithms and techniques to optimize the entire 4D dose planning concept.

1.2 Content

1.2.1 Motivation for developing an accurate 4D dose planning model

Due to the continuous development and improvement of dose application systems for lung SBRT, static dose calculations do not longer fulfill the requirements of an accurate planning approach. For example, dynamic tumor tracking systems are available, e.g. the VERO™ SBRT distributed by the *Brainlab AG* [60, 45], the Cyberknife™ (Accuracy Inc.) [16] or individual dynamic MLC-based tracking machines [51]. In contrast to the static approach, which considers a static dose delivery for the full breathing cycle, the new methods apply temporally modified dose distributions. It is not possible to simulate these temporal dose variations with static methods. Several studies investigated the difference of static approaches compared to 4D dose calculations. For example, *Admiraal et al.* [2] and Chan et al. [17] revealed significant differences for the tumor control probability (over 5 %), for volumes irradiated with the prescribed dose (more than 5 %) or for high dose values D_{99} (more than 10 %). The analysis have shown that such deviations are not negligible for clinical treatments [95]. Additionally, experimental studies haven proven characteristic differences between static and 4D dose planning approaches. For example, *Ahnen et al.* [3] investigated the general 4D dose planning work flow with the aid of film measurements and an artificial phantom that simulates respiration induced tumor motion and mass density variations. The conclusion was a provable impact of motion and deformation, which is not negligible for dose calculations. Only the use of 4D dose calculation concepts enabled a sufficient agreement of simulated and measured dose data. The results of all mentioned studies are motivation enough to develop an accurate 4D dose planning model that is feasible for future clinical practice.

1.2.2 Outline

The previous sections explained the need of an accurate 4D dose planning approach. As mentioned in Fig. 1.1, the basic work flow is well known and widely used for research purposes. However, the step sequence concept has to be calculated carefully. Due to the continuous processing of precalculated data in a series of complex algorithms, the method is getting error-prone. For example, systematic errors generated by deformable image registration have an influence on all subsequent steps, e.g. dose transformation, and thus affect the final 4D dose distribution. Particularly important are the deformable image registration and the dose transformation.

A large number of algorithms were proposed for both topics with varying benefits and drawbacks. Because of this, the present thesis deals especially with the mentioned sub-steps. Known algorithms are compared with new implementations. The aim is to find accurate algorithms either for deformable image registration or for dose transformations. Furthermore, this thesis investigates the global interaction of all sub-steps of the 4D dose planning process with regard to their clinical influence. The goal is the definition of a specific process that is able to generate precise results for clinical practice. For this purposes, the investigations in the present thesis are separated into single chapters:

Chapter 2 *(Elastic image fusion for respiration induced deforming patient models)* deals with the first large topic of this thesis, the deformable image registration for respiratory correlated 4DCT. It is necessary to determine the motion inside the measured data. For this purpose, basic knowledge of 4DCT data acquisitions is introduced. Furthermore, the chapter explains state of the art algorithms and compares their properties. It is distinguished between information driven patterns and physical elasticity models. In addition, a new hybrid deformation algorithm for lung data is introduced. The registration quality of the different approaches is quantified by specific landmark tests that validate motion detection with the aid anatomical coordinates defined by medical experts.

Chapter 3 *(4D dose calculation based on accumulation of time dependent dose distributions)* discusses dose transformations for 4D dose calculations in context of lung SBRT. Therefore, the main concept, numerical requirements and problems that occur during dose transformation are illustrated. This is also explained and investigated with biological models. The chapter describes a number of dose transformation algorithms that are suitable for 4D dose accumulation. Furthermore, the new divergent dose mapping model is introduced. The study compares the accuracy of the mentioned algorithms with the aid of a new error metric, which is based on the conservation of the dose mass histogram.

Chapter 4 *(Evaluation of the 4D treatment planning concepts)* explains the clinical influence of the findings mentioned in chapter 2 and 3. To apply the whole concept, a new 4D *iPlan™ RT* prototype is developed and a series of comparative studies are introduced. Clinical influences are measured with the aid of the dose volume histogram for targets and organs at risk. Furthermore, gamma tests and dose line profiles analyze spatial differences. With the aid of different treatment modalities and motion management systems, the chapter compares the proposed 4D dose planning approach with conventional static methods. Finally, opportunities for future developments are shown.

Chapter 5 *(Summary and Outlook)* summarizes and discusses the whole thesis and offers an outlook.

Chapter 2

2 Elastic image fusion for respiration induced deforming patient models

Stereotactic body radiation therapy (SBRT) requires an accurate planning procedure. First of all, this includes a precise patient data acquisition, because the data is the base of all succeeding steps, such as dose calculation or plan optimization. If the data is imprecise, the propagation of this error leads to inaccuracy in all separate steps of the dose planning process. Thereby, the last consequence is a discrepancy of the planned and the treated dose. 4D approaches, i.e. respiration induced motion of the lung and abdomen during SBRT, have considerably more requirements on the accuracy of the acquired patient data. Whereas standardized 3D processes have a high demand on the spatial resolution, 4D methods generate additional demands on the time component. Hence, patient data that serve as a 4D planning tissue model have to be measured in high temporal and spatial resolution. Basic data acquisition work flows in the field of 4D radiotherapy are well established by Rosu et al.[79], Keall et al.[52], Janssens et al.[41] and Soehn et al. [94].

3D methods use in most cases static computer tomography (CT) scans with respect to the location of the patient indication. For 4D approaches, methods that consider breathing induced motion during radiation treatment, four dimensional computer tomography (4DCT) scans [91] are being established. A 4DCT process produces a complete series of static image sets, covering the entire respiration cycle. Hence, every static geometry is assigned to a single breathing phase. Dose calculations are performed on a specific time due to the assignment of the underlying geometry. A series of dose calculations has to be generated to take the motion of the full breathing cycle into account. For clinical analysis and radio-biological assessment of a 4D plan, the summarized dose calculations for certain organs at risk (OAR) or the planning target volume (PTV) are inevitable. However, the CT data sets represent several detached and independent coordinate systems. The main task of image fusion is the spatial correlation of all series to enable global coordinate transformations. Thus, it is necessary to know the biological structures and their movement during the breathing cycle. This chapter describes the methods to generate a deformation field that spatially connects every single data set especially in the field of breathing induced motion. During the past years several methods that are based on totally different approaches (see section 2.2.1 and 2.2.2) have emerged. This work introduces a new hybrid model (see section 2.2.3) by combination of established methods. The chapter explains the full elastic fusion procedure, starting from the basic data acquisition to the fundamental elastic fusion models up to the new hybrid approach. The investigation is completed by an landmark evaluation study for verification.

2.1 Data acquisition with 4DCT

2.1.1 Physical principles

Static CT image data are the basis in almost all common 3D dose calculations. The image data provides a tissue model that enables the realistic description of matter and tissue with a high spatial resolution. The desired

object is irradiated with X-rays from different angles Φ. The reconstruction of the stacked images is realized with the aid of the measured attenuation projections p_Φ^{CT}. The X-ray tubes generate a polychromatic radiation spectrum. Hence, the intensity I, which is measured on the detector side, is describable with a summarized integral of all attenuated initial intensities $I_0(E)$ taking the full energy spectrum into account ($0 \ldots E_{max}$). The application of Lambert Beer's attenuation law enables a ray investigation regarding the traced way l starting from the X-ray tube and ending inside the detector. The measured intensity is defined by [75]:

$$I = \int_0^{E_{max}} I(E)dE = I_0 \cdot \int_0^{E_{max}} S(E)e^{-\int_0^l \mu(E,\vec{x})d\vec{x}}dE \tag{2.1}$$

μ being the total mass attenuation coefficient. $S(E)e^{-\int_0^l \mu(E,\vec{x})d\vec{x}}$ describes the modification of the energy spectrum for higher depths. However, the strong energy dependency disables the determination of the spatial distribution of μ along the trace l. Therefore, an average energy $\bar{E}$ is assumed[1]. This simplification reduces the energy dependent set of values $\int_0^{E_{max}} S(E)dE$ to a single term 1. Specifically, the relation of an angle related attenuation profile p_Φ^{CT} and the distribution of the attenuation coefficients $\mu(\bar{E}, x)$ can be described in the following way:

$$p_\Phi^{CT} = -\ln\left(\frac{I}{I_0}\right) = \int_0^l \mu(\bar{E}, \vec{x})d\vec{x} \tag{2.2}$$

The projection of a set of angles Φ enables the reconstruction of $\mu(x, y)$ as a planar object. From several radiation directions, intensity profiles were measured along the orthogonal path direction η, distributing along the trace coordinate ξ to cover the full object. The introduction of new coordinates is necessary to describe measurement process. x, y illustrate the distribution of μ inside the object as fixed global coordinates, the projection angle Φ and its associated coordinates η and ξ explain the position in relation to the measurement space. The coordinate relations are illustrated in Fig. 2.1. The coordinate transformation is be defined as [36]:

$$\begin{aligned} x &= \xi \cdot \cos(\Phi) - \eta \cdot \sin(\Phi) \\ y &= \xi \cdot \sin(\Phi) + \eta \cdot \cos(\Phi) \end{aligned} \tag{2.3}$$

Equation (2.3) enables the exact definition of η in relation to the defined coordinate x, y and the projection angle Φ. ξ is negligible due to the definition of the projection angle. Hence, η depends on Φ, x, y:

$$\eta(\Phi, x, y) = \frac{y - x \cdot \tan(\Phi)}{\tan(\Phi) \cdot \sin(\Phi) + \cos(\Phi)} \tag{2.4}$$

In summary, it is possible to describe $\mu(x, y)$ with the aid of a suitable number of projections. A single measurement is defined by its properties Φ and η:

$$p^{CT}(\Phi, \eta) = -\ln\left(\frac{I(\Phi, \eta)}{I_0(\Phi, \eta)}\right) = \int \mu(\bar{E}, x, y)dl \tag{2.5}$$

The goal of a CT is the reconstruction of $\mu(x, y)$ based on the measurements $p^{CT}(\Phi, \eta)$. Analytically, it can be written as the Radon-Transformation $\mathfrak{R}$ [36]. This is the assignment of a two dimensional function (here:

[1] The simplification leads to X-ray hardening artifacts. On its way through the desired object the ray changes its energy due to interaction with matter. The new energy and the average assumption varies in relation to the traced mass. $\bar{E}$ constantly increases on the way l. Energy fractions with lower values receive more attenuation than higher energies. Hence, the spectrum is displaced to larger values[75].

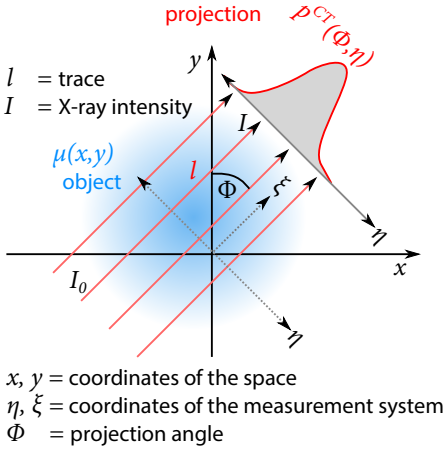

Figure 2.1 : Principles of CT measurements: Two coordinate systems exit, one for the measurement view and one for the global description of the object $\mu(x, y)$. A single projection is based on the integral X-ray intensity investigation I/I_0 (value of attenuation) along the orthogonal beam direction η based on the angle Φ. The measurement of a sufficient value of projections p^{CT} regarding different beam angles Φ enables the reconstruction of the object $\mu(x, y)$.

$\mu(x, y)$) with all one dimensional projections $p^{CT}(\Phi, \eta)$. The transformation is defined by:

$$p^{CT}(\Phi, \eta) = \mathfrak{R}\left[\mu(x, y)\right] \tag{2.6}$$

For the description of $\mu(x, y)$ the inverse Radon-Transformation $\mathfrak{R}^{-1}$ is necessary. An approach for an elementary solution is the trivial back-projection $\mathcal{B}$ [36]:

$$\mu_{\mathcal{B}}(x, y) = \mathcal{B}\left[p^{CT}(\Phi, \eta)\right] = \mathcal{B}\mathfrak{R}\left[\mu(x, y)\right] = \int_0^{\pi} p^{CT}(\Phi, \eta(\Phi, x, y))d\Phi \tag{2.7}$$

The result of the back-projection in (x, y) is the integral of all projections p^{CT} that trace through the coordinate (x, y). For symmetry reasons, it is sufficient to collect all projections from 0° to 180°. The back-projection results not in the exact definition of μ, because the method considers coordinates that are located on the projection line, even if they are far away from (x, y). Such values falsify the value of $\mu(x, y)$. Moreover, the investigation of the operator product $\mathcal{B}\mathfrak{R}$ leads to a convolution of the original function $\mu(x, y)$ with the kernel $h(x, y) = |(x, y)|^{-1}$ [85]:

$$\mathcal{B}\mathfrak{R}\left[\mu(x, y)\right] = (\mu * h)(x, y) \tag{2.8}$$

$h(x, y)$ being the point spread function (PSF). The back-projection of a single Dirac signal $\delta(x, y)$ leads to $h(x, y)$. It describes the important decrease of $1/|\vec{r}|$ sloping outwards. Hence, the goal of the definition of μ should be to eliminate the PSF in $\mathcal{B}$. This could be realized with a filter function, before the back-projection is performed. It is the convolution of the signal $p^{CT}(\Phi, \eta)$ with the inverse kernel h^{-1}. The method is known as filtered back-projection. It realizes the inverse Radon-transformation in the following way:

$$\mu(x, y) = \mathcal{B}\left[(p^{CT} * h^{-1})(x, y)\right] \tag{2.9}$$

The approach assumes parallel beam geometries. The corresponding adjustments are necessary for common fan beam geometries (see Fig. 2.3.a) or other variances. The choice of the filter kernel h^{-1} is also important for numerical reasons. However, there exist, additionally, several iterative methods [36], [85], [75] that solve equation (2.6) considering the numerical effects and incomplete, discrete measurement structures[2].

[2] Detailed investigations regarding tomographic techniques and image reconstruction can be found in [85].

[3] Parts of the figure are taken from the scripts regarding in the lecture about *"Tomographic techniques"* based on *Hietschold et al.*[36]. The illustration is inspired by [85].

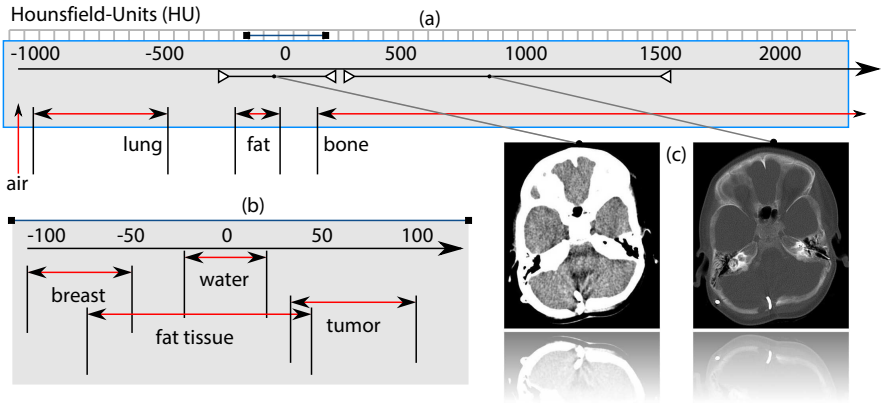

Figure 2.2 : Hounsfield range for matter inside the human body: (a) The full HU range for human tissue is emphasized at the top from: $HU = -1000$ up to $HU = 2000$. Assigned are three groups of typical tissue types that cover the full range. (b) An enlarged detailed range visualizes a specific extract (window) from: $HU = -100$ up to $HU = 100$. Specific body compounds are marked in this small area. (c) An example cranial CT image is illustrated in two different states: soft tissue window (left), bone window (right).[3]

The X-ray computer tomography illustrates the reconstructed attenuation ($\mu_{CT} = \mu(\tilde{E}, x, y)$) coefficients with the aid of a scaled relative format, so called Hounsfield-Units (HU). The HU values are defined according to the attenuation in water $\mu_{CT}(H_2O)$. The conversion of the measured CT data μ_{CT} into unit-less CT values [75] is described by:

$$HU = \frac{\mu_{CT} - \mu_{CT}(H_2O)}{\mu_{CT}(H_2O)} \cdot 1000 \tag{2.10}$$

The HU value describes the deviation of the specific tissue and water in thousandth. Water is defined with zero HU. Theoretically the HU scale is infinity, but the clinical practice established a suitable range of $-1000 \leq HU \leq 2000$ [75]. For illustration in radiological diagnostics, HU values are defined with grey scales. The data is illustrated using a windowing mode, where a specific range of HU values defines the full range of grey scales. Every pixel outside the defined HU-range is either black (lower value) or white (larger value). The full distribution of HU values is illustrated in Fig. 2.2. The assigned ranges of tissue types regarding specific values are emphasized. In Fig. 2.2, a special cranial image is visualized with the aid of two different windows, a bone window (right) and a soft tissue mode (left).

Common CT scanning devices acquire a stack of data images to cover the full patient geometry. In this case, every single layer of the patient geometry is irradiated. The X-ray tube rotates around the object and the opposing detector field acquires the X-ray intensity attenuation from a fan-beam signal (fan beam CT see Fig. 2.3.a). The rotating unit is called gantry, which consists of the tube and the detector. To speed up the procedure, modern devices irradiate simultaneously several axial patient slices, so called multislice CT [27], i.e. the X-ray tube generates a fan-beam that covers a three dimensional area for detection of a two-dimensional attenuation profile (Fig. 2.3.b). During the measurement the tube helically rotates around the patient by using a moving table to shift the patient. The mentioned coordinate system ($x - y$ for planar images, z in axial direction) is established in almost all measurement setups. The definition of the scanning region and the time it takes to scan this region determines the moving table speed of a common static measurement. For example, a whole body CT scanning time should be shorter than 15 seconds to avoid breathing related motion artifacts. In order to achieve this, the table speed for a 525 mm region is set to 35 mm per second [82]. Modern devices generate image data with 1 mm pixel sizes (x,y) and of $1 - 2$ mm slice distances (z). The resolution depends

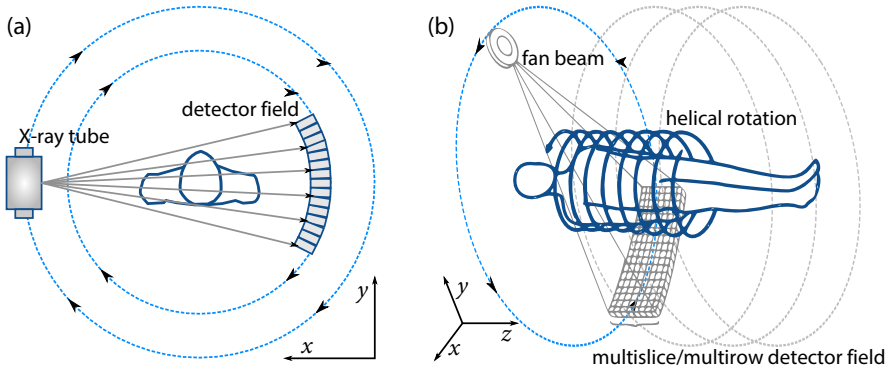

Figure 2.3 : Principle construction of a common CT device: (a) Principles of a fan-beam CT in planar view, (b) Principles of a spiral CT: Tube and detector field helically rotate around the patient to cover the full range in axial direction. The figure is inspired by: [36], [75].

on the beam collimation[4] and the number of detectors inside the multislice detector field.[5]

2.1.2 Temporal requirements on dynamic imaging

Several conditions exists for CT measurements that periodically reconstruct deforming patient geometries [72], [19]. The data acquisition with a 4DCT has to fulfill these requirements to realize a sufficient reconstruction and to be clinical applicable. First of all, the scanning time T_d for a single slice should obviously be smaller than the time T_b for a full period of the physiological cycle. As mentioned in (2.7), one slice can be reconstructed by a half gantry rotation. The typical time for a breathing cycle is: $3s \leq T_b \leq 5s$. Hence, a gantry rotation time T_g of about 0.5 s is already sufficient for 4DCT data acquisition of breathing induced motion. This is equivalent to a temporal resolution of 0.25s or the acquisition of four slices per second [75]. For imaging of breathing induced motion further requirements are necessary: Despite the large axial coverage ($\geq$ 150 mm for lung measurements), the contrast resolution and the spatial resolution ($\geq$ nine line pairs per cm) should be as good as the standard properties of current medical CT scanners [97]. Hence, no reduction of T_d is possible compared to static approaches. At least, all devices need real-time capabilities, i.e. fast image processing and controlling methods are necessary to control and process the data directly. All the mentioned conditions are required to be clinical applicable for the 4D approach. Another temporal condition for modern CT devices (helical multislice CT), which is the pitch factor, is the limit of the maximum periodic duration time T_b of the physiological cycle. The international standard formula (by IEC) is [15]:

$$P = \frac{TF[mm]}{N \cdot SC[mm]} \tag{2.11}$$

The pitch P is the fraction of the table feed TF (the table movement in mm per 360° gantry rotation T_g) and the collimation of the multislice CT, where N identifies the value of the detector rows and SC describes the slice collimation in mm. For $P = 1$ the CT unit scans exactly the length of one beam collimation during one gantry rotation. The pitch is essential for the speed of the axial image processing time. It leads to the following formula that identify the maximum period duration time T_b [75]:

$$T_b \leq \frac{N-1}{N} \cdot \frac{T_g}{P} \tag{2.12}$$

[4] In CT measurements collimation is responsible for the photon quality of the detected beam. A high collimation leads to very sharp images, but reduces the value of detected photons and increases the radiation for the patient [15].
[5] A detailed analysis regarding technical details of modern CT units can be found in [15], [27].

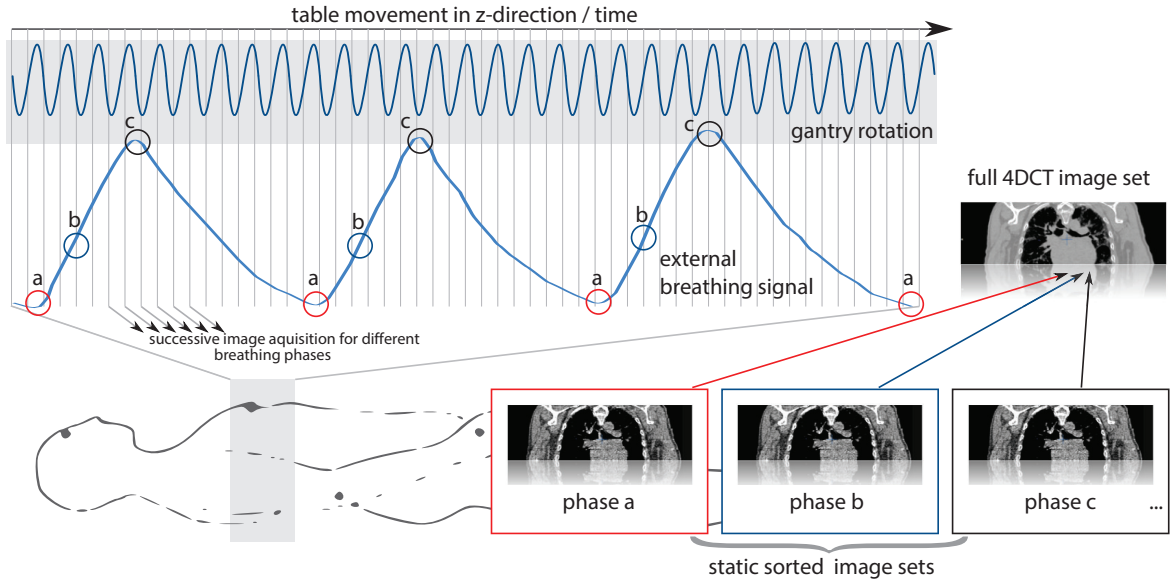

Figure 2.4 : Image reconstruction with a respiratory correlated 4DCT: During a slow table movement (see temporal requirements in section 2.1.2) the CT detector helically rotates around the breathing patient geometry. The procedure, successively generates image data that belong to different breathing phases (e.g. a,b,c). The data is acquired unsorted. With the aid of the external breathing signal the data is assigned to a special phase. The list of static CT image series results in a 4DCT set.

$\frac{N-1}{N}$ being a correction factor for multislice CT devices. It is required that N (simultaneously scanned) slices have to overlap at least in one slice with the next portion of N slices. $\frac{T_g}{P}$ describes the temporal coverage of any desired detection point [75]. For example, a $N = 16$ multislice scanner with a gantry rotation time of $T_g = 0.5s$ needs a pitch value of $P = 0.1$ to measure the breathing period cycles with a maximum of $T_b = 5s$. Otherwise, systematic artifacts could not be avoided. In contrast to static approaches, such a pitch value is very low. This increases the full scanning time and the radiation exposure of the patient. Modern 4D approaches allow pitches up to 0.5 [49].

2.1.3 4D image reconstruction

The reconstruction of respiratory correlated 4DCT is well described by: [97], [58], [23]. The most important approach is the dynamic volumetric imaging method with an external breathing signal (respiratory correlation) [49]. One has to distinguish between cine mode and helical rotation. The cine mode is a stepwise table movement. For every step, the data acquisition of the full breathing cycle and a respective axial region is measured [42]. However, modern devices use a helical rotation with a continuous table movement. To achieve image data without artifacts temporal requirements and technical prerequisites are illustrated in section 2.1.2. The basic idea of image reconstruction is the oversampling of images at every couch position along the desired patient axis. Every measured image is assigned to a specific moment inside the respiratory cycle by the correlation to an external breathing signal (respiration correlation). The unsorted stack of image data is retrospectively sorted with the aid of the corresponding breathing signal. The result is a set of many static CT data sets, each for its corresponding breathing phase. Together, they constitute the full 4DCT that cover the entire breathing cycle. The full procedure is illustrated in Fig. 2.4. The external breathing signal can be obtained using either a patient positioning system, an abdominal belt or the variation distance of the patient's anterior surface inside the CT image. The retrospective image sorting can be done inside the sinogram space[6]or inside

[6]The sinogram is the mathematical space that results after processing of all single projections p^{CT} without any reconstruction.

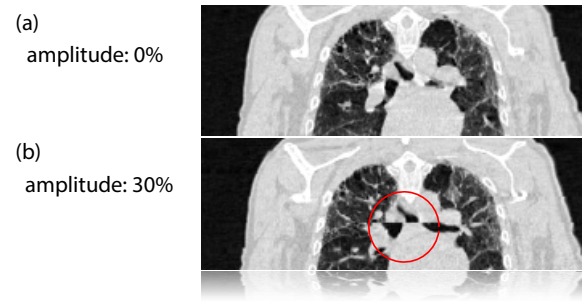

Figure 2.5 : Typical artifact due to irregular breathing: (a) Static reagular image set at 0 % of the breathing cycle, (b) Faulty image reconstruction in the middle of the axial area. The irregular breathing at 30 % of the patient's breathing cycle restricts a congruent assembling and the right retrospective sorting.

the reconstructed image space. The quality of the image data is essential for dose calculations, but 4DCT imaging is more susceptible to artifacts than static CT methods due to the complexity of the approach. Most of the artifacts belong to irregular breathing and are therfore systematic, which unfortunately can not be excluded. *Keall et al.* [50] investigated the empiric distribution of different 4D artifact types. The survey revealed the following:

1. 85 **%:** Irregular breathing
2. 8 **%:** Inadequate respiratory monitors
3. 3 **%:** Sorting in image space instead of the sinogram space
4. 3 **%:** Use of phase number instead of displacement amplitude for reconstruction
5. 2 **%:** Gantry rotation is too slow

The survey also revealed that many medical physicists recommend to do a patient breathing training to minimize the probability of typical 4D artifacts. The conclusion of the artifact investigation is that model related artifacts occur less than random irregular breathing related errors. Fig. 2.5 illustrates a typical example for an irregular breathing induced artifact.

2.2 Deformable image registration

In principle, the dynamic detection of respiration induced motion is possible using respiratory correlated 4DCT. The result is a set of static image spaces that cover the full breathing cycle. There is no information about spatial dependencies and physiological movement of inherent structures. Deformable image registration (DIR) is an automated method to describe tissue movement. The goal of DIR is the generation of spatial relationships. The algorithm aims to create transformation matrices that describe the position of any physiological coordinate inside the full breathing cycle. Hence, the movement of any organ or corresponding structures is described through coordinate transformations between single CT geometry spaces. Finally, the full registration of all 4DCT-sets enables a summarized biological assessment of the simulated dose calculation. DIR is necessary to successive stage of the 4D dose planning process. Every error propagates through the full 4D treatment planning procedure without elimination. Hence, the selection of an accurate model is essential for a precise 4D planning approach.
Different models regarding DIR were proposed in the field of adaptive radiotherapy, especially for lung SBRT. However, one approach is the base of all. The adequate generation of deformation fields that defines the transformation between two static image spaces with the aid of a grid based motion vector field $v_{ij}(\vec{x}_j)$. The vector field describes the movement of any point $\vec{x}_j$ in the source image space J that transforms to the target image space I.[7] The standard approach is the definition of one static space I as a reference set (e.g. the inhale phase of the breathing cycle). All other sets are linked to the reference space. Hence, the movement of all

[7] Members of a certain space J, I are marked in the subscript with the related small letter i, j.

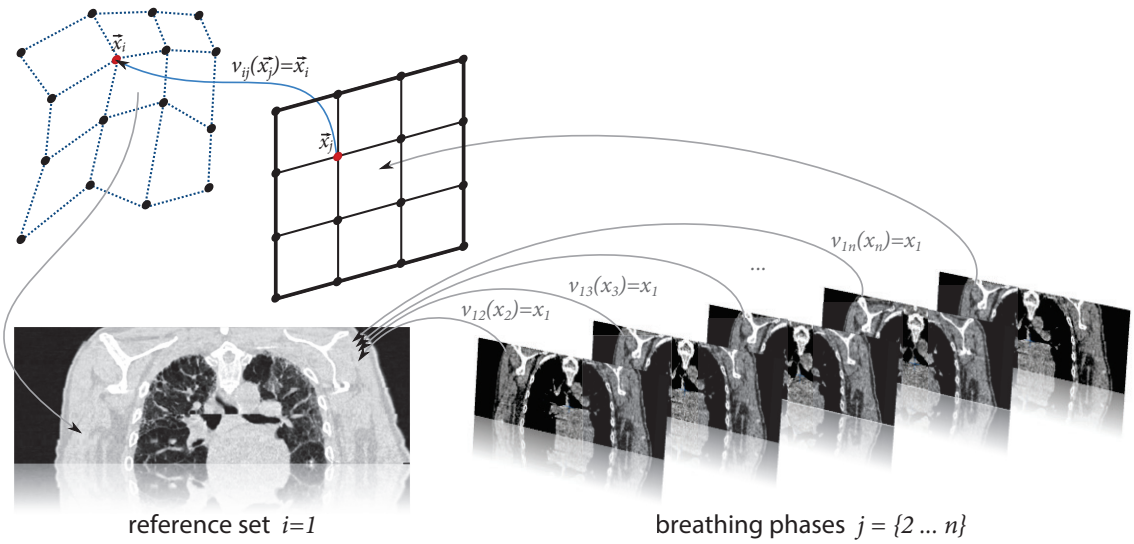

Figure 2.6 : Basic idea of deformable image registration: DIR in the field of 4D planning for SBRT is used to model the full movement of the respiratory cycle. All static CT sets j are connected with one reference set i. The connection is realized using deformation fields. The full movement detection inside a 4DCT containing n data sets is possible with $n-1$ vector fields $v_{ij}(\vec{x})$.

phases J is described by their connection to I (see Fig. 2.6). For a respiratory correlated 4DCT, which contains n (usually n=8 ... 10) static breathing phases, the calculation results in $n-1$ vector fields:

$$\vec{x}_i = v_{ij}(\vec{x}_j); \quad x \in \mathbb{R}^3; \quad i = 1; \quad j = \{2 \dots n\} \tag{2.13}$$

There are several algorithms and methods[47] that are able to generate suitable vector fields. DIR has been studied for many years. Brain surgery and neurosciences generated a large number of techniques. In 1981, the first approach was introduced by *Sederberg et al.* [87] based on cubic polynomial B-splines defined by grid based nodes. The concept deforms objects by the distortion of nodes in the geometrical space. This pioneer invention of DIR was improved in 1987 by *Terzopoulos et al.* [98]. The introduced model combined physical properties directly in the graphical object to simulate the deformation. Based on this, a lot of different applications for medical image processing were derived: [11] [12] [100] [64] [121]. Any new application of DIR can be attributed to one of the two basic inventions of *Sederberg* or *Terzopoulos*. Hence, the classification of two basic groups for DIR algorithms in the field of respiration detection is useful. The first approach, information driven patterns (IDP) are intensity related techniques, i.e. analytical and numerical methods try to verify the movement at least with the aid of the HU signals inside the image data. The other group, physical elasticity models (PEM), simulates the deformation of single objects and structures with the knowledge about the elasticity of matter based physical definitions. Both groups are explained in the following two sections.

2.2.1 Information driven patterns (IDP)

This sections gives an overview of one possible IDP procedure based on *Rueckert et al.* [81]. The method is known as Free-Form-Deformation (FFD). FFD is purely algorithmic without any physical foundation. The approach converts the object's grey values and calculate similarity estimators. Within an optimization process the method is intended to adapt the parameters of the vector field for the best similarity outcome [73]. The main features of IDP are: global registration, transformation, optimization and similarity measures. The sections ends with a discussion about registration of 4DCT breathing geometries. To cover all types of mo-

tion, IDP begins with a split of transformation into a global and a local fraction. This first step enables the distinction of affine or nonrigid movements, as they are used for breathing motion. For this purpose, v_{ij} can be written as [81]:

$$v_{ij}(\vec{x}_j) = v_{ij}^{\text{global}}(\vec{x}_j) + v_{ij}^{\text{local}}(\vec{x}_j) \tag{2.14}$$

Global transformation

The global model describes the overall movement of any static CT set. It is more or less a connection of affine structures like bones or different static shapes of the back. However, the global motion is necessary to initiate the IDP method and to get primary parameters. The trivial approach considers six degrees of freedom for rotation and translation, Additionally, another six degrees of freedom are necessary to depict shearing and scaling, proposed by *Rueckert et al.* [81]. In 3D, any rigid transformation can be written as:

$$v_{ij}(x_j, y_j, z_j)^{\text{global}} = \begin{pmatrix} \theta_{11} & \theta_{12} & \theta_{13} \\ \theta_{21} & \theta_{22} & \theta_{23} \\ \theta_{31} & \theta_{32} & \theta_{33} \end{pmatrix} \cdot \begin{pmatrix} x_j \\ y_j \\ z_j \end{pmatrix} + \begin{pmatrix} \theta_{41} \\ \theta_{42} \\ \theta_{43} \end{pmatrix} \tag{2.15}$$

Regarding their different space directions, $\vec{x}_j$ is splitted into its single coordinate members x_j, y_j, z_j. Rigid transformations are expressed with $\theta_{11} - \theta_{43}$, being the twelve degrees of freedom. This model serves only for the affine registration of all CT spaces. The exact non-rigid description of the movement needs an additional local component.

Local transformation

The affine transformation supposes only the registration of rigid structures inside the CT spaces. Local deformations, such as spatial expansion and compression of lung tissue, need additional components. The deformation of the lung varies significantly across different patients. The deformation can be expressed by v_{ij}, a vector field that contains a number of control points with spatially attached displacements vectors. The deformation field is defined by a linear combination of class or basis functions [47]. Different basic functions were proposed. The most important function is the B-Spline. B-Splines are efficient due to their local behavior. During optimization, the associated parameter adjustments affect the deformation field. However, the modification of spatially limited neighborhoods enables the recalculation of even relevant areas instead of a global remodeling. This is an important advantage and is efficient for any optimization method.
The basic idea of B-Splines on local motion is the deformation of an object by distortion of the underlying mesh. The mesh is a grid structure represented by uniform spaced control points Φ. Φ contains a mesh of $n_x \times n_y \times n_z$ of nodes identified by $\Phi_{o,p,q}$ with uniform spacing δ [81]. The manipulation of the nodal points controls the shape of the 3D object and results in a smooth continuous transformation. The one dimensional version of a B-Spline is a piecewise polynomial. The three dimensional B-Spline for FFD can be written as a 3D tensor product of the familiar one dimensional cubic B-Spline [116]. Thus, the local transformation of v_{ij} is defined by:

$$v_{ij}(x_j, y_j, z_j)^{\text{local}} = \sum_{l=0}^{3} \sum_{m=0}^{3} \sum_{n=0}^{3} B_l(u) B_m(v) B_n(w) \Phi_{o+l,p+m,q+n} \tag{2.16}$$

The full image volume in J is limited to $\Omega_j = \left\{(x_j, y_j, z_j) | 0 \leq x_j < X, 0 \leq y_j < Y, 0 \leq x_j < X\right\}$. The value of the subscripts o, p, q is defined by the relation of desired coordinate x_j, y_j, z_j and the nearest control points in Φ

[81]. Hence, o, p, q references the number of the specific control in the respective direction:

$$o = \lfloor \frac{x_j}{n_x} \rfloor - 1, \quad p = \lfloor \frac{y_j}{n_y} \rfloor - 1, \quad q = \lfloor \frac{z_j}{n_z} \rfloor - 1 \tag{2.17}$$

Furthermore, u, v, w define the distance to the direction related lower control point [81]:

$$u = \frac{x_j}{n_x} - \lfloor \frac{x_j}{n_x} \rfloor, \quad v = \frac{y_j}{n_y} - \lfloor \frac{y_j}{n_y} \rfloor, \quad w = \frac{z_j}{n_z} - \lfloor \frac{z_j}{n_z} \rfloor \tag{2.18}$$

The respective local Spline function B is defined by the distance u, v, w. The polynomial degree of the basis is described by its subscript. Exemplary for all three space directions, the four polynomials of $B_l(u)$ representing the l^{th} basis of the B-Spline can be written as [81]:

$$\begin{aligned} b_0(u) &= \frac{(1-u)^3}{6} \\ b_1(u) &= \frac{3u^3 - 6u^2 + 4}{6} \\ b_2(u) &= \frac{-3u^3 + 3u^2 + 3u + 1}{6} \\ b_3(u) &= \frac{u^3}{6} \end{aligned} \tag{2.19}$$

With the aid of this procedure the full transformation is only defined with the description of the mesh respectively with the definition of the control points. The equations (2.17), (2.18), (2.19) enable the calculation of any transformation $v_{ij}(x_j, y_j, z_j)$ in Ω_j simply by knowing the coordinates of the mesh $\Phi_{o,p,q}$. Any distortion of the control points locally modifies the transformation. The local deformation based on B-Splines is illustrated in Fig. 2.7. The local support of the model is clearly visible, i.e. the modification of any control point $\Phi_{o,p,q}$ affects the transformation only in its spatial neighborhood. Hence, $\Phi_{o,p,q}$ act as parameter for the FFD optimization process. The resolution of the mesh defines the degree of modeling. A large spacing with a low value of nodes is suitable for a global nonrigid deformation. A finer spacing enables the local transformation of highly non-rigid structures. The value of control points is equivalent to the number of degrees of freedom in the optimization process. There exists a direct dependency between the value of nodes and the computational efficiency. For example, a FFD field with $10 \times 10 \times 10$ nodes results in an optimization with 3000 degrees of freedom [81].

However, to get the best compromise between resolution and efficiency, a hierarchical multi-step approach has gained acceptance. The method starts with a coarse mesh and proceeds stepwise to finer structures. The hierarchy is denoted by $\Phi^1, \Phi^l, ..., \Phi^L$, whereas the superscript l identifies the step of the optimization. The resolution of the control mesh increases with l. The respective transformation $[v_{ij}(x_j, y_j, z_j)^{\text{local}}]^l$ is derived from Φ^l. The sum of all steps is the total local transformation written as [81]:

$$v_{ij}(x_j, y_j, z_j)^{\text{local}} = \sum_{l=1}^{L} \left[v_{ij}(x_j, y_j, z_j)^{\text{local}} \right]^l \tag{2.20}$$

During calculation, the mesh successively refines itself. A control point mesh at level $l+1$ results by insertion of new control points in l. The value of new control points in Φ^{l+1} is directly computable with the aid of $[v_{ij}(x_j, y_j, z_j)^{\text{local}}]^l$ and the respective B-spline subdivision.

In general, local transformations are characterized as smooth transformations. Smooth transformations are employed not only for modeling thorax geometries, but also for many other dynamic structures [81]. The

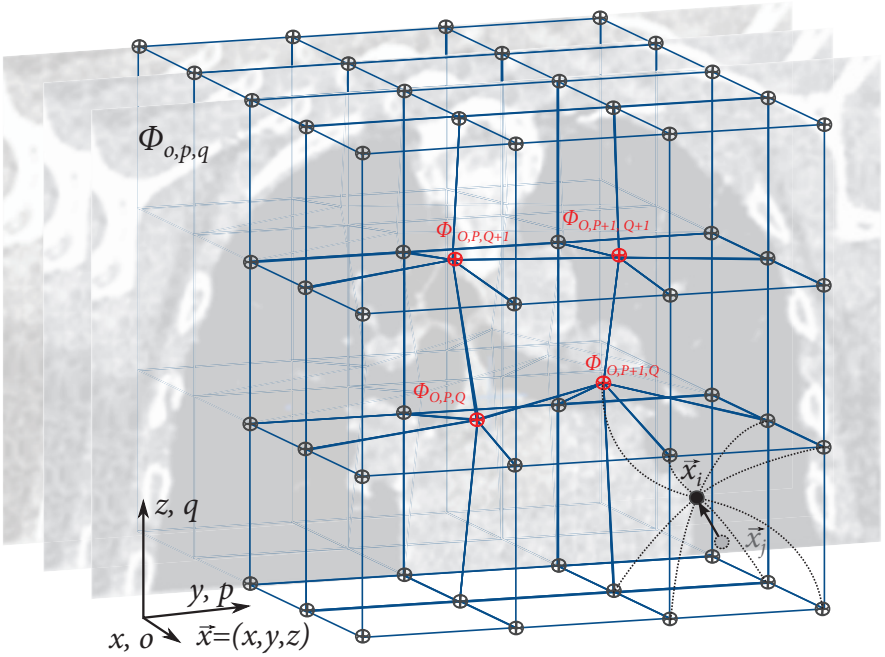

Figure 2.7 : Local transformation with B-Splines: A regular mesh defined by certain control points $\Phi_{o,p,q}$ (black nodes) forms the space of image transformation. The deformation of the space is performed by single control point distortions (red nodes). The B-Splines enable the transformation of any point $\vec{x}_j = (x_j, y_j, z_j)$ merely with the aid of the shifted nodes. For example, $\vec{x}_j$ (grey) is transformed to $\vec{x}_i$ (black) due to the distortion of $\Phi_{O,P+1,Q}$ (red).

deformation transformation $v_{ij}(x_j, y_j, z_j)^{\text{local}}$ is limited by a penalty term. This term regularizes the transformation and enables the smooth FFD. *Rueckert et al.* proposed the following penalty term:

$$C_{smooth}(v_{ij}) = \frac{1}{V_{\Omega_j}} \int_0^X \int_0^Y \int_0^Z \left[\left(\frac{\partial^2 v_{ij}}{x^2} \right)^2 + \left(\frac{\partial^2 v_{ij}}{y^2} \right)^2 + \left(\frac{\partial^2 v_{ij}}{z^2} \right)^2 + 2\left(\frac{\partial^2 v_{ij}}{xy} \right)^2 + 2\left(\frac{\partial^2 v_{ij}}{xz} \right)^2 + 2\left(\frac{\partial^2 v_{ij}}{yz} \right)^2 \right] \cdot dx \cdot dy \cdot dz \tag{2.21}$$

V_{Ω_j} represents the Volume of the image domain Ω_j. C_{smooth} is a typical model for a bending energy [6] and acts like a smoothing filter directly on the deformation field. C_{smooth} is zero for affine transformations. Hence, C_{smooth} affects mostly local non-rigid deformations. C_{smooth} is very important for the registration of 4DCT lung data sets. It ensures the homogeneity of the calculated vector field and avoids unrealistic vortices.

Similarity measures

The goal of DIR is to find the most realistic match of I and J. To find the perfect position of the proposed control points $\Phi_{o,p,q}$, a verification function is necessary. The similarity is a comparison of the parameter between two signals inside the various image spaces $I(\vec{x}_i), J(\vec{x}_j)$. The registration tries to find the transformation $v_{ij}(x_j)$ that maps each point x_j of an image J to the most similar point x_i within image I. During optimization, the similarity measure provides a function that computes the affinity of two signals. A basic approach for similarity is the sum of squared grey value differences (SSD). The SSD criterion for the transformed image

$(v_{ij} * J)(\vec{x})$ can be written as [73]:

$$SSD_J(v_{ij}) = \int \left[(v_{ij} * J)(\vec{x}_i) - I(\vec{x}_i)\right]^2 \cdot dx \tag{2.22}$$

The goal of the optimization is to find the minimum of the SSD. v_{ij} assumes the right overlapping of similar structures, then corresponding grey values are eliminated. SSD works great in mono-modal cases, i.e. registration of images that are acquired with the same technique (e.g. all image sets of a 4DCT). Their intensity values identify the same structures with the same signal. However, SSD is not applicable for multi-modal registration due to the different representation of signal intensities. SSD is very sensitive to values with large intensity differences (outliers). SSD is used in registrations with images that differ only by noise. From a numerical point of view, SSD can be quickly calculated. Hence, it can be combined with any complex optimization algorithm, e.g. the Newton approach or the conjugated gradient technique [47] [31].
Another, more robust approach, is the cross correlation (CC). CC assumes a linear relationship between different image signals. CC is defined by [94]:

$$CC_J(v_{ij}) = \frac{\int \left[(v_{ij} * J)(\vec{x}_i) \cdot I(\vec{x}_i)\right] dx}{\sqrt{\int (v_{ij} * J)(\vec{x}_i)^2 dx} \cdot \sqrt{\int I(\vec{x}_i)^2 dx}} \tag{2.23}$$

This quadratic term is a numerical efficient and is combinable with many optimization schemes. Despite the consideration of linear shifts inside the image signals, CC is not applicable for multi-modal image registrations as a global linear transformation function cannot be presumed. However, the approach is sufficient for the registration of 4DCT data sets. It should be the first choice for breathing induced fusion of several CT sets due to its robustness. For visualization, Fig. 2.8 illustrates a two-dimensional example of CC.
The following two measures introduce values for multi-modal image registration. CC also works for multi-modal registration, if the investigated area is sufficiently small, i.e. local neighborhoods in the image. This is because of the validity of linear dependencies in small regions. Hence, for a real multi-modal registration, one has to square and accumulate the local values of CC. Then, it is possible to compare total different signals, even positive and negative correlated transitions. The adjusted approach is known as local correlation (LC) and is defined by [47]:

$$LC_J(v_{ij}) = \left[\frac{1}{n} \cdot \sum_S \left(\frac{\int_{\vec{x}_i \in S} \left[(v_{ij} * J)(\vec{x}_i) \cdot I(\vec{x}_i)\right] dx}{\sqrt{\int_{\vec{x}_i \in S} (v_{ij} * J)(\vec{x}_i)^2 dx} \cdot \sqrt{\int_{\vec{x}_i \in S} I(\vec{x}_i)^2 dx}} \right)^2 \right]^{\frac{1}{2}} = \left[\frac{1}{n} \cdot \sum_S CC_J(v_{ij}, S)^2\right]^{\frac{1}{2}} \tag{2.24}$$

For this approach image J is splitted in n sub-regions S. Hence, multi-modal comparison is enabled due to the condition of linear dependencies in sufficiently small areas S.
The information theory enables also measures for multi-modal registration. The basic idea is to measure the similarity of independent distributed variables such as the image signals I and J. From this one can derive the mutual information (MI). The MI describes the power of the statistical dependence of the different images. It is defined by [47]:

$$MI_J(v_{ij}) = \int \int p\left[(v_{ij} * J)(\vec{x}_j), I(\vec{x}_i)\right] \cdot \log\left(\frac{p[(v_{ij} * J)(\vec{x}_j), I(x_i)]}{p[(v_{ij} * J)(\vec{x}_j)] \cdot p[I(\vec{x}_i)]} \right) \cdot dx_j dx_i \tag{2.25}$$

$p\left[(v_{ij} * J)(\vec{x}_j), I(\vec{x}_i)\right]$ is the joint histogram of the transformed image $(v_{ij} * J)(\vec{x}_j)$ and the target image I. $p[I(\vec{x}_i)]$ describes the probability distribution of the values in I respectively in the transformed image $(v_{ij} * J)(\vec{x}_j)$. MI is a value that describes the distribution of two independent values in relation to their

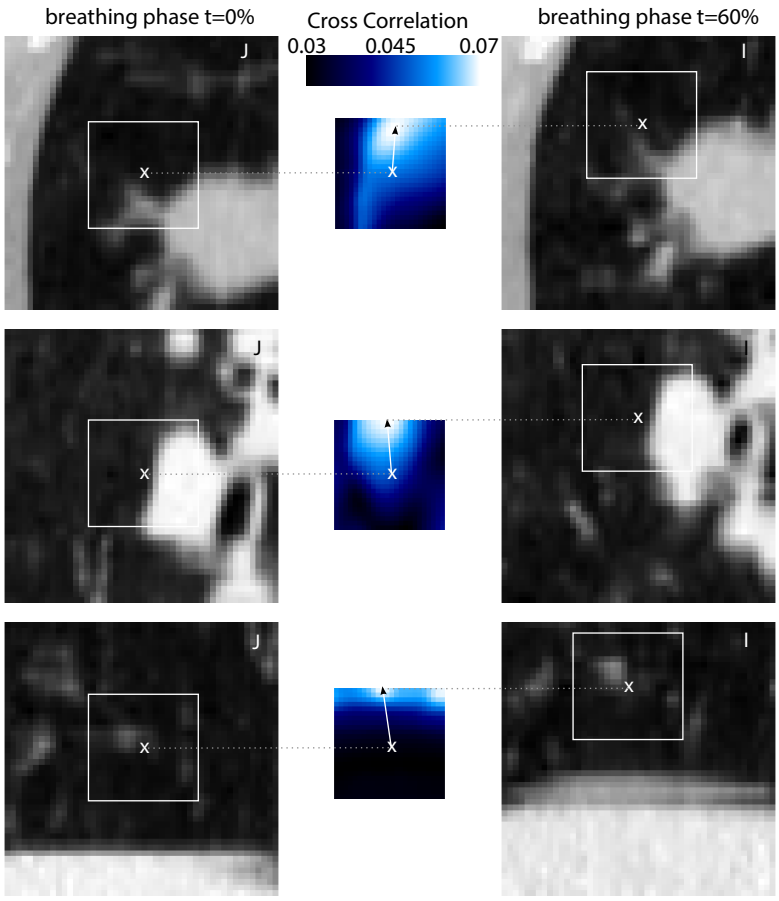

Figure 2.8 : Example calculation for the CC similarity measure: The figure illustrates a two-dimensional calculation of a ROI based CC for a respiratory 4DCT. The left side shows three areas of a static CT space (t = 0 %). Every area contains a quadratic ROI with a center. The right side shows the spatial related areas at the breathing phase t = 60 %. The best registration of the ROI at t = 0 % in t = 60 % is also emphasized on the right side. The middle shows the spatial distribution of the CC value when the center of the ROI (0 %) is pushed over the target structure (60 %). The maximum CC is white, the minimum CC is black. The individual maximum is characterized with the corresponding displacement vector. All introduced similarity measures work similarly.

overlapped distributions. Hence, if signal pairs $I(\vec{x}_i)$ and $J(\vec{x}_i)$ occur very often overlapped and rarely alone, then it is an indication for a good registration and vice versa. MI is a robust solution, but not time efficient compared to SSD or CC. However, MI has become the accepted standard for image registration of multi-modal applications in medical solutions [54].

Optimization

The calculation of the optimal transformation is controlled by the global cost function [81] $\mathcal{C}$, which derives from the full transformation v_{ij} (2.14) and its corresponding global (2.15) and local (2.16) equations, as well as the penalty term (2.21) for smoothness and the similarity measure (2.23). Hence, for $\mathcal{C}$ applies as follows:

$$\mathcal{C}(\Theta, \Phi) = -S_J(v_{ij}(\Theta, \Phi)) + \lambda C_{smooth}(v_{ij}(\Theta, \Phi)) \tag{2.26}$$

with Θ being the parameters of the global registration, Φ being the FFD control points of the local transformation. This cost function is associated with image registration of a respiratory 4DCT. S_j is used as similarity

measure (SSD, CC, MI ,LC). The minimization of $\mathcal{C}$ is the intention of the global optimization process, wherein the method tries to find a solution for two competing goals. On the one side, the optimization has to find v_{ij} with the most similar $(v_{ij} * J)(\vec{x})$ in comparison to I controlled by $S_J(v_{ij})$. On the other side, $v_i j$ should be as smooth as possible for the most realistic breathing simulation of the vector field. The latter is determined by $C_{smooth}(v_{ij})$. The compromise parameter for both constraints is λ. It regulates the power of C_{smooth} in relation to S_J. For many applications, λ is determined by trial and error. In general, $\lambda = 0.01$ provides a good compromise [81]. λ has more impact to a high control point resolution. The first calculation steps with a low value of nodal points remain unaffected. The following algorithm provides a simple technique for the minimization of $\mathcal{C}$:

Algorithm 1 FFD optimization with the gradient descent method based on *Rueckert et al.* [81]

1: **calculate** the global transformation (*maximization of* S_J):
$\Theta = \underset{\Theta \in \mathbb{R}^{12}}{\operatorname{argmax}} \left[S_J(v_{ij}(\Theta)^{\text{global}}) \right]$
2: **initialize** the control points Φ_0^0
3: **for** $l = 0$ **to** $l = L$ {→ iterator for the control point resolution, see (2.20)} **do**
4: $k = 0$ { → iterator for the optimization progress}
5: **repeat**
6: **calculate** the gradient vector of the cost function $\mathcal{C}$ with respect to Φ_k^l:
$\nabla \mathcal{C} = \frac{\partial \mathcal{C}(\Theta, \Phi_k^l)}{\partial \Phi_k^l}$
7: **calculate** the new control points:
$\Phi_{k+1}^l = \Phi_k^l - \mu \cdot \frac{\nabla \mathcal{C}}{||\nabla \mathcal{C}||}$
8: $k = k + 1$
9: **until** $||\nabla \mathcal{C}|| \leq \xi$
10: **calculate** the new control point field Φ_0^{l+1} through insertion in Φ_k^l *(B-Spline sub-divsion)*
11: **end for**

The scheme in algorithm 1 optimizes the global transformation with the aid of gradient descent (GD). The GD method is a simple numerical approach for a non-linear optimization. The transformation process registers at first the static CT spaces via global transformation (algorithm 1→ step 1). Therefore, the global parameters Θ are adjusted through maximization of the similarity measure S_J. The result is a global affine transformation. Then, the actual optimization (GD) begins. The optimization parameters Φ_k^l for the algorithm are initialized at the lowest control point resolution in a regular grid Φ_0^0. The algorithm starts the optimization with the calculation of the cost functions gradient $\nabla \mathcal{C}$ (algorithm 1→ step 6). With the aid of the gradient, the new control point set is calculated Φ_0^1, which is closer to the optimum. The approximation to the minimum of $\mathcal{C}$ follows the rules of gradient descent. The optimization iterates in negative direction of the gradient with a certain step size μ. The approximation process repeats until a sufficient small gradient is reached. The stopping value is defined by ξ, a positive small score. A sufficient small gradient is an indication for the local optimum of $\mathcal{C}$ with regard to Φ_k^0. Hence, the best configuration for the respective resolution is found. The full optimization is repeated for finer control point resolutions $l + 1 \rightarrow L$, wherein the start parameters Φ_0^{l+1} of every new sub-level $l + 1$ are calculated from the optimized values Φ_k^l of the last sub-step l with B-Spline based insertion of additional control points (algorithm 1→ step 10).

The basics of the mentioned optimization scheme is identical for all optimization algorithms. The mentioned idea is illustrated in Fig. 2.9 using the data of a respiratory 4DCT. In addition to GD, a number of various optimization models exists: the Newton-approach, the Quasi-Newton-approach and the conjugated gradient (CG) technique [31]. In the field of DIR, CG is especially used widely. The advantage of CG in comparison to GD is the lower number of iteration steps (here: k) inside a single optimization cycle. Usually, CG needs

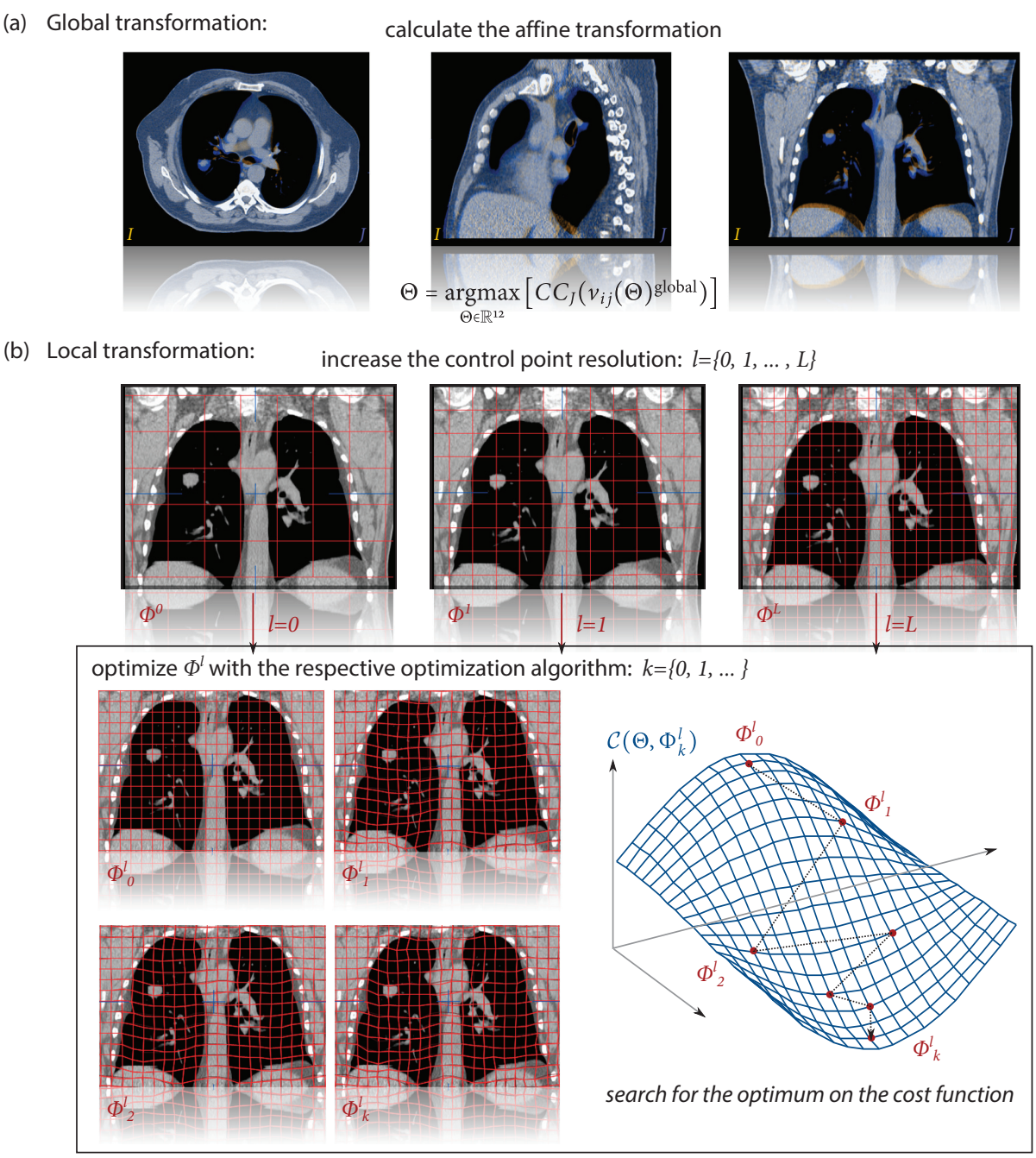

Figure 2.9 : Basic idea of DIR with IDP: The full deformation with IDP is splitted into a global (a) and a local (b) transformation. (a) is an affine overlapping of two rigid image structures in axial, coronar and sagital view (gold → I, blue → J). (b) is the actual non-rigid optimization realized with two iteration processes. The outer loop increases the nodal point resolution Φ^l. The inner loop optimizes the given mesh with the respective optimization model (e.g. GD, CG).

less than half of the iteration steps. This is very important due to the large number of free parameters. The fast conversation is caused by a memory variable, which includes, additionally to the current gradient $\nabla \mathcal{C}^l_k$, the gradient of the past iteration $\nabla \mathcal{C}^l_{k-1}$. Due to gradient memory, the algorithm chooses an improved search direction for the new parameters. The most important methods of CG are the approaches of *Fletcher and Reeves* and the modification of *Polak and Riebiere* [31]. Algorithm 2 introduces the FFD optimization with CG:

Algorithm 2 FFD optimization with the conjugated gradient technique

1: **calculate** the global transformation (*maximization of* S_J):
$\Theta = \underset{\Theta \in \mathbb{R}^{12}}{\operatorname{argmax}} \left[S_J(v_{ij}(\Theta)^{\text{global}}) \right]$
2: **initialize** the control points Φ_0^0
3: **for** $l = 0$ **to** $l = L$ {→ iterator for the control point resolution, see (2.20)} **do**
4: $k = 0$ { → iterator for the optimization progress}
5: **initialize** the line search d_0:
$d_0 = -\nabla \mathcal{C}_0^l = -\frac{\partial \mathcal{C}(\Theta, \Phi_0^l)}{\partial \Phi_0^l}$
6: **repeat**
7: **calculate** the new control points:
$\Phi_{k+1}^l = \Phi_k^l + \mu \cdot d_k$
8: **calculate** the memory term:
$\underbrace{\beta_k = \frac{\|\nabla \mathcal{C}_{k+1}^l\|}{\|\nabla \mathcal{C}_k^l\|}}_{\text{Fletcher and Reeves}}$ or $\underbrace{\beta_k = \frac{\nabla \mathcal{C}_{k+1}^{l\ T} \cdot (\nabla \mathcal{C}_{k+1}^l - \nabla \mathcal{C}_k^l)}{\|\nabla \mathcal{C}_k^l\|}}_{\text{Polak and Riebiere}}$
9: **initialize** the new line search:
$d_{k+1} = -\nabla \mathcal{C}_{k+1}^l - \beta_k d_k$
10: $k = k + 1$
11: **until** $d_k \leq \xi$
12: **calculate** the new control point field Φ_0^{l+1} through insertion in Φ_k^l *(B-Spline sub-divsion)*
13: **end for**

Suitability of IDP for respiratory motion problems

The full registration of a 4DCT data set serves for evaluation of the IDP process regarding respiratory motion handling. This test uses the 4DCT patient data of the *POPI-model* [105], a Point-validated Pixel-based Breathing Thorax Model. It is provided by the *Léon Bérard Cancer Center* and the *CREATIS Laboratory* (Lyon, France). The used IDP registration follows the rules of the shown FFD procedure based on *Rückert et al.* [81]. DIR was performed with the aid of the software framework *iPlan™ RT* (*Brainlab AG, prototype*). For the best possible outcome this test uses an advanced solution of the FFD optimization with the conjugated gradient technique. This specific process sequence is the result of an experimental verification (trial and error). This scheme leads to the best results in the experiments of this work and is based on algorithm 2. The approach is optimized for the best quality without calculation time minimization. Algorithm 3 explains the used configuration.

The experiment mentioned in this section describes the registration between the reference set i and a breathing phase j. The method works with two resolution parameters. The control point resolution Φ^l increases with R as shown in the basic algorithm of CG (algorithm 2). The second parameter is the image data resolution I, which ensures that the registration process registers rough structures (e.g. $I[0] = 8$) at first. This is important for a positive outcome. At first the optimization algorithm has to find global, large motion structures. With progressive calculation time the algorithm increases the image data resolution (e.g. $I[3] = 2$) to find detailed, local motion spots. The combination of both resolution parameters lead to the optimal registration. The procedure works using a windowing of all HU-values. A switch between bone and lung windowing procedures does not produce better results.

The next improvement is the combination of two similarity measures. Different similarity measures may result in different deformation fields as they affect the cost function $\mathcal{C}$ with different sensibility values. This lead to different parameter settings and lastly to a different deformation. It is part of an experimental verification

Algorithm 3 Customized implementation of IDP (FFD with CG)

calculate the global transformation (*maximization of* S_J) with $S_J = CC$
initialize the control point resolution array $R = [64, 32, 16, 8]$
  control point resolution → isotropic voxel distance between each node Φ
initialize the image resolution array $I = [8, 4, 3, 2, 1]$
  resolution of the image data: voxel unification, e.g. 8 → 8x8x8 voxels receive one HU value
for $l = 0$ **to** $l = 3$ **do**
  set Φ_0^l with R[l] → *set control point resolution with B-Spline sub-division*
  if $l == 0$ {*control point resolution → 64 voxels per node*} **then**
    set $S_J = MI$ → *use Mutual Information*
    set image resolution with $I[0]$
    optimize Φ_k^l with CG and β_k = *Polak and Riebiere* (see algorithm 2)
  else if $l == 1$ {*control point resolution → 32 voxels per node*} **then**
    set $S_J = MI$ → *use Mutual Information*
    for $i = 0$ **to** $i = 1$ **do**
      set image resolution with $I[i]$
      optimize Φ_k^l with CG and β_k = *Polak and Riebiere* (see algorithm 2)
    end for
  else if $l == 2$ {*control point resolution → 16 voxels per node*} **then**
    set $S_J = MI$ → *use Mutual Information*
    for $i = 1$ **to** $i = 3$ **do**
      set image resolution with $I[i]$
      optimize Φ_k^l with CG and β_k = *Polak and Riebiere* (see algorithm 2)
    end for
  else if $l == 3$ {*control point resolution → 8 voxels per node*} **then**
    set $S_J = LC$ → *use Local Cross Correlation*
    for $i = 3$ **to** $i = 4$ **do**
      set image resolution with $I[i]$
      optimize Φ_k^l with CG and β_k = *Polak and Riebiere* (see algorithm 2)
    end for
  end if
end for

to find the best model for the respective application. Generally in this work, MI acquired the most accurate results for this exemplary 4DCT registration. MI is not the fastest model. Also, MI seems to be overstressed for many control points Φ and large image data resolutions. Hence, MI has been replaced by LC in the last processing cycle (see algorithm 3 → $l = 3$), which generates more accurate results in total.

The results of the explained registration strategy are described in Fig. 2.10. It shows the motion vector fields for the registration of the two most apart breathing sequences. The reference set (i) is equivalent to the maximum inhale position and the breathing phase ($j = 6$) represents the peak of the exhale position. The figure shows the CT data of the reference set and the distance vectors that illustrate the movement from $\vec{x}_i$ to $\vec{x}_j$ with $\vec{x}_j = v_{ji}(\vec{x}_i)$. Exemplary planes are visualized in three different views (a → coronal, b → sagital, c → axial). Furthermore, the figure compares the results of the customized IDP implementation of this work (left) and the results of the published (POPI-model) parametric deformation model (right). This deformation model is also an advanced implementation of the already described FFD method and works similarly. The parametric model is described in *Vandemeulebroucke et al.* [105].

The assessment of the shown vector fields can only be performed subjectively. Both implementations (1,2)

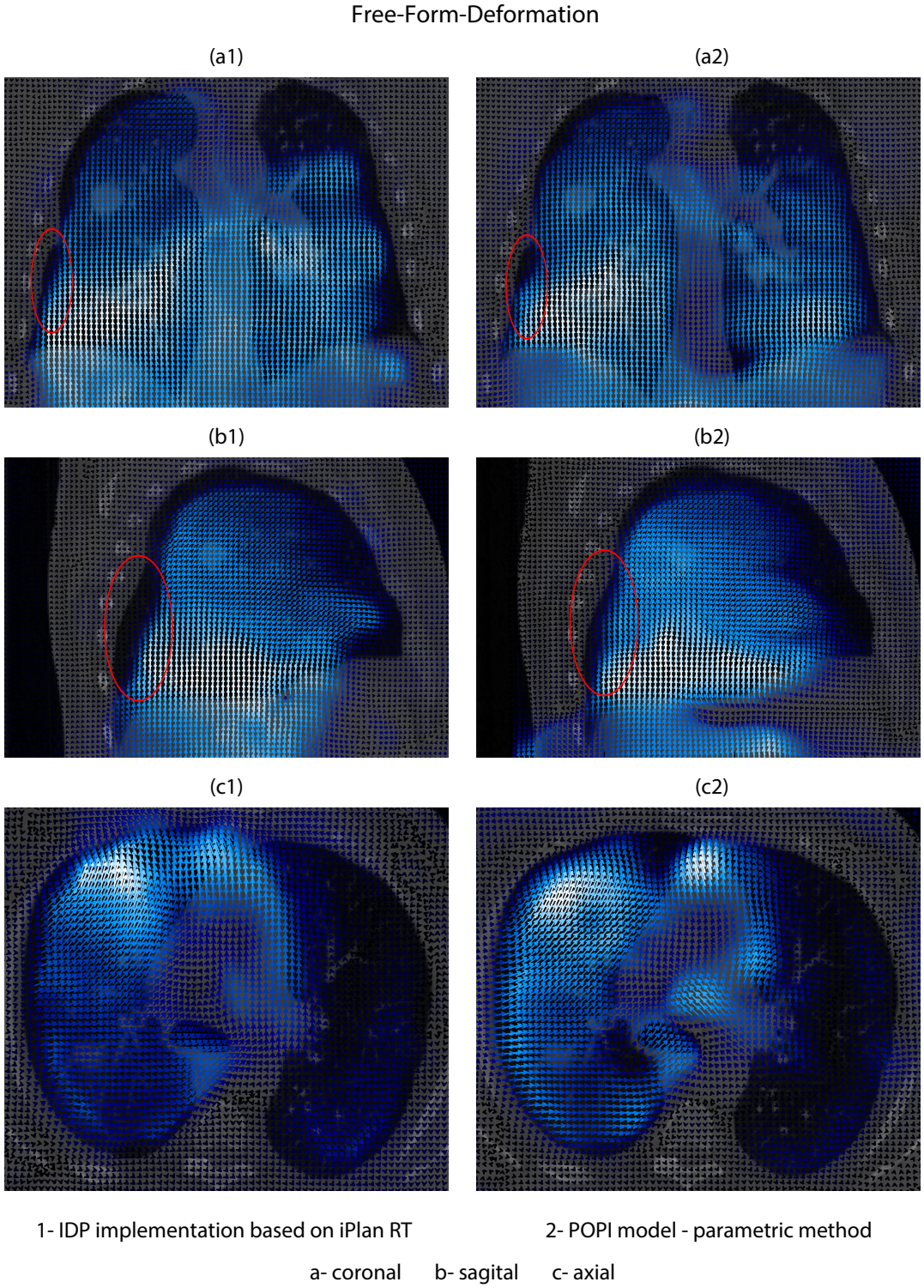

Figure 2.10 : Registration of 4DCT data with FFD: This illustration shows the CT data of the reference set i (inhale) and the distance vectors that illustrate the movement from $\vec{x}_i$ to $\vec{x}_j$ (exhale). The figures describe the resulting vector motion fields for three exemplary planes in three different views (a,b,c). Every view shows the projected 2D displacement for the respective plane. The left side visualizes the results of the IDP implementation shown in algorithm 3. The right side illustrates the results based on the FFD implementation published in the scientific POPI-model [105]. Dark blue or black (minimum) scaled vectors are equivalent to minimal motion. Large movements are shown in bright blue or white (maximum) colors. The red zones enclose areas with underestimated motion at the borders of the lung.

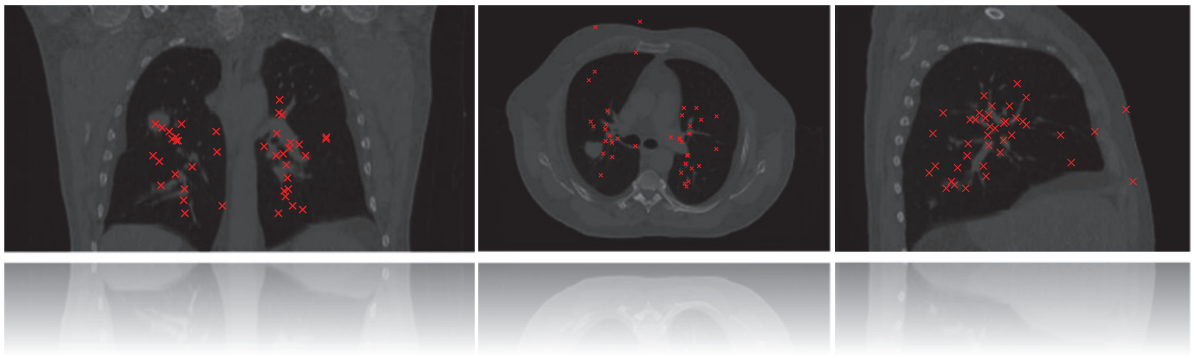

Figure 2.11 : Landmarks for qualitative assessment: The POPI-model [105] came with 40 landmarks identified by medical experts. Every landmark is located in each single breathing phase. This figure shows the projected position of every investigated landmark for the respective body plane based on the reference set. The deformation is assessable with the aid of the target registration error.

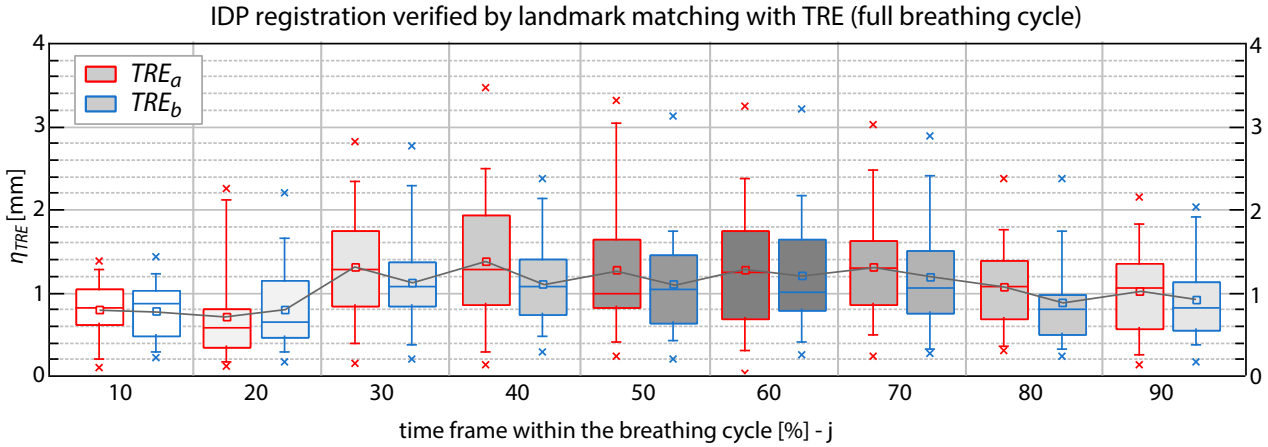

Figure 2.12 : Target registration error (TRE) for a full 4DCT registration: This figure visualizes the results for a full registration of the data inside the POPI-model. The Box-Plot shows $\eta_{\mathrm{TRE}}[mm]$ for the set of 40 landmarks in relation to all breathing phases j. The percentage progress at the abscissa describes the time j within the breathing cycle. j = 60 % is equivalent to the maximum exhale. 10 % and 90 % are closed to the inhale (reference set i) position. The plot distinguishes between the results of the IDP implementation based on *iPlan™ RT* (TRE_a) and the FFD implementation of the POPI-model (TRE_b). The results of every time frame are based on the registration of the reference set i and the respective breathing phase j. The plot illustrates the behavior of the error with increasing motion. 60 % represents the largest shift.

work according to the introduced FFD principle. Thus, the evaluation refers to the model presented in the previous section. Both vector fields show a physiologically plausible behavior. That means, they display the trigger points that cause the physiological respiration process. Fig. 2.14.b shows two muscular actions which are responsible for the physiology. Breathing is caused through a longitudinal diaphragm movement and a lateral rib cage expansion. Both points are visualized in Fig. 2.10. Especially at the sagital view (b1, b2 → diaphragm motion) and the axial view (c1, c2 → rib cage motion), maximum motion areas are found exactly at the mentioned physiologic structures. A subjective plausibility test is not enough to prove the suitability of the FFD model for the registration of 4DCT data. However, it shows that the model is capable of covering anatomical movement. A qualitative scientific assessment is possible with landmarks detection. Landmarks were identified by medical experts. They are located at anatomical recognizable structures, e.g. bronchial bifurcation or points of the bronchial tree. 40 landmarks are provided within the POPI-model. By calculating the distance between these points and the corresponding deformed points proposed by the model (based

Table 2.1 : Mean and maximum values of the target registration error for a full 4DCT registration: This table displays the exact values for a full registration of the data inside the POPI-model. The first column identifies the original distance of the landmarks. The following columns visualize the TRE values (mean and maximum) distinguished between the results of the IDP implementation based on *iPlan™ RT* (TRE_a) and the parametric FFD implementation of the POPI-model (TRE_b).

time frame		mean distance	mean η_{TRE_a}	mean η_{TRE_b}	max. η_{TRE_a}	max. η_{TRE_b} [mm]
10 %	$j = 1$	0.5	0.8	0.8	1.4	1.5
20 %	$j = 2$	0.5	0.7	0.8	2.2	2.2
30 %	$j = 3$	2.2	1.3	1.1	2.8	2.8
40 %	$j = 4$	4.3	1.3	1.1	3.4	2.4
50 %	$j = 5$	5.8	1.3	1.2	3.3	3.2
60 %	$j = 6$	6.1	1.3	1.2	3.2	3.2
70 %	$j = 7$	5.0	1.3	1.1	3.0	2.9
80 %	$j = 8$	3.7	1.0	0.9	2.3	2.3
90 %	$j = 9$	2.1	1.0	1.0	2.1	2.0
total		3.3	1.1	1.0	3.4	3.2

on the reference phase), a target registration error (TRE) can be calculated [105]. The TRE for a landmark coordinate $\vec{l}_j$ inside the breathing phase j is defined as:

$$\eta_{TRE} = \left|\vec{l}_j - v_{ji}(\vec{l}_i)\right| \tag{2.27}$$

with $\vec{l}_i$ being the position of the respective landmark inside the reference geometry i. The vector field v_{ji} describes the predicted landmark position generated by the deformation model. To prove the quality of the FFD regarding 4DCT registration this experiment calculated the TRE for the full breathing cycle based on POPI-model data. The results of the suitability test are shown in Fig. 2.12. Additionally, it is distinguished between the IDP implementation of this work TRE_a and the FFD approach of the parametric POPI-model TRE_b (see Fig. 2.10).

The main conclusion of this test is the general suitability of FFD for a full 4DCT registration. This can be proven with low average error values for every time dependent vector field. The exact values are displayed in Tab. 2.1. The table shows that the total mean TRE (for all breathing phases) is 1.1 mm for TRE_a and 1.0 mm for TRE_b. All mean values (a,b) vary around 1.0 mm for every single breathing phase. The overall maximum values are 3.4 mm for TRE_a and 3.2 mm for TRE_b. They are distributed from 2.0 mm to 3.0 mm within the respiratory cycle. Taking into account that all images have a slice spacing of 2 mm, consequently, landmark identification can induce an error of up to 2 mm [105] and the results of both models are acceptable. A more detailed investigation of Fig. 2.12 reveals that all distributions of TRE_b are more accurate than the results of TRE_a. Indeed both methods cause satisfactory results, but the distributions of TRE_b are slighty more compressed and the values are stronger shifted to lower errors (e.g. $j = 5$). However, there exist no systematic difference. This can be proven by a detailed analysis shown in Fig. 2.13. The results investigate the most apart time frame ($j = 6$). There are no significant differences visible, neither in a space oriented view (x,y,z) nor in a systematic landmark investigation (Bland-Altman plot). In contrast to TRE_a, the model of TRE_b simply seems to be a more complex and a more detailed implementation strategy of the shown FFD approach. The exact strategy is not published [105]. Generally, it can be said that FFD includes great capabilities to register a global 4DCT patient geometry. The landmark tests have clearly shown the mentioned potential.

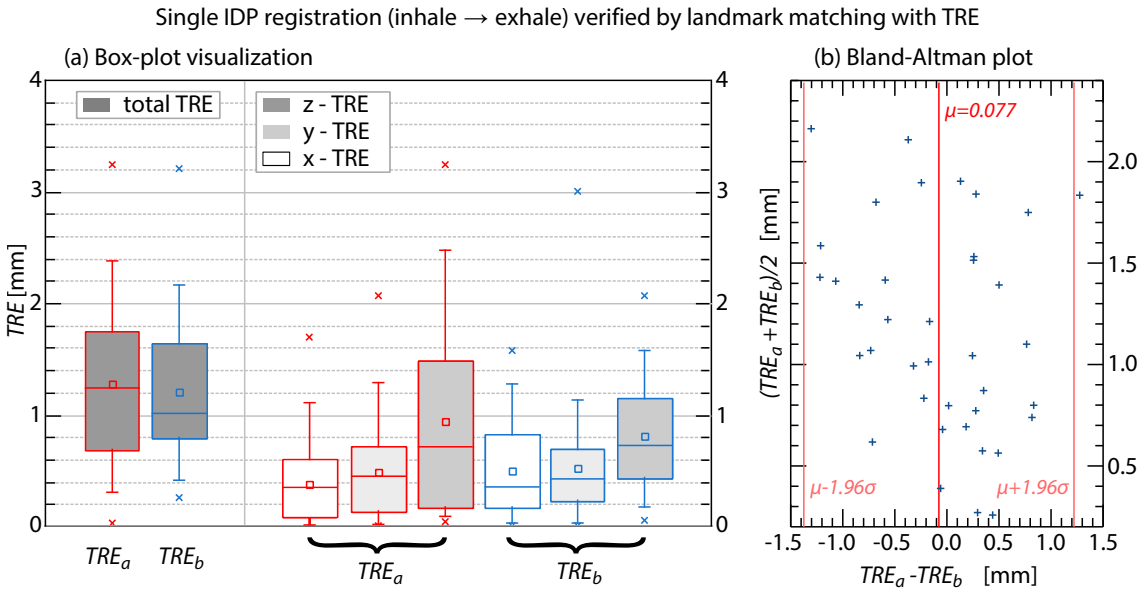

Figure 2.13 : Detailed analysis of the TRE for a single time frame: This analysis regards to the time frame $j = 6$ (60 %) (see Fig. 2.12). It shows a splitted Box-Plot in (a) with space oriented distinction (x,y,z). The view shows the error fraction for every single coordinate axes. The Bland-Altman plot (b) investigates systematic differences between both models (TRE_a, TRE_b). The result of every single landmark is investigated. The ratio of the mean value and difference of both measurement models is the sole criterion. A shift of all landmarks to the left/right or the top/bottom is significant for systematic differences. This is not the case here. It is a homogeneous scattered plot distributed over the full area without point clouds or peaks.

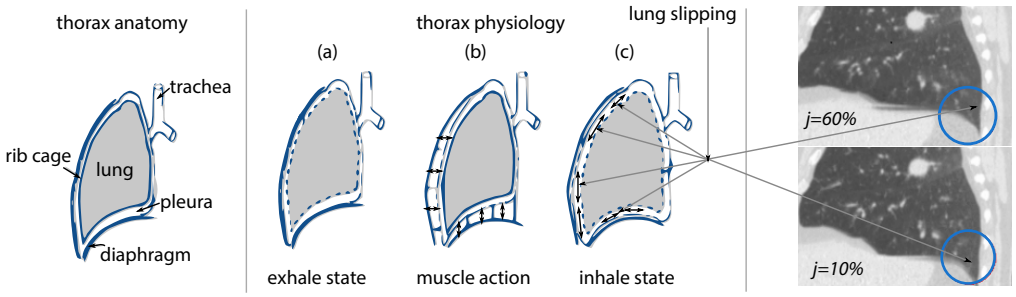

Figure 2.14 : The lung slipping effect: The sketch on the left side illustrates the basic lung anatomy with its most important components. The sequence in the middle explains the physiology of the breathing process. (a) → The initial state with the deflated compressed lung. (b) → Due to muscle action at the diaphragm and the rib cage expanses and the air inflates into the lung. (c) → During inflation the shape of the lung moves freely along the pleura interstice, while outer structures firmly remain (e.g. rib cage). This behavior is called lung slipping. The example image data on the right visualizes the lung slipping effect. The figure is inspired by [109].

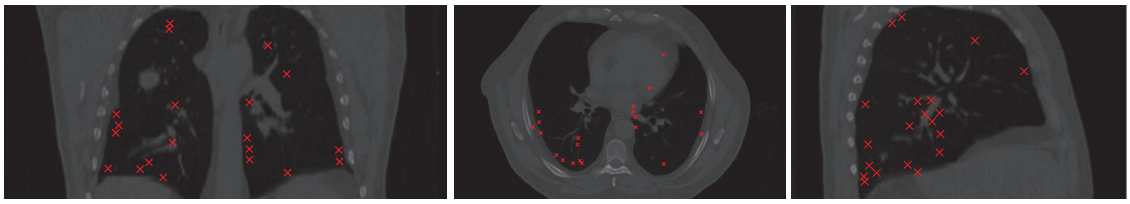

Figure 2.15 : Advanced landmarks in lung border areas: These additional 20 landmarks are related to the breathing phase $j = 6$ (60 %) and the reference set i. All coordinates are located near the shape of the lung to measure the motion estimation in critical border areas.

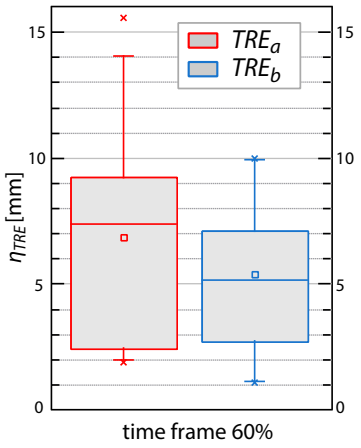

Figure 2.16 : TRE analysis for lung border area landmarks: This Box-Plot evaluation investigates the TRE error η_{TRE} for advanced landmarks located in lung slipping areas. The data is only acquired for the time frame (60 %) with the largest landmark shift (breathing amplitude). The plot distinguishes between the results of the IDP implementation based on *iPlan™ RT* (TRE_a) and the FFD implementation of the POPI-model (TRE_b).

A close look on the deformation fields in Fig. 2.10 and the landmark distribution in Fig. 2.11 initializes detailed investigation. These landmarks do not cover the full lung. They are mainly located in medial regions, which are most the important, but they do not cover the full motion area. Regions near the lung shape (lung borders like the rib-cage or the diaphragm, see Fig. 2.14) are neglected. The physiology of the lung and the breathing process is also explained in Fig. 2.14. The outcome of this investigation is an expected homogeneous motion within the full lung. Border areas underlie a similar movement as the medial zones due to the slipping effect. One would expect a hard rise for the deformation field in the lung border areas. However, the results of the mentioned simulations show a smooth increase instead (in medial direction of the vector field). This underestimated motion is marked in Fig. 2.10. However, a hard rise of the vector field is not possible with the mentioned implementation strategy of FFD. The piecewise polynomial functions cause a smooth slope between several nodal points within the deformation field. One needs an infinite number of control points Φ to represent the real motion, but this is not possible for any optimization strategy. The simulations have shown that a higher number of control points (more than 8 voxels per node) increase a noisier deformation field. The large number of parameter variations do not lead to a more accurate global maximum of the cost function. It rather generates wrong and noisy local optima. Furthermore, the C_{smooth} in (2.26) tries to smoothen the deformation field during optimization. C_{smooth} is very important for a homogeneous motion, but it prevents a real motion estimation in lung border areas. The effect of wrong motion estimation in lung border areas is measurable. For this purpose, 20 additional landmarks were added, which are especially located in lung border areas. These landmarks are also identified by the medical experts. They are merely defined for the reference set i and the maximum exhale phase $j = 6$. Fig. 2.15 shows the projected distributions of their coordinates for three important body planes. The TRE results are distinguished by the two mentioned deformation models TRE_a and TRE_b. Fig. 2.16 visualizes the distribution of the error. As suspected, these errors are bigger than those of the first tests. The average values of both methods are located at η_{TRE_a} =4.9mm and η_{TRE_b} = 5.1. The maximum values grow up to 10-15mm[8]. This is a large shift in comparison to the other landmarks and not acceptable for those regions. Thus, it can be assumed that the mentioned FFD strategy covers lung border areas with faulty motion estimation. Usually, it is a motion underestimation.

The suitability of FFD for 4DCT registration was demonstrated with the accurate landmark tests in Fig. 2.12. One has to consider that motion estimation is less accurate in lung border areas (see Fig. 2.16). The results of the lung border experiments should not be overrated, because their share of the volume in relation to whole lung is comparatively small (see Fig. 2.10). Furthermore, these regions are less affected in many treatment plans. Nonetheless, lung slipping regions are not accurately mapped by IDP with FFD.

[8]The FFD implementation of the POPI-model presents significant better results then the IDP implementation of this work for the advanced landmark tests (see Fig. 2.15) due to more complex settings. However, both results are insufficient.

2.2.2 Physical elasticity models (PEM)

The knowledge about the physiology of the lung can be used beneficially for the registration process. This section explains PEM on the simulation of lung motion. The following models are driven by basic mechanic laws that physically simulate the movement of lung tissue. These approaches are able to integrate constraints into the simulation process. Hence, it enables possibilities to model typical physiological exceptions (e.g. the lung slipping effect) more lifelike then information driven algorithms.
Different PEM techniques were implemented. *Meier et al.* [64] proposed a far-reaching overview of algorithms. In the last two decades, such methods were often analyzed in the field of medical technology: [108], [24], [71], [110], [98], [106]. Approaches based on mass spring models (MSM) [88], particle systems [24, 18, 5], finite element method (FEM) [9] have been used to efficiently represent 3D objects or deformable 2D structures [66]. Important applications for these algorithms are surgery simulation, image guided surgery and the registration of medical image data. In the field of lung motion estimation *Villard et al.* [106], [110], [107], [108] contributed much basic research. Their results confirm that FEM and MSM are best suited for this specific field. Furthermore, *Teschner et al.* [99] describes an algorithm that elegantly combines FEM and MSM. The additional advancement of their approach is the possibility to compute deformation in real-time. This allows much more opportunities in the field of SBRT for lung cancer treatments (e.g. real-time motion estimation). Representing PEM, this chapter explains in detail the algorithm according to *Teschner et al.* [99].

FEM discretization model as basis for physical deformation

FEM discretization is necessary to model single organs as deformable 3D objects. PEM has to model all organs and all single structures separately. Hence, the full simulation is a very complex process. Deformation calculation, motion estimation and collision detection are necessary tools to simulate the breathing motion inside the complete dynamic thorax anatomy. At first, the motion of the lung, as the most important organ, must be simulated individually. Therefore, the single object has to receive a topological structure. The structure results from the basic FEM assumptions. FEM is a numerical approach that solves partial derivative equations in several fields of physics and engineering sciences. The idea behind the solution is the description of an infinitesimal calculation area with the aid of finite elements. The complete area is splitted into a sufficient value of sub-areas which are completely describable by a finite number of parameters. This results in an approximation of the partial derivative equation which could be more accurate through a higher value of sub-areas [107].
The lung movement and the lung deformation, i.e. the time dependent (t) displacement of each coordinate $\vec{x}$ inside the 3D organ Ω, can be described analytically by a partial derivative equation. The theory of elasticity is a part of continuum mechanics. It deals with the prediction and calculation of the effect of applying an external load on some body with elastic physical characteristics. *Terzopoulos et al.* [98, 63] described the motion of a continuous elastic deformable object with the aid of a partial derivative equation in Lagrange's form as follows:

$$\frac{\partial}{\partial t} \cdot \left(\rho \frac{\partial \vec{x}}{\partial t} \right) + \gamma \frac{\partial \vec{x}}{\partial t} + f_{\text{int}}(\vec{x}) = f_{\text{ext}}(\vec{x}, t) \tag{2.28}$$

ρ being the mass density and γ being the damping coefficient. $f_{\text{int}}(\vec{x})$ being a function that represents the internal forces. It is also the variational derivative of the internal potential $f_{\text{int}}(\vec{x}) = \frac{\delta E(\vec{x})}{\delta \vec{x}}$ [98]. It represents the systemic internal deformation as a result from applied external forces $f_{\text{ext}}(\vec{x}, t)$. t being a single time step. The partial derivative equation in (2.28) suggests to split the 3D lung object into sub-areas to approximate the equation numerically by FEM. The function of FEM in this part is to simulate a sufficient 3D model that

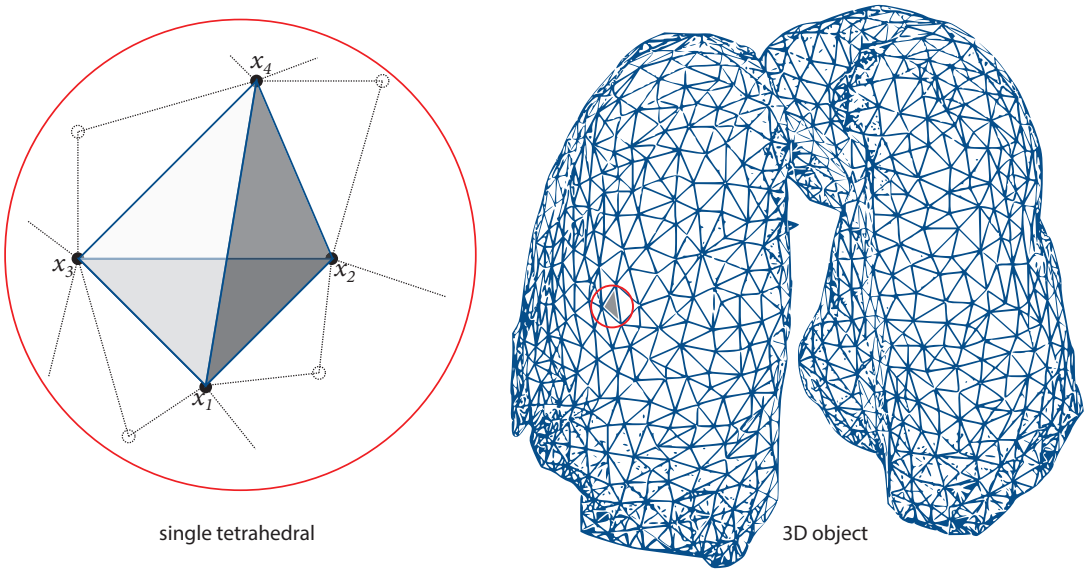

Figure 2.17 : Tetrahedralization of 3D structures: The process splits the 3D object (right) into a sufficient number of tetrahedral. Every tetrahedron contains four vertices (x_1, x_2, x_3, x_4 → left) that describe the shape, inner angels and the location of the local structure. Every tetrahedron is equivalent to a single finite element. This work uses the constrained delaunay algorithm to produce a sufficient mesh of the object [92]. The method generates preferably high quality tetrahedral. They contain no skinny angels and have a good radius edge ratio.

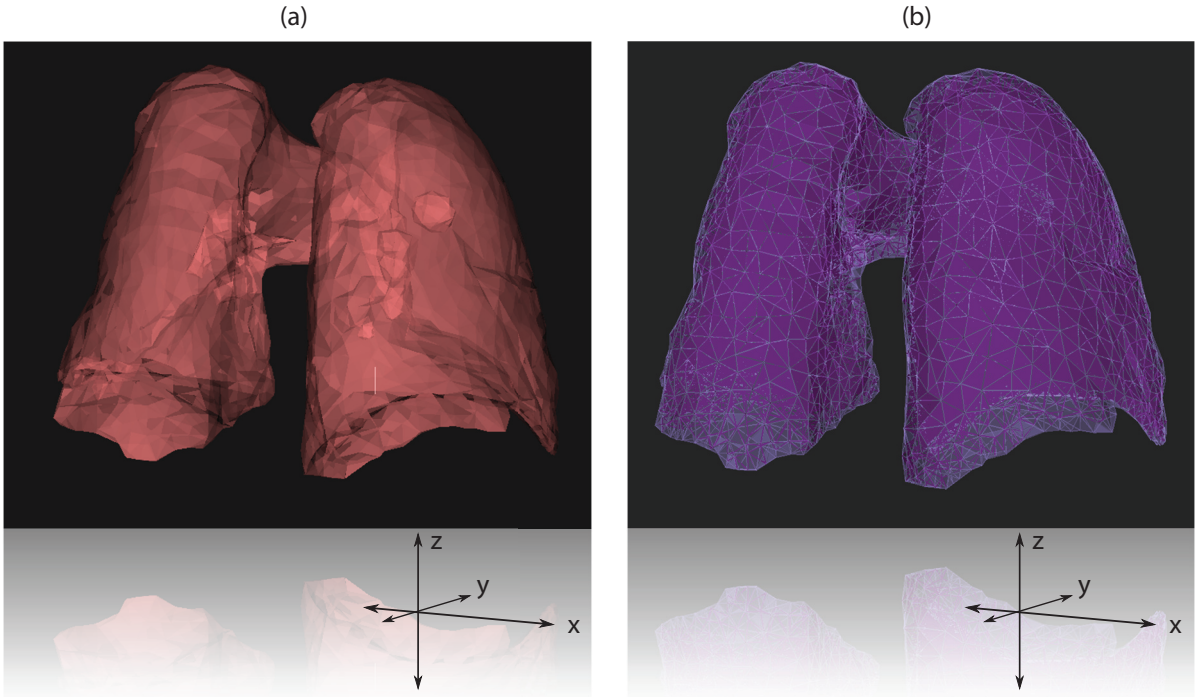

Figure 2.18 : Example of a lung tetrahedralization: This figures illustrates an example calculation of the constrained delaunay algorithm. The CT data of the inhale phase (POPI-model) were used to extract the three dimensional shape of the lung (→ a). The constrained tetrahedralization algorithm built a sufficient mesh based on the 3D shape of the lung (→ b).

represents 3D sub-areas. The integration of all sub-areas results in the approximated description of the full organ. 3D objects are representable by tetrahedral mesh topologies, which are a result of a tetrahedralization process. This work uses the constrained *Delaunay* algorithm [88] of the *TetGen framework (Version 1.4)* [92] to produce a sufficient 3D mesh structure. The constrained tetrahedralization decomposes the 3D object Ω into a mesh. The boundary is equivalent to the faces of the mesh. Mesh vertices are connected in a tetrahedral shape (see Fig. 2.17). Hence, they delimit FEM regions (tetrahedral). The constrained delaunay tetrahedralization maximizes the minimum angles inside the tetrahedron and avoids skinny tetrahedral [92]. The dimension of the region is controlled by the algorithm. It is responsible for the accuracy of the approximation as well as for the calculation time. The integration of all sub-areas results in the shape of the object. Fig. 2.18 explains the process for the lung object of the POPI-model in inhale position.

Mass spring model (MSM)

The MSM introduces two simple concepts to model the elasticity of a homogeneous object: springs and mass points $x_a = [x, y, z]^T$ [66]. Mass points are moving in space under the influence of external forces $f(x_a, t)$ (see (2.28)). The model has a fixed topology. Adjacent particles are connected through springs. These connections generate relations between the mass points. The springs transfer the energy with damping and stiffness to the whole system due to displacements (time, velocity, acceleration) and external forces. Therefore the elasticity of macroscopic objects such as the lung can be simulated. An object Ω is defined as a number of particles $x_a \in \mathbb{R}^3$ where $x_a \in \Omega$ and $a \in \{1, 2, ...n\}$. Particles represent masses and inertia but they have no volume. The spring forces are connections between two particles that affect each other with forces based on their distance. With the aid of the FEM discretization and the tetrahedral mesh, this model assumes tetrahedral vertices as mass points and edges as springs. The topology is illustrated in the left part of Fig. 2.19. The discretization enables the simplification of the partial derivative equation of continuous objects in (2.28). The position of the mass point in the space is describable with the aid of Newtons second law of motion: $f = m \cdot a$, where f is the applied force, m identifies the mass and a is the acceleration of the particle, i.e. the second derivative $\ddot{x}_a$ of the position x_a. The full organ contains n particles that approximate the shape of the object Ω with $a, b \in \{1, 2, ...n\}$. Under the assumption of a constant damping γ in Ω, results the following deformation law for a complete MSM model is based on (2.28) [66]:

$$m_a \ddot{x}_a + \gamma \dot{x}_a - \sum_{b=1}^{n} g_{ab} = f_a \tag{2.29}$$

$\dot{x}_a$ being the velocity v_a of particle which may be enforced through the damping coefficient γ. A comparison of the discrete formula (2.29) and the continuous equation (2.29) explains the parameter g_{ab}. It implements the saved potential energy by internal forces. It applies between two connected mass points x_a and x_b. The summation of all internal forces yield the deformation of the object. The simplicity of MSM enables the use of Hooks law of elasticity for the potential energy and the internal force for two connected mass points. The mode of action regarding Hooks law is visualized in the left part of Fig. 2.19. With the aid of a spring stiffness coefficient k_D it is possible to define g_{ab} [66]:

$$g_{ab} = k_D \cdot (d_0 - |x_a - x_b|) \cdot \frac{x_a - x_b}{|x_a - x_b|} \tag{2.30}$$

d_0 being the initial length of the springs during the undeformed condition (see Fig. 2.19 → *a*). It is apparent that the sum of all internal forces g_{ab} equates to the potential energy of the system (see 2.28).

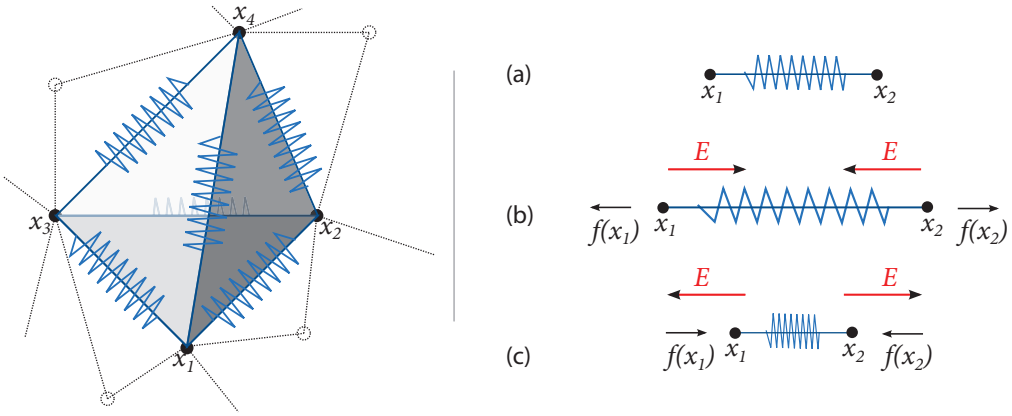

Figure 2.19 : Tetrahedral mass spring model: The topology on the left describes the MSM. Tetrahedral vertices (mass points x_i) are connected via springs along the edges. The right illustration explains the mode of action. The influence free situation in (a) entails no shift of the mass points. The expansion of two points as a consequence of external forces f in (b) result in a contrary reaction of the system (E) and vice versa in (c).

Potential energies

Potential energies are crucial for the deformation process. The MSM describes the potential energy by Hooks law of elasticity for two mass points as a distance preservation effect. The used model (*Teschner et al.*) goes a step further. It uses the FEM mesh to define additional energies that affect all vertices (mass points) of a single tetrahedron. The energy depends on defined constraints $C(x_1, ..., x_n)$. This scalar function relies on the mass point positions x_a. The result of the constraint is zero for an undeformed object[9]. The potential energy, which is necessary to compute forces, results from the constrain based on Hooks law of elasticity:

$$E(x_1, ..., x_n) = \frac{1}{2} k C^2 \tag{2.31}$$

k is the stiffness coefficient, depending on the type of potential energy. In MSM it is the stiffness of a spring and must be evaluated for each type of energy. Potential energies are independent of rigid body movements, because C measures the spatial relation of the particle system. An undeformed object leads to $E = 0$. E is also known as the deformation energy [99]. The force for a single mass point x_a results from the partial derivative of the potential energy of the system:

$$f_a(x_1, ..., x_n) = -\frac{\partial}{\partial x_a} E = -kC \cdot \frac{\partial C}{\partial x_a} \tag{2.32}$$

The overall force of a mass point is the sum of all forces that lead to potential energies that consider this point. One can incorporate the damping coefficient γ into the dynamic system. This increases the possibility for stable simulations. f_a can be defined in the following way [99]:

$$f_a(x_1, ..., x_n, v_1, ..., v_n) = \left(-kC - \gamma \sum_{b=1}^{n} \frac{\partial C}{\partial x_b} v_b \right) \cdot \frac{\partial C}{\partial x_a} \tag{2.33}$$

where v_a is the mass points velocity. This model does not use any other constraints or boundary conditions (cf. (2.28)). The direction of a force vector f is based on the potential energy. It is equivalent to the negative gradient of E.

[9] For comparison: The term $(d_0 - |x_a - x_b|)$ in formula (2.30) is zero during the undeformed condition.

Distance preservation

Distance preservation (DP) considers only pairs of mass points (x_a, x_b) that are connected via springs over tetrahedral edges (see Fig. 2.19). The crucial parameter is the stiffness coefficient k_D. The displacement $|x_b - x_a|$ in comparison to the initial distance of the particles with $d_0 \neq 0$ will also be considered. E_D is defined as (c.f. (2.30)):

$$E_D(x_a, x_b) = \frac{1}{2} k_D \left(\frac{|x_b - x_a| - d_0}{d_0} \right)^2 \tag{2.34}$$

The related force f^D is calculated with the aid of the damping approach in (2.33). *Teschner et al.* [99] highly recommend on using the damping approach for a stable simulation when using the distance preservation. All other following energies and their related forces neglect the damping with formula (2.32). *Teschner et al.* determined experimentally that damping has no effect in the cases of a tetrahedral mesh.

Surface area preservation

The surface area preservation (SAP) is a potential energy that applies over the surfaces of the tetrahedron. Hence, it affects three mass points (x_a, x_b, x_c). The crucial parameters are the area stiffness k_A and the variation of the initial area a_0 with $a_0 \neq 0$. E_A is defined as:

$$E_A(x_a, x_b, x_c) = \frac{1}{2} k_A \left(\frac{\frac{1}{2}|(x_b - x_a) \times (x_c - x_a)| - a_0}{a_0} \right)^2 \tag{2.35}$$

f^A is calculated with the aid of (2.32) without damping.

Volume preservation

The volume preservation (VP) considers the whole tetrahedron with all four mass points (x_a, x_b, x_c, x_d). E_V results from the difference of the current and the initial volume V_0 with $V_0 \neq 0$ for tetrahedral mesh topologies. Again, a stiffness parameter k_V is introduced. E_D is defined as:

$$E_V(x_a, x_b, x_c, x_d) = \frac{1}{2} k_V \cdot \left[\frac{\frac{1}{6}(x_b - x_a) \cdot ((x_c - x_a) \times (x_d - x_a)) - V_0}{V_0} \right]^2 \tag{2.36}$$

where F^V results from (2.32). All stiffness coefficients k_D, k_A, k_V are scale invariant due to the normalization of the constraints. They are used to mimic a wide range of materials. For this application, it is necessary to approximate the lung tissue via k. Experiments for lung simulations with this model are missing. Hence, the stiffness parameter have to be determined by a set of experiments in a trial and error mode. A single tetrahedron (see Fig. 2.19) imposes six DP forces $f^D(x_a, x_b)$, four SAP forces $f^A(x_a, x_b, x_c)$ and one VP force $f^V(x_a, x_b, x_c, x_d)$ for deformation simulation.

Numerical integration

With Newtons second law of motion, containing $f = m\ddot{x}$, $\dot{v} = \ddot{x}$ and $v = \dot{x}$, it is possible to compute the dynamic behavior of the 3D object. The simulation is based on the initial values for positions and velocities. Single time steps Δt are generated to calculate the progress. Internal forces result from external forces. They are defined using deformation energies E_D, E_A, E_V. The combination of the above formulas results in a numerical

integration scheme [99]. There exist several methods for a numerical solution of such a derivative equation. Acceptable approaches are the *Runge Kutta* integration, the *Explicit Euler* integration or the *Verlet* integration. Verlet is assumed to be the most stablest method [66]. Furthermore, it is the most common model for physical applications and is therfore used in this work. The *Verlet* algorithm uses positions and forces at time t, and positions at the previous time step $t - \Delta t$ to predict new positions at next time step $t + \Delta t$. With the aid of *Verlet* the following integration scheme results [99]:

$$\begin{aligned} x(t+\Delta t) &= 2x(t) - x(t-\Delta t) + \Delta t^2 \cdot \frac{f(t)}{m} + O(\Delta t^4) \\ v(t+\Delta t) &= \frac{x(t+\Delta t) - x(t-\Delta t)}{2\Delta t} + \Delta t^2 + O(\Delta t^2) \end{aligned} \tag{2.37}$$

$f(t)$ is the accumulated force that derives from all mentioned potential energies. $f(t)$ is defined as:

$$f(t) = f^D(t) + f^A(t) + f^V(t) \tag{2.38}$$

The velocity is only crucial for $f^D(t)$. *Verlet* has a lot of computational advantages. Only one force calculation per time step is necessary, which is very useful for real-time applications due to the expensive computation of a single force. The integration of positions have a local discretization error of $O(\Delta t^4)$ [99]. Additionally, the position x is independent of the velocity v. For extremely fast requirements the system is getting computational improved when using an undamped approach in f^D. This is also useful for real-time applications, but it is not used for the implementation of this work.

Suitability of PEM for respiratory motion problems

A single PEM solution is not practical to simulate the whole deformation of the breathing thorax. On the one hand, it is too complicated to simulate all structures of the human thorax. Liver, rib cage, diaphragm, lung and other soft tissue organs must be simulated individually. Collision detection, rotational movements and other interactions of the organs additionally impede the simulation. The complete simulation of the dynamic thorax anatomy on an accurate deformation simulation is not possible based on the current technology. At least, it is usable for clinical practice or treatment planning. However, the simulation of individual organs is possible. Hence, it is feasible to simulate the respiratory deformation of the lung to predict each displacement vector inside of its structure. Also this concept is not trivial. An important conclusion after analysis of the simulation instructions in (2.37) is that any simulation of the position for a time step is merely possible, if external forces are known. The simulation needs accurate input data (forces) regarding the deformation. Therefore, PEM has to be combined with other techniques to get a realistic motion estimation. External forces that define the true deformation have to be known before the simulation starts. Another disadvantage of PEM is the dependence of numerous parameter values. Since every parameter has to be defined in a trial and error procedure, it could be time expensive to conduct a large number of experiments.
The basic suitability of PEM to calculate the lung deformation could be demonstrated with a single experiment. For this purpose the 3D structure of the lung object was extracted from the inhale phase of the CT data inside the POPI-model [105]. The exported data was simulated with the aid of the FEM discretization and the accompanied tetrahedralization process (see 2.2.2). The deformation was simulated by the mentioned advanced MSM model. External sample forces, which especially embody the pressure of the diaphragm, were generated to simulate the complete lung deformation from inhale to exhale. The results are illustrated in Fig. 2.20[10]. This experiment served merely for the demonstration of the principal suitability. The generated deformation data

[10] This simulation is based on an individual python software, which is also developed for this thesis.

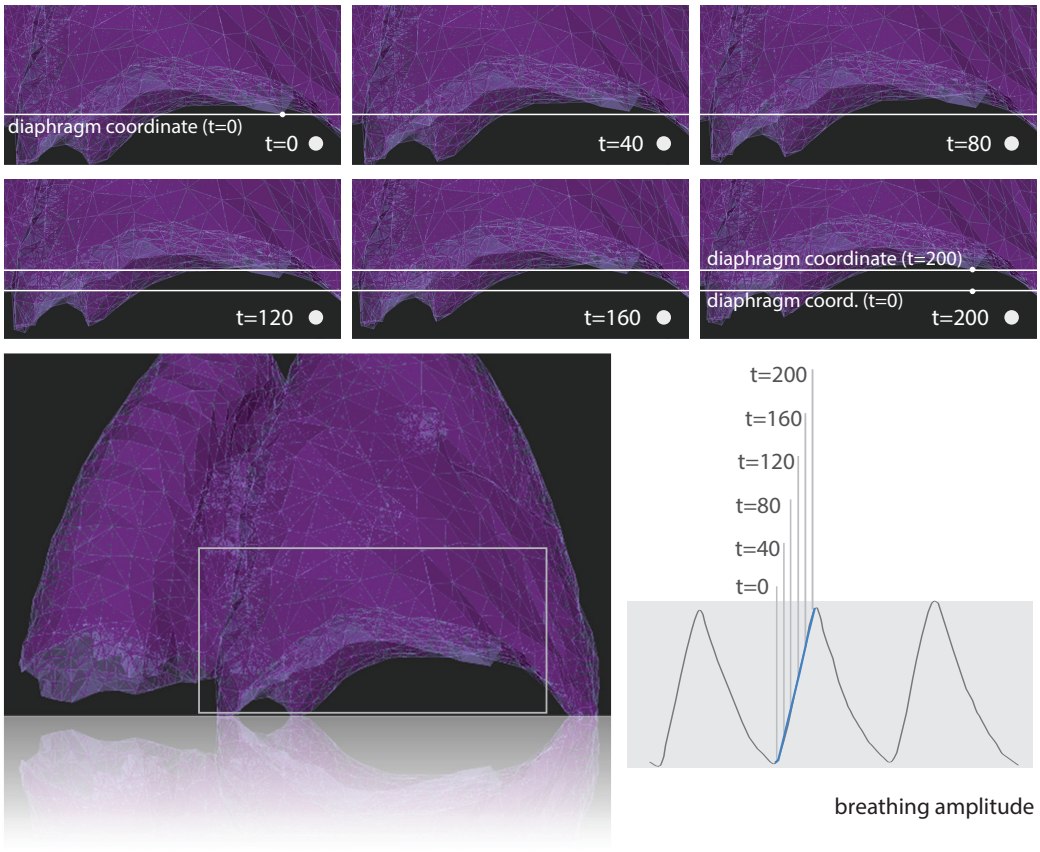

Figure 2.20 : Sample lung deformation simulation with PEM: This lung deformation simulation is based on the 3D shape of the inhale lung structure. The CT data is part of the POPI-model. The clipped illustrations explain the movement near the diaphragm. Two diaphragm coordinates visualize the total motion. The deformable model includes all mentioned components: tetrahedralization, potential energies (DP, SAP and VP) and Verlet integration scheme. Non-realistic force data were used to cause external pressure of the diaphragm. A total of 200 time steps were generated to simulate the deformation from inhale to exhale. The experiment merely serves for demonstration. The used parameters were: $\gamma = 0.2$, $k_D = 0.8$, $k_A = 0.3$, $k_V = 0.1$;

left a physiologically plausible impression. However, a qualitative assessment is only acceptable with the aid of real landmark verification. For this purpose, realistic external force vectors are needed. Hence, the exact analysis of PEM is only applicable when combining PEM with other solutions. This is explained in the following section.

2.2.3 Hybrid approach

The hybrid approach is the combination of IDP and PEM in order to use the advantages of both methods for a more accurate lung motion estimation. To explain the approach, it is necessary to summarize benefits and drawbacks of IDP and PEM. IDP is a robust model for global registrations of 4DCT lung data. It does not need any input data. It directly works with HU values of the CT. Despite good results of global landmark verification tests (average displacements of about 1.2 mm, Fig. 2.12), it generates unrealistic deformation fields for explicit areas (e.g. the lung slipping effect). Those false vector fields occur inside the lung in areas close to the lung boundary. In contrast to IDP, PEM requires realistic input data. It needs external forces as constraint. PEM also offers the possibility to simulate very precise motion and deformation inside the organ. However, a global patient registration is not possible due to the interaction and the complexity of numerous structures. The attributes of both approaches suggest to combine IDP and PEM. The hybrid approach performs a stepwise

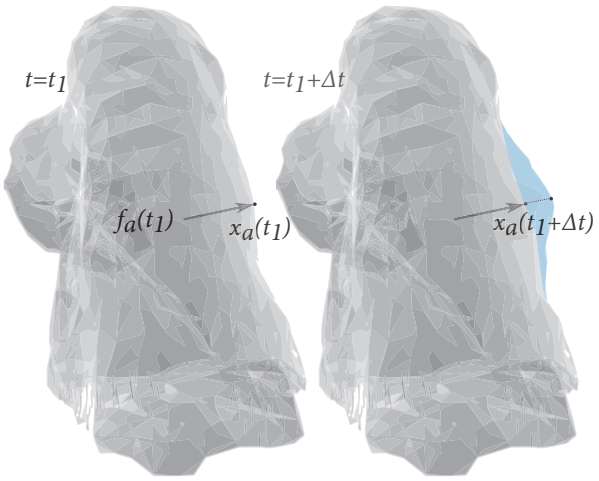

Figure 2.21 : Constraint for deformation: The figure shows the 3D object of the left lung (POPI-model) at two different time steps t_1 (left) and $t_1 + \Delta t$ (right). At t_1, an external force $f_a(t_1)$ acts on the particle at the surface with the coordinate $x_a(t_1)$. The particle shifts to $x_a(t_1 + \Delta t)$ at $t_1 + \Delta t$ as a result of the force. The force value is not necessary. The displacement vector can be calculated implicitly with $x_a(t_1 + \Delta t) - x_a(t_1)$. This leads to internal forces that deform the full body. Hence, f_a leads also to the displacement of other particles with the aid of PEM's deformable model (blue area).

registration, which generates a global IDP registration first. Moreover, it optimizes the vector field inside the lung with the aid of PEM to wipe out the lung slipping effect.

Lagrangian condition

Terzopoulos et al. [98] defined the basic equation for continuous deformable objects in (2.28). This formula is written as a Lagrange equation. Furthermore, the paradigms of PEM is the description of a system with the aid of constraining conditions. Such conditions are external forces. That means, it is known that there exist external forces that cause a pressure on the lungs shape such as diaphragm movements or rib-cage motion. The result is the motion and the deformation of the lung. Hence, the result of the condition is known, but the exact values of the external forces are unknown. This is a basic principle of the Lagrange equations. With the help of the defined condition, it is possible to generate generalized coordinates, which decreases the value of independent parameters. Therefore, one can create the standard Lagrange equation [70]:

$$L = T - V \tag{2.39}$$

where L is a functional term that includes the independent parameters q and the time t. T being the kinetic energy term and V being the the potential energy term of the system. Based on the basic Lagrange equation it is possible to derive the full equation of the deformable system shown in (2.28). For example, the deformation of the lung is clearly visible in the data of the 4DCT. However, the values of external acting forces are unknown. To explain the hybrid solution with PEM, it is necessary to repeat the basic equation written with explaining subscripts:

$$L_{external\ forces} = T_{mass\ damping} - V_{potential\ energies} \tag{2.40}$$

(2.40) is a generic form of (2.29) or (2.33), the basic formula for PEM. Fig. 2.21 illustrates the shift of a particle on the lung's surface as a result of a performing external force. The conclusion of this section is: If the displacement of some particles x_a within the 3D organ is known as a result of an external force, the model is able to simulate the residual deformation of the object as a result of the acting forces. The accuracy of the simulation is accompanied with the number of known predefined particle displacements.

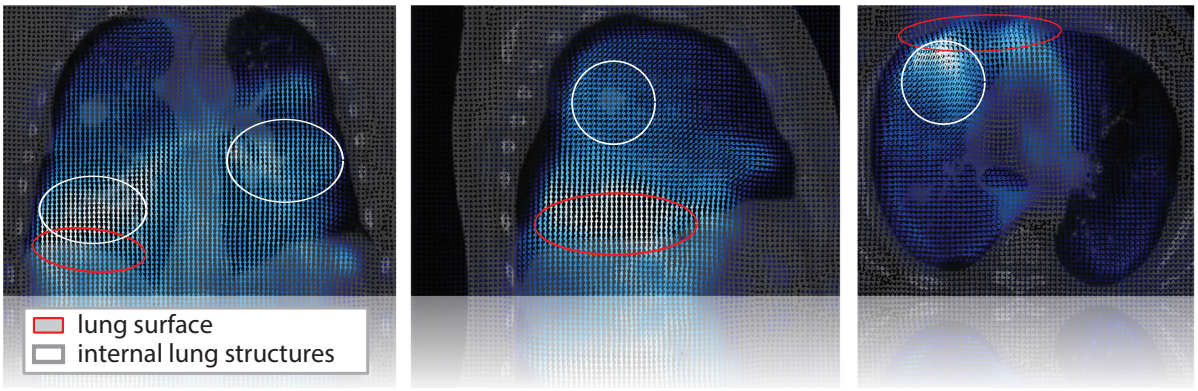

Figure 2.22 : Areas with high accuracy in an IDP vector field: The algorithm is able to find a very accurate deformation prediction in regions with significant structures. The illustration shows the deformation vector field based on the IDP algorithm mentioned in section 2.2.1 for three different sample views (coronal, sagital, axial). The vectors describe the displacement from inhale to exhale. Large deformations are bright blue (maximum → white), small shifts are dark blue (minimum → black). The surface areas (red ROI) such as internal structures with density gaps (white ROI) show large displacements. In these regions motion prediction is more accurate than in other zones (e.g. the lung slipping in Fig. 2.10).

Crossover deformation process

Section 2.2.1 has shown that deformations of global heterogeneous objects can be sufficiently modeled with IDP. Furthermore, homogenous 3D objects can be sufficiently modeled with the PEM. The first approach is erroneous (e.g. lung slipping) and the second needs a constraint to work accurately. A combination of both appears to yield the best outcome. This is the concept of this work. The hybrid model realizes the deformation stepwise. The first step is the generation of the global deformation field by the IDP approach optimized for lung deformations (see Fig. 2.10). With this approach, it is possible to generate a vector field for breathing phases of the 4DCT data set. IDP is an information based technique that works with similarity measures applied on HU values of the image data. Hence, IDP is able to find accurate transformations at areas with strong density deviations. This could be the surface of the lung, because there is a strong gradient between the density of the rips, the soft tissue and the low dense lung tissue. Even other structures inside the lung could provide such properties. Examples of these areas are illustrated in Fig. 2.22. The usage of the displacement vectors in the mentioned regions as constraint for PEM is the main idea of the hybrid deformation process. Hence, the work flow contains several steps. The global IDP registration performs at first. The next step is the extraction of the 3D lung object. Then, the IDP based constraint for PEM, so called vector filter, is extracted. For example: This could be the particle displacements on the surface of the lung. After the definition of the constraint (filter), the deformation of the lung has to be simulated with PEM. This recalculation of lung internal displacement vectors improves the accuracy of the motion prediction. For instance, the lung slipping effect should be taken into account after recalculation. An update of the global deformation field terminates the procedure. Fig. 2.23 explains all steps of the hybrid deformation process.

Predefined constraint (filter) to select applying forces

The hybrid deformation process requires a constraint (vector filter). The challenge is a sufficient selection of particles (vertices of the tetrahedral topology) that are shifted by IDP and apply as forces for PEM. The previous outline particularly suggests that external forces have to apply directly on the surface of the lung. However, external forces f_a could also be forces inside the lung. It must be ensured that the selected vector

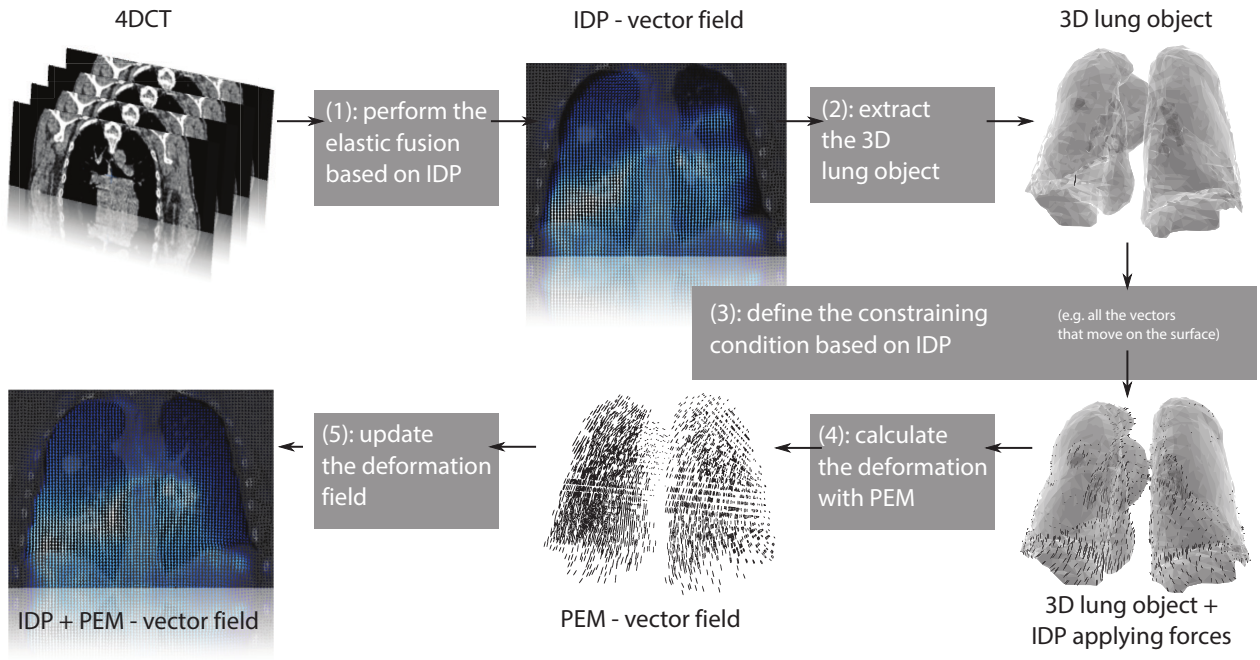

Figure 2.23 : Hybrid deformation workflow: The illustration splits the hybrid deformation process into five steps. The most important step is (3), the selection of the vector filter. Parts of the IDP vector field apply as external forces for PEM. Those predefined particle shifts are the constraint for PEM. The updated vector field in (5) should inherent more realistic motion vectors.

shift is accurately simulated with IDP. Fig. 2.22 shows that also particular areas inside the lung have good motion prediction. The requirements for high accuracy matching regions are local structures with large density deviations. These gaps could be registered by the similarity measure of the IDP algorithm. A good indicator for a solid match is the strength of the shift. A large vectorial displacement is accompanied with the assumption that IDP recognizes a special feature inside the image data. Hence, a large particle shift is a hint for an accurate motion prediction of IDP. Under consideration of particle positions $x_a = [x, y, z]^T$ that are a member of the lung organ Ω_{lung} with a defined set:

$$A_L = \left\{ x_a \in \Omega_{lung} \right\}, \tag{2.41}$$

it is possible to define a barrier b that selects only large displacement shifts. The defined set A_B includes merely strong displacements and can be written as:

$$A_B = \left\{ x_a \in \Omega_{lung} \middle| \left\| x_a(t_1) - x_a(t_2) \right\| > b \right\} \tag{2.42}$$

t_1 and t_2 being the respective breathing phases (e.g. inhale and exhale) in this investigated case. b is equivalent to the strength of the displacement. It has to be adjusted (e.g. 0.5mm → 20mm) in relation to the respective application how strong the constraint should apply. As mentioned, it is also useful to define a set that select particles that are located on the surface $\Omega_{surface} = 1, 2, ...m$ of the lung with $\Omega_{surface} \subset \Omega_{lung}$. This is meaningful, because the surface is accompanied with density gaps. It is assumed that the IDP algorithm works very accurately for this region. The filter for surface particles can be defined as:

$$A_S = \left\{ x_a \in \Omega_{surface} \right\} \tag{2.43}$$

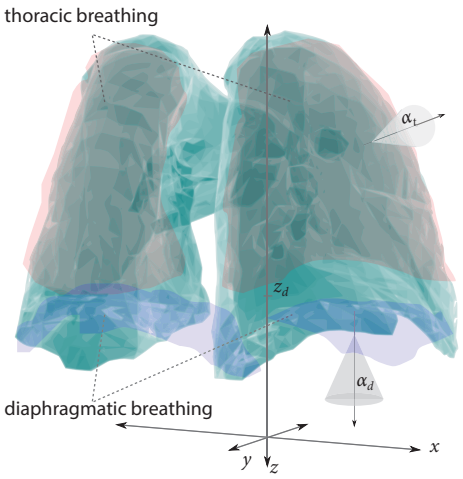

Figure 2.24 : Constraint for physiological breathing: The figure illustrates the areas for thoracic breathing (red) and diaphragmatic breathing (blue). The applying forces are located on the surface. Diaphragmatic breathing is a result of the diaphragm motion in z-direction with a maximum angle tolerance of α_d. Thoracic breathing is generated by the rib-cage and includes shifts in y-direction with a maximum angle tolerance of α_t.

IDP has a low accuracy in regions where the lung slipping effect occurs. This was particularly mentioned in section 2.2.1. Since theses areas have to be recalculated by PEM, vertices in such regions are not supposed to be part of the constraint Such a filter set considers only particles that are located with minimal point surface distance d. In the area between surface and the point in distance d should act the lung slipping. d has to be adjusted experimentally (e.g. 20mm). The distance set can be written as:

$$A_D = \left\{ x_a \in \Omega_{lung} \middle| \min_{x_b \in \Omega_{surface}} \|x_a - x_b\| > d \right\} \tag{2.44}$$

The lungs physiology of respiration is mainly driven by two different types of breathing [108] (see Fig. 2.14.b). One the one hand, there exists the diaphragmatic breathing. On the other hand, there exists the thoracic breathing. Diaphragmatic breathing is initialized by the motion of the diaphragm in z direction. Thoracic breathing is created by the raise of the rib cage in the upper thoracic regions. Both types are illustrated in Fig. 2.24. It is possible to create filters that are designed to especially consider one of these effects (Fig. 2.24). For diaphragmatic breathing it is necessary to focus on particles $x_a = [x, y, z]^T$ in the lower area of the lung. This can be realized if the z fraction of the coordinate is higher than a defined limit z_d. Furthermore, the direction of the displacement vector $x_a(t_2) - x_a(t_1)$ has to be in a range within a defined angle α_d around the z-axis to simulate the movement of the diaphragm. Also, the breathing should only affect particles on the surface. The filter can be written as:

$$A_{DB} = \left\{ x_a \in \Omega_{surface} \middle| (x_a \cdot [0,0,1]^T > z_d) \wedge \left(\arccos \left(\frac{[x_a(t_2) - x_a(t_1)] \cdot [0,0,1]^T}{\|x_a(t_2) - x_a(t_1)\|} \right) < \alpha_d \right) \right\} \tag{2.45}$$

Such a set equally can be defined for the thoracic breathing. In this case the angle α_t applies around the y-coordinate. It considers only vertices in upper regions, lower than z_d. The set is defined by:

$$A_{TB} = \left\{ x_a \in \Omega_{surface} \middle| (x_a \cdot [0,0,1]^T < z_d) \wedge \left(\arccos \left(\frac{[x_a(t_2) - x_a(t_1)] \cdot [0,1,0]^T}{\|x_a(t_2) - x_a(t_1)\|} \right) < \alpha_t \right) \right\} \tag{2.46}$$

It is possible to combine several filters. The best filter set for a specific application has to be adjusted experimentally. For example, a combined set allows surface particles A_S and inner particles A_D with a point surface distance d. All considered vectors must have at least a strength of b (A_B). Since all the vectors are located in the lung object Ω_{lung}, the combined set can be written as:

$$(A_S \cup A_D) \cap A_B \tag{2.47}$$

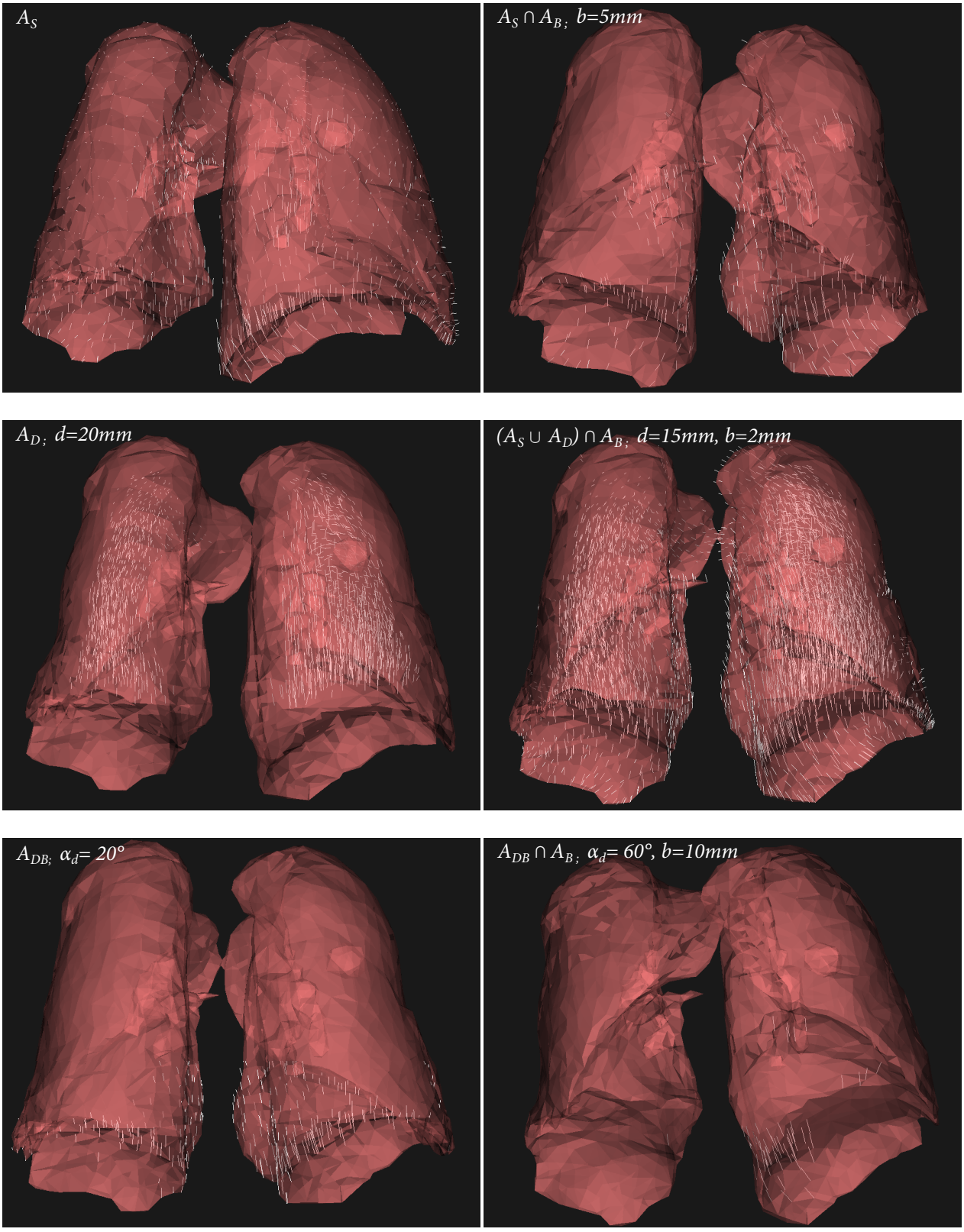

Figure 2.25 : Examples for filtered constraints: The six filters in this illustration belong to the set definitions in (2.41) to (2.48). The 3D lung object is extracted from the reference set (inhale) of the POPI-model. The IDP algorithm calculates the deformation field from inhale to exhale (time frame 60 %). Hence, the shown filtered deformation fields belong to $v_{ji}(\vec{x}_i)$ with $j = 6$. The illustration of A_{TB} was neglected due to very small shifts in these areas. This patient data is generated primarily through diaphragmatic breathing.

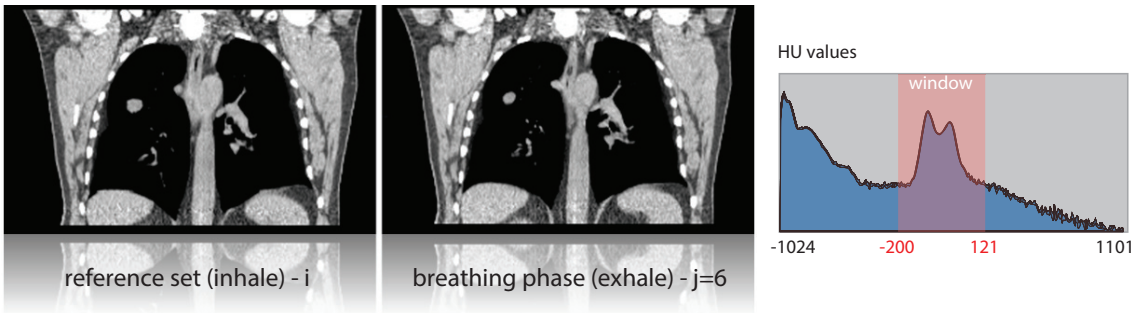

Figure 2.26 : Data windowing for suitability test: This figure explains the window for the following experiment. The IDP algorithm tries to register the reference set (i) onto the breathing phase (j). For this experiment, a special windowing is applied on both data sets. The graph on the left shows the selected scaled window. Most of the structures inside the lung are not visible. Hence, IDP will mainly match the surface of the lung. Displacements inside the organ will be neglected.

Another set combines the thoracic A_{TB} and the diaphragmatic filter A_{DB}, where all displacements must have at least the strength of b. The combination is defined as:

$$(A_{TB} \cup A_{DB}) \cap A_D \tag{2.48}$$

Further examples and their related three dimensional renderings for the data of the POPI-model are illustrated in Fig. 2.25.

Suitability for respiratory motion problems

The suitability of the hybrid approach for the application of this work can be shown with the aid of a trivial experiment. For this purposes, the IDP approach registers the data with a strong windowing. The used HU scaling is illustrated in Fig. 2.26. The special setting distinguishes directly between soft tissue, bone and lung tissue. Finer structures are more or less invisible. Hence, IDP will mainly match the surface of the organ. Inner lung structures are invisible. No motion prediction is expected for the main parts of the inner lung. The results of the IDP registration experiment confirm the assumptions. The algorithm deformed the reference set (inhale) of the POPI-model for registration with the breathing phase at time frame 60 % (exhale). The resulting deformation fields are shown in Fig. 2.27. The IDP result is illustrated with sample sagital and a sample coronal view in the first row of the figure. The pure IDP algorithm predicts the motion simply at the surface of the lung. It is visible in diaphragmatic regions for both views, which in turn is physiologically very logical (see diaphragmatic breathing in Fig. 2.24). All parameter settings and installation properties are explained in detail in the description of Fig. 2.27. The second row of the figure describes the results of the hybrid approach. After updating of IDP with PEM inner structures show a significant motion inside the lung. The demonstration of additional motion by PEM is given by the difference vector field in the last row of the figure. The inner structures of the lung is moved uniformly in physiological consistent direction.
The experiment clearly confirms the power of the hybrid approach. Even with the aid of an insufficient deformation field (IDP with windowed image data) remarkable results can be achieved. This is also verified by a landmark test for the same experiment. The same data is used (previous experiment). The landmarks regard to the definitions of the POPI-model (see Fig. 2.11). The results are shown in Fig. 2.28. The data distinguishes between the landmark matching of the pure IDP algorithm and the hybrid approach. The mean of the total TRE is improved from 4 mm to 2.5 mm. The median is improved from 3.4 mm to 2.6 mm. Even the distribution (quartiles) of the error is significantly better. If one composes the TRE into

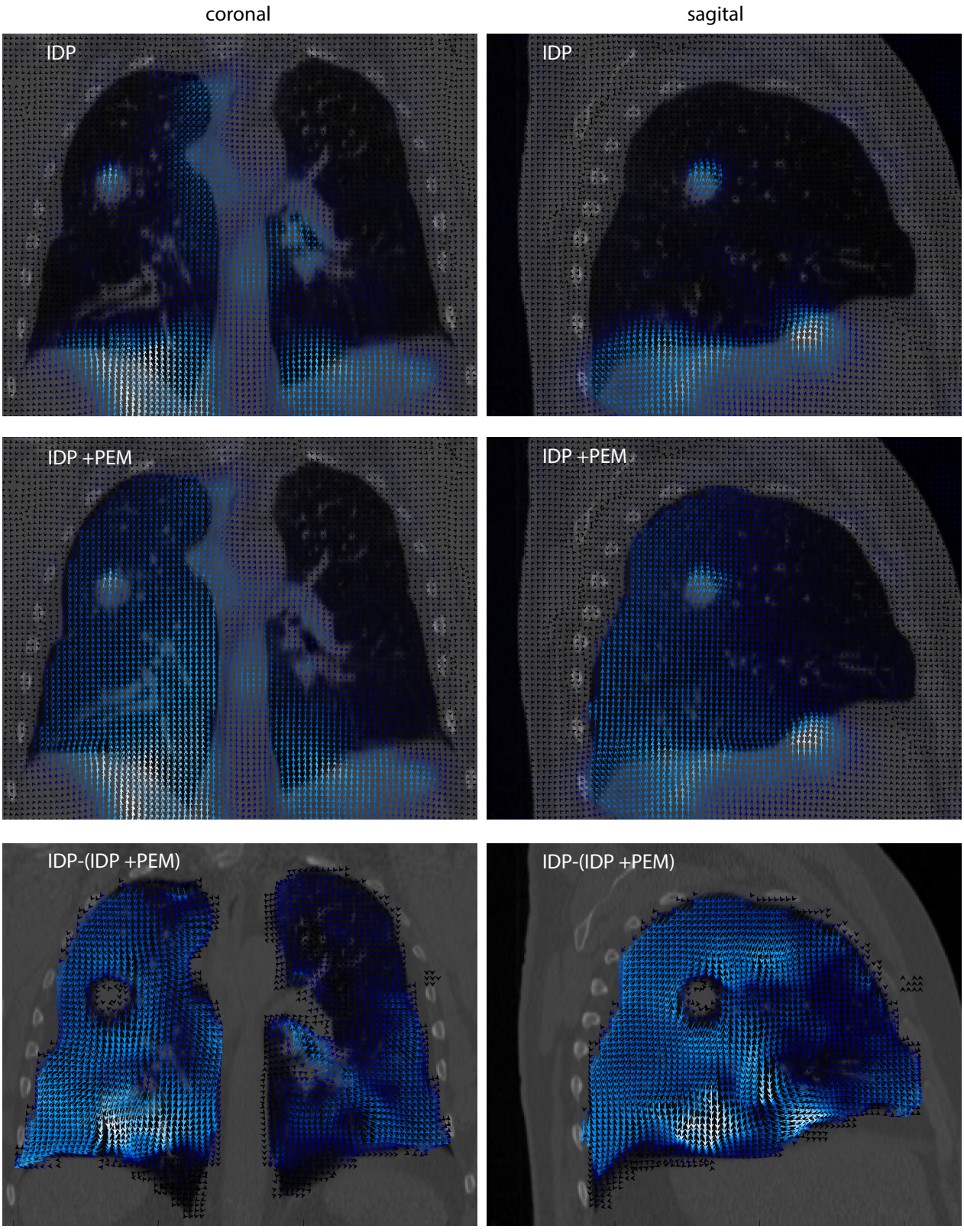

Figure 2.27 : Registration of a sample 4DCT with the hybrid approach: The figure shows the result of the basic experiment. The first row illustrates the deformation field for a pure IDP analysis in coronal (left) and sagital view (right). The second row shows the updated data of the hybrid deformation approach with the aid of PEM. The last row describes the difference of both deformation fields, i.e. the difference vector set of IDP and the hybrid approach. It symbolizes the additional movement that was added by PEM. The used IDP parameter configuration is equivalent to the simulation mentioned in Fig. 2.10 → model a. The used filter set for PEM is based on $A_S \cap A_D$ with $b = 5\,\text{mm}$ (see Fig. 2.25). The used PEM parameters are: $t = 200$ time steps, $\gamma = 1 \cdot 10^{-4}$, $k_D = 1 \cdot 10^9$, $k_A = 0.01$, $k_V = 0.01$;

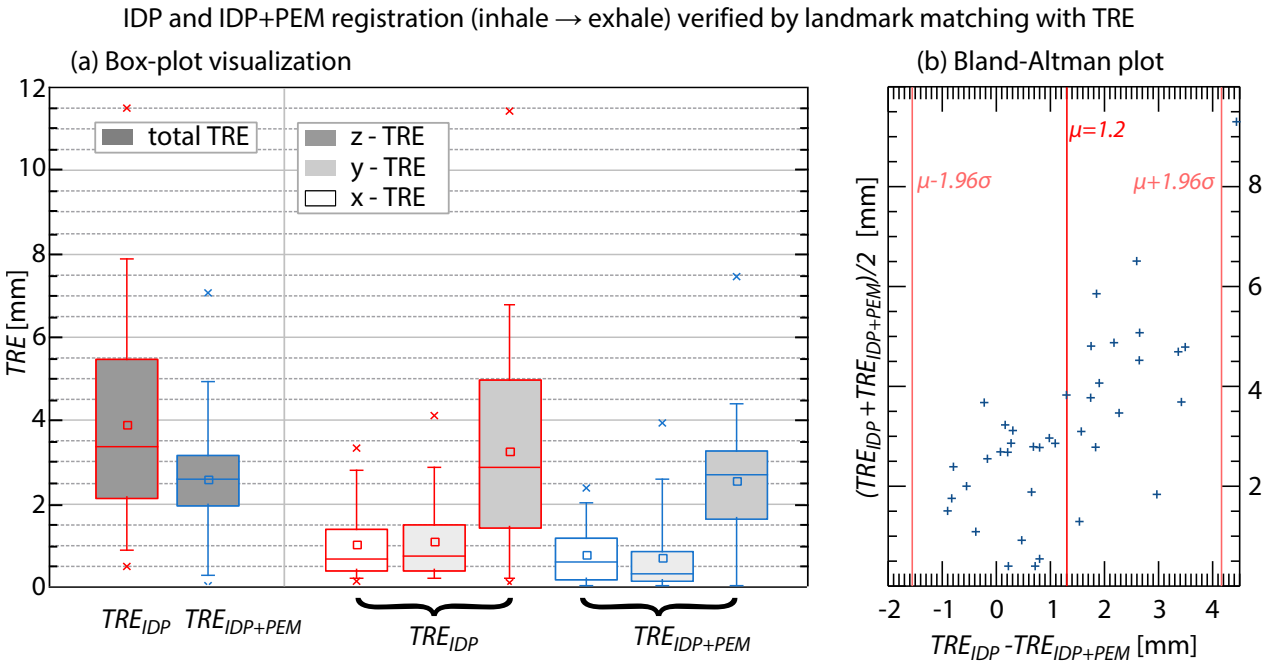

Figure 2.28 : Detailed TRE analysis for the hybrid approach: The figures show landmark error data for the experiment mentioned in Fig. 2.27. The analysis regards to the deformation of time frame $j = 6$ (60 %). It shows a splitted Box-Plot in (a) with a space oriented distinction (x,y,z). The view shows the error fraction for every single coordinate axes. The Bland-Altman plot (b) investigates systematic differences between the pure IDP algorithm and the hybrid approach. The result of every single landmark is investigated. A shift of all landmarks to the right is a sign for a systematic difference. In this case the hybrid approach improves the motion estimation for landmarks signficantly.

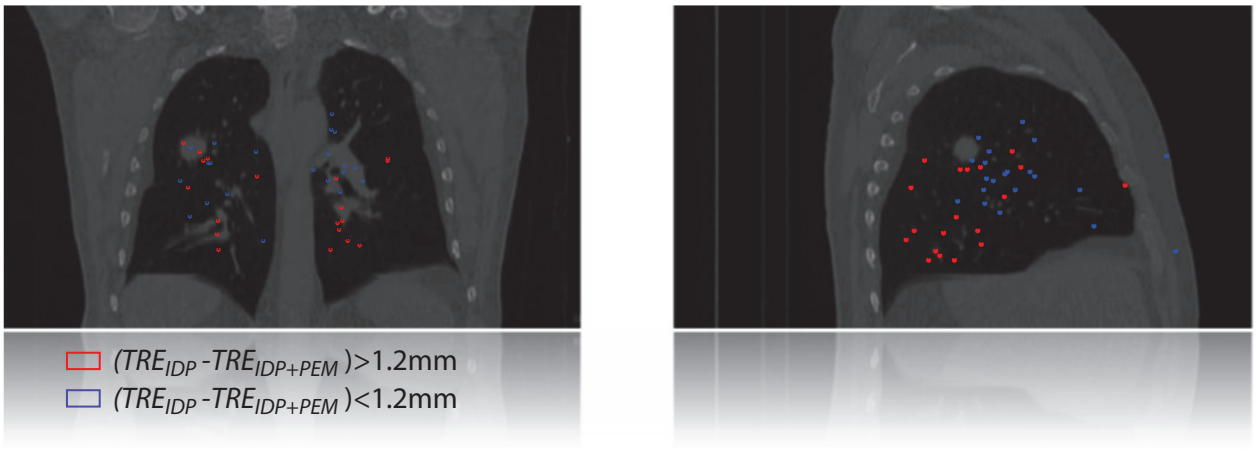

Figure 2.29 : Investigation of improved landmarks: The figure refers to the data of Fig. 2.28. Two sample views (coronal → right, sagital → left) displays the landmarks of the POPI-model inside the reference set. Landmarks are distinguished by their improvement. Significantly improved values (data on the right of the mean asymptote in the Bland Altman plot of Fig. 2.28) are red, all other values are blue. Strongly improved values are mainly located in the inner lung.

its components of the space-directions (x,y,z), especially the z-component refines. Due to diaphragmatic breathing the movement occurs mainly in the z-direction. The Bland-Altman plot in Fig 2.28.b also illustrates the improvement. Almost all landmarks improve their TRE because their abscissa values are positive: $TRE_{IDP} - TRE_{IDP+PEM} > 0$ mm. It is clearly shown that mainly landmarks with a large TRE (large values on the ordinate) strongly contribute the improvement. Significantly improved values appear with a large value on the abscissa: $TRE_{IDP} - TRE_{IDP+PEM} > 1.2$ mm (the mean of all values). Such significantly improved landmarks are typical coordinates of inner lung structures. The effect is confirmed by Fig. 2.29 that distinguishes between significantly improved landmarks (red) and all other coordinates (blue).

2.3 Evaluation of the hybrid approach

Section 2.2.3 demonstrates the principal suitability of the hybrid approach for the deformable registration of 4DCT lung data. The experiment was based on a trivial, an insufficient IDP deformation grid. This evaluation study goes a step further and tries to investigate a real improvement of the hybrid approach (section 2.2.3) in contrast to a fine adjusted, powerful IDP implementation (c.f. Fig. 2.12). Once again, this analysis is based on landmark tests accompanied with the TRE. The landmarks of the POPI-model (Fig. 2.11) and the advanced landmarks of this work (Fig. 2.15) are used.

2.3.1 Disadvantages of the surface filter

Section 2.2.3 investigated in detail the hybrid approach. Essential for the quality of the model is the choice of a good filter model. Several solutions are mentioned in Fig. 2.25. The main idea of the hybrid approach is the deformation of 3D objects driven by external forces. Lung internal displacements are recalculated by PEM. The filter model A_S (see 2.2.3) fulfills this first idea. The model considers only vector displacements on the surface. It is combinable with various barrier conditions A_B that sort out short vectors. To assess the quality of such a model in contrast to a fine adjusted IDP solution, it is necessary to calculate the TRE. The used landmarks should mainly cover the full area to rate the general quality. Hence, the base landmarks of the POPI-model are suitable for a first experiment. This test investigates the main deformation quality exemplary for the registration of the reference set (inhale) i and the breathing phase (exhale) $j = 6$. The test distinguishes between three surface filter models $A_S \cap A_B$ with b=7mm, b=5mm and b=3mm. The test compares the results of both IDP implementations ($IDP_a \rightarrow$ FFD implementation based on *iPlan™ RT*, $IDP_b \rightarrow$ FFD implementation regarding the POPI-model) before and after the recalculation with the hybrid model. The results are illustrated in Fig. 2.30.

The Box-Plot illustration reveals that any solution of the hybrid approach, in combination with a surface filter, yields poor results. Generally, the mean TRE and the median TRE of the landmark set is 0.6mm-1.1mm larger after hybrid recalculation. Maximum values even grow up from 3.2mm to 7mm. The significant loss of quality is independent from the used barrier b. It is also independent from the used IDP approach (IDP_a, IDP_b). All six solutions show similar statistical properties. The models lack of accuracy can be directly derived from the used filter model (surface). Therefore, the surface-filter should not be used for stereotactic dose planning. Reasons for inaccuracy of the surface filter can be evaluated with the vector field motion plot (see Fig. 2.31). This plot shows the results of the experiment for $A_S \cap A_B$ with b=5mm. The sample view image column on the left describes the pure IDP motion prediction. The column in the middle explains the recalculated deformation field. This view clearly shows that lung slipping areas are not neglected anymore, because motion estimation is distributed over the full lung up to the outermost shape. The full distributed motion is not visible for the pure IDP calculation. In principle, the model achieves the desired results, but the calculated motion estimation is lost in accurate modeled areas. A lot of zones are well deformed through IDP. This is shown

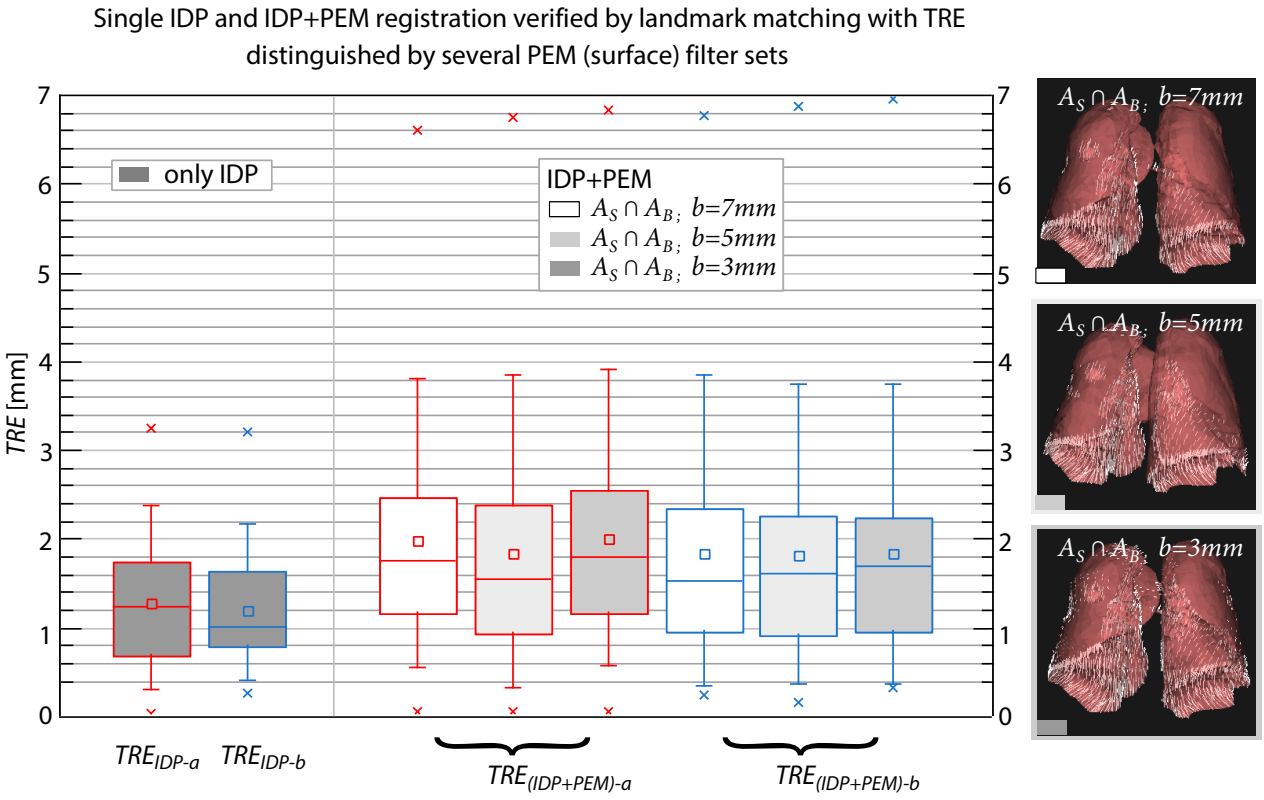

Figure 2.30 : Detailed TRE for hybrid simulation with different surface filters: The plot distinguishes between both IDP implementations ($IDP_a \rightarrow$ FFD implementation based on *iPlan™ RT*, $IDP_b \rightarrow$ FFD implementation regarding the POPI-model). The data is based on the registration of the reference set (inhale) and the breathing phase $j = 6$ (exhale). The used landmarks are part of the POPI-model (see Fig. 2.11). The TRE plot on the left shows the error distribution of the pure IDP implementations. The different plots in the middle describe the updated error data after recalculation with the hybrid approach. Three different surface filters for evaluation (right) were used.

by large displacements of inner lung structures and the good TRE results. This accurate motion estimation is damped by the surface filter and the PEM deformation model. This can be proven by the deformation difference plot in the right column of Fig. 2.31. Lung slipping areas are optimized by the model (see additional motion in near outline regions), whereas accurate modeled structures inside the lung are damped. A lot of motion estimation gets lost and the model receives a loss of quality for TRE tests. The conclusion of this experiment is, that any well modeled motion prediction of inner lung structures should be considered for the hybrid approach. It would be a discard of well calculated structures and it would be a double calculation of data that could be time expensive. The model with a pure surface filter does not fulfill the requirements for an accurate stereotactic dose calculation. However, the model is able to predict an adequate motion for an insufficient, erroneous IDP deformation field (see section 2.2.3). The model is able to approximate the tumor position for an extremely reduced deformation field. It may be able to calculate time depended tumor positions without any 4DCT data information. Hence, the surface filter should not be rated as a erroneous approach.

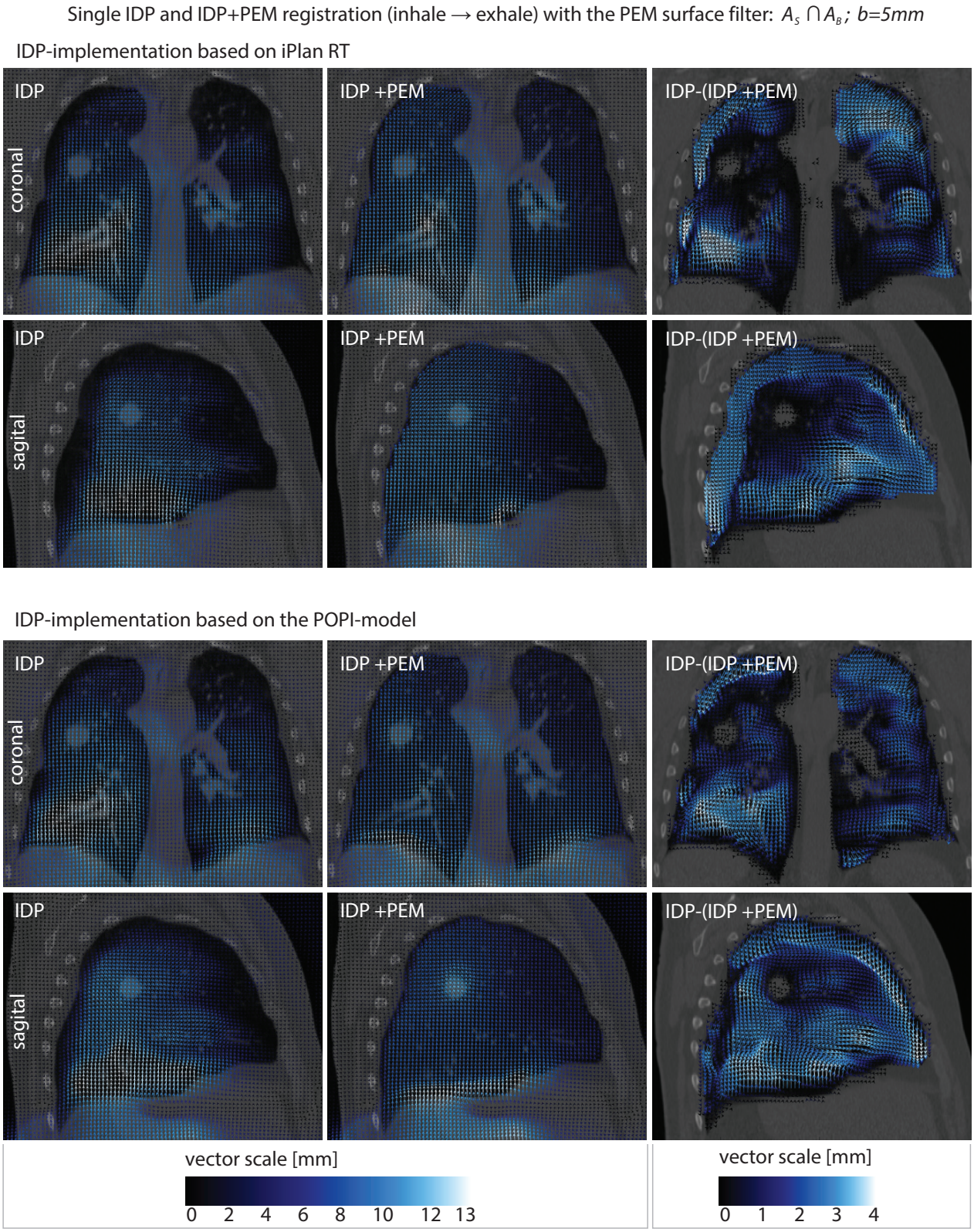

Figure 2.31 : Deformation field for the hybrid approach with surface filter: The illustration distinguishes between both IDP implementations. The data is based on the registration of the reference set (inhale) and the breathing phase $j = 6$ (exhale). The image shows the geometry of the reference set for sample planes in coronal and sagital view. The data describe the local displacement through the breathing phase. The value of the displacement is scaled by the ratio in the legend below. The left column illustrates the pure IDP deformation. The middle describes the hybrid deformation data. The right illustrates the difference of both vector fields with an own vector scaling. The used PEM parameters are: $t = 200$ time steps, $\gamma = 1 \cdot 10^{-4}$, $k_D = 1 \cdot 10^{9}$, $k_A = 0.01$, $k_V = 0.01$;

2.3.2 An optimized filter model

Section 2.2.3 gives an overview over many possible filter models that even consider displacement vectors inside the lung. The power of the respective model has to be evaluated experimentally. The last section has shown that a large number of precalculated vectors should be considered. A strong reduction of the already calculated vector field leads to a damping effect in areas that are modeled accurately with IDP. This results in a large error for TRE tests. Hence, the following tested filter models do all consider constrained vectors that are distributed in the full organ. The following experiment investigates the main deformation quality exemplarily for the registration of the reference set (inhale) i and the breathing phase (exhale) $j = 6$. Again, the basic landmarks (POPI-model) are used to measure the general deformation quality. Due to the large value of filters the experiment uses merely the IDP implementation of this work ($IDP_a \rightarrow$ FFD implementation based on *iPlan™ RT*). Fig. 2.32 illustrates the results of eight different filter models[11].

All filter models achieve more or less equally good results in comparison to the pure IDP approach. The results vary in a small range. The mean TRE values are arranged from 1.1 mm up to 1.8 mm, the median TRE values are distributed from 1 mm to 1.7 mm and the maximum values are located in range from 2.8 mm to 4.2 mm. Hence, the results are much better than the measurements based on the surface filter. They all achieve suitable results. Again, it is visible that too much vector reduction causes a loss of quality for the TRE test. For example, filter (e) $(A_S \cup A_D) \cap A_B$ with $d = 12\,\text{mm}$, $b = 7\,\text{mm}$ and filter (g) A_B with $b = 7\,\text{mm}$ apply the strongest vector reduction due to the large barrier b. The attached vector plot illustrates the effect, because there are just a few vectors left in the left lung. Both models achieve the worst results for this test series. Using filters (a)-(d) similar results are yielded. They are not significantly better or worse than the pure IDP approach. The best score is achieved by the most trivial approach (f) A_B with $b = 5\,\text{mm}$. The method uses a good compromise of constrained IDP vectors and free zones that are recalculated by PEM. Also interesting is, that method (h) achieved almost the same results. However, the small constrain A_{DB} leads to a shift of the maximum TRE and thee result is getting more inaccurate.

The findings of this section suggests that a strong vector reduction leads to a loss of quality during PEM recalculation. Hence, one should avoid too many constraints for the filter. The best method is the most elementary approach A_B with $b = 5\,\text{mm}$. It assumes that IDP calculates accurate vector displacements in regions that have recognizable gray-value structures. The full IDP deformation is driven precisely with aid of those regions. Hence, the displacement is large at these areas. The displacements of surrounding structures is estimated with the aid of smoothing filters or other tools. Those regions have smaller shifts. A_B with $b = 5\,\text{mm}$ exactly sort out these areas. They are recalculated and physiologically optimized. Due to the content of these findings all following experiments use the basic filter model A_B.

In order to investigate the quality of the obtained model A_B, the registration was tested by additional experiments. For this purpose, all breathing phases j of the entire POPI-model were registered with the hybrid approach. The generated TRE data was compared to the pure IDP implementation of this work IDP_A. The results are illustrated in Fig. 2.33. Due to smaller displacements of mid-exhale breathing phases, the barrier b has to be adjusted for every breathing phase. For example, the mean original landmark displacement at $j = 80\,\%$ is $\mu = 3.5\,\text{mm}$. Hence, a barrier of $b = 3.0\,\text{mm}$ was chosen. The results of all breathing phases do not show any loss of quality in contrast to pure IDP implementation. Usually, all statistical properties (mean, median, maximum values) are even slightly better after the PEM recalculation process. The test series confirm the power of the model regarding TRE tests with a full landmark distribution. The filter A_B fulfills the same requirements as the pure IDP implementation. Therefore, it is suitable for practical applications regarding stereotactic dose planning.

[11] The filter models are developed by the theory mentioned in 2.2.3

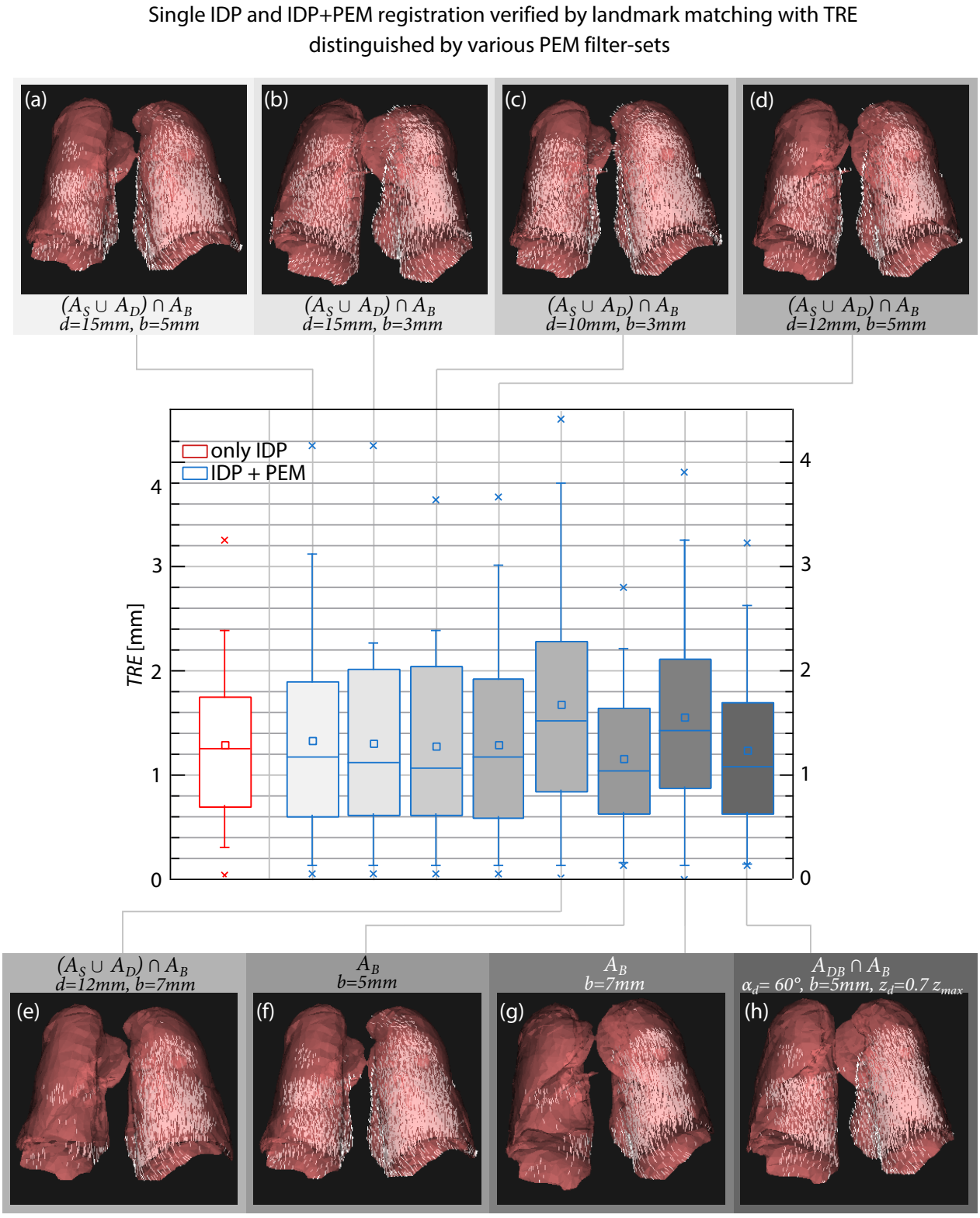

Figure 2.32 : Detailed TRE for the hybrid approach with different PEM filters: The plot regards to the IDP implementation of this work ($IDP_a \rightarrow$ FFD implementation based on *iPlan™ RT*). The data is based on the registration of the reference set (inhale) and the breathing phase $j = 6$ (exhale). The used landmarks are part of the POPI-model (see Fig. 2.11). The TRE plot on the left shows the error distribution of the pure IDP implementation. The different plots in the middle describe the updated error data after recalculation with the hybrid approach. Eight different PEM filters were used for evaluation. The simple filter A_B with b =5mm achieved the best result.

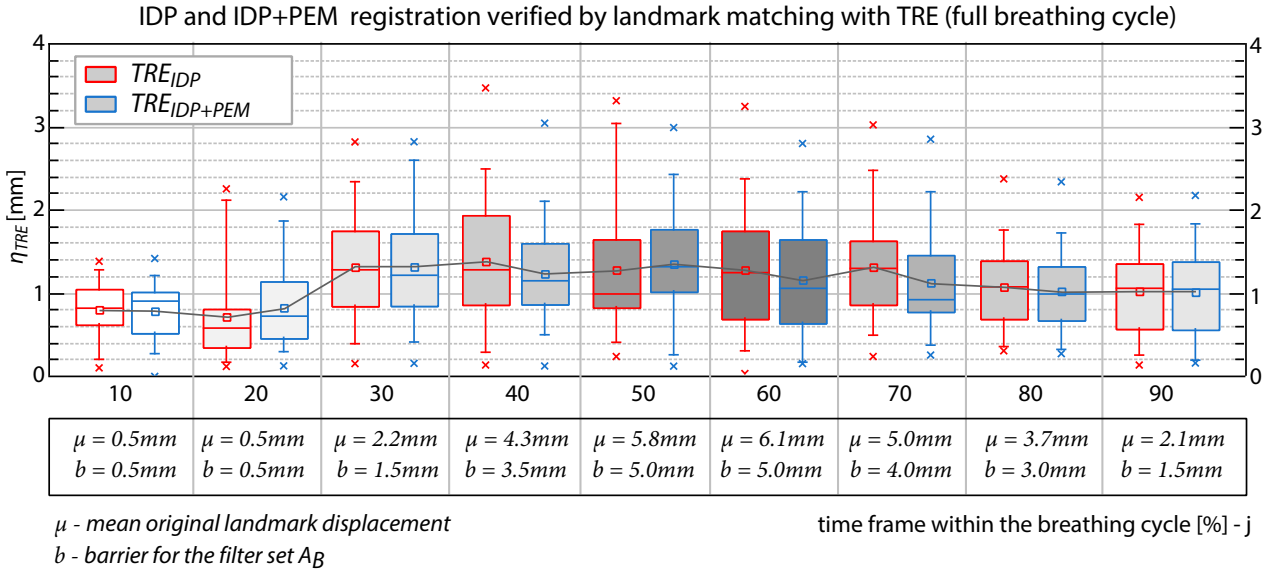

Figure 2.33 : Detailed TRE for the hybrid approach regarding all breathing phases: The plot regards only to the IDP implementations of this work ($IDP_a \rightarrow$ FFD implementation based on *iPlan™ RT*). The data is based on the registration of the reference set (inhale) and all other breathing phase $j = 1...9$. The used landmarks are part of the POPI-model (see Fig. 2.11). The used PEM filter is A_B with different barriers in relation to the original landmark displacement μ of the breathing phase. Each error distribution distinguishes between the pure IDP implementation (red) and the hybrid approach (blue).

2.3.3 Investigation of the lung slipping effect

All previous tests have merely proven that the hybrid approach achieves no loss of quality in contrast to the pure IDP implementation. A real improvement was not demonstrated yet. The main idea of the model is a better motion estimation inside lung slipping areas (see section 2.2.1). A first positive assessment of the hybrid approach is based on the vector field plot in Fig. 2.34. Again, the illustration explains the deformation results for the single registration of the reference set (inhale) and breathing phase $j = 6$ (exhale). The data is based on both IDP implementations (IDP_a, IDP_b). The sample views of the hybrid implementation (IDP+PEM) clearly show the improvement. Lung slipping is not neglected anymore. The motion estimation is distributed over the full lung. The effect is visible for both views (sagital and coronal) and for both IDP implementations. Whereas the surface filter (Fig. 2.31) dampens inner motion regions, the filter A_B does not affect such areas. The difference plot on the right confirms, that only lung slipping areas receive additional motion from PEM. Inner zones are unchanged. The lung slipping effect is particularly strongly visible in z-direction for both views (sagital, coronal) in outline near regions. This could be explained by the predominant diaphragmatic breathing technique of the patient. The improvement of the hybrid model is directly verifiable with the aid of the advanced landmarks introduced in section 2.2.1. The accompanied TRE test confirms the refinement. Again, a TRE experiment was accomplished for the single registration of the inhale and the exhale phase. The results are illustrated in Fig. 2.35. For both IDP implementations (IDP_a, IDP_b) a significant improvement is visible. For IDP_a the TRE median shifts from 7.1 mm down to 4.2 mm, for IDP_b the TRE median shifts from 5 mm down to 2 mm. A similar improvement is visible for all other TRE properties: mean, maximum, quartiles. These values also improve by 3 – 4 mm. The Bland-Altman plot on the right investigates the improvement for every single landmark. Again, the plot confirms the improvement of the model. Almost all values are plotted with positive abscissa values. PEM is better than the pure IDP implementation ($x = TRE_{IDP} - TRE_{IDP+PEM}$). More than the half of the landmarks are significantly improved, because their abscissa value $TRE_{IDP} - TRE_{IDP+PEM}$ is larger than the mean parameter ($\mu = 2.54$ for a, $\mu = 2.74$ for b). Especially large deviations (large ordinate

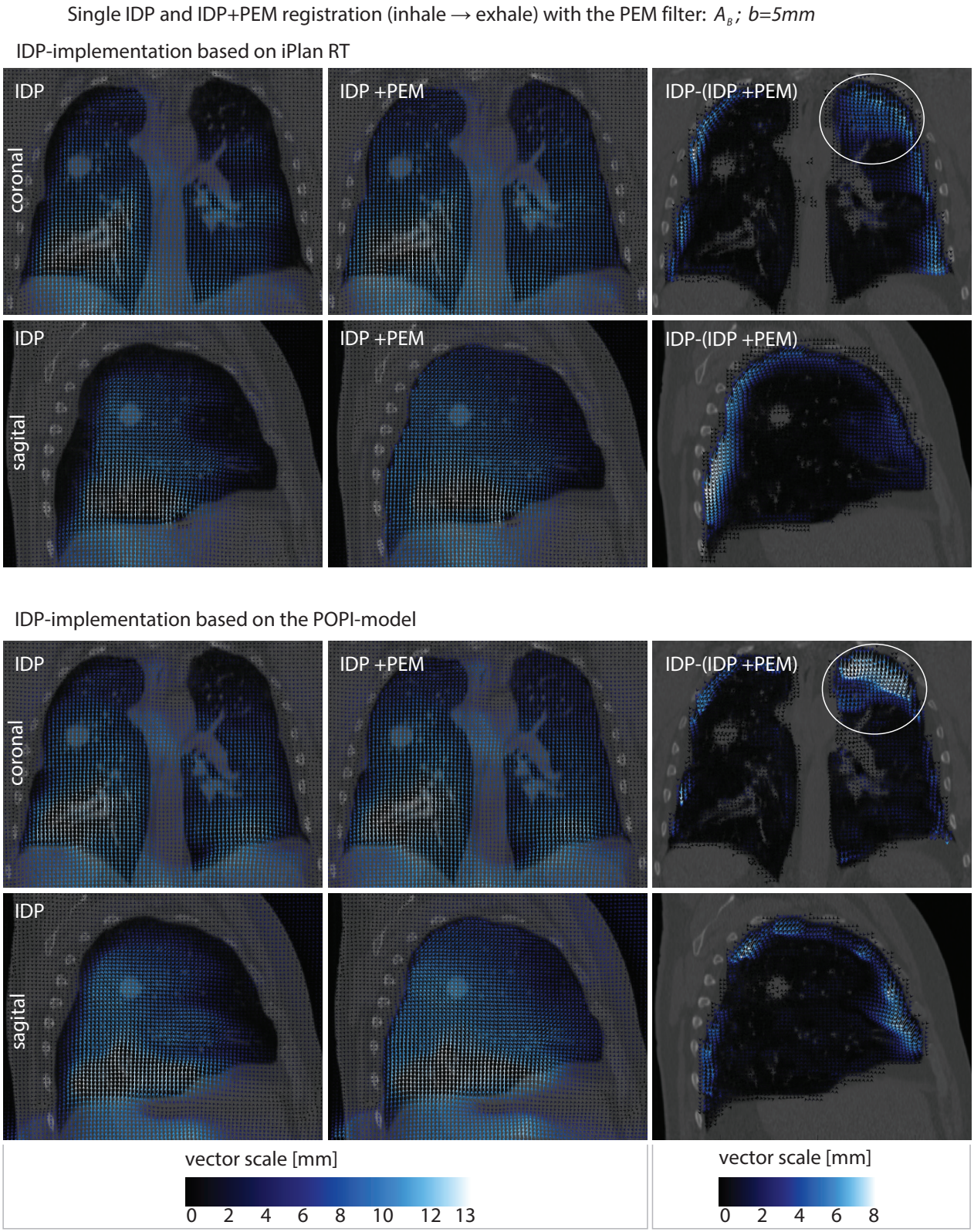

Figure 2.34 : Deformation field for the hybrid approach with the barrier filter: The illustration distinguishes between both IDP implementations. The used PEM filter regards to the best result in Fig. 2.32. The data is based on the registration of the reference set (inhale) and the breathing phase $j = 6$ (exhale). The image shows the geometry of the reference set for sample planes in coronal and sagital view. The data describe the local displacement through the breathing phase. The value of the displacement is scaled by the ratio in the legend below. The left column illustrates the pure IDP deformation. The middle describes the hybrid deformation data. The right illustrates the difference of both vector fields with an own vector scaling. The used PEM parameters are: $t = 200$ time steps, $\gamma = 1 \cdot 10^{-4}$, $k_D = 1 \cdot 10^9$, $k_A = 0.01$, $k_V = 0.01$;

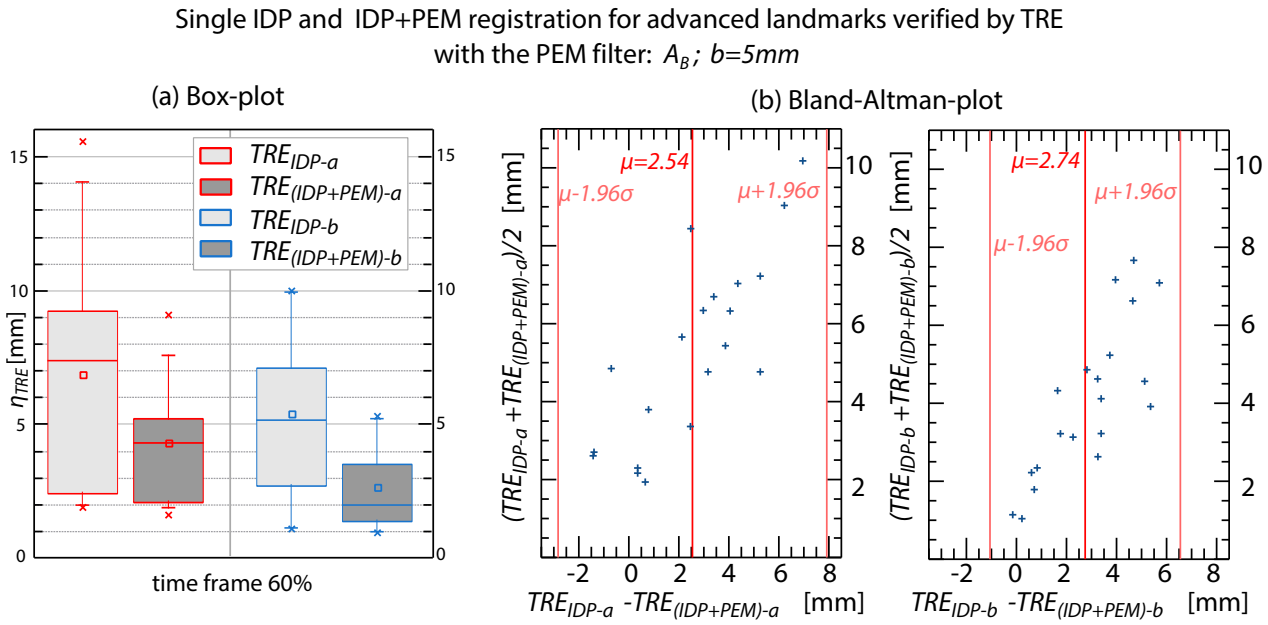

Figure 2.35 : Detailed TRE for the hybrid approach investigating the lung slipping effect: The plot distinguishes between both IDP implementations (IDP_a → FFD implementation based on *iPlan™ RT*, IDP_b → FFD implementation regarding the POPI-model). The data is based on the registration of the reference set (inhale) and the breathing phase $j = 6$ (exhale). The used landmarks are the advanced landmarks of this work for lung slipping investigation (see Fig. 2.15). Each error distribution distinguishes between the pure IDP implementation and the hybrid approach in (a). (b) explains the respective Bland-Altman plots for both IDP implementations.

values → $\frac{1}{2}[TRE_{IDP} + TRE_{IDP+PEM}]$) improved significantly. This is confirmed with both Bland-Altman plots illustrated with an increase of ordinate values accompanied with large abscissa scores. It seems that the noisy data depend on a linear increasing function.

During investigation of all the positive advantages of the hybrid approach, one should take into account that the model could have drawbacks. A trivial assumption is that the model does not know where the lung slipping really occurs. The model estimates lung slipping for surface near areas that inherent low motion in contrast to strong displaced structures in the middle of the lung. In contrast to real slipping regions, which are measured with the advanced TRE test, there exist regions that are not subject of the natural displacement. A detailed investigation of the already mentioned deformation plot in Fig. 2.34 provides clarity. The difference plot on the right describes all supposed lung slipping areas. In real lung slipping occurs in almost all calculated regions. Additional motion does not occur in the cranial upper area of the left lung marked with a white circle in the coronal sample views. A view on the coronal sample views of the pure IDP implementations (left) shows that both models detect no motion in this specific region. There is no motion estimated in the center of this region, although there are clearly defined (HU value gaps) bronchial structures. In reality, there occurs no motion. These false positive lung slipping areas receive additional motion with the hybrid approach. The filter model does not consider such effects. The subsequent reaction is local stress applied through expansion of the PEM deformation model. It could result in large deformation errors. The effect is particularly observable for both implementations in Fig. 2.34 (IDP_b).

False positive lung slipping effect has not been verified by the previous TRE tests. The statistics obscured the result. A detailed investigation of single deformation data regarding IDP_b in Fig. 2.34 reveals the finding. For this purpose, an additional experiment compared the basic TRE landmarks with Bland-Altman plots for IDP_b and the breathing phase $j = 6$. Fig. 2.36 illustrates the outcome. The statistical Box-Plot of the TRE in (a) shows

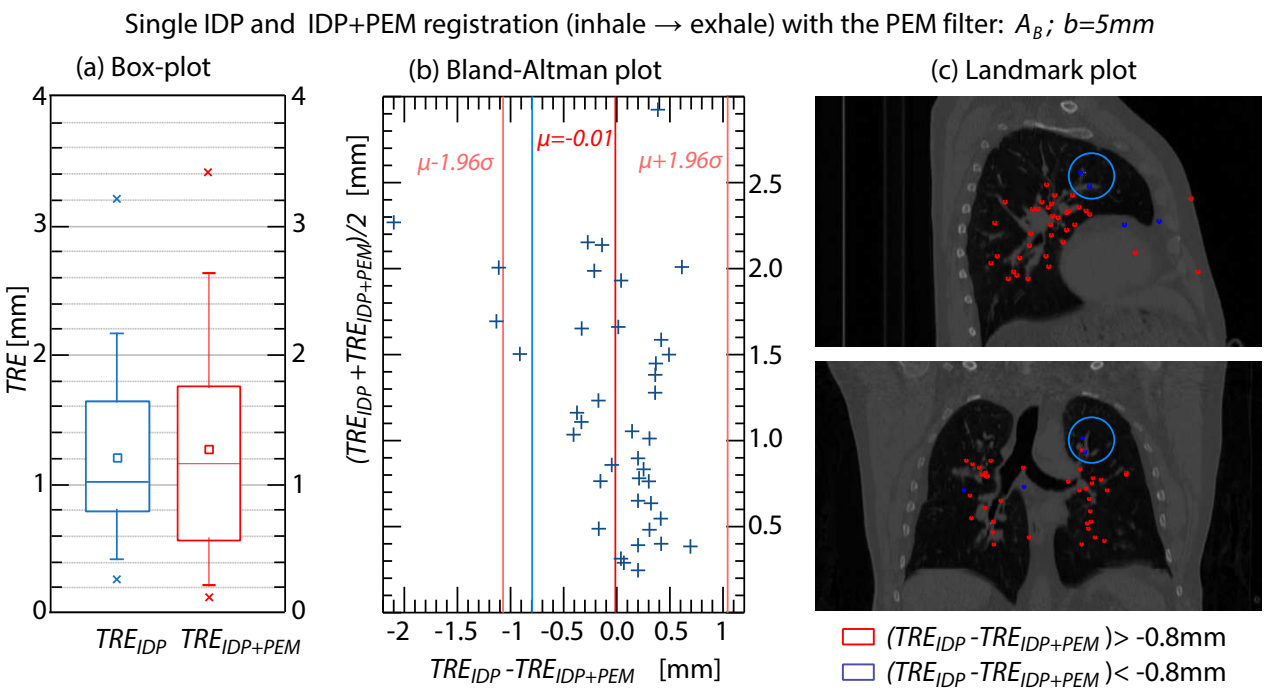

Figure 2.36 : Detailed TRE for the hybrid approach with the barrier PEM filter: The plot regards only to the IDP implementations of the POPI-model (IDP_b → FFD implementation based on the POPI-model). The data is based on the registration of the reference set (inhale) and the breathing phase $j = 6$ (exhale). The used landmarks are part of the POPI-model (see Fig. 2.11). The TRE Box-plot in (a) explains the error distribution of the pure IDP implementation and the hybrid approach. The Bland-Altman plot in (b) investigates the shift of any landmarks, whereas low values (< 0) on the abscissa became significantly worse due to the hybrid approach. Most of the landmarks are shifted really well and many are even better than before. However, there are three outliers with $TRE_{IDP} - TRE_{IDP+PEM} < -0.8$ mm. These outliers are marked blue in the landmark plot in (c). Two of them are located in a special lateral region (bright blue).

no loss of quality. There is no significant change form the pure IDP to IDP+PEM. The maximum values rise slightly, but lower values even become better. In general, the results are suitable. However, the direct landmark verification in (b) shows four outliers that become significant worse through the hybrid recalculation. These landmarks have a very low abscissa value (< 0.8 mm). The geometric landmark plot in (c) shows that two of the mentioned outliers are directly located in the false positive lung slipping area. This verification confirms the drawback of the hybrid approach. An extension of the model should distinguish between real and false positive lung slipping areas.

2.4 Discussion

The previous sections have shown that pure IDP implementations are very accurate for global landmark tests. These TRE tests try to cover the full deformation area of the patient. They are good tools for general deformation assessment. In the results of this tests, the mean TRE is located at 1.0 mm–1.5 mm for the maximal breathing deformation. Common 4DCTs have a slice spacing of 2 mm in z-direction. With regard to this fact, the IDP results are acceptable. The algorithm is generally suitable for 4D dose planning in SBRT. The lung slipping is a local effect. It affects even small fractions of the lung, i.e. small lung border volumes. The motion inside these zones is predicted incorrectly by IDP. This could be proven with the advanced landmark tests (see Fig. 2.15, Fig. 2.16). The presented hybrid approach significantly improves the motion estimation of this regions. This is confirmed by the deformation field plot in Fig. 2.34 and the corrected TRE results in

Fig. 2.35. After recalculation, motion estimation covers the full organ. It looks much more realistic than before. Nonetheless, also this solution embeds faults. The model defines false positive lung slipping areas and predicts motion where naturally no motion occurs. This leads also to errors. However, this work has shown that the deformation quality of the hybrid approach strongly depends on the used vector filter model. Hence, it is probably possible to minimize the erroneous effect with the aid of an improved filter model. For example, stopping terms (i.e. low motion vectors) in the center of the lung far away from the surface, could prevent any additional motion. They prevent unrealistic motion and wipe out false positive lung slipping effects. Prospective studies should investigate this filter dependencies.
Since the hybrid model merely optimizes a small fraction of the full organ, one has to evaluate the effort of the implementation for dose calculation. The hybrid approach is a very complex system with a high degree of undefined parameters. A computationally intensive process is necessary to yield sufficient results. If a 4D dose planning approach uses a trivial treatment setup that merely treat a small fraction of lung slipping regions, the hybrid approach will conclusively not achieve better results than the pure IDP implementation. The effect is investigated by chapter 4. However, the hybrid approach simulates the motion estimation more realistic then the pure IDP approach.
Nonetheless, the hybrid approach achieves other advantages. The model is able to calculate lung motion for extremely reduced vector fields (see Fig. 2.27). Such vector fields are insufficient and they are not useable to describe a global deformation. The 3D deformation of the mentioned experiment is illustrated in Fig. 2.37. The image series show a stepwise deformation based on a single inhale and exhale CT. Since it is possible to calculate the full deformation only with an extremely reduced vector field, the model enables the calculation of deformation without any 4DCT data. If displacement vectors are extracted from other modalities (e.g. diaphragmatic laser scanning or thorax fluoroscopy) the model could determine the deformation merely based on a 3D shape derived from a static CT. Such calculations are not as accurate as the presented complex hybrid approach, but they are processable in real-time and approximately suitable for the calculation of the tumor displacement. Finally, the following list summarizes the properties of the hybrid elastic image fusion model:

1. **Advantages of the hybrid deformation model:**
    a) Solution to simulate the lung slipping effect
    b) No loss of quality in contrast to an adequate IDP implementation
    c) Possible motion calculation for reduced filter sets
    d) Deformation calculation for non discrete CT time steps
    e) Past planning adjustment if breathing patterns differ a lot
2. **Disadvantages of the hybrid deformation model:**
    a) Very complex strategy with high degrees of freedom
    b) The effect of false positive lung slipping areas
    c) Slight improvement for 4D planning due to the small share of lung slipping

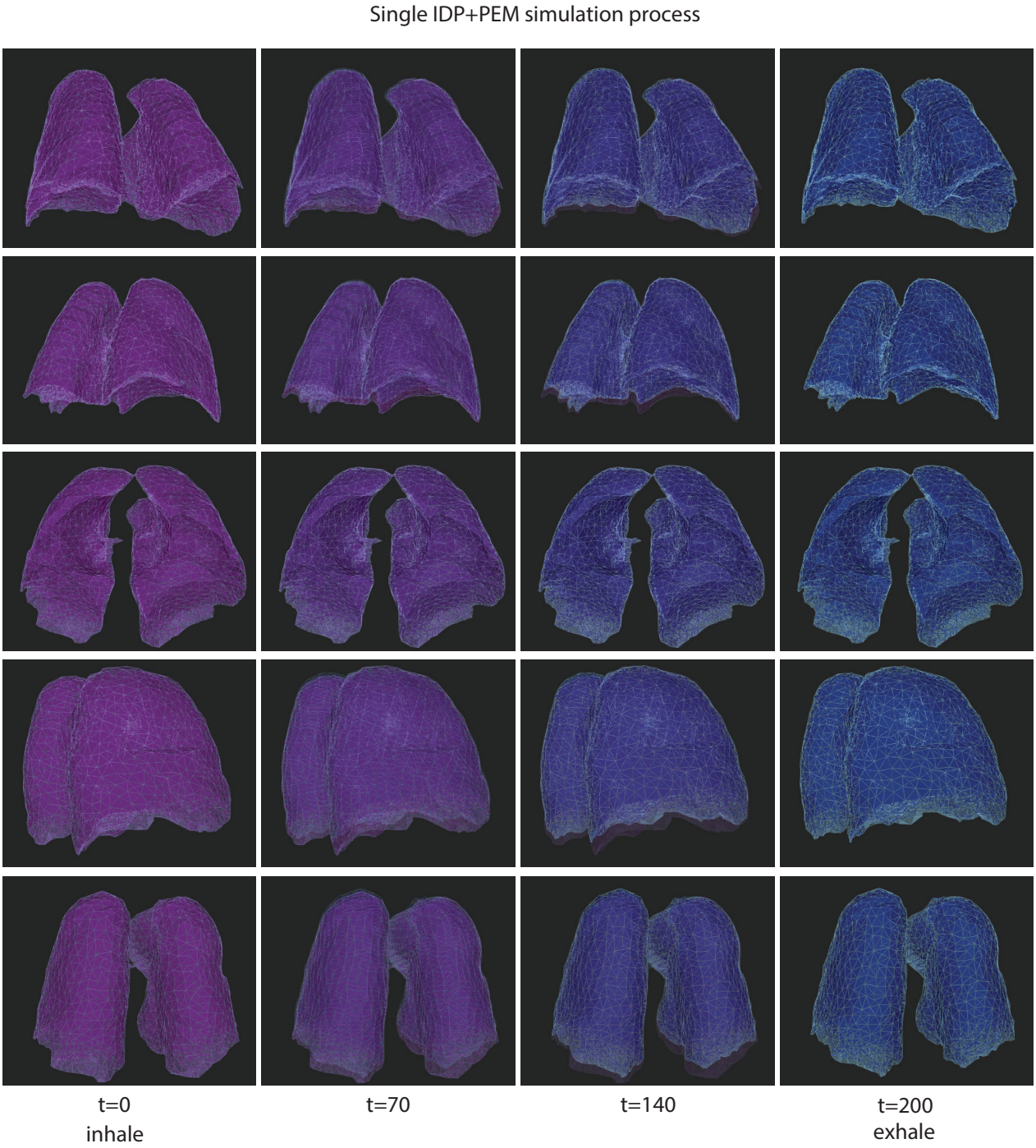

Figure 2.37 : Simulation with the hybrid approach: The image illustrates a typical 3D IDP+PEM simulation with 200 time steps from inhale to exhale in five different views. The shown example regards to the experiment mentioned in Fig.2.27. It uses an insufficient vector field and the PEM surface filter model: $A_S \cap A_D$ with $b = 5$ mm. The used PEM parameters are: $t = 200$ time steps, $\gamma = 1 \cdot 10^{-4}$, $k_D = 1 \cdot 10^{9}$, $k_A = 0.01$, $k_V = 0.01$;

Chapter 3

3 4D dose calculation based on accumulation of time dependent dose distributions

The previous analysis has shown that respiration-induced motion is not negligible for Stereotactic Body Radiation Therapy (SBRT). Intrafractional breathing induced motion influences the dose distribution delivered to the dynamic patient geometry. A static simulation might not be sufficient. There can be a large discrepancy between a treatment plan in 3D only and the real applied dose. Such deviations, i.e. dose differences between static dose calculations and four dimensional dose accumulations, shall be analyzed in this chapter. For this purpose, the following outline analyzes and explains the basics of breathing induced 4D dose accumulation such as its numerical implementation. Furthermore, the investigations include a dose error evaluation study for 4D dose calculations, where specific dose transformation algorithms were analyzed regarding their dose transformation quality.

3.1 Principles

3.1.1 Schematic dose accumulation work flow

The technical opportunities in the field of precise dose calculation and accumulation inside the dynamic anatomy of the human body are not fully exploited in clinical practice [93, 40]. Dose accumulation is widely used in several tasks of radiotherapy, such as dose summation for different beams as well as the integration process of beamlets in case of a dynamic IMRT [114].
However, all these applications are based on a static geometry. For lung cancer treatments, an accurate dose accumulation has to consider the full deformation process inside the lung and the abdomen. It is necessary to consider the dose distributions of each separate breathing phase which is constituted by a separate geometry. The different geometries are recorded by a respiratory correlated 4DCT scan of the breathing cycle. A deformation grid [94] v_{ij} connects these geometries in an algorithmic way (see chapter 2). The full registration is a group of vector fields that represent the spatial relationships. This allows single dose transformations between the considered CT geometries. The definition of a reference set enables the calculation of the total accumulated dose distribution. Thus, it is possible to evaluate the clinical quality of the final dose distribution in a conventional way. Fig. 3.1 explains the basic 4D dose accumulation principle. The figure describes the goal of dose accumulation in the context of this work.
A set of respiratory correlated (whole breathing cycle) arranged dose distributions is given to model the full treatment process. Whereas one distribution, i.e. the underlying geometry, counts as reference set. The necessary tissue information is derived from time indifferent static CT measurements within the 4DCT scan (see section 2.1.3). The static, but time dependent dose calculations, are generated by appropriate dose algorithms. To evaluate the clinical outcome, it is necessary to prepare a 4D data content for a conventional result. As a matter of fact the main assessment of a clinical plan is based on the dose distribution, the detection of the Planning Target Volume (PTV) and the evaluation of the dose volume histogram (DVH). All these param-

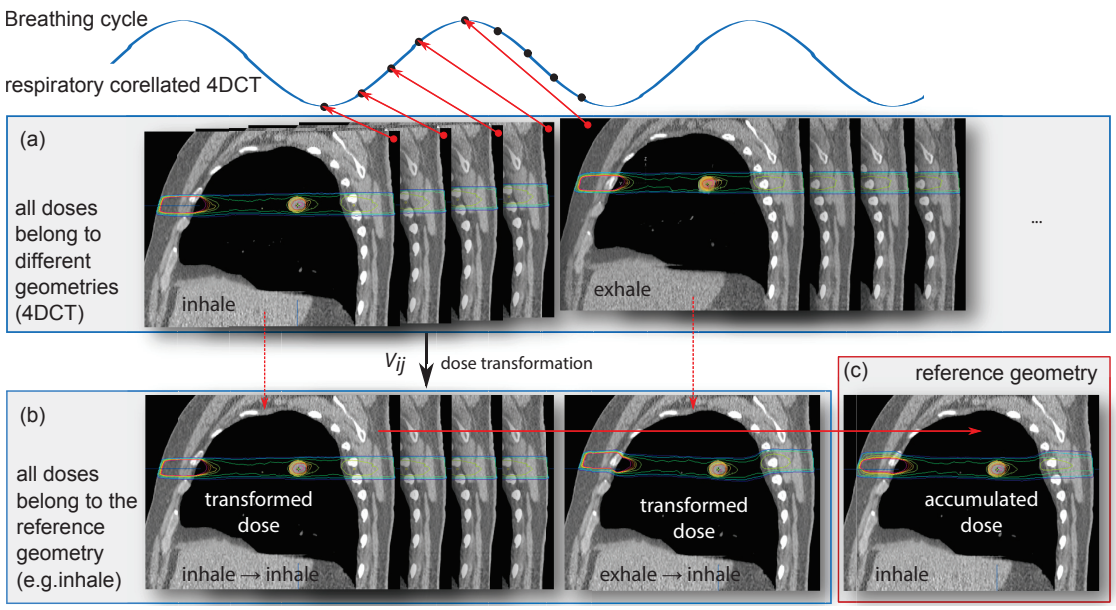

Figure 3.1 : Principle dose accumulation work flow for breathing induced 4D calculations: (a) Generation of several dose distributions arranged over the whole breathing cycle. (b) Transformation of every dose distribution into the reference geometry. (c) Summation of all deformed distributions inside the reference geometry.

eters refer to a static dose distribution, which is sufficient in most cases. It is impractical and confusing to evaluate a set of time depended dose distributions individually. For clinical practice it is necessary to calculate an accumulated 3D dose distribution without losing 4D dose information. For this purpose, all generated time dependent dose distributions have to be transferred into the same static geometry. The basic 4D dose accumulation principle is well established and verified with different applications by *Rosu et al.*[79], *Keall et al.*[52], *Janssens et al.*[41] and *Söhn et al.* [95].

The 4DCT (with $j = 1...n$ static CTs) and the related static dose distributions $D_j(\vec{x}_j)$ with the coordinates $\vec{x}_j \in \mathbb{R}^3$ in the geometry j form the prerequisites for the dose accumulation process. Furthermore, the deformation information $v_{ij}(\vec{x}_j)$ (see chapter 2.2) connects every space j (breathing phase) to the reference set i:

$$v_{ij}(\vec{x}_j) = \vec{x}_i; \quad v_{ij}^{-1}(\vec{x}_i) = v_{ji}(\vec{x}_i) = \vec{x}_j \tag{3.1}$$

i defines the target space for all dose transformations. $v_{ij}^{-1}(\vec{x}_i)$ being the inverse transformation. A suit deformation function v_{ij} is not invertible[1]. v_{ij}^{-1} does not exist. It follows, v_{ij} and v_{ji} have to be calculated separately, either according to the established procedures (see chapter 2) or with an inverse approximation (e.g. Newton-Raphson optimization). Defined is a simplified formula for the accumulated dose $D_{i\sum}$ in the system of i:

$$D_{i\sum}(\vec{x}_i) = \sum_{j=1}^{n} w_j \cdot D_j(v_{ij}^{-1}(\vec{x}_i)) \tag{3.2}$$

with w_j being a simple weighting factor. w_j denotes the fraction of time how long the system stays in state

[1]The non-invertibility arises through the discrete structure (e.g. grid based voxels) of the dose/density distribution as they are used in numerical dose calculations. Numerical solutions are able to approximate the inverse vector field with negligible deviations. For this purpose, the Newton-Raphson optimization algorithm is used in this work. An example calculation with the *iPlan™ RT* framework revealed a mean deviation of 0.03 mm and a maximum deviation of 0.4 mm.

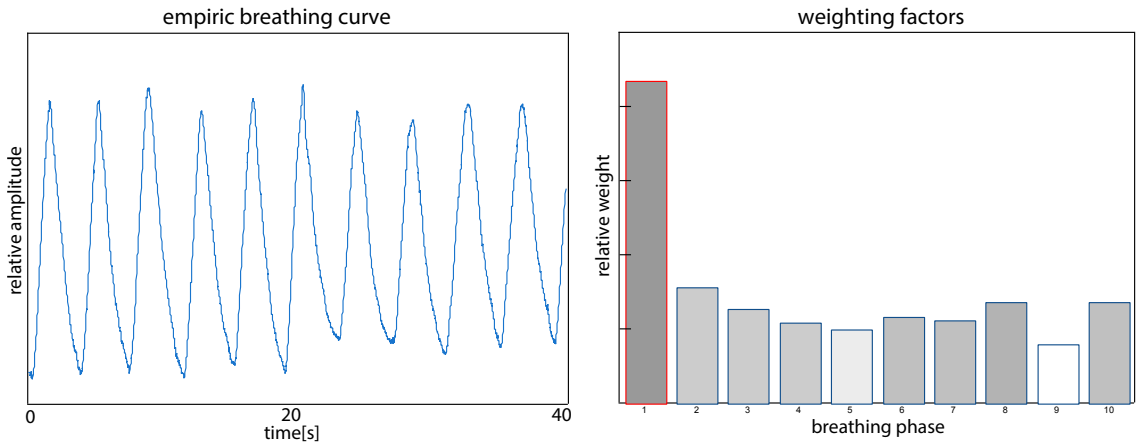

Figure 3.2 : Determination of breathing phase weighting for dose distributions: (a) Example breathing curve measured during the acquisition of a 4DCT (e.g. ten breathing cycles). (b) Relative time within a separate breathing phase (1 → maximum exhale ... 6 → maximum inhale ... 11 → maximum exhale) based on the mean probability from (a). In this example, the maximum weight receives the exhale phase (red).

j in relation to the whole breathing cycle, because a nonlinear respiration curve has to be assumed. Thus, not all distributions contribute with the same fraction. It is easy to determine the weighting empirically [95]. The description of the breathing motion has to be approximated by the average of many breathing cycles (see Fig 3.2.a) due to significant irregularities within the breathing motion. The motion average, so called probability density function (PDF) [95], enables the description of the relative time spent within a single CT phase (see Fig 3.2.b). The normalized weighting factor derives from: $w_j < 1; \sum_{j=1}^{n} w_j = 1$.

3.1.2 The deformation effect

Equation (3.2) works accurately for affine transformations, i.e. a bijection between two affine spaces. This could be a translation, a scaling, a rotation, a shear mapping or a combination of those. However, the physiology of the lung is more complex, geometrical deformations like expansion or compression are predominant[2]. Assumed is a local set of coordinates in system j that merge to a single point in i and vice versa (see Fig 3.3). This deformation effect impacts the dose calculation during accumulation. A large set of points $\vec{x}_j^1, \vec{x}_j^2 ... \vec{x}_j^p ... \vec{x}_j^n$ in j with $v_{ij}(\vec{x}_j^p) = \vec{x}_i$ is assumed that affects the dose $D_{i\sum}(\vec{x}_i)$ in one specific point $\vec{x}_i$. Fig. 3.3 illustrates the deformation effect. An advanced solution for the accumulated dose considering the deformation effect inside a volume V is defined by:

$$D_{i\sum}(\vec{x}_i) = \sum_{j=1}^{n} w_j \cdot \left[\int_{\vec{x}_j \in V} \delta_j(\vec{x}_i, \vec{x}_j) \cdot D_j(\vec{x}_j) \cdot d\vec{x}_j \right] \tag{3.3}$$

where the delta function $\delta_j(\vec{x}_i, \vec{x}_j)$ describes points that have an impact to the dose in $\vec{x}_i$. $\delta_j(\vec{x}_i, \vec{x}_j)$ is defined by:

$$\delta_j(\vec{x}_i, \vec{x}_j) = \begin{cases} 1 & \text{for } v_{ij}(\vec{x}_j) = \vec{x}_i \\ 0 & \text{for } v_{ij}(\vec{x}_j) \neq \vec{x}_i \end{cases} \tag{3.4}$$

For evaluation of dose compression effects, it is necessary to focus on the physical concept of absorbed doses.

[2]Image analysis with *iPlan™ RT* revealed that lung volumes could differ up to 250 cm^3 – 500 cm^3 between exhale and inhale state.

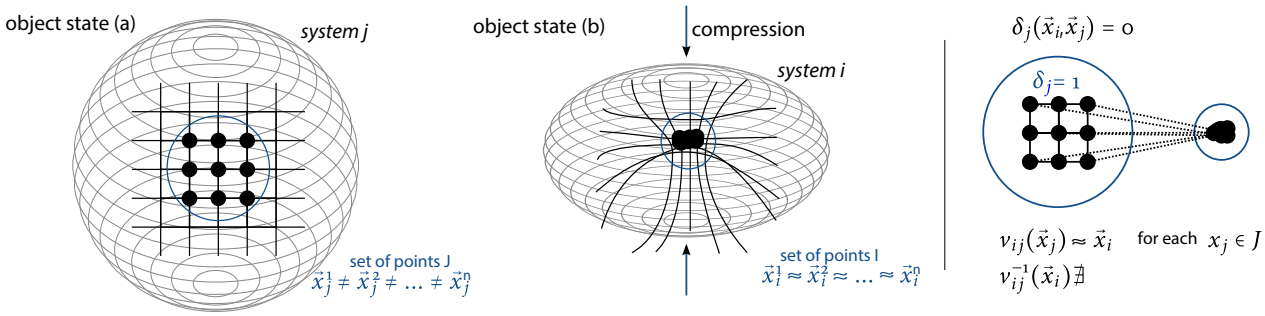

Figure 3.3 : Schematic constellation of point merging: An object could change his constitution (a→b) due to compression. A cloud of different point coordinates in the system j could fuse to a single coordinate in system i. Hence, the numerical deformation function is not invertible.

$D(\vec{x})$ is a local value. Generally, $D(\vec{x})$ is less suitable to describe macroscopic dose distributions. $D(\vec{x})$ is point specific with a locally departed energy value E_{absorbed} regarding a specific local mass density ρ_{local} [55]. The spatial dose is defined by:

$$D_{\text{local}} = \frac{dE_{\text{absorbed}}}{dm_{\text{local}}} = \frac{1}{\rho_{\text{local}}} \cdot \frac{dE_{\text{absorbed}}}{dV} \tag{3.5}$$

This concept is well suited for numeric dose calculations as they are used in medical planning systems [95][3]. It is straightforward to calculate the dose D directly for a numeric voxel dV with the aid of a grid related mass density ρ derived from a CT scan. Analytically, the point dose is written as:

$$D(\vec{x}) = \frac{1}{\rho(\vec{x})} \cdot \frac{dE}{dV} \tag{3.6}$$

Equation (3.6) reveals the major problem for dose accumulation. The dose depends on the local density ρ and on the local energy dE. If a spatial deviation for ρ is assumed in the human lung with values from $0.044\ \frac{\text{g}}{\text{cm}^3} - 0.302\ \frac{\text{g}}{\text{cm}^3}$ (ICRU lung tissue) up to $0.302\ \frac{\text{g}}{\text{cm}^3} - 1.101\ \frac{\text{g}}{\text{cm}^3}$ (ICRU soft tissue), at least some areas or neighboring dose points strongly differ in ρ [93]. If these dose points are fused to a single coordinate (see Fig 3.3), the resulting dose will not be the dose average. The final dose is a construct of all affecting doses, of all related densities or all related energy values[4]. This affects the dose formulated in (3.3). For this reason, a dose compound function ω is introduced:

$$D_{i\sum}(\vec{x}_i) = \sum_{j=1}^{n} w_j \cdot \left[\int_{\vec{x}_j \in V} \delta_j(\vec{x}_i,\vec{x}_j) \cdot \omega(\vec{x}_i,\vec{x}_j) \cdot D_j(\vec{x}_j) \cdot d\vec{x}_j \right] \tag{3.7}$$

ω illustrates that not all dose points, which merged to a single point, contribute with the same fraction of their dose values. The definition of ω is a challenge for dose accumulation in the context of this work. ω ensures the correct union of dose points which are based on a heterogeneous object. The major problem is demonstrated in Fig. 3.4.

[3] The mentioned equation explains the accurate dose definition declared as dose-to-medium. This is implemented for several dose algorithms, e.g. Monte Carlo. It explains the energy absorbed in a tissue element (voxel) divided by the mass of the tissue element. However, traditional algorithms (e.g. Pencil Beam) calculate a simplified dose, so called dose-to-water. It describes the energy absorbed in a small cavity of water divided by the real mass (tissue) of the cavity. Further implementations and evaluations regard exclusively to dose-to-medium.

[4] Jeffrey V. Siebers investigated in his publication of 2008 [93] in a quite simple example of two voxels that there is a significant discrepancy between the real applied dose and the mean dose of several voxels if the mass density is not homogeneously distributed (see 3.1.3).

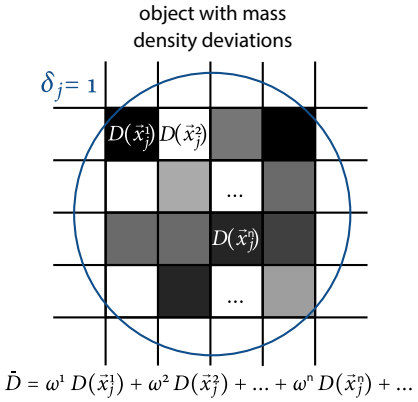

Figure 3.4 : Problem of dose accumulation: The average dose is not applicable to describe the individual object dose $\bar{D}$ for an object with a heterogeneous structure ($\Delta\rho >> 0$). The compound function ω ensures a different complex weighting of the involved dose points $D_j(\vec{x}_j)$.

It exists a dose definition that deals with the approximation of an absorbed dose for a non-uniformly and inhomogeneous irradiated object (IIO) with a heterogeneous mass structure. The International Commission on Radiological Protection (ICRP) published this definition in their recommendations of 2007 [39]. Also *Brahme et al.*[8] published the definition in their biological investigations about dose response behaviors[5]. The approximated dose for an IIO is defined by the mass weighted average of all involved (object related) dose points:

$$\bar{D}_{\text{Def.}} = \frac{\int D(\vec{x}) \cdot dm}{\int dm} = \frac{\int_{\vec{x}\in V} D(\vec{x})\rho(\vec{x}) \cdot d\vec{x}}{\int_{\vec{x}\in V} \rho(\vec{x}) \cdot d\vec{x}} \tag{3.8}$$

It may be written as a numerical approach dealing with voxels x instead of coordinates $\vec{x}$:

$$\bar{D}_{\text{Def.}} = \frac{\sum_{x\in V} D(x) \cdot m(x)}{\sum_{x\in V} m(x)} = \frac{\sum_{x\in V} E(x)}{\sum_{x\in V} m(x)} \tag{3.9}$$

Exemplary, the following compound function arises for equation (3.7) with the aid of the dose definition for IIOs:

$$\omega_{\text{Def.}}(\vec{x}_i, \vec{x}_j) = \frac{\rho(\vec{x}_j)}{\int_{\vec{z}_j\in V} \delta_j(\vec{x}_i, \vec{z}_j)\rho(\vec{z}_j) \cdot d\vec{z}_j} \tag{3.10}$$

The preceding disquisition discovered the non-triviality of point dose summations to evaluate individual object doses that goes with the topic of dose accumulation in the field of 4D treatment planning. The aim of this chapter is to investigate the mentioned problem with biological models, different numerical algorithms and empirical tests.

3.1.3 Numerical procedure

The discrete structure of dose distributions (grid based voxels) requires simplifications for the numerical implementation of dose accumulation. The following numerical formula for a dose $D_{i\sum}(x_i)$ in a voxel x_i of the reference set I is derived from (3.7):

$$D_{i\sum}(x_i) = \sum_{j=1}^{n} w_j \cdot \left[\sum_{x_j = v_{ji}(x_i)-\Delta_j}^{v_{ji}(x_i)+\Delta_j} W_{ji}(x_i, x_j) \cdot D_j(x_j) \right] \tag{3.11}$$

[5] Section 3.2 investigates the approach from a biological point of view.

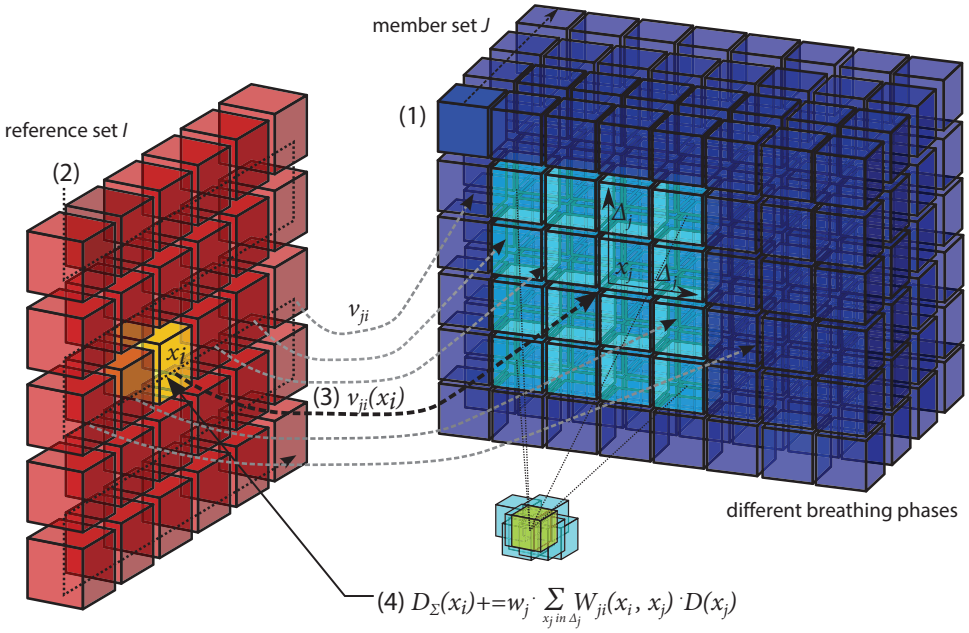

Figure 3.5 : Numerical procedure of dose accumulation. For illustration this sketch contains two dimensions for every geometry (red = reference geometry; blue = set of different breathing grids). However, all real implementations must have three dimensions. The voxels are arranged in a practical grid based structure (e.g. red reference grid). The chronological procedure behaves as follows: (1) Select one (J) of all target geometries (blue); (2) Select one voxel (x_i) that accumulated dose has to be calculated inside the reference set (red); (3) Find the related coordinate x_j inside the target with the aid of the deformation grid $x_j = v_{ji}(x_i)$; (4) Calculate the fractionated dose portion for x_i with regard to the used accumulation model (W_j, Δ_j) and with regard to a set of dose voxels D_j around x_j; (5) Select the next voxel in I; After this has been performed for all voxels, go over to the next target geometry $J + 1$ until the whole breathing cycle is completed.

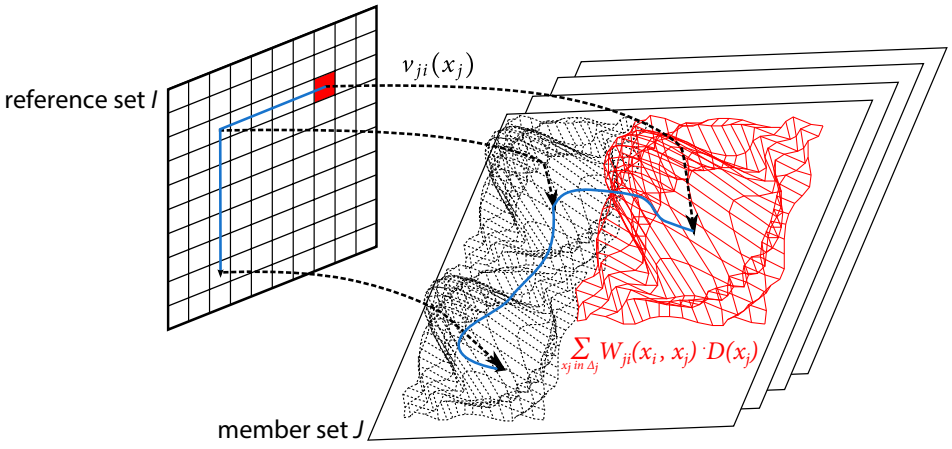

Figure 3.6 : Dose accumulation as discrete dynamic convolution: The numerical procedure works like a dynamic convolution. The convolution kernel depends on the used accumulation model. While the calculation is running, the kernel is pushed over the target geometry (blue trace). The trace depends on the deformation grid and is related to the voxel in the reference set (blue trace). The kernel shape dependents on compression or expansion and is defined by $W_j(x_i, x_j)$ (red shape).

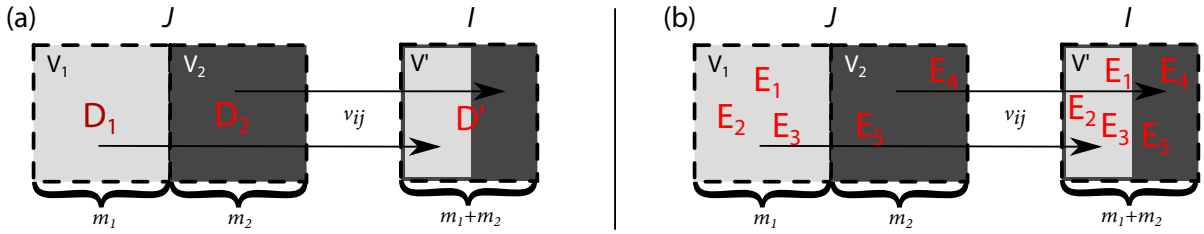

Figure 3.7 : Simple voxel system to evaluate transformational dose errors. The voxels V_1 and V_2 inside the member set J migrate through deformation to voxel V' (reference set I). (a) describes dose transformations and (b) illustrates the energy scenario.

Fig. 3.5 illustrates the numerical procedure. $\pm\Delta_j$ denotes a neighborhood interval in the breathing phase set J. It describes the maximum possible compression inside the processed tissue and has to be defined carefully before calculation. $\Delta_j \to \infty$ mostly applies for analytical theorems, e.g. (3.7). $\pm\Delta_j$ is introduced for practical reasons. It outlines how far voxels x_j^1, x_j^2 could be placed in J, if they may migrate through deformation to the same target x_i in I. Within the defined interval, an algorithm collects coordinates x_j which largely contribute to the target dose in voxel x_i. The method of contribution depends on the accumulation model itself. Also, the definition of Δ_j goes with the individual accumulation model. Several algorithms are illustrated in section 3.3. Therefore, the generic accumulation operator $W_{ji}(x_i, x_j)$ is introduced to illustrate the task of the accumulation model related algorithms. Each voxel in I will be calculated separately. For every voxel x_i, there exists a set of voxels $v_{ji}(x_i) \pm \Delta_j$ in J which contribute with different fractions to the accumulated dose.
Finally, the procedure works as a discrete dynamic convolution. The accumulated dose is the convolution result of the member space J integrated over all member spaces within the breathing cycle. The convolution kernel $W_{ji}(x_i, x_j)$ is dynamically adjusted based on the individual dose voxel x_i, the related target dose coordinate $v_{ji}(x_i)$ and the influence (deformation) of the neighborhood dose area around the target dose point $v_{ji}(x_i) \pm \Delta_j$ (see Fig. 3.6). Basically the accumulation of dose is describable by the following expression[6]:

$$D_{i\sum} = \sum_{j=1}^{n} W_{ji}(v_{ji}) * D_j \tag{3.12}$$

Possible dose errors for discrete calculations

The numerical explanation shows the specific convolution approach. Discrete dose unions are inevitable during the dose accumulation calculation. The model of accumulation W_{ji} is important for the accuracy. Different models are illustrated in section 3.3. The following explanations describe general dose differences. The overview takes the different accumulation approaches into account. The validation model is a simplified (one dimension) scenario based on a two-voxel-system inspired by *Siebers et al.* [93]. Two voxels V_1 and V_2 are observed at the different times J and I. During the breathing cycle (in J), the coordinates of the voxels are spatially different, whereas they migrate to a single dose voxel V' in the reference system I at the beginning of the breathing cycle (see. Fig. 3.7.a). In order to calculate dose distributions inside the lung, both voxels contain different masses (m_1 and m_2). The task of the calculation is the dose transformation (D') to the reference voxel V'. In order to the definition of dose (see formula (3.5)), that describes object doses as summarized energy deposition per object mass, an exemplary draft is illustrated in 3.7.b. Random energy events are distributed

[6] This trivial expression is used in many publications in the context of dose accumulation. The equation itself is not sufficient and neglects a lot of important facts. It should be used for general assumptions. However, the formula mentioned in (3.11) is more informative.

inside the object to explain the dose creation process within several voxels. The dose definition (3.5) enables to describe the transformed dose for $D'_{\text{Def.}}$. In the outlined scenario, it is defined by[7]:

$$D'_{\text{Def.}} = \frac{\overbrace{E_1 + E_2 + E_3}^{E_{V_1}} + \overbrace{E_4 + E_5}^{E_{V_2}}}{m_1 + m_2} = \frac{E_{V_1} + E_{V_2}}{m_1 + m_2} \tag{3.13}$$

With the aid of an introduced mass parameter ($\gamma = \frac{m_2}{m_1}$, [93]), that handles possible mass deviations, (3.13) can be written as:

$$D'_{\text{Def.}} = \frac{D_1 + D_2 \cdot \gamma}{1 + \gamma} \tag{3.14}$$

A very trivial model to unify dose voxels is the dose interpolation method (DIM) [78, 80] (see section 3.3.1 for a detailed explanation).[8] DIM follows the rules of arithmetic interpolation. For this one dimensional example, the model calculates the mean value of all source voxels to create the transformed dose D'_{DIM}. This average is defined by:

$$D'_{\text{DIM}} = \frac{D_1 + D_2}{2} = \frac{\frac{E_{V_1}}{m_1} + \frac{E_{V_2}}{m_2}}{2} \tag{3.15}$$

At this point, it is possible to define the dose transformation error η for DIM. The error η regards to the dose definition mentioned in formula (3.13). It outlines the dose difference in the following way [93]:

$$\eta = \left| D'_{\text{DIM}} - D'_{\text{Def.}} \right| = \frac{|(D_2 - D_1) \cdot (1 - \gamma)|}{2 \cdot (1 + \gamma)} \tag{3.16}$$

The error depends on the specific mass deviation γ. Since this work is focused on lung treatments, γ could increase up to values larger than 20. This arises from the ICRU proposals for soft tissue densities ($0.044 \frac{g}{cm^3}$ – $0.302 \frac{g}{cm^3}$) and lung tissue densities ($0.302 \frac{g}{cm^3}$ – $1.101 \frac{g}{cm^3}$) [93]. A large mass deviation has a strong effect on η. In areas of dose gradients, beam edges or build up regions significant differences up to 100 % may be observable for DIM. η discloses the importance of a precise dose accumulation model. Inaccurate methods predict wrong voxel doses. This could have an influence on the clinical outcome (section 4.3). Therefore, section 3.3 introduces and compares a selection of accumulation algorithms which are investigated regarding their quality and practicality in lung cancer treatments.

3.2 Biological aspects and methods

The previous section describes the accumulation of absorbed doses for different time states from a physical point of view. Absorbed doses are calculated to estimate the biological damage of tumor cells and healthy organs. The question is whether dose transformations and, above all, dose accumulations are applicable under the assumption that they leave a biological harm. Is it possible to transform time and point related dose damages between different geometries? The following explanations confirm the transformation concept with the

[7] In this case $D'_{\text{Def.}}$ exactly agrees with the already discussed basic dose definition for IIOs in (3.8).

[8] The reason why DIM is often used, is entirely its simplicity. Most of the necessary functions are already implemented in many medical calculation systems, because DIM is frequently used for other important dose problems (e.g. scaling of dose distributions or dose coordinate transformations).

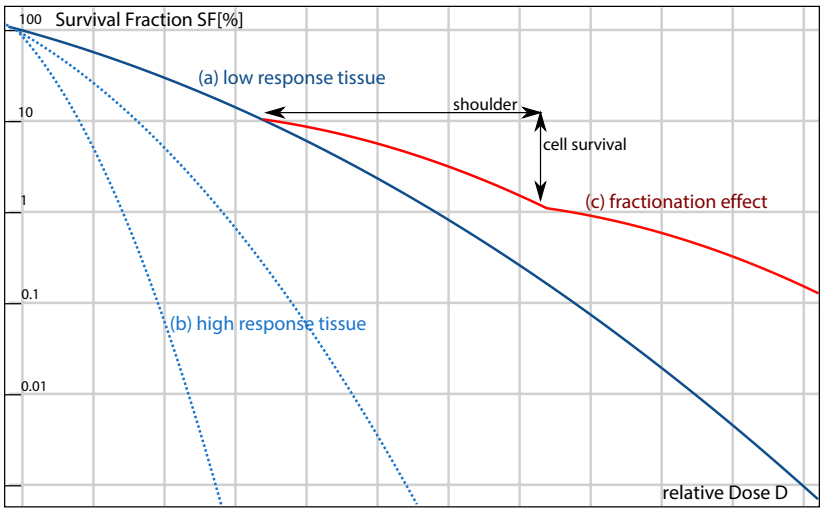

Figure 3.8 : Exemplary cell survival curve with the linear-quadratic approach $SF(D) = e^{-\alpha D-\beta D^2}$: (a) The effect with a given dose is slight (low α/β ratio). (b) Doses leave large lethal cell rates (high α/β ratio). (c) Fractionated treatments provide cell recovery. Tissue types with a wide shoulder ($\uparrow \beta$) recover better. The quadratic term is important for these cases. Compared with that, linear curves are mainly influenced by the linear term $\uparrow \alpha$ (b).

aid of biological models. In general, biological models were used to evaluate the clinical response of prescribed doses [67, 8, 30, 69, 59].

3.2.1 Survival rate

Almost all biological models are based on the cell survival curve. It describes the relationship between the surviving cell fraction SF and the absorbed dose D after irradiation of a given cell population N_0. SF outlines the number of surviving cells $N(D)$. $SF(D)$ is defined by:

$$SF(D) = \frac{N(D)}{N_0} \tag{3.17}$$

In practice, the most commonly model is the linear quadratic (LQ) model [1]:

$$SF(D) = e^{-\alpha D-\beta D^2} \tag{3.18}$$

The behavior of the LQ model described by Fig. 3.8. The coefficients α and β depend on the tissue type and the radiation quality. In absorbed doses, α determines the slope of the survival curve. The quadratic term β determines the shoulder shape of the survival curve. A collection of survival parameter data for human tissue types is published in [35]. A simplification of the LQ model was proposed by *Brahme et al.* [8], the one hit model (OHM):

$$SF(D) = e^{-\alpha D} \tag{3.19}$$

The approximation in (3.19) is sufficient for many cases in conventional fractionated treatments where the linear term is crucial [34]. The mentioned assumption was also used by *Niemierko et al.* [69] in their proposal about the equivalent uniform dose (EUD)[9]. Especially in this essay, where the surviving fraction supports the

[9]The EUD investigates a similar dose accumulation problem that tries to reduce an inhomogeneous dose distributions to a single dose value. However, the EUD is focused on the description of different tissue types with regard to their clinical outcome.

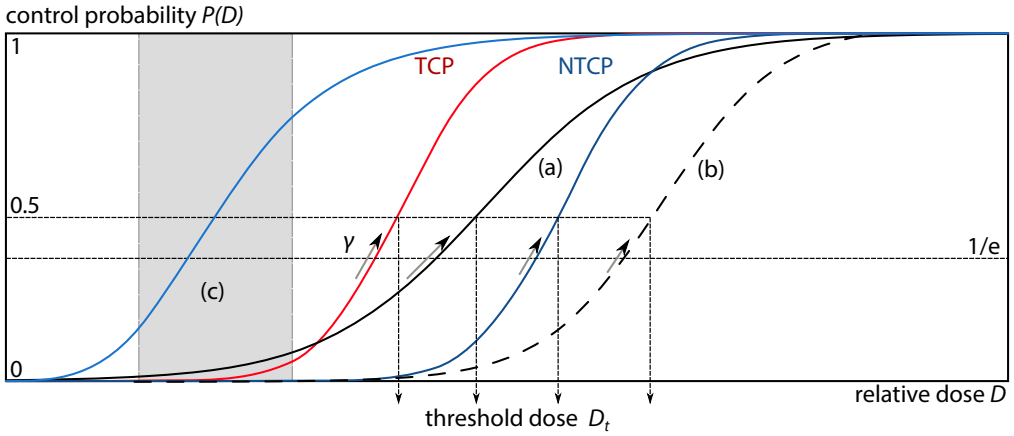

Figure 3.9 : Graphical dose response overview: Different shapes of dose responses are based on equation (3.20). Colored lines schematically obtain an optimal radiation reaction with a large response dose ΔD_{50} (at P(D)=0.5) difference for tumor cells and healthy cells ($D_{t_{TCP}} < D_{t_{NTCP}}$). Furthermore, (a) and (b) differ additionally in the dose response gradient γ. (c) describes an approximated linear area within the sigmoid function.

calculation of local dose unions and accumulations, the OHM (3.19) is sufficient. To simplify the complexity, the fractionation effect β is neglected in the following studies.

3.2.2 Relationship between control rate, dose and mass

In clinical practice, important dose planning parameters that describe the response of the treatment are introduced: the tumor control probability (TCP) and the normal tissue complication probability (NTCP)) [8]. They are determined on the survival fraction. The clinical effect depends on the applied dose and the true number $N(D)$ of surviving cells after irradiation. This could be approximated with the Poisson distribution of destroyed cells. Basically, the control probability $P(D)$ is used to describe the clinical outcome [8]:

$$P(D) = e^{-N(D)} = e^{-N_0 \cdot SF(D)} \tag{3.20}$$

Fig. 3.9 gives an overview of different dose response shapes. A sigmoid dependence between the response and the dose can be observed [1]. Nevertheless, the function varies for several tissue types and different radiation qualities. The response dose D_{50} enables a characterization that represents the dose at the half maximum response. In an optimal scenario of radiation therapy exists a huge deviation between D_{50} of TCP and NTCP (see Fig. 3.9). Desirable is an applicated dose with the maximum tumor response accompanied with the lowest side effect for organs at risk (OAR). Another individual parameter is the slope of the shape. Dose response curves based on (3.20) are slightly asymmetric. The inflection point, known as the value with the steepest slope, is located at $P(D) = e^{-1}$. Small dose adjustments around this area achieve large response variations. Using (3.19) and (3.20), the gradient can be written as:

$$\frac{dP(D)}{dD} = e^{-N_0 e^{-\alpha D}} \cdot N_0 e^{-\alpha D} \cdot \alpha = P(D) \cdot [-\ln(P(D))] \cdot \alpha \tag{3.21}$$

The controlled gradient around the inflection point $P(D) = e^{-1}$ can be applied:

$$\frac{dP_{\text{infl}}}{dD} = e^{-1} \cdot \alpha \tag{3.22}$$

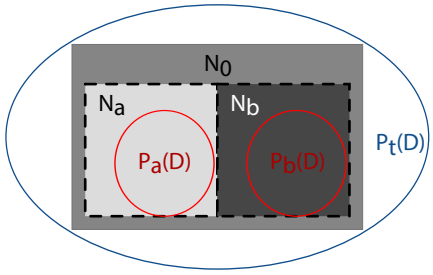

Figure 3.10 : Simple system based on two individual voxels. The object is divided into the cell populations N_a and N_b which create a heterogeneous structure. The control probability of the object $P_t(D)$ depends on the local control rates $P_a(D)$ and $P_b(D)$.

A dose increase of α^{-1} implies a 37 % ($\approx e^{-1}$) higher control rate [8]. At the same time formula (3.22) is a good estimator for the slope between the values of 10 % and 70 % (Fig 3.9.c) of the maximum control probability, because an approximately linear dependency is assumed. Also this property affects the shapes of different tissue types (e.g. Fig 3.9.a and Fig 3.9.b). Thereby, the importance of α is significant to indicate the radio sensitivity of a specific tissue type in relation to the radiation quality. The slope of the control probability is known as the normalized dose gradient γ defined by:

$$\gamma = D \cdot \frac{dP}{dD} \tag{3.23}$$

with γ being dimensionless, describing the expected control probability variation for a given relative dose increase[10]. All mentioned approaches suppose a uniform dose distribution for the entire tissue volume. However, as already demonstrated in section 3.1, realistic dose distributions are seldom uniform. This applies in particular for inhomogeneous mass structures with large spacial density deviations such as lung geometries. Therefore, $P(D)$ has to presuppose a inhomogeneous dose dependency $D + \Delta D$. Hence, the full increase of the control probability $P(D + \Delta D)$ due to a dose increase of ΔD can be written as:

$$P(D + \Delta D) = P(D) + \frac{dP}{dD} \cdot \Delta D = P(D) + \gamma \cdot \frac{\Delta D}{D} \tag{3.24}$$

In addition to dose fluctuations, mass deviations are largely responsible for the control rate variations. For illustration, the given cell population N_0 could be divided into different populations $N_0 = N_1 + \ldots + N_n$ to reflect various densities in the object. The behavior of the control probability for cell mixtures can be shown for a trivial model with two densities expressed with two populations $N_0 = N_a + N_b$. Again, this is illustrated with one dimensional two-voxel-system (see Fig 3.10). Using (3.20), two individual control probabilities for separate cell populations a and b can be written as:

$$\begin{aligned} P_a(D) &= e^{-N_a \cdot SF_a(D)} \\ P_b(D) &= e^{-N_b \cdot SF_b(D)} \end{aligned} \tag{3.25}$$

The probability $P_t(D)$ to control the entire object is given by the conditional probability of P_a and P_b assuming a statistical independence of both [8]. Finally, the conditional term $P_t(D)$ is expressible with the survival rate. It is defined by:

$$\begin{aligned} P_t(D) &= e^{-(N_a \cdot SF_a(D) + N_b \cdot SF_b(D))} \\ &= P_a(D) \cdot P_b(D) \end{aligned} \tag{3.26}$$

[10] For example: A dose increase of $\Delta D = +1$ % is followed by: $\Delta P(D) \approx +"\gamma"$ % in a range of 10 % < $P(D)$ < 70 % [8]. A list of tissue depended examples for γ can be found in [8].

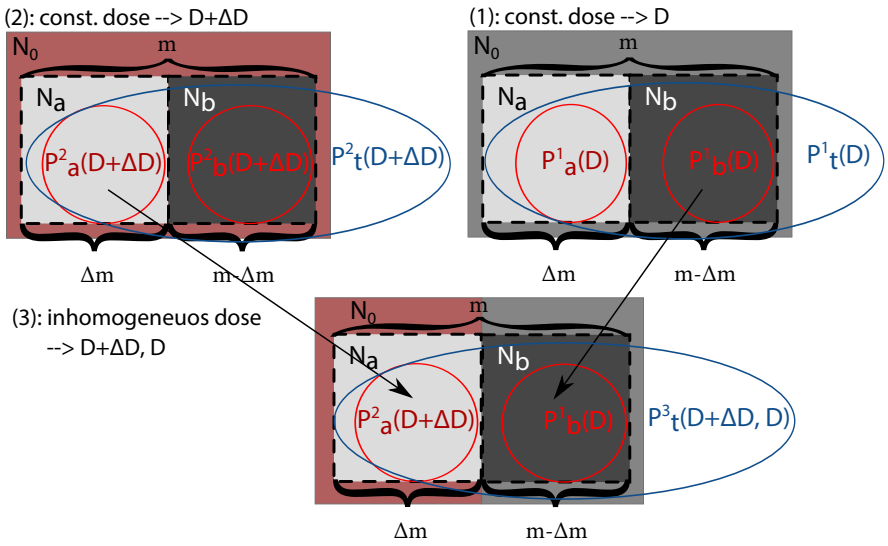

Figure 3.11 : Simple voxel system treated with three different doses. The voxel system composites of two different masses Δm and $m - \Delta m$. (1) The full object is treated with the same dose D. (2) The full object receives a dose increase of ΔD. (3) The object is treated with an inhomogeneous dose ($\Delta D + D$ and D). Hence, total control rate respectively dependents on its individual control rates.

To point out the mass effect, a homogenous dose in the object is assumed exceptionally for the next equation. An equal survival rate inside the object ($SF(D) \approx SF_a(D) \approx SF_b(D)$) follows. Moreover, the relation of cell values is proportional to the relation of the local masses ($\frac{N_a}{N_0} \approx \frac{m_a}{m_0}$). Consequently, the individual control probability (e.g. P_a) is describable by:

$$\begin{aligned} P_a(D) &= e^{-N_a \cdot SF_a(D)} = e^{-[SF(D)\cdot N_0]\cdot \frac{N_a}{N_0}} = e^{-[N_a \cdot SF(D) + (N_0 - N_a)\cdot SF(D)]\cdot \frac{N_a}{N_0}} \\ &= P_t(D)^{\frac{N_a}{N_0}} = P_t(D)^{\frac{m_a}{m_0}} \end{aligned} \tag{3.27}$$

Affected masses have a large impact on the dose response. The exponent in (3.27) directly results in a shift of the control rate. Hence, in relation to a constant dose, low masses have a higher individual control probability than heavier masses. This is an important paradigm in SBRT particularly for high dose prescriptions of immense tumors [8].[11] The mentioned mass effect (3.27) is consistent (with respect to (3.26)) with the cell distribution and the mass distribution: $\frac{N_a}{N_0} + \frac{N_b}{N_0} = 1$ and $\frac{m_a}{m_0} + \frac{m_b}{m_0} = 1$. Imagine two scenarios for both cell populations (see Fig. 3.11.1 and Fig. 3.11.2), whereas one population is composed by a significantly different mass Δm, then the other one. The mass of the full object is m. In scenario one, the entire object is treated with a constant dose D; while in scenario two, the whole object is treated with a constant dose $D + \Delta D$. As a result, the total control rate for both cases is defined by the following equations (with respect to (3.24)):

$$\begin{aligned} P_t(D) &= P(D) \\ P_t(D + \Delta D) &= P(D) + \gamma \cdot \frac{\Delta D}{D} \end{aligned} \tag{3.28}$$

Due to the homogenous dose in both scenarios, the total control rate can be splitted into one of their components using 3.27. Therefore, the individual control rates for a in case two and b in case one are defined by:

[11] The mass effect has already been introduced in the early years of radiation therapy (e.g. 1979 by *Goitein et al.* [26] and 1983 by *Schultheiss et al.* [86]).

$$\begin{aligned} P_b(D) &= P_t(D)^{1-\frac{\Delta m}{m}} = P(D)^{1-\frac{\Delta m}{m}} \\ P_a(D+\Delta D) &= P_t(D+\Delta D)^{\frac{\Delta m}{m}} = \left[P(D) + \gamma \cdot \frac{\Delta D}{D}\right]^{\frac{\Delta m}{m}} \end{aligned} \tag{3.29}$$

In a last scenario (see Fig. 3.11.3), a non-uniformly distributed dose is assumed for the object. Hence, one part of the object Δm is treated with dose $D + \Delta D$ and the other part $m - \Delta m$ is treated with dose D. In such a case, the total control probability $P_t(D + \Delta D, D)$ arises from the basic statistical condition (3.26):

$$P_t(D + \Delta D, D) = P_a(D + \Delta D) \cdot P_b(D) \tag{3.30}$$

The combination of (3.29) and (3.30) allows the description of the total control probability $P_t(D + \Delta D, D)$ for a heterogeneous object $(\Delta m, m - \Delta m)$ treated with a non-uniformly distributed dose $(D + \Delta D, D)$:

$$\begin{aligned} P_t(D + \Delta D, D) &= \left[P(D) + \gamma \cdot \frac{\Delta D}{D}\right]^{\frac{\Delta m}{m}} \cdot P(D)^{(1-\frac{\Delta m}{m})} \\ &= \left[1 + \gamma \cdot \frac{\Delta D}{D \cdot P(D)}\right]^{\frac{\Delta m}{m}} \cdot P(D) \end{aligned} \tag{3.31}$$

For simplification of this explanation, small dose gradients and low mass deviations ($\frac{\Delta D}{D} \cdot \frac{\Delta m}{m} << 1$) in relation to their total values are assumed. Hence, one can approximate the following construct using the power expansion [8]:

$$\begin{aligned} P_t(D + \Delta D, D) &= \underbrace{\left[1 + \gamma \cdot \frac{\Delta D}{D \cdot P(D)}\right]^{\frac{\Delta m}{m}}}_{1+\frac{\Delta m}{m}\gamma\frac{\Delta D}{D\cdot P(D)}\cdots} \cdot P(D) \\ &\approx P(D) + \gamma \cdot \frac{\Delta D}{D} \cdot \frac{\Delta m}{m} \end{aligned} \tag{3.32}$$

The resulting control rate is comparable to the total control probability in scenario one (Fig. 3.11.1), where a homogenous dose D was assumed. The difference of both probabilities reflects the control increase, if a part of the object Δm receives a dose increase ΔD. The approximated change in the control rate can be expressed by:

$$\Delta P \approx \gamma \cdot \frac{\Delta D}{D} \cdot \frac{\Delta m}{m} = \gamma \cdot \frac{\Delta E}{E} \tag{3.33}$$

The control rate is a good estimator for the local damage. (3.33) describes the dependencies and the impact, if a non-uniformly distributed dose is assumed for a heterogeneous object. It clearly shows that the combination of the dose and the mass forms an integral dose response [8]. This is the main conclusion of this outline. In order to create numerical dose unions for 4D dose accumulations, dose values as well as their related mass values have to be taken into account. In the field of dose transformations, the neglection of mass would mean a loss of important information. It results in a wrong interpretation of the given dose grid. It would result in a wrong dose transformation. A simple dose interpolation without mass weighting is not sufficient, particularly for rough approximations. Secondly, the outline has shown that the combination of terms in formula (3.33) is replaceable with energy distributions which could also suit as calculation for transformation.

3.2.3 Unifying inhomogeneous dose distributions

The previous section suggests that the basic dose definition model for IIOs in formula (3.10) may be a good solution to unify inhomogeneous dose distributions during dose accumulation. The following outline supports and explains the correctness of the suggested hypothesis from the biological point of view. For this purpose, an inhomogeneous object with a non-uniformly distributed dose is assumed. Furthermore, let N_0 be the total number of cells in the object before irradiation and let $\rho(\vec{x})$ be the cell density at $\vec{x}$. After irradiation, considering the survival fraction SF and the inhomogeneous dose distribution $D(\vec{x})$ the resulting value of survived cells N [125] is defined as:

$$\begin{aligned} N_0 &= \int_{\vec{x}\in V} \rho(\vec{x}) \cdot d\vec{x} \\ N &= \int_{\vec{x}\in V} SF(D(\vec{x})) \cdot \rho(\vec{x}) \cdot d\vec{x} \end{aligned} \tag{3.34}$$

This is a typical example for a discrete mixture model [125], because the non-uniform density $\rho(\vec{x})$ and the survival fractions $SF(D(\vec{x}))$ vary across the volume due to the inhomogeneous dose distribution. The value of surviving cells N can be determined by its probability function, with one of its parameters, here: SF, being a random variable itself. In this case, the probability function is a mixed distribution. The mixture model takes into account that values of $SF(D)$ can be determined by the absorbed dose distribution D [125]. Discrete mixtures, also known as uncountable mixture functions, are often introduced in empirical problems. Therefore, a conditional probability function $p(x, \lambda)$ for x, parametrized by λ, is considered. This applies for each λ in the arbitrary set of Λ. $g(\lambda)$ is a mixed density function that describes the distribution of this parameter as a random variable. The combination of the previous terms results in a probability function for x again with the generic formula for a discrete mixture distribution [125, 13, 46]:

$$p(x) = \int_{\Lambda} p(x|\lambda) \cdot g(\lambda) \cdot d\lambda \tag{3.35}$$

For the radiological procedure, the density function $g(\lambda)$ is equal to the individual treated cell value $g(D)$, where it summarizes all cells that are treated with the not uniformly distributed value D. $g(D)$ is approximately similar to the dose volume histogram (DVH), if a proportional relationship between the cell values and the tissue volume is assumed. Considering a dose range of $D_{\min}...D_{\max}$ the total number of cells N_0 is:

$$N_0 = \int_{D_{\min}}^{D_{\max}} g(D) \cdot dD \tag{3.36}$$

To describe the probability of surviving cells $p(x)$, the conditional probability function $p(x|D)$ is necessary[12]. This is the Poisson survival model for a particular value of D that describes the probability of surviving cells, if an arbitrary value of dose for index x is provided. According to [125], it is defined by:

$$p(x|D) = \frac{SF(D)^x \cdot e^{-SF(D)}}{x!} \tag{3.37}$$

Combining (3.35), (3.36) and (3.37), the probability function $p(x)$ of surviving cells irradiated with a heterogeneous dose distribution may be written as:

$$p(x) = \int_{D_{\min}}^{D_{\max}} \frac{SF(D)^x \cdot e^{-SF(D)}}{x!} \cdot g(D) \cdot dD \tag{3.38}$$

[12] x is an alternative value and different to a coordinate $\vec{x}$. The Poisson statistic assigns probabilities to this variable.

Due to the dose union process of dose transformation, it is important to know the mean value of surviving cells. Therefore, it is necessary to find the expectation value $E[X]$ of $p(x)$. How it is determined, is a meaningful property of the discrete mixture model [46, 125] and given by:

$$E[X] = \int_{D_{\min}}^{D_{\max}} E_{x|D}[X] \cdot g(D) \cdot dD \tag{3.39}$$

$E_{x|D}[X]$ is the mean conditional expectation value with $E_{x|D}[X] = SF(D)$ in case of the Poisson survival model. Thus, the mean number of surviving cells N after irradiation with an inhomogeneous dose distribution is defined by[13]:

$$N = E[X] = \int_{D_{\min}}^{D_{\max}} SF(D) \cdot g(D) \cdot dD \tag{3.40}$$

The main goal of this section is the definition of a single dose value $\bar{D}$, which exactly results in the same biological response as an inhomogeneous dose distribution $D(\vec{x})$. The main parameter for the biological damage is the number of surviving cells N. With the aid of (3.17) and (3.19) it is possible to postulate the following cell conservation law to compare the damage of a single dose value $\bar{D}$ with the damage of an inhomogeneous dose distribution D:

$$\begin{aligned} N(\bar{D}) &= N(D) \\ N_0 \cdot SF(\bar{D}) &= \int_{D_{\min}}^{D_{\max}} SF(D) \cdot g(D) \cdot dD \\ N_0 \cdot e^{-\alpha \bar{D}} &= \int_{D_{\min}}^{D_{\max}} e^{-\alpha D} \cdot g(D) \cdot dD \end{aligned} \tag{3.41}$$

For simplification, a linear dependence between dose and effect is assumed for small local areas (e.g. neighboring voxels). The first ordered Taylor series ($e^x = \sum_{n=0}^{\infty} \frac{x^n}{n!}$) is helpful to substitute all exponential terms in (3.41). This is applicable for a small local dose range in relation to the mean dose value: ($|D_{\max} - D_{\min}| << \bar{D}$)[14]. The simplified equation is written as:

$$N_0 \cdot (1 - \alpha \cdot \bar{D}) \approx \int_{D_{\min}}^{D_{\max}} (1 - \alpha \cdot D) \cdot g(D) \cdot dD \tag{3.42}$$

Converted to the single dose value $\bar{D}$ (taking a constant α into account)[15] the following scenario is assumed:

$$\begin{aligned} \bar{D} &= \frac{1}{\alpha} - \frac{1}{\alpha \cdot N_0} \cdot \int_{D_{\min}}^{D_{\max}} (1 - \alpha \cdot D) \cdot g(D) \cdot dD \\ \bar{D} &= \frac{1}{\alpha} - \frac{1}{\alpha \cdot N_0} \cdot \left[\int_{D_{\min}}^{D_{\max}} g(D) \cdot dD - \int_{D_{\min}}^{D_{\max}} g(D) \cdot \alpha D \cdot dD \right] \end{aligned} \tag{3.43}$$

With the aid of (3.36), it is possible to substitute N_0 in (3.43):

$$\bar{D} = \frac{1}{\alpha} - \frac{\int_{D_{\min}}^{D_{\max}} g(D) \cdot dD - \int_{D_{\min}}^{D_{\max}} g(D) \alpha D \cdot dD}{\alpha \int_{D_{\min}}^{D_{\max}} g(D) \cdot dD} \tag{3.44}$$

[13] If a set of cells irradiated with different doses and a integral over all these dose values is imagined, then the product of the individual cell survival fraction $SF(D)$ and the separate treated cell values $g(D)$ arises to the total number of surviving cells N.

[14] The correctness of equation (3.42) can be illustrated with the numerical calculation process ($\Delta D << D_1, D_2 ... D$):
$N_0 \cdot (1 - \alpha \cdot \bar{D}) \approx \sum_{D \epsilon \Delta D} (g(D) \cdot (1 - \alpha \cdot D))$; $N_0 \cdot (1 - \alpha \cdot \bar{D}) \approx (N_1 + N_2 + ...) \cdot (1 - \alpha \cdot D)$; $N_0 \cdot (1 - \alpha \cdot \bar{D}) \approx (N_0) \cdot (1 - \alpha \cdot D)$

[15] This theoretical argumentation is a rough approximation to support a dose transformation method that works for dose accumulation in the context of this work. Therefore, it is applicable to assume a constant tissue (α) in small voxel areas.

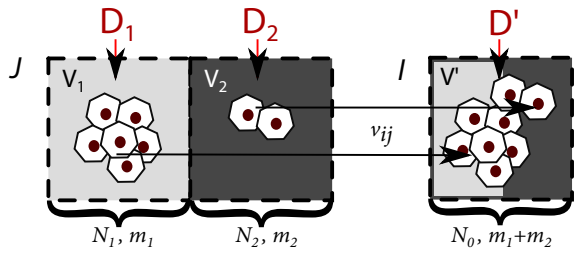

Figure 3.12 : Simple voxel compression with cell conservation: The object is divided into two cell populations N_1 and N_2 distributed over two voxels V_1 and V_2. Through compression the voxels unite to a single voxel V' which contains the total cell value N_0. Hence, the number of cells is known before and after compression.

which may be written as:

$$\bar{D} = \frac{\int_{D_{\min}}^{D_{\max}} g(D) D \cdot dD}{\int_{D_{\min}}^{D_{\max}} g(D) \cdot dD} \tag{3.45}$$

The spatial resolution of the dose distribution helps to convert the treated cell value $g(D)$ with the aid of the cell density $\rho(\vec{x})$ in the following way (with respect to (3.34) and (3.36)):

$$\begin{aligned} \int_{D_{\min}}^{D_{\max}} g(D) \cdot D \cdot dD &= \int_{\vec{x} \in V} \int_{D_{\min}}^{D_{\max}} g(D, \vec{x}) \cdot D(\vec{x}) \cdot dD \cdot d\vec{x} \\ &= \int_{\vec{x} \in V} \rho(\vec{x}) \cdot D(\vec{x}) \cdot d\vec{x} \end{aligned} \tag{3.46}$$

Then, for (3.44) arises through substitution with (3.46):

$$\bar{D} = \frac{\int_{\vec{x} \in V} \rho(\vec{x}) D(\vec{x}) \cdot d\vec{x}}{\int_{\vec{x} \in V} \rho(\vec{x}) \cdot d\vec{x}} \tag{3.47}$$

Formula (3.47) exactly corresponds to the basic dose definition for IIOs mentioned in equation (3.8) (see section 3.1.1). The numerical formula is[16]:

$$\bar{D} = \frac{\sum_{x \in V} m(x) \cdot D(x)}{\sum_{x \in V} m(x)} = \frac{\sum_{x \in V} E(x)}{\sum_{x \in V} m(x)} \tag{3.48}$$

In conclusion, the analysis has shown that the basic dose definition for IIOs is a good approximation to calculate a numerical dose unification value during dose accumulation. It ensures the conservation of mass information for an accurate biological response. Furthermore, the numerical definition allows the calculation either with dose distributions or with the deposited energy values in combination with their fractionated masses.

Biological dose accumulation in a two-voxel system

The outline of the shown cell conservation law allows the calculation of the dose error η (see section 3.1.3) mentioned in (3.16). For this explicit purpose, the well known two-voxel model (see Fig. 3.7) has to be extended by its biological components. This means, cell distributions has to be considered inside the voxels. The biological scenario is shown in Fig. 3.12 and describes a common voxel compression. Given are the cell values N_1 and N_2 for both voxels which migrate through compression to a single voxel containing the total cell value N_0. Both voxels are treated with different doses D_1 and D_2.
For error calculations, the unified dose D' in voxel V' is necessary. Therefore, the same biological damage is expected for the two doses D_1, D_2 and for the unified dose D'. The biological damage is equivalent to the

[16] x represents a voxel instead of a coordinate $\vec{x}$.

number of surviving cells inside the object, which is independent to the compression process. Hence, it is possible to form the cell conversation postulate (mentioned in (3.41)) for the discrete structure:

$$N(D') = N(D_1) + N(D_2) \tag{3.49}$$

With the aid of the survival fraction and the related OHM (see (3.17)), (3.19)), it may be written as:

$$\begin{aligned} N_0 \cdot SF(D') &= N_1 \cdot SF(D') + N_2 \cdot SF(D') \\ (N_1 + N_2) \cdot e^{-\alpha D'} &= N_1 \cdot e^{-\alpha D_1} + N_2 \cdot e^{-\alpha D_2} \end{aligned} \tag{3.50}$$

As a matter of fact, the first order of the Taylor series ($e^{-\alpha D} \approx 1 - \alpha D$, (3.42)) helps to eliminate all exponential terms:

$$\begin{aligned} (N_1 + N_2) \cdot (1 - \alpha \cdot D') &= N_1 \cdot (1 - \alpha \cdot D_1) + N_2 \cdot (1 - \alpha \cdot D_1) \\ (N_1 + N_2) \cdot D' &= N_1 \cdot D_1 + N_2 \cdot D_2 \end{aligned} \tag{3.51}$$

The cell-mass relation ($\frac{N_1}{N_2} \approx \frac{m_1}{m_2}$, see Fig. (3.12) (3.51) is convertible to D' which is defined by:

$$D' = \frac{N_1 \cdot D_1 + N_2 \cdot D_2}{N_1 + N_2} = \frac{m_1 \cdot D_1 + m_2 \cdot D_2}{m_1 + m_2} \tag{3.52}$$

(3.52) also corresponds to the basic dose definition for IIOs (3.8). Since D' is defined, it possible to discuss the accumulation error η mentioned in section 3.1.3. η also regards to dose definition $D'_{\text{Def.}}$ (3.11). The error takes the mass relation into account ($\gamma = \frac{m_1}{m_2}$). For this biological approach (dose definition for IIOs), it is defined by:

$$\eta = \left| D'_{\text{Bio.}} - D'_{\text{Def.}} \right| = \left| \left[\frac{m_1 \cdot D_1 + m_2 \cdot D_2}{m_1 + m_2} \right] - \left[\frac{D_1 + D_2 \cdot \gamma}{1 + \gamma} \right] \right| \approx 0 \tag{3.53}$$

The low error corroborates the precision of the dose definition. One has to keep in mind that the error is based on a theoretical model. Realistic errors towards zero are not possible due to a lot of other influences (e.g. numerical structures). However, the outline shows as a rough approximation that (3.8) is a good model for accumulation in the context of this work. Different algorithms for dose transformation are presented in the following section 3.3. They implement more or less the basic dose definition (3.8) in different ways.
Finally, there exists no biological reason that restricts the term of dose transformation in the context of dose accumulation for 4D calculations[17]. Biological models even support the correctness of the dose definition for IIOs (3.8) understandably in (3.47) and (3.48). Hence, the mass effect is very important for the integral dose unions and for the accompanied 4D dose transformations.

[17] This postulation considers no other sources of error. For example, a wrong deformation grid could also falsify dose transformations.

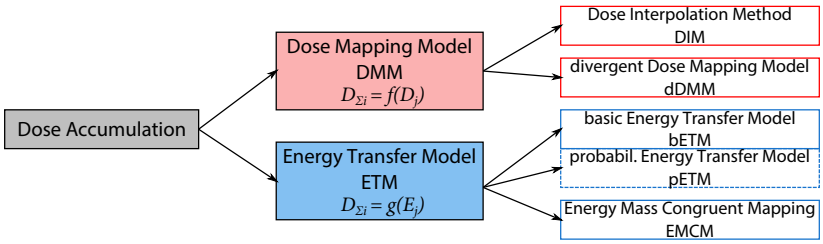

Figure 3.13 : Graphical overview of established and introduced accumulation models: Every model is related to a basic approach (DMM, ETM). Particularly, pETM is an author-specific adjustment of bETM. Thus, it represents not a separately new defined method.

3.3 Comparison of various dose transformation models

The previous discussion investigates the accumulation of dose analytically. It points out problems for numerical solutions. If it is necessary to calculate dose unions during accumulation, the solution for a good accumulation model is given by the dose definition for IIOs in (3.8), (3.48). The accuracy of the approach is supported from different points of view (e.g. biological outline in section 3.2.3 or the dose error η in section 3.2.3). The content of the following section builds on the basic numerical procedure illustrated in section 3.1.3. It extends the work flow by different individual accumulation models. The following presentation compares five different methods.

Previous studies regarding 4D dose accumulation in the recent years established a number of different transformation methods: [52, 51, 32, 93, 25, 124, 119, 80]. An improvement for precise dose transformations is the energy model and its adaptions established by *Siebers et al.*[93], [124]. Another meaningful method is the direct voxel tracking method invented by *Heath et al.*[32].[18] However, due to the complexity of the task and the high requirements on methods of dose transformation, a list of fundamentally different solutions were published [80] with more or less precise comparative studies. The investigation of the used algorithms reveals two elementary branches. Almost every popular method is associated with one of these two groups. The classification is based on the dose definition. As a matter of fact, section 3.2 revealed two numerical representations of the basic dose definition for IIOs defined by:

$$\tilde{D}_{\text{Def.}} = \frac{\sum_{x\in V} m(x)\cdot D(x)}{\sum_{x\in V} m(x)} = \frac{\sum_{x\in V} E(x)}{\sum_{x\in V} m(x)} \tag{3.54}$$

From a biological point of view, section 3.2.2 additionally shows, that a dose increase ΔD inside a special part of an object Δm results in control rate change ΔP for the entire object m. Here exist also two possible types of expression:

$$\Delta P \approx \gamma \cdot \frac{\Delta D}{D} \cdot \frac{\Delta m}{m} = \gamma \cdot \frac{\Delta E}{E} \tag{3.55}$$

These formulas describe the composition of the unified dose, the behavior the dose response and two significant dependencies for dose accumulation. Both are illustrated by a mass weighted dose operator as well as a function of the absorbed energy distribution. Therefore, two groups for dose accumulation algorithms can be derived: the dose mapping model (DMM), which deals with the transformation of the applied dose distributions; the energy transfer model (ETM), which realizes dose transformation with the aid of the trans-

[18] One important model, proposed by *Heath et al.* [32], is neglected in the evaluation of this work. The model works with the direct voxel tracking for 4D Monte Carlo dose calculations. As it uses crooked, unregular voxel structures, it results in a high technical effort. It also needs a huge time expenditure during calculation. Finally, it is not practical for the investigation of this work. A detailed explanation can be found in the related reference.

fer of deposited energy points. The following list presents a number of algorithms related to one of the basic approaches. All these methods are tested and compared in section 3.4. A graphical overview is illustrated in Fig. 3.13. The following outline is a detailed numerical explanation of the listed algorithms.

3.3.1 Dose mapping models

Dose Interpolation Method (DIM)

DIM is a trivial, but widely used model. The following references give an overview of DIM related implementations and evaluations in the field of 4D dose accumulation: [10, 76, 83, 77, 78, 80]. However, DIM is very important for other dose problems (e.g. scaling of dose distributions for illustration, summation of beams, etc.). Hence, a lot of related functions are implemented in many medical dose planning systems. This is one reason for its frequent use. It could be implemented for 4D approaches without a huge technical effort by using the already implemented framework. A survey of the main idea of DIM is given by section 3.1.3. DIM follows the conventional rules of trilinear interpolation. The graphical overview and the way of calculating a transformed dose point for a single breathing phase is given by Fig. 3.14. Due to interpolation, the method considers only the direct neighbor voxels of the target point $\vec{x}_j$[19]. Hence, the neighborhood interval $\pm\Delta_j$ (see section 3.1.3) are only two discrete voxels for every direction X, Y, Z. Basic trilinear interpolation works with distance weighted averages. The dose weight of every neighbor voxel depends on the distance to the target point $\vec{x}_j$. The approach is expressible with the aid of the numerical procedure mentioned in formula (3.11) considering a substitution of $\pm\Delta_j$ and the operator W_{ji}:

$$\begin{aligned} D_{i\sum}(x_i) &= \sum_{j=1}^{n} w_j \cdot \left[\sum_{x_j=v_{ji}(x_i)-\Delta_j}^{v_{ji}(x_i)+\Delta_j} W_{ji}(x_i, x_j) \cdot D_j(x_j) \right] \\ D_{i\sum}(x_i) &= \sum_{j=1}^{n} w_j \cdot \left[\sum_{x_j=v_{ji}(x_i)-1_{XYZ}}^{v_{ji}(x_i)+1_{XYZ}} f\left(d(x_j, v_{ji}(x_i))\right) \cdot D_j(x_j) \right] \end{aligned} \tag{3.56}$$

A detailed space oriented execution leads to:

$$D_{i\sum}(x_i) = \sum_{j=1}^{n} w_j \cdot \left[\sum_{X=0}^{1} \sum_{Y=0}^{1} \sum_{Z=0}^{1} \left[\frac{\sqrt{3} - |d(x_j^{XYZ}, v_{ji}(x_i))|}{\sqrt{3}} \right] \cdot D_j(x_j^{XYZ}) \right] \tag{3.57}$$

with $d\left(x^{XYZ}, v_{ji}(x_i)\right)$ being the metric or distance function which measures the interval of the target point $\vec{x}_j = v_{ji}(x_i)$ and one of the eight nearest neighbor voxels x_j^{XYZ} in J. d is normalized to the maximum possible space $\sqrt{3}$: the lower the distance, the larger the dose contribution. The superscript X, Y, Z distinguishes between the lower (0) and the higher (1) neighbor voxel for the related direction. Hence, the dose in a voxel x_j is given by a fractionated sum of the neighborhood dose voxel around x_j (dark blue area, Fig. 3.14). All other dose points are neglected (bright blue area, Fig. 3.14).

The neighborhood deciphers the first disadvantage of DIM. The approach fully rejects the deformation effect (see section 3.1.2). That means, the dose points outside the neighborhood, which also compress to x_i and may largely contribute to the dose $D_{i\sum}(x_i)$, are ignored. Additionally, the metric is measured in the wrong system J. It is more important how far the coordinates are located in I as they are related in J.

The basic definition in formula (3.9) to unify inhomogeneous dose volumes is ignored in DIM. Hence, DIM neglects the mass effect. There is no dose-mass relation in equation (3.57). Once a voxel dose is calculated, the

[19] For clarity, this outline distinguishes between floating coordinates $\vec{x}$ and integer voxel indices x. Both describe spatial locations.

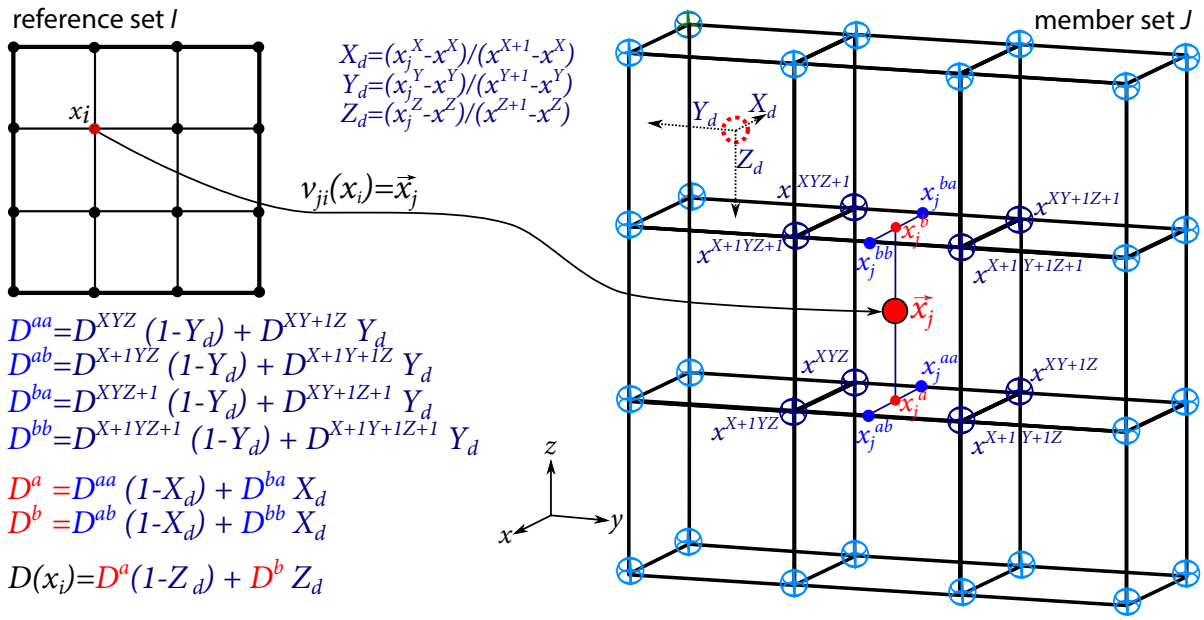

Figure 3.14 : Graphical overview of dose interpolation mapping: The method follows the rules of conventional trilinear interpolation. An example calculation of $D(x_i)$ is illustrated on the left. Therefore, the dose of a reference voxel x_i is composed of dose fractions given by the eight neighbor voxel (dark blue) of its related target point $\vec{x}_j$. Usually, $\vec{x}_j$ is a floating point vector. The fraction value of each dose point is determined by its distance to $\vec{x}_j$ (X_d, Y_d, Z_d). Voxels outside the neighborhood (bright blue area) have no influence.[20]

dose is considered to be independent from its voxel mass. The result is a possible loss of biological information. Due to the loss of the relevant mass information, dose could be under- or overestimated up to 100 % by DIM (see the possible dose error for numerical procedures in section 3.1.3).

Another disadvantage of DIM is the rearrangement of dose underlying energy distributions (see Fig. 3.15, [93]). While the center of dose point D_1 is mapped to the target D', the model assumes that all inherent energy events E_1, E_2, E_3 contribute to the same target dose D'. However, D' is even the target of the voxel center V_1. Not all energy events are located in the same target voxel V'due to deformation process. In the given example E_3 is shifted incorrectly to E_3' (Fig. 3.15.a). This energy point does not contribute to D', but the model predicts the effect. A wrong value for D' is a possible result. This drawback could related to every model of DMM. Once a dose distribution is calculated, the information of the energy distribution gets lost. This means, a set of energy points is summarized to a single dose voxel, without knowing their exact values and coordinates. Nevertheless, this also provides a positive effect. The energy independence allows DMM to combine with every possible dose algorithm, because not every dose algorithm provides access to high resoluted energy distribution fields.

The motivation for using DIM is the hope for a negligible small dose error in macroscopic clinical cases by using sufficiently small voxel resolutions. Furthermore, the simplicity allows an implementation without a huge technical effort. In summary, all the described properties are compared:

1. **Advantages of DIM:**
   a) Simplicity, easy implementation, low technical effort
   b) Combinable with every dose algorithm (e.g. Pencil Beam, Monte Carlo, ...)

[20] For clarity: A voxel center in this figure is represented by an intersection of the grid, a nodal point in the grid based structure (e.g. blue spheres). This serves for a better illustration of the DIM model. This visualization is different to the following method describing figures: 3.17, 3.18, 3.23; There, a voxel is represented by the suspected voxel shape and the grid represents the barrier of the voxels.

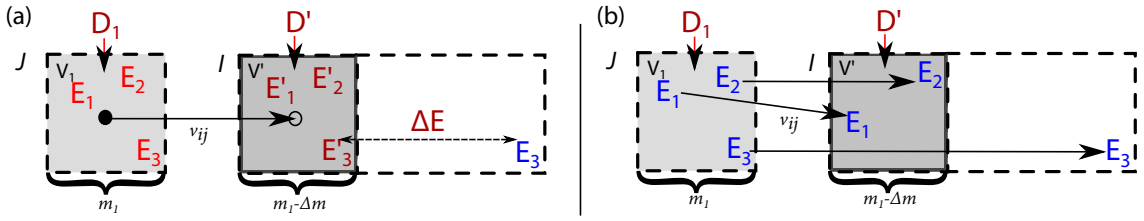

Figure 3.15 : Energy rearrangement during dose mapping: The drawback of any dose mapping model is the displacement ΔE of dose related energies between different geometries J and I. (a) illustrates a dose mapping scenario. Due to dose voxel centralization, a portion of energy points (red) gets a wrong coordinate (e.g. E_3). (b) describes the real location of the involved energy deposition points (blue). The comparison deciphers the energy shift ΔE.

2. **Disadvantages of DIM:**

   a) Neglection of the deformation effect
   b) Neglection of the mass effect defined for IIOs in formula (3.8)
   c) Possible energy rearrangement

Divergent Dose Mapping Model (dDMM)

The new divergent dose mapping model is introduced by this thesis. The model tries to improve disadvantages of DIM. The methods name is derived from the mathematics, the vector analysis. The model implements the basics of the sources and the sink theories within the dose accumulation problem. Inside the vector field $v_{ij}(\vec{x}_j)$ (deformation grid), which describes the movement of the tissue between different breathing phases, exist also sinks for dose accumulation. Grossly, sources and sinks are expressed by compression and expansion. They a have big influence on the dose grid during the accumulation process (see Fig. 3.16). For compensation of the deformation effect (section 3.1.2) dDMM takes the dynamics of sources and sinks into account. Analytically, the divergence $\mathrm{div}(v_{ij}(\vec{x}_j))$ of a deformation field is given by:

$$\mathrm{div}(v_{ij}(\vec{x}_j)) = \begin{cases} > 0, & \text{source} \\ < 0, & \text{sink} \\ = 0, & \text{source free} \end{cases} \tag{3.58}$$

The divergence $\mathrm{div}(v_{ij}(\vec{x}_j))$ is a value inside the system J (breathing phase), which expresses how large the tissue compresses, expanses and moves in relation to the reference set I. It is not calculated during accumulation, but its definition in (3.58) illustrates the direction of calculating the accurate numerical procedure in dDMM. While DIM calculates every single voxel x_i starting inside the reference set I with projection $v_{ji}(x_i)$ on the breathing state J, dDMM has to go the opposite way. Therefore, formula (3.58) provides clarity. To integrate all the divergent dose relationships, dDMM calculates the full dose distribution for I, starting from the breathing phase J with the opposing deformation grid to DIM $v_{ij}(x_j)$. Hence, not every voxel x_i is calculated individually, the computation is performed in parallel. For numerical reason, all voxels x_j in J are splitted into a sufficient value of sub-voxels $x_{j_{\mathrm{sub}}}$. Every sub-voxel $x_{j_{\mathrm{sub}}}$ receives the dose $D_j(x_j)$ of its parent. The calculation is discretely performed, which means: With the aid of a high resolved deformation grid $v_{ij}(x_{j_{\mathrm{sub}}})$, the algorithm determines even one target x_i for every sub-voxel $x_{j_{\mathrm{sub}}}$. Hence, every voxel x_i in I receives dose

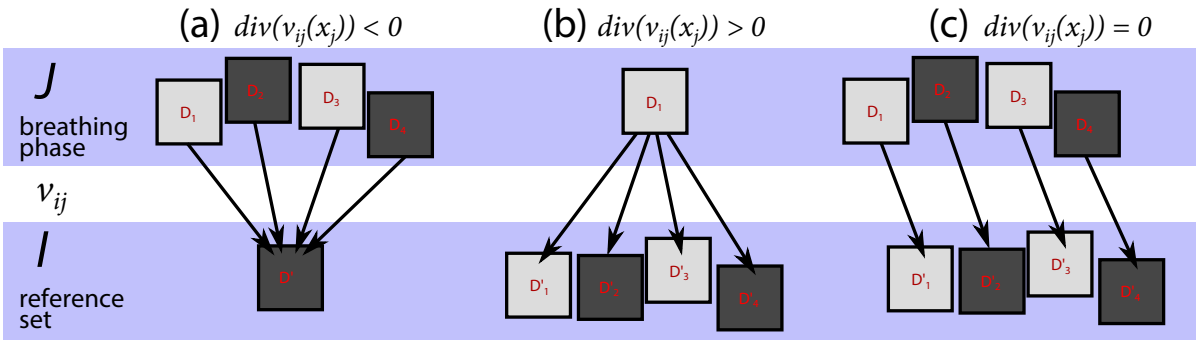

Figure 3.16 : Divergence in a dose grid due to tissue movement: (a) sink → compression; (b) source → expansion; (c) source free → affine movements

from the sub-voxels related to J in parallel. The accumulated dose transformation can be written as:

$$D_{i\sum}(x_i) = \sum_{j=1}^{n} w_j \cdot \left[\sum_{x_{j_{\text{sub}}} \in W_{x_i}} \frac{D_j(x_{j_{\text{sub}}})}{|W_{x_i}|} \right]; \quad W_{x_i} = \left\{ x_{j_{\text{sub}}} | x_i = v_{ij}(x_{j_{\text{sub}}}) \right\} \tag{3.59}$$

with W_{x_i} being a mathematical set that inherent all sub-voxels $x_{j_{\text{sub}}}$ which have a connection to x_i. This results in the average of all involved dose values $D_j(x_{j_{\text{sub}}})$ for $D_{i\sum}(x_i)$. As shown in section 3.2, the average value for doses is the neglection of biological information. With the aid of the dose definition for IIOs (3.54), dDMM also compensates the mass effect (neglected in DIM) and avoids this loss of biological information. Therefore, every sub-voxel $x_{j_{\text{sub}}}$ is composed by the fractionated mass of its parent $m(x_{j_{\text{sub}}}) = \frac{m(x_j)}{l}$. l indicates the sub-voxel resolution, it is the number of sub-voxels inside a parent voxel. The dose $D_j(x_{j_{\text{sub}}})$ of a sub-voxel is weighted by its mass $\frac{m(x_j)}{l}$. The summarized dose $D_{i\sum}(x_i)$ is normalized to the set of all sub-masses that migrate to x_i. Hence, (3.59) can be adjusted in the following way, as a full specification for dDMM:

$$D_{i\sum}(x_i) = \sum_{j=1}^{n} w_j \cdot \left[\frac{\sum_{x_{j_{\text{sub}}} \in W_{x_i}} m(x_{j_{\text{sub}}}) \cdot D_j(x_{j_{\text{sub}}})}{\sum_{x_{j_{\text{sub}}} \in W_{x_i}} m(x_{j_{\text{sub}}})} \right]; \quad W_{x_i} = \left\{ x_{j_{\text{sub}}} | x_i = v_{ij}(x_{j_{\text{sub}}}) \right\} \tag{3.60}$$

The entire approach is also illustrated in Fig. 3.17 with an example calculation of a single dose point. Compared to DIM, dDMM solves the deformation effect and the mass effect. However, the problem of of dose dependent energy rearrangement is not solved (see Fig. 3.15) in dDMM, because the dose of every sub-voxel is related to the centralized parent dose without spatial energy resolution. Another disadvantage is the higher technical complexity and the increasing calculation time compared to DIM. Finally, all properties of dDMM are listed below:

1. **Advantages of dDMM:**
   a) Solution for the deformation effect (divergent assumption)
   b) Solution for the dose-mass relation (consideration of the dose definition for IIOs (3.8))
   c) Combinable with every dose algorithm (e.g. Pencil Beam, Monte Carlo, ...)
2. **Disadvantages of dDMM:**
   a) Higher complexity in relation to DIM
   b) Increasing calculation time due to the high sub-voxel resolution
   c) Possible energy rearrangement

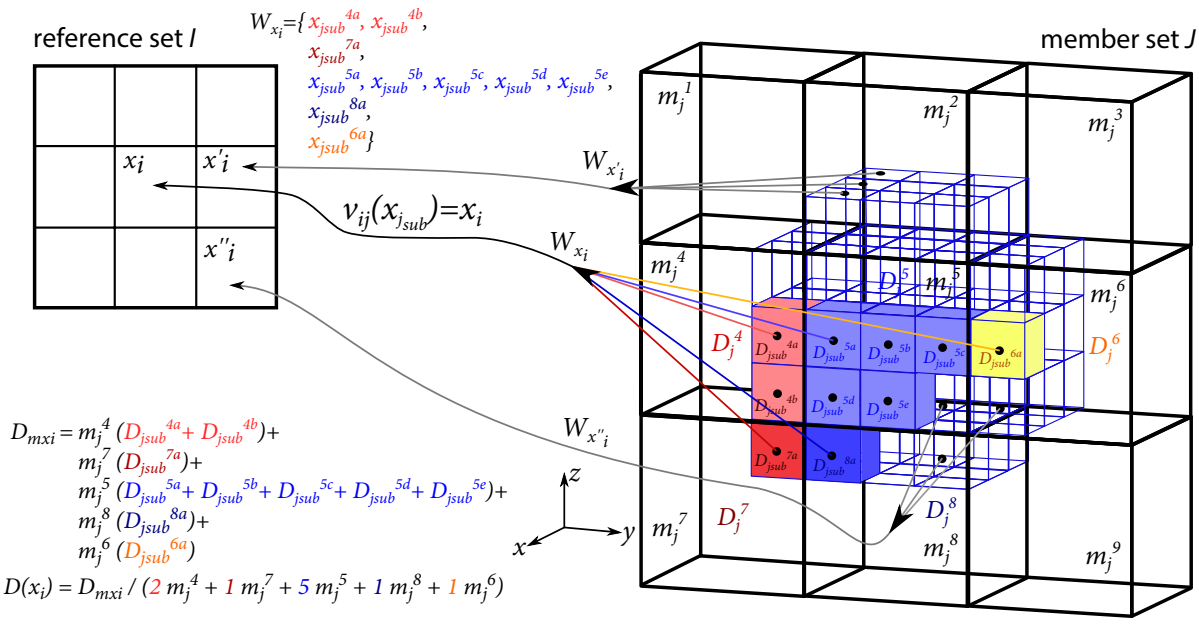

Figure 3.17 : Graphical overview of the divergent dose mapping model: Voxels x_j inside the member set J are divided into sub-voxels $x_{j_{\text{sub}}}$ (e.g. 3^3 sub-voxels per voxel). The algorithm determines each target x_i for every sub-voxel $x_{j_{\text{sub}}}$ successively. Hence, the calculation of $D(x_i), D(x'_i), D(x''_i), \ldots$ is performed in quasi parallel. The summarized dose for $D(x_i)$ arises from the mass weighted average (left) of all involved sub-voxels $x_i = v_{ij}(x_{j_{\text{sub}}})$, members of the set W_{x_i} (color filled sub-voxels).

3.3.2 Energy transfer models

Basic Energy Transfer Model (bETM)

The bETM is related to the basic dose definition mentioned in formula (3.13) (section 3.1.3). As shown in the dose definition for IIO (3.54), the accumulated dose is expressible with the aid of dose underlying energy distributions. bETM was introduced by *Siebers* and *Zhong* [93]. An overview of model-related examples, implementations and evaluations can be found in: [124, 119, 80]. The basic idea is the solution of the energy rearrangement problem (see Fig. 3.15, section 3.3.1). This requires access to the energy distributions with a high spatial resolution. This is not possible for all dose algorithms. For example, kernel based methods, like Pencil Beam (PB) or Collapsed Cone, are not combinable with bETM. At the moment, the method is closely related to the Monte Carlo (MC) dose algorithm. This restricts the flexibility compared to DMM.
The basic idea of the model is not to transform doses, as to transform the values $E_j(\vec{x}_j)$[21] of energy deposition points. It works in the same direction as dDMM. Starting in the member set J with projection $v_{ij}(\vec{x}_j)$ to I. The dose algorithm (usually MC) has to provide the energy deposition points $E_j(\vec{x}_j)$. While the dose algorithm is calculating inside the member geometry J, deposition points (including their energy values) are tracked to the reference set I. After finishing all projections, the final dose calculation is performed inside the reference set I with the aid of the masses $m(x_i)$ located there. bETM is illustrated in Fig. 3.61 with exemplary calculations for two transformed dose points. The full approach is defined by:

$$D_{i\sum}(x_i) = \sum_{j=1}^{n} w_j \cdot \left[\frac{1}{m(x_i)} \sum W_{E \to x_i} \right]; \quad W_{E \to x_i} = \left\{ E_j(\vec{x}_j) | x_i = v_{ij}(\vec{x}_j) \right\} \tag{3.61}$$

[21] It has to be noted that $\vec{x}_j$ is a real stationary vector and different to the discrete voxel x_j, because an energy deposition event can be located everywhere in the space of a voxel. However, the exact position is significant in bETM.

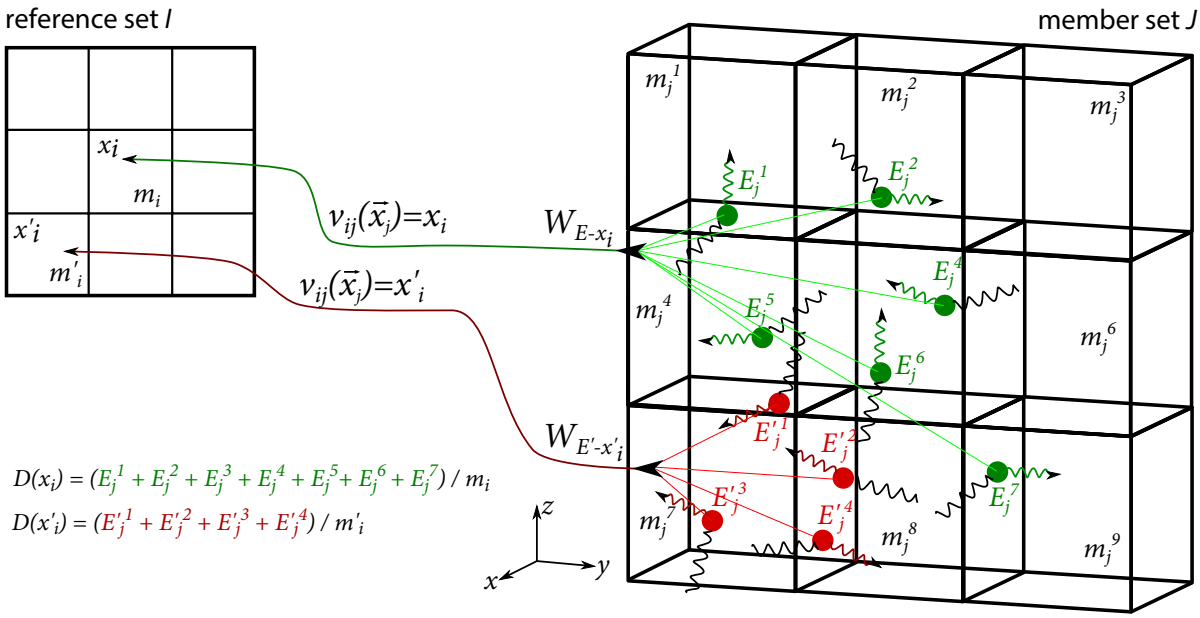

Figure 3.18 : Graphical overview of the basic energy transfer model: During dose calculation inside the member set J, bETM determines the energies that are deposited (e.g. E_j, E'_j). The depositions points are tracked with the aid of $v_{ij}(\vec{x}_j)$ to their related target in I. For example, all green energy depositions E_j are tracked to x_i, while all red absorption points E'_j being projected to x'_i. After finishing of all energy depositions, the approach performs the actual dose calculation inside the reference set (left) with the aid of the masses m_i, m'_i related to I.

with $W_{E\to x_i}$ being the mathematical set that considers all member deposition points $E_j(\vec{x}_j)$ which are tracked to the reference voxel x_i. This is the same basic direction as implemented in dDMM. Hence, the deformation effect has no influence to bETM. Another view on (3.61) provides that bETM fulfills the biological requirements to consider the mass effect. It implements the dose definition for IIOs in (3.54) for the energy-related notation. It summarizes all local energies (tracked from a different breathing phase) and divides the sum of energies by the local mass $m(x_i)$ in x_i for final dose calculations.

Explanation of the mass energy discrepancy (MED) error : At this point, the hypothesis regarding the integration of the basic dose definition for IIOs has to be analyzed from are numerical point of view. Energy deposition points, especially their values $E_j(\vec{x}_j)$ are related to different particle reactions inside the voxel x_j in J. The most significant reactions for radiotherapy are the *Photo Effect*, the *Compton Effect* and the *Pair Production* [22]. The summarized probability of these mechanisms is approximated by its macroscopic cross section μ. μ closely depends on the the local mass $m(x_j)$. This means, a different mass results in a different energy deposition event. Hence, in a trivial scenario, the energy deposition value is a function of the mass $m(x_j)$ which finally causes the deposition event:

$$E_j(\vec{x}_j) = f(m_j(x_j)) \tag{3.62}$$

Furthermore, a static dose calculation assumes that the dose in a voxel x_j is calculated by the same mass $m_j(x_j)$ that causes the energy deposition:

$$D_j(x_j) = \frac{E_j(\vec{x}_j)}{m_j(x_j)} = \frac{f(m_j(x_j))}{m_j(x_j)} \tag{3.63}$$

Table 3.1 : Properties of lung equivalent compounds and elements: The table lists the density ρ and the mass attenuation coefficient μ (1 MeV, 3 MeV, 6 MeV) for a set of compounds and elements regarding the possible density range inside the lung (0.044 – 1.101 $\frac{g}{cm^3}$, see section 3.1.2). The data is based on the measurements of the *National Institute of Standards and Technology (NIST) for X-Ray Mass Attenuation Coefficients* [37]. The definitions of: *Lung Tissue, Soft Tissue, Adipose Tissue* regard to the specifications of the ICRU Report 44 [7].

		$\mu[10^{-2} \cdot cm^{-1}]$ for:		
compound/element	$\rho[\frac{g}{cm^3}]$	E = 1 MeV	E = 3 MeV	E = 6 MeV
Lung Tissue (ICRU 44)	1.05	7.36	4.13	2.88
Soft Tissue (ICRU 44)	1.0	7.00	3.93	2.74
Adipose Tissue (ICRU 44)	0.95	6.72	3.76	2.59
Polyethylene	0.93	6.75	3.76	2.57
Potassium	0.68	4.23	2.49	1.98
Lithium	0.5	2.75	1.52	1.02
Helium	0.176	1.12	0.617	0.406

However, this can not be guaranteed during accumulation with bETM as the dose in the reference voxel x_i is often calculated with a mass $m(x_i)$ that differs a lot from the energy producing mass $m(x_j)$. Hence, another possible dose error η_{med} could be defined, the *mass energy discrepancy dose error* (MED), which applies for all energy transfer methods. η_{med} compares the calculated dose of bETM with the real applied dose in voxel x_i. With the aid of (3.62) the error is defined by:

$$\eta_{\text{med}} = |D_i(x_i)_{\text{bETM}} - D_i(x_i)_{\text{real}}| = \left| \frac{E_j(\vec{x}_j)}{m_i(x_i)} - \frac{f(m_i(x_i))}{m_i(x_i)} \right| \tag{3.64}$$

The functional $f(m_i(x_i))$ is describable with the aid of the total attenuation coefficient μ in relation to the energy event $E_j(\vec{x}_j)$. μ is a good approximation for the macroscopic probability of interaction inside matter. Hence, the functional is defined by the fractionated probability:

$$f(m_i(x_i)) \approx \frac{\mu_{m_i}}{\mu_{m_j}} \cdot E_j(\vec{x}_j) \tag{3.65}$$

For illustration, (3.63) describes a deviation of a voxel mass between the energy deposition and dose calculation that would be reflected in a changed value of transferred energies $E_j(\vec{x}_j)$, if the mass $m_j(x_j)$ increases to $m_i(x_i)$ for dose calculation. Then, it would produce a larger number of events E_j (by factor $\frac{\mu_{m_i}}{\mu_{m_j}}$) which are mapped to x_i and vice versa. For the error approximately results[22]:

$$\eta_{\text{med}} \approx \left| D_i(x_i)_{\text{bETM}} \cdot \left(1 - \frac{\mu_{m_i}}{\mu_{m_j}} \right) \right| \tag{3.66}$$

[22] A more accurate study should use the mass energy-absorption cross section μ_{en} instead of the total macroscopic cross section μ for calculation, as it not includes the coefficient of away transported energies, but pure local departed energies. The following report is used for illustration. Hence, μ_{total} is sufficient in this context, because the error coefficients will not differ strongly. Example for 6 MeV (the data is based on [37]):
$\frac{\mu_{\text{total}}(\text{Lung Tissue})}{\mu_{\text{total}}(\text{Polyethylene})} \approx \frac{2.88 \cdot 10^{-2} cm^{-1}}{2.57 \cdot 10^{-2} cm^{-1}} \approx 1.12$
$\frac{\mu_{\text{en}}(\text{Lung Tissue})}{\mu_{\text{en}}(\text{Polyethylene})} \approx \frac{1.88 \cdot 10^{-2} \text{cm}^{-1}}{1.67 \cdot 10^{-2} \text{cm}^{-1}} \approx 1.13$

Table 3.2 : Possible dose errors for energy tracking inside the lung: The table lists the normalized MED error for compounds and elements defined by Tab. 3.1 regarding E = 6 MeV, E = 1 MeV. It is a cross over comparison with mass varying source voxels (row) and mass varying target voxels (column). The diagonal ($11 \rightarrow nn$) of the matrix represents $\Delta m = 0$, no mass change.

normalized dose error $\frac{\eta_{\text{med}}}{D_{\text{bETM}}} \approx \lvert 1 - \frac{\mu_{m_i}}{\mu_{m_j}} \rvert$							
compound/element	→ target voxel m_i						
source voxel m_j	*LT*	*ST*	*AT*	*PE*	*K*	*Li*	*He*
	E_j = 6 MeV						
Lung Tissue (LT)	0.000	0.050	0.102	0.110	0.313	0.648	0.859
Soft Tissue (ST)	0.053	0.000	0.055	0.063	0.276	0.629	0.852
Adipose Tissue (AT)	0.114	0.058	0.000	0.008	0.234	0.608	0.843
Polyethylene (PE)	0.123	0.067	0.009	0.000	0.228	0.605	0.842
Potassium (K)	0.455	0.382	0.306	0.295	0.000	0.488	0.795
Lithium (Li)	1.841	1.699	1.550	1.529	0.953	0.000	0.600
Helium (He)	6.101	5.746	5.376	5.322	3.882	1.500	0.000
	E_j = 1 MeV						
Lung Tissue (LT)	0.000	0.049	0.087	0.083	0.426	0.626	0.848
Soft Tissue (ST)	0.051	0.000	0.040	0.036	0.396	0.607	0.840
Adipose Tissue (AT)	0.095	0.041	0.000	0.004	0.371	0.591	0.833
Polyethylene (PE)	0.090	0.037	0.004	0.000	0.374	0.593	0.834
Potassium (K)	0.742	0.657	0.591	0.598	0.000	0.349	0.735
Lithium (Li)	1.676	1.545	1.444	1.455	0.536	0.000	0.593
Helium (He)	5.576	5.254	5.005	5.032	2.775	1.457	0.000

To evaluate possible dose errors inside the lung, Tab.3.1 gives an exemplary overview of lung equivalent compounds and elements as well as their related total X-Ray mass attenuation coefficients μ for several energies. The selection is within a realistic density range of $0.044 - 1.101 \frac{\text{g}}{\text{cm}^3}$ (see section 3.1.2). It is obvious that a higher density accompanies a higher attenuation coefficient. This leads to a higher interaction probability. If a mass difference Δm is assumed during energy mapping, it entails dose errors if the masses of the source voxel m_j and the target voxel m_i differ largely. Such dose errors are listed in Tab. 3.2 regarding a lung equivalent selection of compounds and elements. The table lists a cross over comparison for varying sources m_j and target voxels m_i. The graphical visualization of the data is given by Fig. 3.19. For clarity, every row in Tab. 3.2 represents a single series in Fig. 3.19. For evaluation of the data, one has to distinguish two scenarios:

(1) $m_j > m_i$: The mass m_j used for energy production is higher then the mass m_i of the mapped endpoint used for dose calculation. The value of the produced energy E_j is larger then its fictitious real energy E_i inside the endpoint in x_i. Resulting dose errors are shown right from the minimum zero in Tab. 3.2 and left from the minimum of one series in the graphs of Fig. 3.19. The higher Δm, the higher is the resulting dose error $\frac{\eta_{\text{med}}}{D_{\text{bETM}}}$. The predicted dose for D_i is to large. The maximum possible error is one, meaning 100 % of $D_i(x_i)_{\text{bETM}}$. The illustrated realistic cases show errors up to 85 % for extreme mass deviations (e.g. LT→ He). Such a difference could be caused by a defective deformation grid, for example.

(2) $m_i > m_j$: The mass m_j used for energy production is lower then the mass m_i of the mapped endpoint used for dose calculation. The value of the produced energy E_j is lower then its fictitious real energy E_i inside the endpoint in x_i. The resulting dose errors are shown left of the minimum in Tab. 3.2 and right of the minimum

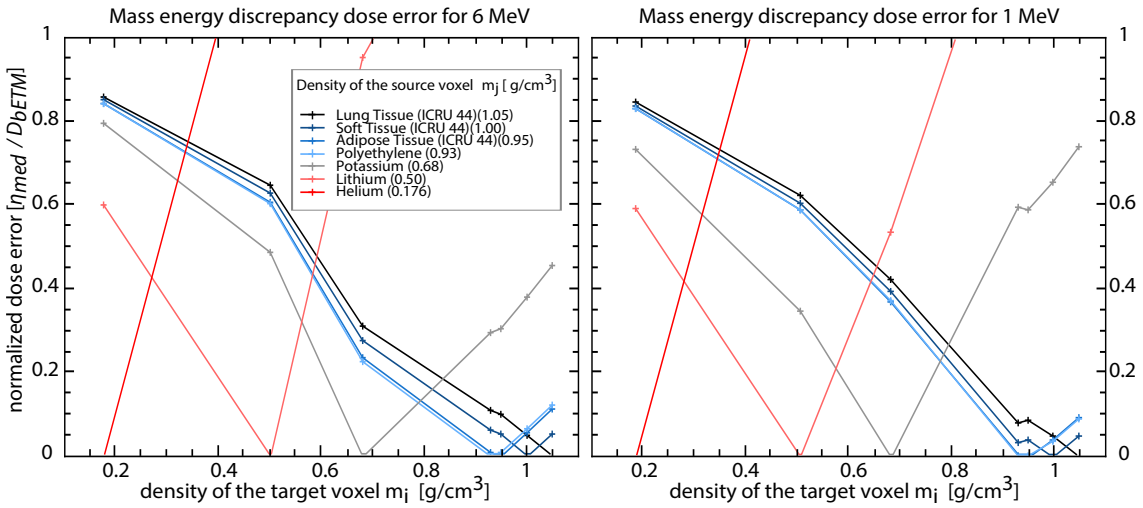

Figure 3.19 : Mass energy discrepancy dose errors for E = 6 MeV (left) and E = 1 MeV (right). The data is based on the selection of compounds and elements regarding Tab. 3.1 and Tab. 3.2. The graphs illustrate the normalized $\frac{\eta_{\text{med}}}{D_{\text{bETM}}}$ dose error in dependence of the density ρ inside the target voxel x_i. Every series is based on the same source voxel density (see series name). Hence, a energy mapping case (cross) is fully described by abscissa and series name.

of one series in the graphs of Fig. 3.19. The mass deviation results in an underestimation of D_i. The normalized dose error has no upper barrier, because the calculated doses $D_i(x_i)_{\text{bETM}}$ are usually extremely small due to the energies which are based on very low densities. The values of the dose differences are not larger then the absolute values in scenario (1), but their percentage values regarding $D_i(x_i)_{\text{bETM}}$ are higher.
Both scenarios clearly reveal the problems that occur by splitting voxel doses into masses and energies. A composition of erroneous components may results in larger errors. In comparison to ETM, DMM deals with the regulated value of D which is a advantage for this topic. Furthermore, a distinction is necessary. The manner of MED error generation is important. In an ideal world, the deformation grid v_{ij} is a perfect reflection of the reality. Mass deviations between source and target voxel should be negligible small. Nevertheless, there will always be differences (see section 2). The deformation effect, the numerical structure of the geometry[23] and measurement properties could cause significant deviations that result in MED errors up to 10 %. Those factors are classified into the group of the *discretization based MED error*. Furthermore, a perfect deformation grid can not be assumed. Erroneous vector fields must be taken into account due to complexity of the structures and unforeseen movements inside the 4D geometry (section 2.1). Extreme mass deviations, as discussed in scenario (1), are not unrealistic. For example, a high valued energy event $E_j \uparrow$ based on a massive ($m_j \uparrow$) source voxel results in a large overestimation of the dose $D_i(x_i)_{\text{bETM}} \uparrow$, if a defective location assignment transforms to a low mass ($m_i \downarrow$) inside the endpoint (e.g. see Fig. 3.19: LT → He). This calculates spatial dose peaks that are not present and vice versa. The error is based on the defective deformation grid. It is far more significant due to higher error values. Usually, this rarely occurs. The frequency goes with the quality of the registration algorithm. Fig. 3.20 illustrates the mechanism of both error types. The MED error is neglected in the bETM model. Hence, the model should be used carefully.

Integration into the dose algorithm: Due to the energy tracking method, bETM needs a high resolved energy distribution. Secondary electrons, which are primary responsible for energy deposition inside matter (photon radiation), transfer energy not in discrete coordinates. The depositions happens along energy path

[23] Mass discretization for voxel calculations along image gradients could cause significant differences.

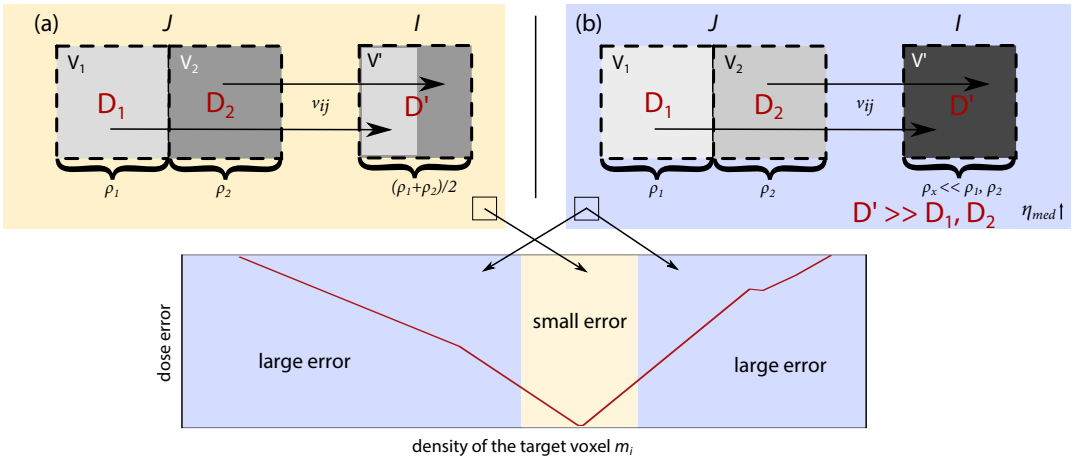

Figure 3.20 : Two types of the mass energy discrepancy dose error distinguished by the manner of generation. (a) *Discretization based MED error*: Mass discretization for voxel calculations along image gradients and mass discretization due to deformation compensation could cause significant mass differences Δm between source and target voxel. (b) *Defective deformation grid based MED error*: Mass differences are caused by a defective deformation grid. Dose errors could be very large (e.g. $\Delta m \rightarrow 1\ \frac{\mathrm{g}}{\mathrm{cm}^3}$).

ways. During energy tracking, the algorithm cannot transfer discrete depositions points $E_j(\vec{x}_j)$, the algorithm has to transfer whole path lengths $E_j(\overrightarrow{X_j^0 X_j^1}, \overrightarrow{X_j^1 X_j^2}, \ldots)$. bETM is closely related to the MC dose algorithm. MC deposits energies along path ways, the method requires an additional model that reduces path lengths to single coordinates. *Siebers et al.* [93] proposed a model that selects a random point d on the path length. Finally, the energy mapping is related to that coordinate d. Techniques of the Finite-Element-Method (FEM) are also conceivable. The main conclusion is the need of an additional energy discretization module for bETM, which produces a higher degree of technical complexity.

The combination with the MC dose algorithm also provides benefits, for example, the basic dose calculation time. While dose accumulation in combination with kernel based strategies (e.g. Pencil Beam, Collapsed Cone, ...) requires the n-fold (n is the value of CT image sets) multiple calculation time, MC does not need additional calculation time apart from the technical overhead. The former has to produce n dose calculations, one for every single breathing set, exactly the multiple calculation time equivalent. As known from the statistics of MC, the accuracy largely depends on the number of simulated particles N. The calculation time of a single plan also depends on N. To get the same accuracy, a single dose distribution should be calculated with $\frac{N}{w_j}$ ($\sum_{j=1}^{n} w_j = 1$) particles. Due to the laws of the statistics, the dose calculation achieves the same accuracy after accumulation as a static plan calculated with N particles. The time complexity $T(n)$ (see Fig. 3.21) for kernel based methods (usually PB) and MC dose accumulations is given by:

$$\begin{aligned} T_{PB}(n) &\in O(n) \\ T_{MC}(n) &\in O(1) \end{aligned} \tag{3.67}$$

In order to accumulate dose distributions, (3.67) shows no basic increase of the calculation time for MC. In combination with bETM, this hypothesis should be analyzed carefully. It is not the pure dose calculation time, but the increase of mapping events, which could also be time expensive. For example: DIM needs one mapping event per dose voxel. In contrast to DIM, bETM needs hundreds or thousands of mapping events per dose voxel. The value depends on the accuracy of MC. As a matter of fact, the dose of a voxel is the product of many energy events, which have to be transferred individually. Thus, the basic time advantage may be obsolete. As a summary, all important aspects about bETM are listed below:

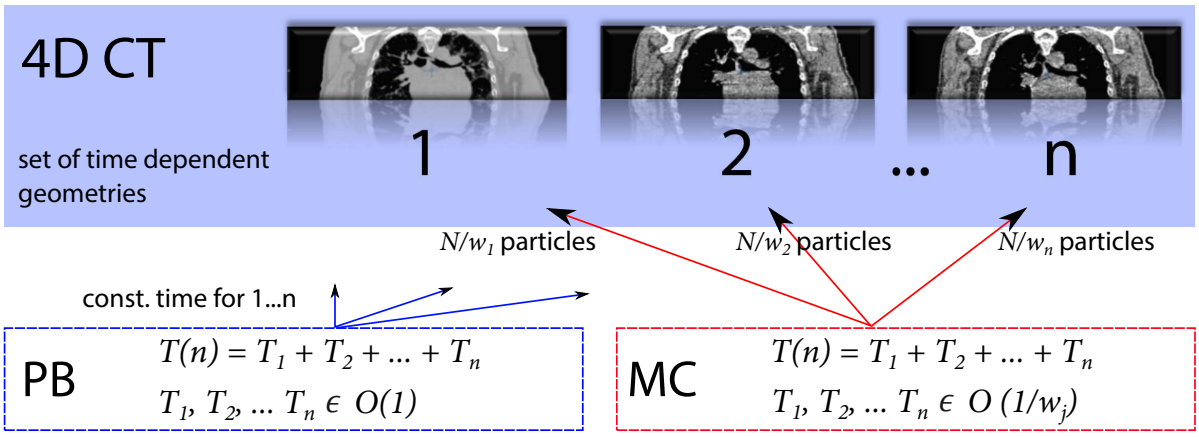

Figure 3.21 : Basic dose accumulation time improvement due to MC coupling: The calculation time for PB (left) is the n-fold multiple of a static distribution. MC (right) achieves no time increase due to the decrease of the individual time values. The accuracy is not degraded.

1. **Advantages of bETM:**
   a) Solution for the deformation effect (divergent assumption)
   b) Solution for the dose-mass relation (consideration of the dose definition for IIO (3.8))
   c) Solution for possible energy rearrangement
   d) Basic dose accumulation time improvement due to MC combination
2. **Disadvantages of bETM:**
   a) Not combinable with other dose algorithms (only MC)
   b) Discretization based MED error
   c) Defective deformation grid based MED error
   d) The need of an energy discretization module, which converts path ways to single points
   e) Large number of energy mapping events (time expensive)

Probabilistic Energy Transfer Model (pETM)

This thesis introduces a probabilistic Energy Transfer Model (pETM) as an advanced solution of bETM based on the large outline of the MED error. pETM tries to solve the problem accompanied with MED. pETM is refers to the definition of η_{med} mentioned in (3.66). The explanation about the MED error (section 3.3.2) serves for illustration. In contrast, the accurate calculation has to take the mass energy absorption coefficient μ_{en} into account. In comparison to the total cross section μ, this probability is related to the local deposited energy, excluding the spatial energy transported due to bremsstrahlung or other processes. Hence, η_{med} is defined by:

$$\eta_{\text{med}} \approx \left| D_i(x_i)_{\text{bETM}} \cdot \left(1 - \frac{\mu_{en_i}}{\mu_{en_j}}\right)\right| \tag{3.68}$$

Generally, the same procedure as shown in bETM (see Fig. 3.18; (3.61)) is applied for the algorithm. The adjustment is calculated during energy tracking. Every mapping event is weighted by the cross section coefficient

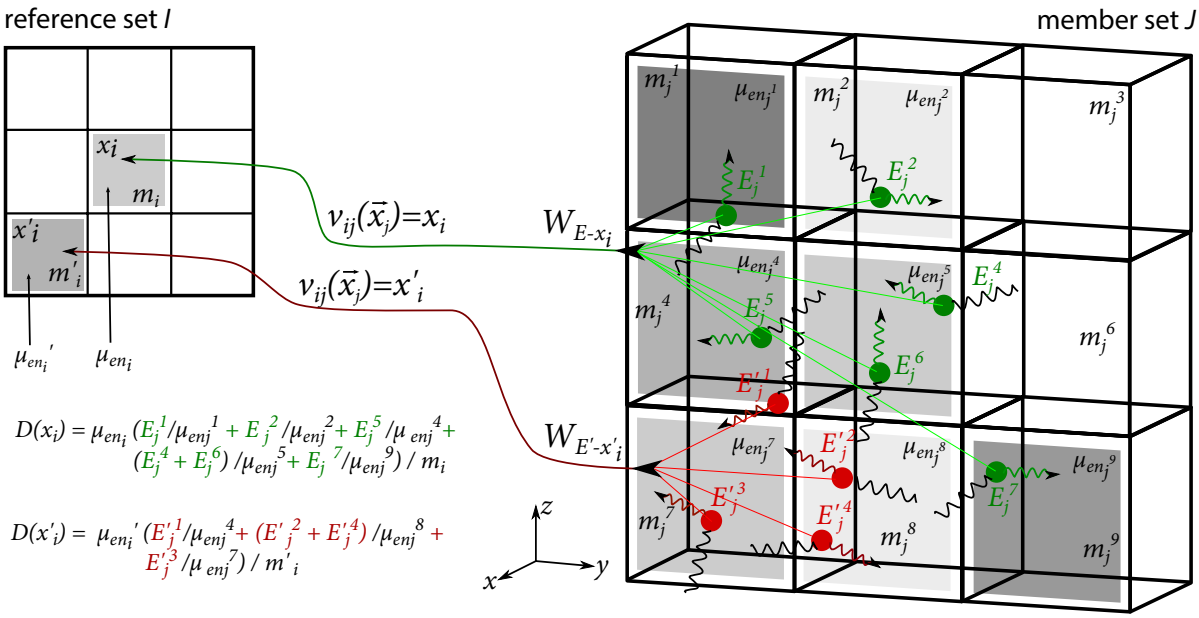

Figure 3.22 : Graphical overview of the probabilistic energy transfer model: In comparison with bETM (see Fig. 3.18), pETM weights every energy deposition E_j with the depending energy mass absorption coefficients μ_{en} of the deposition source x_j and the deposition target x_i. For example: Without weighting the mapping process of E_j^2 would overestimate the target dose in x_i due to the high mass gradient between m_j^2 and m_i. $\mu_{en_i}(E_j^2)/\mu_{en_j}(E_j^2)$ regulates the term. For graphical purposes, the figure neglects the energy dependence of μ_{en}. The implementation has to follow these dependencies.

$\frac{\mu_{en_i}}{\mu_{en_j}}$ in order to achieve the smallest possible MED error. Hence, the procedure can be defined with (3.61):

$$D_{i\sum}(x_i) = \sum_{j=1}^{n} w_j \left[\frac{1}{m(x_i)} \sum_{E_j \in W_{E\to x_i}} \frac{\mu_{en_i}(E_j)}{\mu_{en_j}(E_j)} \cdot E_j(\vec{x}_j) \right]; \quad W_{E\to x_i} = \left\{ E_j(\vec{x}_j) | x_i = v_{ij}(\vec{x}_j) \right\} \tag{3.69}$$

Fig. 3.22 gives an overview of pETM. It has to be noted that μ_{en} depends on the mass and additionally on the related energy. This implies another calculation step. Studies also have to investigate how far the basic conservation laws are affected by this adjustment. This means, the energy adjustment implies a kerma correction which is may not realistic. Hence, the conservation of the original dose information is may not guaranteed for areas that have no MED error. Section 3.4 comprehensively evaluates these facts. In conclusion, the properties of pETM are summarized by:

1. **Advantages of pETM:**
   a) Solution for the deformation effect (divergent assumption)
   b) Solution for the dose-mass relation (consideration of the dose definition for IIO (3.8))
   c) Solution for the discretization based MED error
   d) Solution for the defective deformation grid based MED error
   e) Solution for possible energy rearrangement
   f) Basic dose accumulation time improvement due to MC coupling

2. **Disadvantages of pETM:**
   a) Not combinable with other dose algorithms (only MC)
   b) The need of an energy discretization module, which converts path ways to single points
   c) Large number of energy mapping events + energy weighting (time expensive)

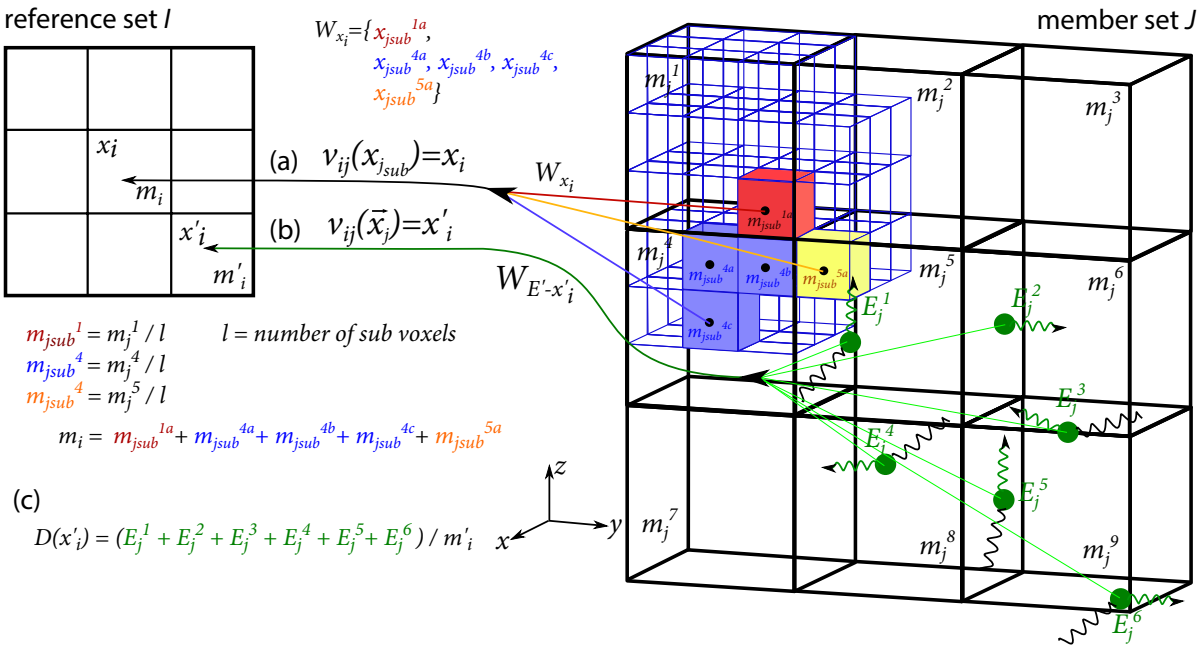

Figure 3.23 : Graphical overview of energy mass congruent mapping: (a) Mass mapping - The mass geometry m_i, m'_i of the reference set is generated by mass mapping of the sub-voxels $x_{j_{\text{sub}}}$ with the aid of the deformation grid $x_i = v_{ij}(x_{j_{\text{sub}}})$. (b) Energy tracking - Every energy deposition event $E_j(\vec{x}_j)$ is tracked ($x_i = v_{ij}(\vec{x}_j)$) to its target voxel x_i. (b) Dose calculation - The dose calculation is based on the mapped masses and the tracked energies.

Energy Mass Congruent Mapping (EMCM)

The EMCM model was introduced by *Zhong et al.* [124]. The primary motivation is a solution for the *defective deformation grid based MED error* (see section 3.3.2). The model splits dose in energy and mass, but using the same components for energy deposition as for dose calculation. Therefore, the basic model (bETM) is used, but the dose calculation inside the reference geometry I is performed with a mass mapped structure of J. Before energy tracking is done, the model creates a new reference geometry I_j based on the mass points in J. For execution of this preceding sub-step, the mass geometry J is divided in sub-voxels $x_{j_{\text{sub}}}$ with a higher resolution. Every sub-voxel receives the fractionated mass $m(x_{j_{\text{sub}}}) = \frac{m_j(x_j)}{l}$ of its parent voxel x_j. l being the number of sub-voxels per dose voxel. After dividing, the mass mapping is performed. The deformation grid determines the target voxel x_i for every sub-voxel in J: $x_i = v_{ij}(x_{j_{\text{sub}}})$. The target receives the mass of every sub-voxel that migrates to x_i: $m(x_i) = \sum m(x_{j_{\text{sub}}})$. After finishing the mass mapping, the algorithm continues with the basic energy model, whereas the dose calculation is performed with the new mapped mass geometry. The full procedure is illustrated by Fig. 3.23. The model is defined by:

$$D_{i\sum}(x_i) = \sum_{j=1}^{n} w_j \left[\frac{\sum_{E_j \in W_{E\to x_i}} E_j(\vec{x}_j)}{\sum_{x_{j_{\text{sub}}} \in W_{x_i}} m(x_{j_{\text{sub}}})} \right]; \qquad \begin{aligned} W_{E\to x_i} &= \left\{ E_j(\vec{x}_j) \middle| x_i = v_{ij}(\vec{x}_j) \right\} \\ W_{x_i} &= \left\{ x_{j_{\text{sub}}} \middle| x_i = v_{ij}(x_{j_{\text{sub}}}) \right\} \end{aligned} \tag{3.70}$$

As a matter of fact, EMCM solves the deformation problem due to its basic approach and direction of voxel mapping. Further EMCM considers the dose definition for IIO and fulfills the requirements of the dose-mass relation for unifying doses. It must be noted that even masses are used for dose calculation that are also used for energy production. This is very close to the basic approach. Additional, this avoids the MED error through a defective deformation grid, because energy points are regulated by its own masses. An outlier of the error is

not possible since both components (mass and energy) for dose calculation are based on the same deformation grid. Despite all, EMCM does not avoid the *discretization based MED error*. The mass discretization itself and the deformation effect can still cause a significant mass difference of the energy deposition mass m_j and the dose calculation mass m_i. For example: An energy is produced by a mass m_j. However, due to deformation, a set of other mass points also migrate to the same target voxel x_i. Hence, the mass m_i for dose calculation will increase significantly. Considering a constant energy, the resulting dose will be underestimated.
Another disadvantage is the high level of technical complexity, which receives a another degree due to the additional mass mapping procedure. Thus, the number of mapping events multiplies again. This could be extremely memory intensive and time expensive considering a repeat of the procedure for every breathing phase. All other properties are consistent with the basic idea of the energy transfer model. The summary of EMCM is given by:

1. **Advantages of EMCM:**
   a) Solution for the deformation effect (divergent assumption)
   b) Solution for the dose-mass relation (consideration of the dose definition for IIO (3.8))
   c) Solution for the defective deformation grid based MED error
   d) Solution for possible energy rearrangement
   e) Basic dose accumulation time improvement due to MC coupling
2. **Disadvantages of EMCM:**
   a) Not combinable with other dose algorithms (only MC)
   b) Discretization based MED error
   c) The need of an energy discretization module, which converts path ways to single points
   d) Large number of energy and mass mapping events (time expensive, memory intensive)

3.4 A dose error evaluation study for 4D dose calculations

To measure the quality of the explained mapping algorithms (3.3.1 and 3.3.2), it is necessary to repeat the mapping process for a set of arbitrary regions of interest (ROI). The analyzed volumes are small cuboid ROIs (Δx = 32 mm, Δz = 24 mm, Δy = 16 mm, inspired by *Yan et al.*[119]) distributed over the full 4D geometry. The large number of test cases m = 900 (value of considered ROIs) enable a qualitative assessment. The dose calculation (see section 3.4.3) and the dose transformation process is performed for every ROI. The results of the different transformation models are compared by error values. The investigation is focused on the transformation itself. Effects of the deformation grid, the dose algorithm and any other sources of error are neglected. Fig. 3.24 illustrates the main idea: The first step is the selection of a randomly located ROI. (a) Then, the breathing phase j is chosen. (b) The ROI in j provides the volume for the dose calculation $D_j(x_j)$. (c) The mapping process is performed with all respective transformation models: bETM, pETM, EMCM, DIM, dDMM. This step generates five different target distributions $D_i(x_i)$. (d) The determination of the mapping error η enables comparative studies. The procedure is carried out for different parameter variations (e.g. four different voxel sizes; gradient distributions). Then, the same calculation is repeated for the next breathing phase until the full breathing cycle is reached. A total of 900 arbitrary ROIs is evaluated.

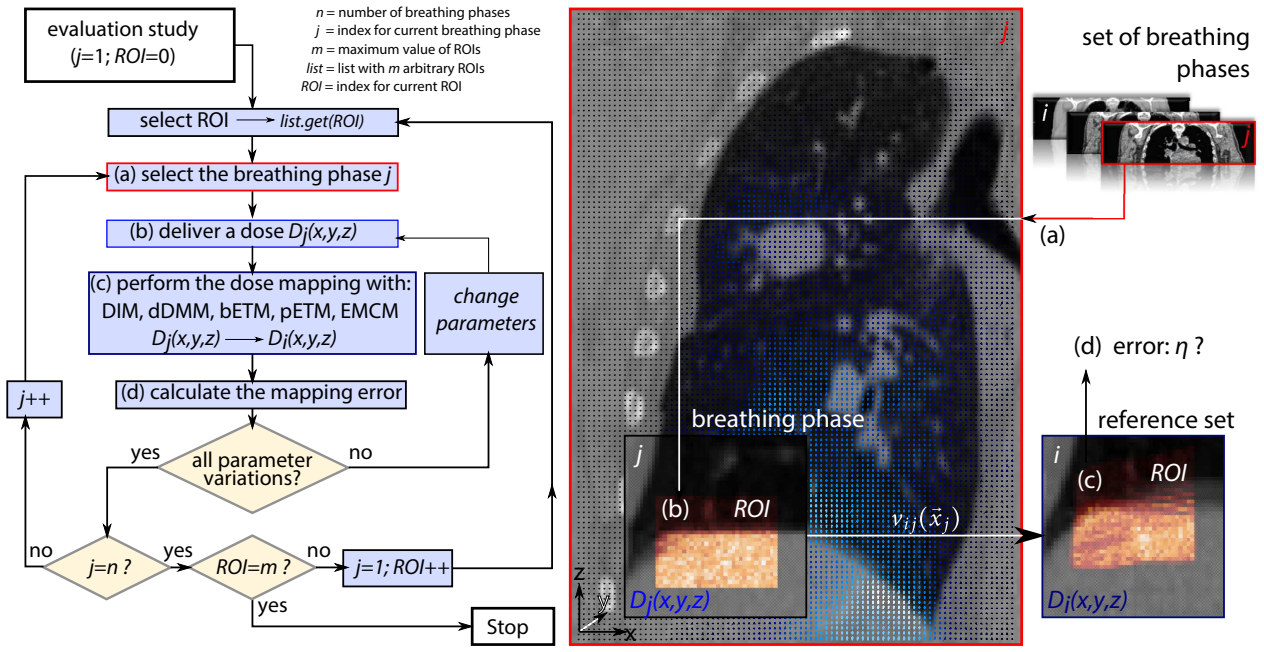

Figure 3.24 : Evaluation study for dose transformations: The left scheme illustrates the basic algorithm sequence plan. The right sketch points out the sub-steps of the procedure. The important outcome of the evaluation is the calculation of the mapping error for every single mapping model (bETM, pETM, EMCM, DIM, dDMM). m is a large value that indicates the number of calculated ROIs.

3.4.1 Primary error evaluation with the dose mass histogram

Yan et al. [119] proposed a mapping error that is introduced by an integral dose for the investigated ROI. Without transformation, the integral dose is defined by: $D_j = E_{\int_{ROI_j}} / m_{\int_{ROI_j}}$. The ratio contains summarized values, i.e. the total deposited energy in the entire mass of the ROI. In order to the mapping algorithm and to the deformation grid, the deviation of the mass conservation and the deviation of the energy conservation is measured. Hence, it is possible to propose the integral dose for the transformed ROI: $D_i = E_{\int_{ROI_i}} / m_{\int_{ROI_i}}$. The proposed error value is based on the dose deviation $|D_j - D_i|$. This error value is valid and reasonable. However, the model does not consider local effects inside the ROI. The law neglects spatial assignments of energies and masses. It cannot be said, which energy share is deposited and is related to a certain fraction of mass. Dose peaks produced by local energy depositions in low mass regions are ignored. For evaluation of the clinical relevance of transformed dose distributions (see section 3.2), it is important to take the mentioned spatial fractions into account. Whether a treatment plan is good or not, is not determined by an integral dose or a single dose value. It is defined by the entire volume based dose distribution and the spatially deposited biological damage. Dose gradients and mass inhomogeneities lead to different dose-mass fractions inside the volume. The transformation process should not alter this dose information, otherwise the accuracy of the basic dose calculation is obsolete.

In clinical practice, one of the most powerful parameter for plan assessment is the dose volume histogram (DVH). However, he DVH assumes a constant mass inside all voxels. This is sufficient for homogeneous organs, but heterogeneous objects are considered in this work. The dose mass histogram (DMH) is an extension of the DVH. It is a more accurate approach. The DMH concept uses the fractionated mass that absorbs a certain dose. *Wei et al.* [112], *Mavroidis et al.* [61] and *Webb et al.* [111] investigated the DMH approach for lung complications in comparison to the DVH. The main conclusion was a dose overestimation associated to the DVH concept. In contrast, the effectiveness of the DMH model was closer related to the real radiation effects.

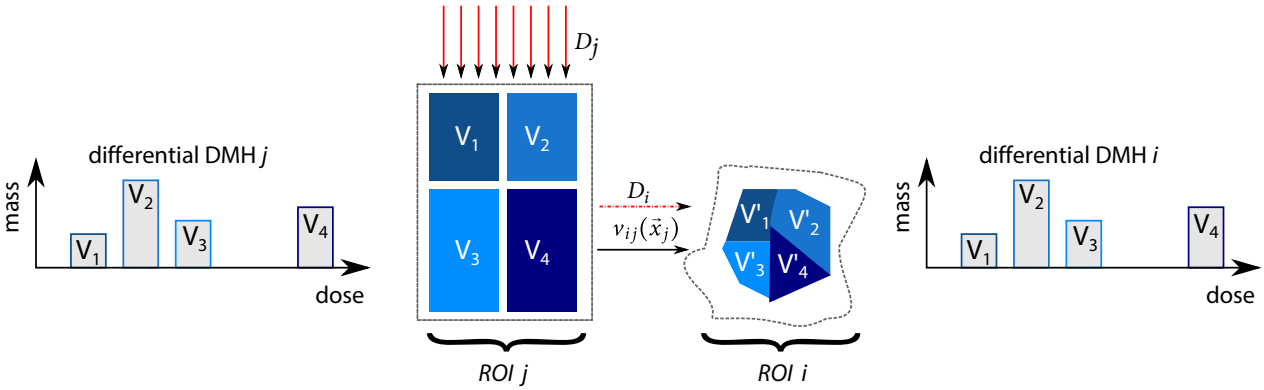

Figure 3.25 : DMH used as mapping assessment parameter: During dose transformation the shape of the ROI and all considered sub-volumes could differ strongly. A certain portion of the volume (i.e. a cell population) receives a defined dose with a related damage. Although the volume varies, the damage remains unchanged, because the mass inside the volume is still the same. In conclusion from a biological point of view, the mapping process should not change the DMH. The goal of transformation is: $DMH_i \approx DMH_j$.

Furthermore, deformation and expansion of anatomical volumes impede the use of the DVH concept in this task. Therefore, the most important assessment for transformation assessment is the analysis of the ROI based DMH. The DMH should not change during dose transformation and this guarantees the conservation of each dose-mass fraction. Due to numerical effects, an exact DMH conservation is not feasible. A good approach should approximate the unmapped DMH (j) as close as possible. Fig. 3.25 explains the suitability of the DMH to assess the quality of a specific mapping approach using the differential dose mass histogram.
It is not suitable to compare the differential DMH. Voxel unions could cause small dose shifts for discrete dose bins. These shifts would cause the same error as large model based dose displacements. In contrast, the cumulative DMH is resistant to this effect. Hence, it is necessary to analyze the cumulative DMH:

$$DMH(D) = \int_{D}^{D_{max}} m(D') \cdot dD' \tag{3.71}$$

The DMH error for a specific dose D is the difference between the mapped (i) and the unmapped cumulative DMH (j). It is defined by:

$$\Delta DMH(D) = |DMH_i(D) - DMH_j(D)| \tag{3.72}$$

It describes the mass discrepancy of both dose distributions with respect to a specific dose D. A cumulative error parameter (over the full dose range $0...D_{max}$) is necessary to compare the entire dose distributions:

$$\begin{aligned} \Delta_{\int} DMH &= \int_{0}^{D_{max}} \left|DMH_i(D) - DMH_j(D)\right| dD \\ &= \int_{0}^{D_{max}} \left| \int_{D}^{D_{max}} m_i(D_i) \cdot dD_i - \int_{D}^{D_{max}} m_j(D_j) \cdot dD_j \right| \cdot dD \end{aligned} \tag{3.73}$$

It is useful to normalize the integral dose difference for a qualitative assessment and to distinguish the outcome of different transformation models and ROIs with different mass fractions. Hence, the total normalized DMH error η_{DMH} is defined by:

$$\eta_{\mathrm{DMH}} = \frac{\int_{0}^{D_{max}} \left|DMH_i(D) - DMH_j(D)\right| dD}{\int_{0}^{D_{max}} DMH_j(D) dD} \tag{3.74}$$

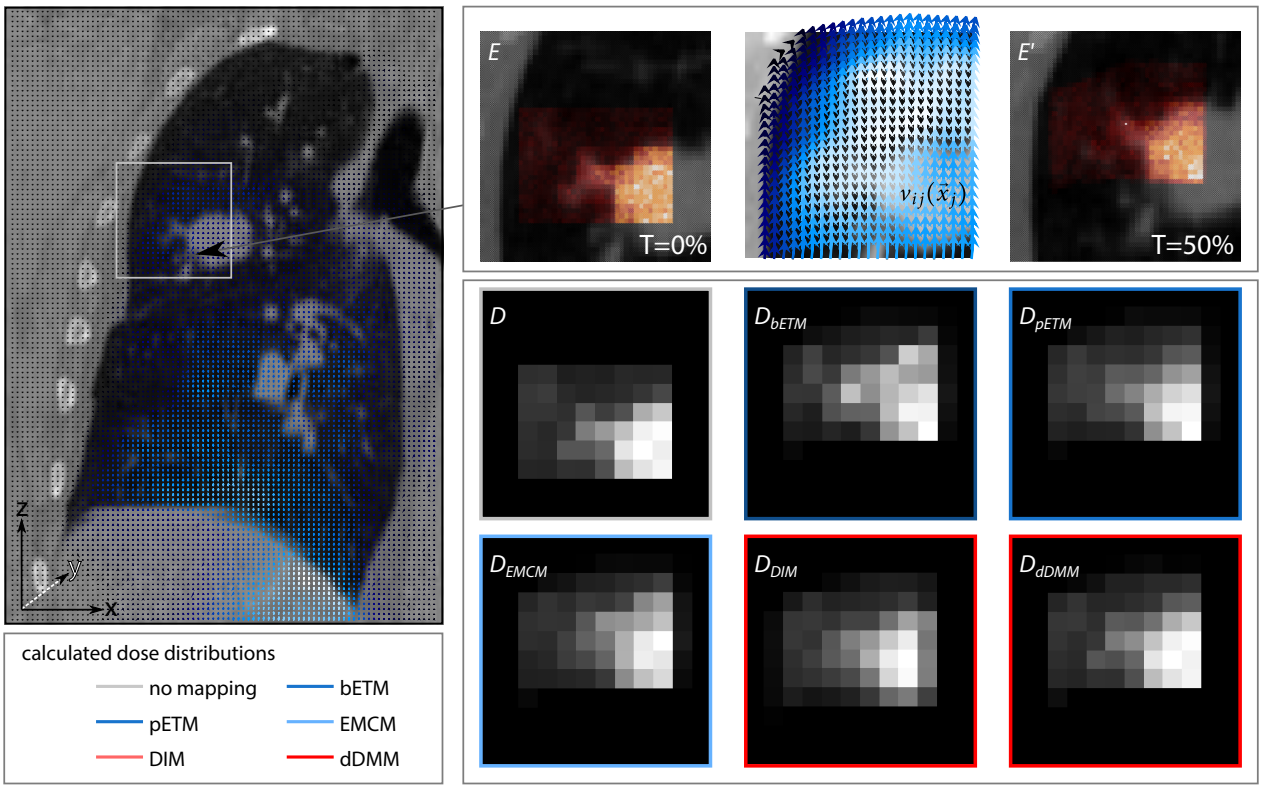

Figure 3.26 : Example of a 2D dose transformation: A small arbitrary ROI, delivered by an homogeneous fluence (at $t = 0\,\%$), creates the resulting unmapped dose distribution D (gray). The dose transformation to another breathing geometry ($t = 50\,\%$) is performed by: bETM (dark blue), pETM (blue), EMCM (light blue), DIM (light red), dDMM (red). A comparison of the unmapped and the mapped dose distribution is necessary to assess all mapping approaches. The y-coordinate is neglected in this example for visualization. A voxel size of $2 \times 2\,(mm)^2$ is used.

Or written as:

$$\eta_{\mathrm{DMH}} = \frac{\int_0^{D_{max}} \left| \int_D^{D_{max}} m_i(D_i) \cdot dD_i - \int_D^{D_{max}} m_j(D_j) \cdot dD_j \right| \cdot dD}{\int_0^{D_{max}} \int_D^{D_{max}} m_j(D_j) \cdot dD_j \cdot dD} \tag{3.75}$$

The power of the DMH is explained in the following outline using a trivial two-dimensional example. Therefore, Fig. 3.26 illustrates six calculated dose distributions[24]. For illustration, the third dimension (y-coordinate) is neglected. An arbitrary ROI (Fig. 3.26 left) is exposed by an homogenous fluence at the beginning of the breathing cycle ($t = 0\,\%$). With the aid of the deformation grid v_{ij}, the delivered dose distribution at $t = 0\,\%$ (gray) is mapped to another breathing geometry $t = 50\,\%$. The resulting dose distributions are generated by different transformation models (blue=ETM, red=DMM). Significant differences of the gray scales inside the dose distributions are already visible in Fig. 3.26.

A detailed analysis is possible with a view on the differential DMH (see Fig. 3.27) regarding the calculated dose distributions. As a matter of fact, a good mapping approach calculates a differential DMH that looks similar as the unmapped DMH (black, upper left graph in Fig. 3.27). In this example, the most similar DMH is created by the dDMM model (red, lower right graph). All models could show significant differences, which have numerical and model related reasons. For example: The significant mass peak in the high dose region of dDMM (at 90 % of maximum dose) has numerical reasons due to a small dose shift of a higher dose bin.

[24] The used data and the implementation is described and explained in section 3.4.3.

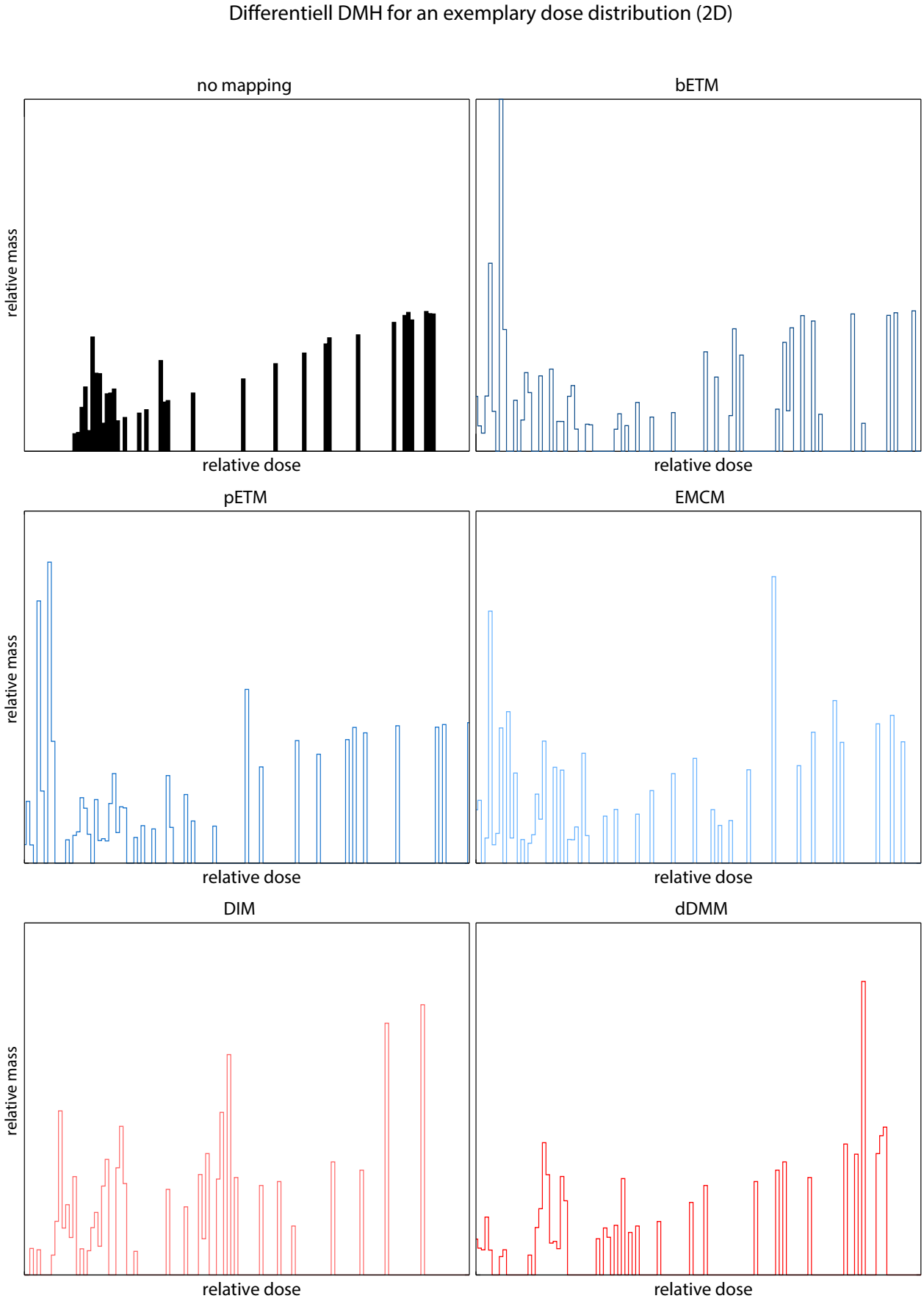

Figure 3.27 : Example for a differential DMH: The figure shows the differential dose mass histograms based on the 2D dose distributions calculated in Fig. 3.26 and distinguished by different transformation approaches. All graphs are normalized to the same maximum dose and to the same maximum mass. The illustration determines the DMH before (black plot) and after transformation (colored plots).

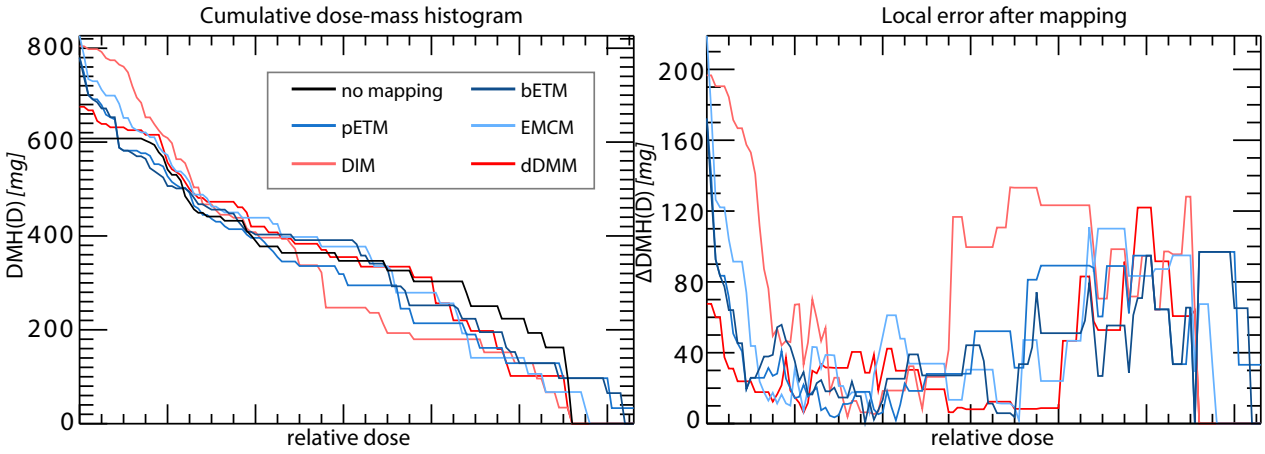

Figure 3.28 : Example for a cumulative DMH and the resulting transformation error: This sample shows the DMH error for a single 2D dose distribution using a voxel size of 2 mm for one sample ROI. The graph compares the DMH of each dose distribution (see Fig. 3.26). The left plot shows the cumulative histogram. The ordinate explains the absolute mass in mg. Mass discrepancies for $D = 0\,\%$ between several dose transformations are based on numerical reasons. The graph on the right illustrates the local DMH error $\Delta DMH(D)$. It is the absolute difference caused by the transformation model in comparison to the untransformed dose distribution. A full integration results in the total error. The dose binning of this method is not equidistant, because each mass fraction could vary between specific voxels.

Finally, the figure illustrate possible differences of the differential DMH caused by various transformation models. This reshaping process may modifies the basic dose information. To distinguish between numerical and model based errors, it is necessary to focus on the cumulative DMH. This enables a qualitative assessment for the study. Fig. 3.28 (left graph) illustrates the cumulative DMH for the mentioned 2D example. The figure distinguishes between all transformation models. Important for the quality of the model is the conservation of the cumulative DMH. This is preferably a small error distributed over the full dose range. The visualization illustrates significant differences for $\Delta DMH(D)$ in Fig. 3.28. The lower the integral value of $\Delta DMH(D)$, the better is the quality of the used model. The DMH error value is the most important and most meaningful error value of this evaluation study, because it considers global ROI-based dose information as well as local mass-energy relations.

It must be noted that numerical issues are responsible for the total mass deviations at $D = 0\,\%$ for $DMH(D)$ in Fig. 3.28 (left). The deformation process leads to the fact that more voxel masses are located inside the numerical ROI after deformation. Hence, more masses are affected by the transformed dose. Due to various calculation rules for the different transformations models, variations at $D = 0\,\%$ are justified by different technical determinations of the $DMH_i(D)$. In this survey, the following detailed solutions are used to determine the DMH after dose transformation:

$$\begin{aligned} DMH_{i,a}(D) &= \int_{D}^{D_{max}} m_i(D') \cdot dD'; \qquad a = \{ETM, bETM, DIM, dDMM\} \\ DMH_{i,b}(D) &= \int_{D}^{D_{max}} m_{j\to i}(D') \cdot dD'; \quad b = \{EMCM\} \end{aligned} \tag{3.76}$$

The final doses D (dose-to-medium, after dose transformation) are calculated either with m_i (voxel masses of the reference set i) for bETM, pETM, DIM, dDMM or with $m_{j\to i}$ (mapped masses of j inside the reference set i) for EMCM. Hence, the model related DMHs have to be calculated differently. EMCM uses $m_{j\to i}$ instead of m_i for DMH determination. This leads to small deviations of the total masses at $D = 0\,\%$ shown in the DMH graph of Fig. 3.28.

3.4.2 Secondary error evaluation with mean doses and energy rearrangement

Error metric based on the mean dose

In some cases, it is also useful to analyze the mean dose error $\eta_{<D>}$. This value is based on the ROI-related average dose. Only voxels x_j are considered that are related to the total number l of exposed voxels inside the ROI. The dose average is written as:

$$< D_j >= \frac{1}{l} \cdot \sum_{x_j=1}^{l} D_j(x_j) \tag{3.77}$$

$\eta_{<D>}$ compares the mean dose before (j) and after (i) dose transformation. Again, the normalization with the untransformed value has to be considered. $\eta_{<D>}$ is defined by:

$$\eta_{<D>} = \left| \frac{< D_i > - < D_j >}{< D_j >} \right| \tag{3.78}$$

This error should be as low as possible. From a physiological point of view, $\eta_{<D>}$ must no be zero. It can be realistic due to expansion, compression and density inhomogeneities that the average dose shifts slightly through transformation. Thus, $\eta_{<D>}$ is less meaningful than η_{DMH}. It serves not for global conclusions. The parameter was mainly introduced to filter dose peaks, which are related to extreme small mass fractions. These peaks are easily possible through wrong energy-mass relations. The mentioned error is not easily observable in the DMH graph, because it is mainly caused by very small mass values. However, the average dose closely depends on every dose value independent of its mass. Hence, the mean dose value clearly illustrates the mentioned effect.

Error metric based on energy rearrangement

Among others, *Siebers et al.* [93] made a detailed analysis of dose mapping. The main conclusion of these proposals is a disadvantage of conventional DMM approaches like DIM. This disadvantage, so called energy rearrangement (see section 3.3.1), describes inaccurate energy depositions due to discrete voxel unions. A wrong mapping of energy deposition points that a far away from the voxel center due to a strong applying deformation gradient (see Fig. 3.15). To avoid such errors, it was recommended to use energy transfer models for dose transformation. The following method describes an approach to measure the energy rearrangement effect of each transformed dose distribution. The main intention is a comparison of ETM and DMM. This error value is less meaningful than η_{DMH}. It merely extends the analysis.
To measure the displacement, it is useful to extract the final energy distribution $E_i(\vec{x}_i)$ using the transformed dose distribution $D_i(x_i)$. The sub-voxel approach of the EMCM method (see section 3.3.2) is also used for calculation. The source set j is splitted into a highly resolved sub-voxel mass grid $m(x_{j_{\mathrm{sub}}})$. The final energy E_i in a voxel x_i results from a division of its transformed dose $D_i(x_i)$ (related to a certain transformation model) and all fractionated masses of the source j that migrate to the target voxel x_i via transformation: $v_{ij}(x_{j_{\mathrm{sub}}})$. Using (3.70), the energy distribution related to the transformation model is defined by:

$$E_{model}(x_i) = \frac{D_i(x_i)}{\sum_{x_{j_{\mathrm{sub}}} \in W_{x_i}} m(x_{j_{\mathrm{sub}}})}; \quad W_{x_i} = \left\{ x_{j_{\mathrm{sub}}} | x_i = v_{ij}(x_{j_{\mathrm{sub}}}) \right\} \tag{3.79}$$

This method ensures the same approach for every model to calculate its energy distribution. The next step is a comparison of the recalculated discrete distribution $E_{model}(x_i)$ and the directly tracked energy distribution

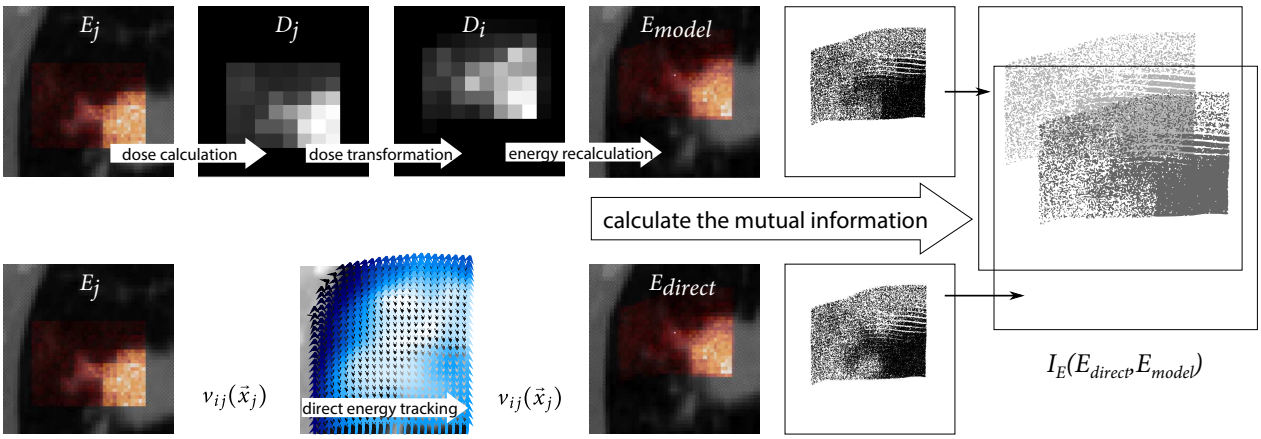

Figure 3.29 : Principle scheme to measure the energy rearrangement: The energy distributions E_{model} (top) and E_{direct} (bottom) are generated by recalculation and energy mapping. The resulting distributions are comparable with the aid of the normalized mutual information $I_E(E_{direct}, E_{model})$. A high MI value is equivalent to a strong similarity.

$E_{direct}(x_i)$ in a target voxel x_i. The directly tracked distribution can be written as:

$$E_{direct}(x_i) = \sum_{E_j \in W_{E \to x_i}} E_j(\vec{x}_j); \quad W_{E \to x_i} = \left\{ E_j(\vec{x}_j) | x_i = v_{ij}(\vec{x}_j) \right\} \tag{3.80}$$

There are a number of methods for similarity measurements of more dimensional distributions. The mutual information (MI) I is an established approach in medical solutions and is suited very well in this case (see section 2.2.1).[25] The MI is a theoretical value (information theory, [54]) that describes the power of the statistical dependence derived from two random variables. Here, it serves to measure the similarity of $E_{real}(x_i)$ and $E_{model}(x_i)$. Hence, it can be written as:

$$I(E_{direct}, E_{model}) = \sum_{E_d(x_i^1)} \sum_{E_m(x_i^2)} p\left(E_d(x_i^1), E_m(x_i^2)\right) \cdot \log\left(\frac{p(E_d(x_i^1), E_m(x_i^2))}{p(E_d(x_i^1))p(E_m(x_i^2))}\right) \tag{3.81}$$

$p\left(E_r(x_i^1), E_m(x_i^2)\right)$ is the joint probability distribution function of $E_r(x_i^1)$ and $E_m(x_i^1)$. It is the combined probability distribution. $p(E_r(x_i^1))$ and $p(E_m(x_i^2))$ are probability distribution functions of $E_r(x_i^1)$ and $E_m(x_i^2)$ respectively.

A perfect match of the recalculated energy distribution results in a large value of $I(E_{direct}, E_{model})$. The greater the MI value is, the better is the resistance of the model against energy rearrangement. To compare MI values of hundreds of arbitrary ROIs for statistical conclusions, it is necessary to normalize $I(E_{direct}, E_{model})$ to the perfect match $I(E_{direct}, E_{direct})$. Otherwise, extreme MI deviations for different ROIs occur due to differences of total energy values and significant mass variances inside different ROIs. The resulting error value I_E is defined by:

$$I_E = \frac{I(E_{direct}, E_{model})}{I(E_{direct}, E_{direct})} \tag{3.82}$$

A perfect match results in $I_E \to 1$. I_E is independent from the structure and the slope of the energy distribution inside the ROI. However, EMCM will cause a approximately perfect matches for very small voxel sizes, because

[25] It is possible to use other approaches for energy verification like cross correlation (CC). However, the choice of the similarity parameter has a minor role in this trivial application. All similarity parameters show a similar results.

the generation of E_{direct} is only the inverse calculation of E_{EMCM}. Since energy rearrangement is especially important for huge voxel sizes, results of small voxel sizes should not be overrated. Furthermore, the whole approach of I_E builds on the basic idea of all ETM models. A good score in I_E does not necessarily result in a good clinical effect of η_{DMH}. The energy rearrangement investigation is an additional analysis. Fig. 3.29 illustrates the basic scheme of the measurement approach.

3.4.3 Full evaluation concept

Deformation grid and patient data

This evaluation study uses the data and the deformation grid of the *POPI-model* (see section 2.2.1), a Point-validated Pixel-based Breathing Thorax Model. It is an established scientific data set with lung cancer patient images containing a full 4DCT. It is provided by the *Léon Bérard Cancer Center* and the *CREATIS Laboratory* (Lyon, France). The model is fully described by *Vandemeulebroucke et al.*[105] (*http://www.creatis.insa-lyon.fr/rio/popi-model*). This study uses the 4DCT series of the preprocessed images containing ten static CT series. The transformation is based on the deformation data (v_{ij}) processed by the parametric deformation method of the POPI-model that particularly implements the FFD approach according to *Rueckert et al.*[81] (see section 2.2.1).The model is verified by point validation (see 2.2.1). The model provides vector fields merely in one direction: reference set → breathing phase ($\vec{x}_j = v_{ji}(\vec{x}_i)$). Inverse vector fields $v_{ij}(\vec{x}_i)$, which are necessary for various transformation algorithms, are approximated with the Newton-Raphson optimization implemented in the *iPlan™ RT* framework. A validation of the inverse fields revealed a mean deviation of 0.003 mm and an maximum deviation of 0.31 mm. However, except of DIM all methods use the inverse vector fields. Hence, almost all transformations are based on the same DIR data. Thus, errors based on the DIR algorithm are negligible for this study.

Dose algorithm

The study uses a very simplified Monte Carlo approach (dose-to-medium, see formula (3.5)) to calculate the dose inside the arbitrary ROIs. To realize a beam that would deliver an equal dose distribution in water without gradients, a spatial homogeneous photon particle fluence Φ is assumed in the entire ROI. The assumed photon particles are independent of any direction and occur isotropic. Hence, integrations over equal specific solid angles would yield additionally constant fluence shares. For example, $\iint_0^{\Pi} \Phi(\vec{\Omega})d\Omega = \iint_{\Pi}^{2\Pi} \Phi(\vec{\Omega})d\Omega = \iint_{2\Pi}^{3\Pi} \Phi(\vec{\Omega})d\Omega = \ldots$ could be assumed. Furthermore, the energy spectrum of the investigated photons is mono-energetic containing exclusively 6 MeV photons. In general, the fluence is defined as:

$$\Phi = \frac{N}{A} = \frac{\sum dl}{dV_{ROI}} \tag{3.83}$$

with N being the number of particles crossing an area A and $\sum dl$ being the sum of all photon path lengths that traverse the defined volume dV_{ROI}. The dose algorithm investigates a defined number N of photon particles. Therefore, specific coordinate $\vec{x}$ of their traversing paths $\sum dl$ are drawn randomly inside the volume of the ROI. These photon coordinates are spatial uniformly distributed to simulate the homogeneous fluence. Furthermore, the algorithm investigates the probability for an interaction with matter in this coordinate. As known from the basics of Monte-Carlo and derived from the probability density function of the attenuation law, the length of the free photon path length s is inversely proportional to mass attenuation μ coefficient of the investigated photon energy [26]. In reverse, a higher mass attenuation coefficient leads to more interaction

[26] The basic law to determine the free path photon length is $s = -\frac{1}{\mu} ln(1 - R_1)$ with R_1 or R_1' being a uniformly distributed number in the interval of $[0, 1]$.

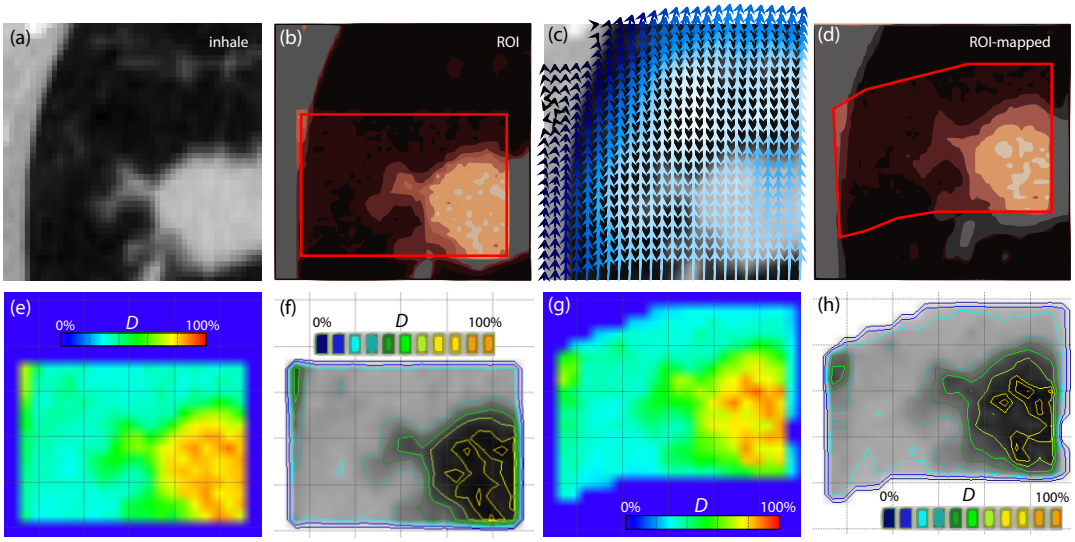

Figure 3.30 : Results of the simplified dose algorithm: The figures illustrates the realistic dose distributions generated by the trivial MC dose algorithm. The method calculates dose-to-medium. In the shown example, a homogeneous fluence is assumed. Dose gradients directly base on the mass density. The figure illustrates a single dose transformation (inhale 0 % → exhale 60 %) with EMCM. The reference set in (a) shows the density distribution (inhale). The respective ROI is illustrated in (b) and (d) (→ mapped). The vector field in (c) is used to transform the dose distributions (e,f → before transformation; g,h → transformation result).

due to the shorter free path lengths. This dose algorithm does not distinguish between different interaction types. Also secondary particles are neglected. Hence, the mass energy absorption coefficient μ_{en} given by *Hubbel et al.* [37] is used to estimate the deposited energy. For this purpose, the algorithm generates for every photon a random number R uniformly distributed in the range of 0 and the maximum absorption coefficient of the ROI $[0, max(\mu_{en})]$. The particle interacts and deposits energy (dose-to-medium), if the random number R is smaller as the coordinate related absorption coefficient $\mu_{en}(\vec{x})$. Otherwise, the particle traverse the volume without interaction. The resulting dose distributions inherent dose gradients that are merely based on mass density variations inside the ROI (see Fig.3.30). The conversion of Hounsfield Units (HU) to mass density values is realized with the aid of the paradigms inside the XVMC code [22]. All energy events occur point wise in single coordinates. A point energy deposition event is not realistic, but sufficient for this application. Furthermore, it simplifies the analysis of various ETM models. For each dose calculation $N = 2 \cdot 10^5$ uniformly distributed photon particles are investigated within the ROI. Due the small size of the ROI, the approach yields very realistic dose distribution illustrated by Fig. 3.30. However, the aim is not to generate particularly accurate dose distributions, but to investigate the dose transformation process.

Moreover, the study proves the effect of inhomogeneous fluence distributions. For example, this could be fluence gradients generated in areas of overlying beams or located at penumbra areas in beam edges. For this purpose, two other fluence distributions are produced for each ROI. In this cases, the coordinates of the investigated photon particles are not uniformly distributed in the space. The coordinates are based on specific spatial probability functions that generate two different fluence gradients. This study focuses on two spatial distributions: (1) A fluence distribution with a smooth gradient in z-direction; (2) A distribution with two strong gradients in x-direction; Both cases are illustrated in Fig. 3.32. In summary, the study investigates three different fluence distributions (one spatial uniform distribution and two spatial inhomogeneous distributions) for investigation of error dependencies in combination with spatial fluence variations.

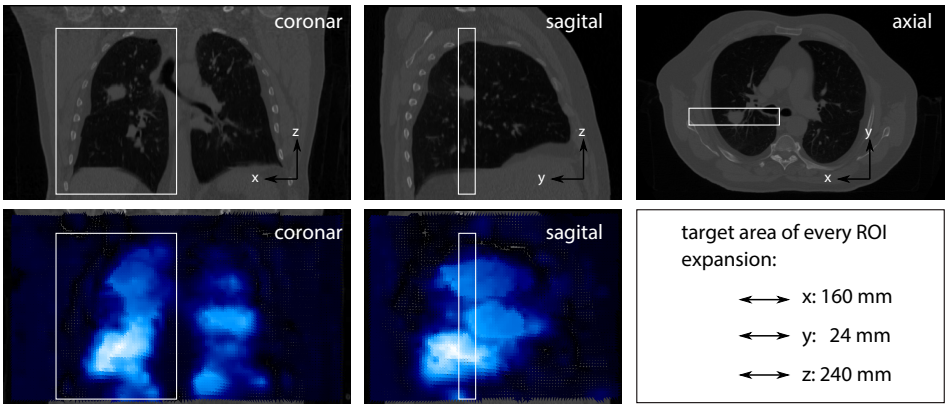

Figure 3.31 : Destination area of every sample ROI: Every ROI of the mapping study is located inside the white area. This area covers the full right lung in x-direction and in z-direction. The size in y-direction is even smaller to investigate spatial dependencies. The lower illustrations (blue) explain the maximum displacement during breathing. Hence, the destination area covers all possible lung displacements.

Table 3.3 : Overview of mapping analysis: The study calculates 900 sample ROIs. Every case uses the following parameter variations. With the aid of these, it is possible to cover all influences for dose transformation. The interpretation of the simulation is very difficult due to the large number of collected values. As much as possible data must be discarded to focus on significant values (see section 3.4.4).

proceeded ROIs	$9 \cdot 10^2$	
a) fluence distributions	3	*one homogeneous, two inhom. distributions*
b) voxel sizes	4	8 mm, 4 mm, 2 mm, 1 mm
c) breathing phases	9	*all phases except the reference set*
d) transformation models	5	*bETM, pETM, EMCM, DIM, dDMM*
e) mapping error values	3	η_{DMH}, $\eta_{<D>}$, I_E
collected data	$1.458 \cdot 10^6$	$= 9 \cdot 10^2 \cdot 3 \cdot 4 \cdot 9 \cdot 5 \cdot 3$

Full implementation and parameter variations

The source code for the transformation methods was written using the software package IDL™ (*Interactive Data Language from ITT, Version 7.1*). In detail, the simulation generates 900 ROIs. The coordinates of the volumes are equally distributed inside the patient geometry. The full destination area is illustrated in Fig. 3.31. It totally covers the right lung in x-direction (160 mm) and in z-direction (240 mm) to include every possible deformation. The coverage y-distance (24 mm) is very small for a better understanding of spatial error dependencies. Hence, all following explanations and evaluations are reduced to the coronar view.
When a sample ROI is randomly selected inside the patient, the evaluation algorithm chooses a coarse voxel size of $8 \times 8 \times 8\,\mathrm{mm}^3$. The procedure generates three different dose calculations (one spatial uniform fluence distribution and two spatial inhomogeneous fluence distributions) for every breathing phase (in total 9 phases) except the reference set. Thereafter, the actual dose transformation is performed using the mentioned transformation models. The transformation targets to the reference geometry and allows to determine the mapping error values: η_{DMH}, $\eta_{<D>}$, I_E. The algorithm repeats the full procedure with lower voxel sizes: 4 mm, 2 mm and 1 mm. Finally, this process is repeated for all ROIs to enable statistical conclusions. In summary, all parameter variations and all proceedings are explained in Tab. 3.3.

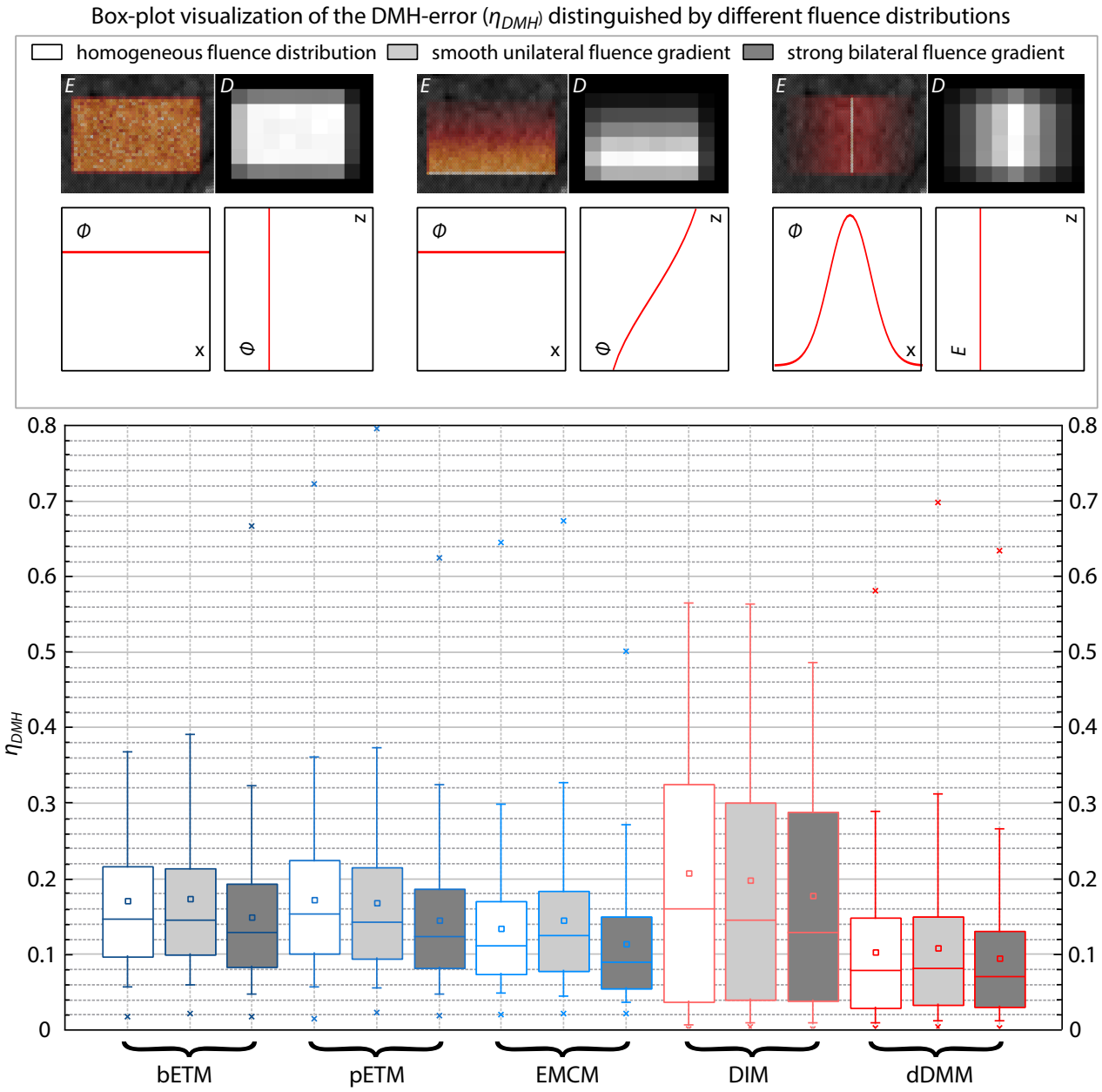

Figure 3.32 : DMH-error distinguished by different fluence distributions: The graph visualizes the box-plot of η_{DMH}. The results are separated by certain transformation models (ETM: blue; DMM: red). Several fluence distributions are marked by gray scale values. Each error distribution includes sample ROIs of all voxel sizes and all breathing phases with a total number of $3.24 \cdot 10^4$ samples. Some maximum errors are out of range and not visible in the plot.

3.4.4 Results

Test 1: Global DMH-error regarding different fluence distributions

The study was created to compare and to asses the quality of different dose transformation models (bETM, pETM, EMCM, DIM, dDMM). The most important error value is the DMH-error. Thus, major conclusions are based on η_{DMH}. The first test investigates the effect of spatial fluence distributions (see Tab. 3.3 and see section 3.4.3) and their influences on the general DMH-error. Furthermore, the test achieves first conclusions regarding the transformation quality of different models. The results are illustrated in Fig. 3.32 using a sta-

Table 3.4 : DMH-error distinguished by different fluence distributions: The table gives an overview with important statistical properties ($\mu_{1/2}$ =median, μ =mean, σ =standard deviation, σ^2 =variance) regarding η_{DMH} based on the box-plot visualization of Fig. 3.32. Every error distribution contains $3.24 \cdot 10^4$ samples.

Model	$\mu_{1/2}$	μ	σ	σ^2	max	min	dose distribution
bETM	1.491	0.171	0.099	0.010	0.802	0.017	*homogeneous fluence*
	1.482	0.174	0.110	0.012	0.909	0.021	*smooth unilateral gradient*
	1.311	0.150	0.086	0.007	0.667	0.018	*strong bilateral gradient*
pETM	1.519	0.173	0.095	0.009	0.723	0.015	*homogeneous fluence*
	1.418	0.168	0.102	0.010	0.796	0.023	*smooth unilateral gradient*
	1.247	0.146	0.087	0.008	0.624	0.018	*strong bilateral gradient*
EMCM	1.115	0.134	0.079	0.006	0.645	0.020	*homogeneous fluence*
	1.240	0.145	0.089	0.008	0.674	0.022	*smooth unilateral gradient*
	0.900	0.113	0.076	0.006	0.501	0.021	*strong bilateral gradient*
DIM	1.632	0.207	0.191	0.036	1.087	0.001	*homogeneous fluence*
	1.453	0.198	0.197	0.039	1.377	0.003	*smooth unilateral gradient*
	1.239	0.179	0.169	0.029	1.206	0.002	*strong bilateral gradient*
dDMM	0.789	0.103	0.091	0.008	0.581	0.002	*homogeneous fluence*
	0.809	0.109	0.098	0.010	0.698	0.003	*smooth unilateral gradient*
	0.711	0.094	0.082	0.007	0.634	0.003	*strong bilateral gradient*

tistical box-plot visualization of η_{DMH}. The data is separated (with varying gray values) by different fluence distributions, whereas single error distributions include samples of all voxel sizes and of all breathing phases.
(1) Differences caused by transformation models: The results of separate models describe significant differences. A view on Tab. 3.4 helps for concrete conclusions. dDMM achieved the best outcome for all statistical values. The median is at least 3 % −4 % better than the median of every other model. The same holds to the average and the upper quartile. A greater difference (4 % −8 %) exists even for the lower quartile and the minimum values compared to all energy models. Regarding η_{DMH}, the most accurate method in test one is the dDMM approach. Furthermore, there is a large error distribution observable for DIM in comparison to any other model. Theses error distributions contain good results for small voxel sizes and very inaccurate results for rough resolutions. Inside the group of the three energy models is the best outcome observable for EMCM. All statistical values (median, mean, all percentiles) are up to 2 % −3% better than the same properties for pETM or bETM. The variance for all three error distributions is similar. Furthermore, there is no significant difference between bETM and pETM. The maximum values of pETM are slightly compressed in contrast to bETM, but the results do not show a significant improvement.
(2) Differences caused by different fluence distributions: Dose transformations are not significantly influenced by certain inhomogeneous fluence distributions like smooth unilateral or strong bilateral fluence gradients. Indeed, there exist are small shift of the median and the average visible for all transformation models, but these effects can be explained with different total energy values and different total dose values respectively. The local energy displacement leads to those effects. Hence, the shifts can be neglected in further investigations. In contrast, the variances of the error distributions are very similar (see Tab. 3.4). The maximum variance deviation inside a model related group is 0.5 %, excepting one outlier in DIM. There are no pattern observable,

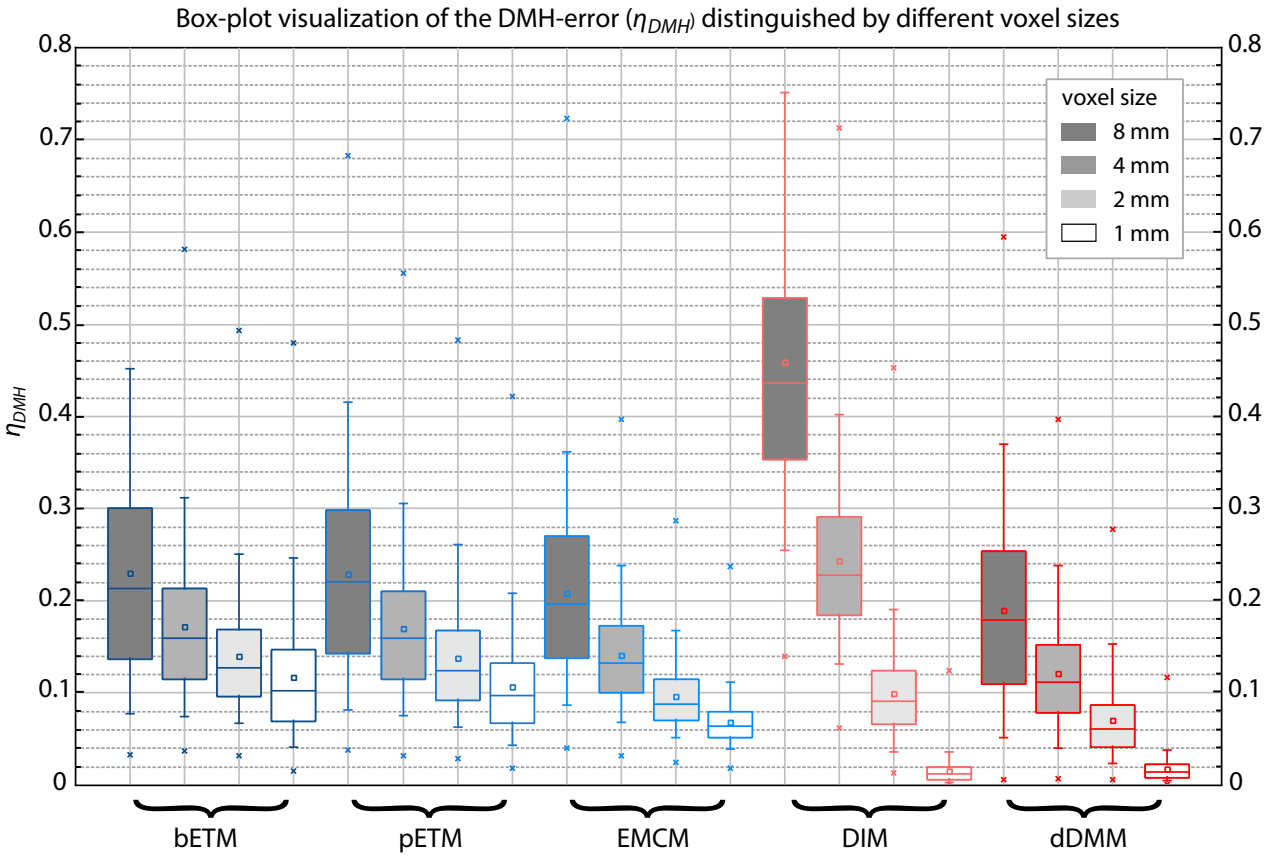

Figure 3.33 : DMH-error distinguished by different voxel sizes: The graph visualizes the box-plot of η_{DMH}. The results are separated by certain transformation models (ETM: blue; DMM: red). Several voxel sizes are marked by gray scale values. Each error distribution includes sample ROIs of all breathing phases (homogeneous fluence distribution) with a total of $8.1 \cdot 10^3$ samples.

which can be attributed to the different artificial fluence distributions.[27]

Test 2: Global DMH-error regarding different voxel sizes

The large variances of the results in test one require additional analysis. Quality limitation for dose transformations could lead to numerical or model specific inaccuracies. Hence, the analysis is performed with different voxel sizes. The results are illustrated in Fig. 3.33. Every model shows a continuous improvement for all statistical parameters (median, mean, percentiles, variance) with a decreasing voxel size, which is generally expected. Low resolutions ordinarily create a worse outcome due to numerical effects. However, the variance of large voxel sizes is particularly large for the DIM approach. While it achieves even the best results for 1 mm voxel size, the results scatter up to 80 % for other sizes. This confirms that DIM is rather unsuitable for practical applications.

Furthermore, dDMM achieves the best results for every voxel size (exception: 1 mm for DIM). The meaningful statistical properties (mean, median) are at least 5 % lower than any other result. The minimum percentiles acquire even better proceeds. All these facts confirm the accuracy of the dDMM approach. Also, the EMCM approach confirms a practical accuracy. However, the results are not as precise as the same for dDMM. A look on the results of the closely related energy models (bETM and pETM) illustrates that they look similar for low

[27] Since no significant effect is observable, all following tests (test 2 - test 7) discard the results of the inhomogeneous fluence distributions.

resolutions. They only change is noticeably for a voxel size of 1 mm. While the variance of the error does not change for bETM ($2mm \rightarrow 1$ mm), pETM reduces the variance significantly. This behavior could be explained with the basic idea of pETM (see section 3.3.2): while weak energy mass displacements play a subordinate role for low resolutions, they occur frequently often for high resolutions. This behavior is attenuated in pETM, but not as strong as intended. The general effect of the attenuation term in pETM could not be confirmed.

Test 3: Spatial dependencies of the DMH-error

Test one and particular test two describe central numerical effects. However, these experiments do not consider spatial dependencies within the deforming geometry. Maybe bad results in some sample groups only occur in certain regions of the geometry? Maybe these regions are negligible or particularly important for radiotherapy? Test three offers a solution. New sample groups are created for the purpose of error localization. A group is unified by a certain destination area inside the reference set. If a sample ROI is located inside the defined area after transformation, it will be considered in the defined group. The test distinguishes between four different areas (see Fig. 3.34). All areas represent different tissue properties. Main distinctive features depend on the density, the value of density deviations and the deformation gradient (∇v_{ij}) inside the ROI. Fig. 3.35 illustrates the results of the mentioned sample groups regarding η_{DMH} for a fixed voxel size of 2 mm. Unfortunately, special inferences regarding spatial dependencies are not verifiable with these results. However, it can be said that the results of test one and test two globally apply for all areas inside the patient geometry. Secondly, the graph confirms the mentioned statements. For all location areas, dDMM achieved the highest accuracy with at least 3 % better medians compared to every other model. Also the measurements for EMCM and DIM show practical precisions.

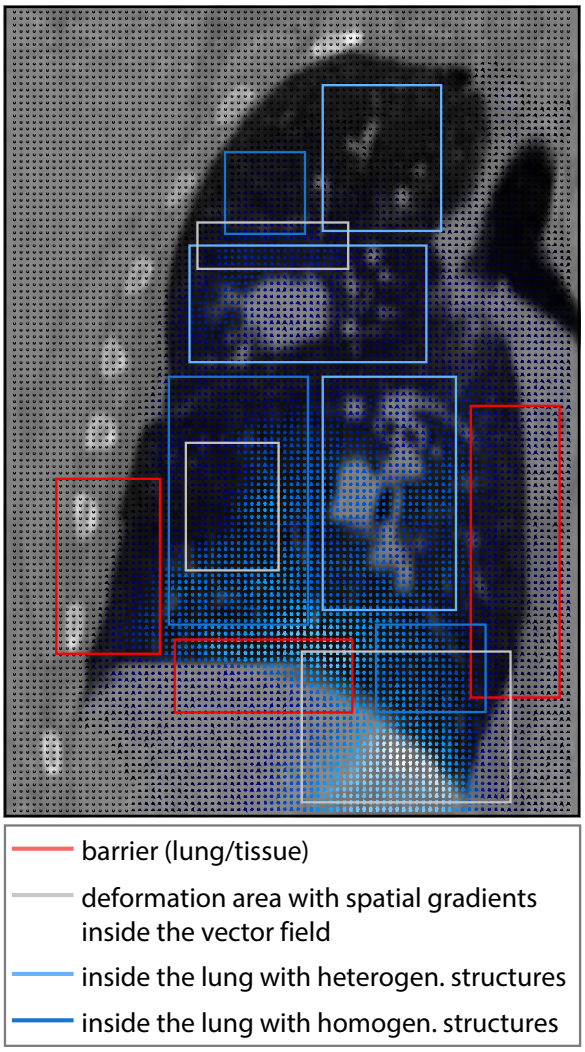

Figure 3.34 : Spatial dependencies: Different areas inside the patient geometry defined by certain regions. The areas regard to different tissue properties (legend).

Due to the high resolution, DIM is even better than pETM or bETM. Both achieve inaccurate error distributions with large variances. Furthermore, coarse outliers are observed. Noticeably observable for EMCM, DIM and dDMM are relatively inaccurate results for the group: *homogeneous lung tissue*, in comparison to other destination areas. However, this effect is may not a spatial dependence, it is based on the error value itself. Here, small errors are more effectual due to the normalization of η_{DMH} with the total ROI-based mass m. In comparison to other areas, the total mass is very low inside the group: *homogeneous lung tissue*. Hence, the absolute error is not necessarily larger. Furthermore, the group *deformation area* provides not even that worse results as expected. This leads to the conclusion that the deformation effect has a minor influence one the transformation accuracy. Finally, this test provides no conclusions about spatial dependencies.

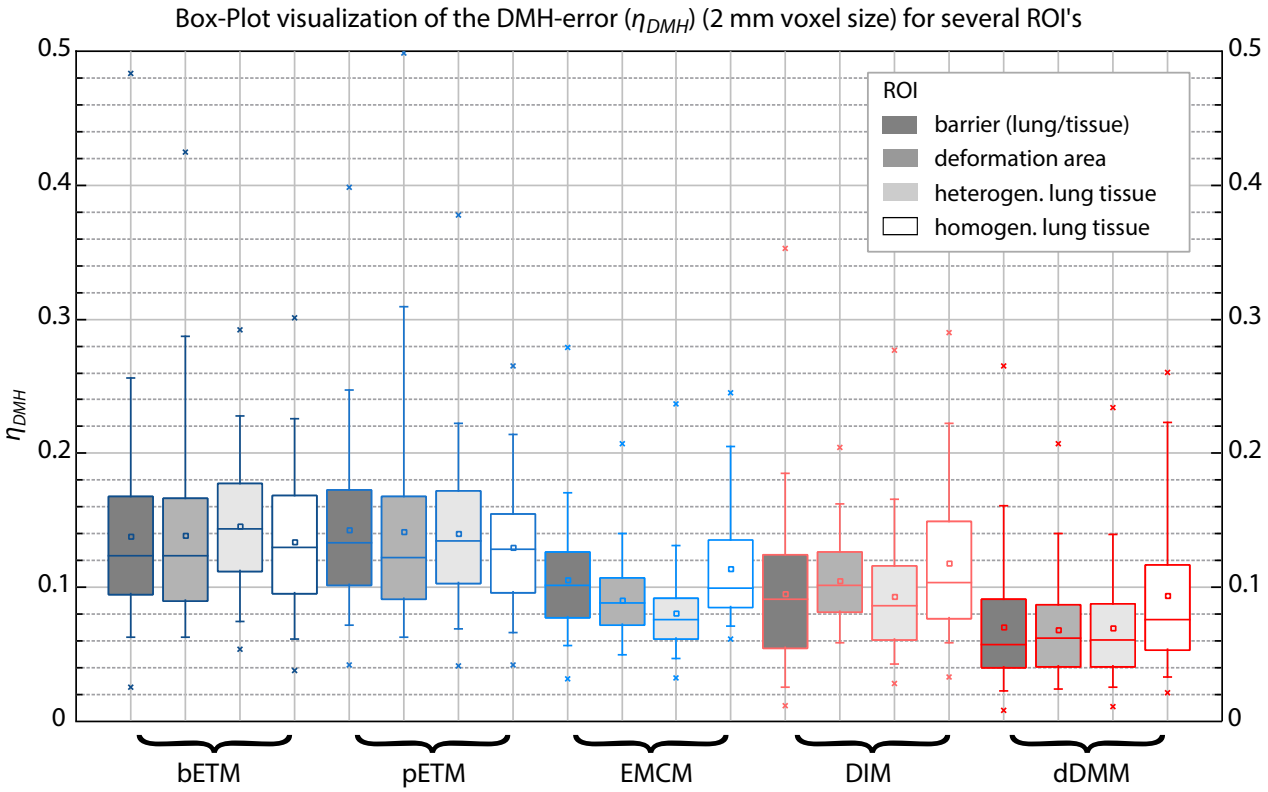

Figure 3.35 : DMH-error distinguished by different spatial locations: The spatial areas regard to the defined groups of Fig. 3.34. The groups are marked with different plot colorings (gray values, see legend above). The results are grouped by certain transformation models (ETM: blue; DMM: red). The results inside a single group include sample ROIs of all breathing phases and a fixed voxel size of 2 mm. The sample value of every group could differ due to different location area sizes.

Test 4: Spatial dependencies of the DMH-error with an error localization map

Since the results of test three were inconclusive regarding the spatial error behavior inside the patient geometry, test four illustrates a more detailed analysis. An error localization map (ELM)[28] provides the possibility to locate large errors without special area definitions. For this purpose the ROI itself is analyzed and not the global position. The main distinctive features (density, value of density deviations) serve as identification parameters. Therefore, ELM splits the properties into a mass index (abscissa) and a homogeneity index (ordinate). The mass index m is equivalent to the total mass inside the ROI and defined by the mass summation[29] of all voxels (l) x_i:

$$m = \sum_{x_i=1}^{l} m_i(x_i) \tag{3.84}$$

The homogeneity index is realized with the aid of the *Sobel* operator S [84]. This operator derives from the image analysis and realizes an edge detection kernel. The filter highlights every edge inside the image and reduces homogeneous areas. For a two dimensional image A applies the following filtered image G realized

[28] The ELM approach is introduced by this thesis. Hence, there exist no references with respect to the following contents.
[29] The HU/mass conversion regards to the methods of section 3.4.3 based on the paradigms of the XVMC framework

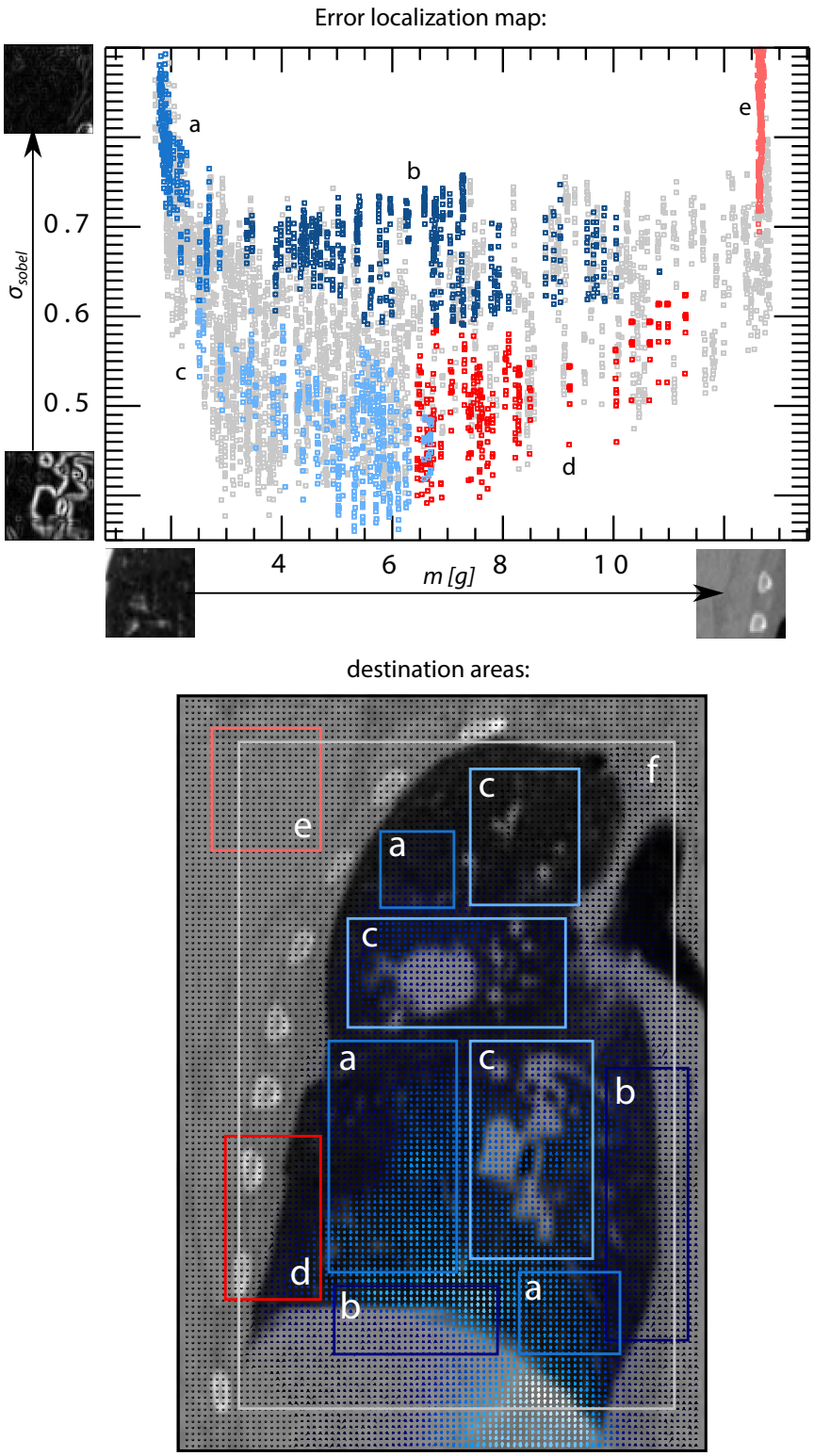

Figure 3.36 : Error localization map (ELM): The ELM (top) enables the location of a sample ROI inside the patient geometry (bottom) based on two properties (m, σ_{sobel}). Samples in the upper right area of the ELM are particularly homogeneous with a large mass (e.g. *e*). Contrary, samples in the lower left region have inhomogeneous, low mass properties (e.g. group c). The operation of ELM is verified by selective destination areas (below), which can be illustrated in the ELM as delineated point clouds due to their different properties.

with the filter kernels G_x, G_y:

$$G = \sqrt{G_x^2 + G_y^2}; \quad G_x = \begin{pmatrix} 1 & 0 & -1 \\ 2 & 0 & -2 \\ 1 & 0 & -1 \end{pmatrix} * A; \quad G_y = \begin{pmatrix} 1 & 2 & 1 \\ 0 & 0 & 0 \\ -1 & -2 & -1 \end{pmatrix} * A \tag{3.85}$$

To get a three dimensional parameter, the *Sobel* operator is applied to every (c-coronar, a-axial, s-sagital) sectional image of the ROI that intersects the center of the exposed region. The three resulting images G_i are edge enhanced pictures that have a density deviation emphasis. One can analyze the gray value (x) distribution $p(G, x)$ of the resulting images to get a good overview on the number of detected edges. That enables the definition of the full homogeneity index:

$$\sigma_{\text{sobel}} = \frac{1}{3} \cdot \sum_{i=c,a,s} \left(\frac{\int_{x_0}^{x_t} p(G_i, x)dx}{\int_{x_0}^{\infty} p(G_i, x)dx} \right) \tag{3.86}$$

where σ_{sobel} is the average of the gray value analyzes related to all three directions. The definition of the threshold parameter x_t is crucial. x_t is located in the lower quarter of the histogram $p(G, x)$. Hence, σ_{sobel} counts all pixels that are located in this dark area (normalized to the full value of possible gray scales). The calculation of a relatively small σ_{sobel} results from many pixel values that are located outside the lower quarter of $p(G, x)$, i.e. *Sobel* detects a lot of edges. This means that there are many density deviations inside the ROI. The contrary, maximum value is $\sigma_{\text{sobel}} = 1$, leading to a total homogenous ROI without density gaps. The full procedure is explained and validated in Fig. 3.36. The ELM shows the scatter of all possible samples (f) in relation to spatial dependend groups (a)-(e). The special groups (regarding special tissue properties) can be recognized as clear delineated point clouds inside the ELM. This confirms the operation of ELM.

This test analyzes the spatial distribution of the DMH-error for all sample ROIs. Therefore, the error is scattered using a color scaling to illustrate the strength. For a specific location, the maximum error is preferred. The results are shown in Fig. 3.37. A fixed voxel size (4 mm) is used for a better distinction of the data. The presumption of test three is consistent with the results of test four. ROIs with lower masses have higher error in the average score. All models show a significant shift of the error strength towards low masses distributed over the full homogeneity range. This is especially observable for DIM. However, this confirms the general assumptions, because the greatest error is located inside the lung. These areas are typically affected by the most displacement.

Furthermore, only bETM and pETM exhibit single outliers (orange/red maximum errors) localized in all areas of the map, even in regions with high masses. This is explainable by the error susceptibility of bETM due to the energy displacement (η_{MED}, see section 3.3.2) which is based on defective deformation grids, therefore, possible in all regions of the geometry. However, pETM could not solve this problem. Additionally, there are even small differences between bETM and pETM, but only pETM shows single outliers. This suggests, that both models use an inaccurate approach. Also in this test, dDMM achieves the best results with a widespread low error distribution (blue) in the ELM. Even EMCM yields good results, but mostly inside a higher error channel (green) as dDMM. Measurements of DIM confirm the resolution dependence with large errors for this rough voxel size (4 mm).

The ELM in Fig. 3.37 merely gives an overview of the maximum error. On the one hand, Fig. 3.35 has shown that a large number of samples is lower than the maximum error. Hence, one has to prove the location of the median and the lower quartile error inside the ELM. This serves for a realistic spatial dependency analysis of the full error distribution. Since a color scaled ELM is unsuitable to show the full error distributions, this test works with a single axis projection. The mass index and the homogeneity index are respectively applied to

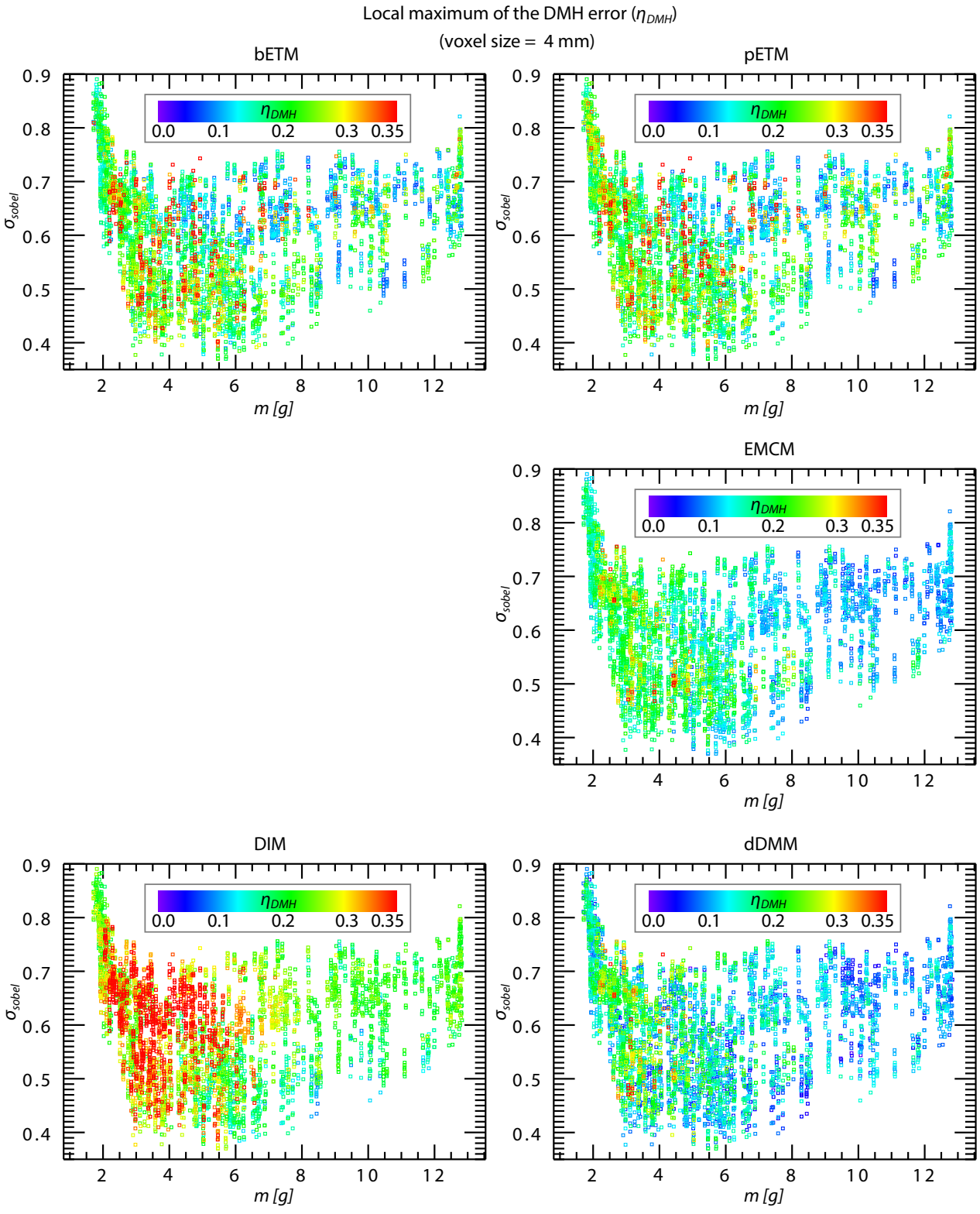

Figure 3.37 : The maximum DMH-error localized by the ELM: The results are separated with single graphs by certain transformation models. The graph describes always the local maximum of η_{DMH}. The data is color scaled to identify the strength of the maximum error. The results inside a graph include sample ROIs of all breathing phases and a fixed voxel size of 4 mm. Thus, every graph contains $8.1 \cdot 10^3$ samples.

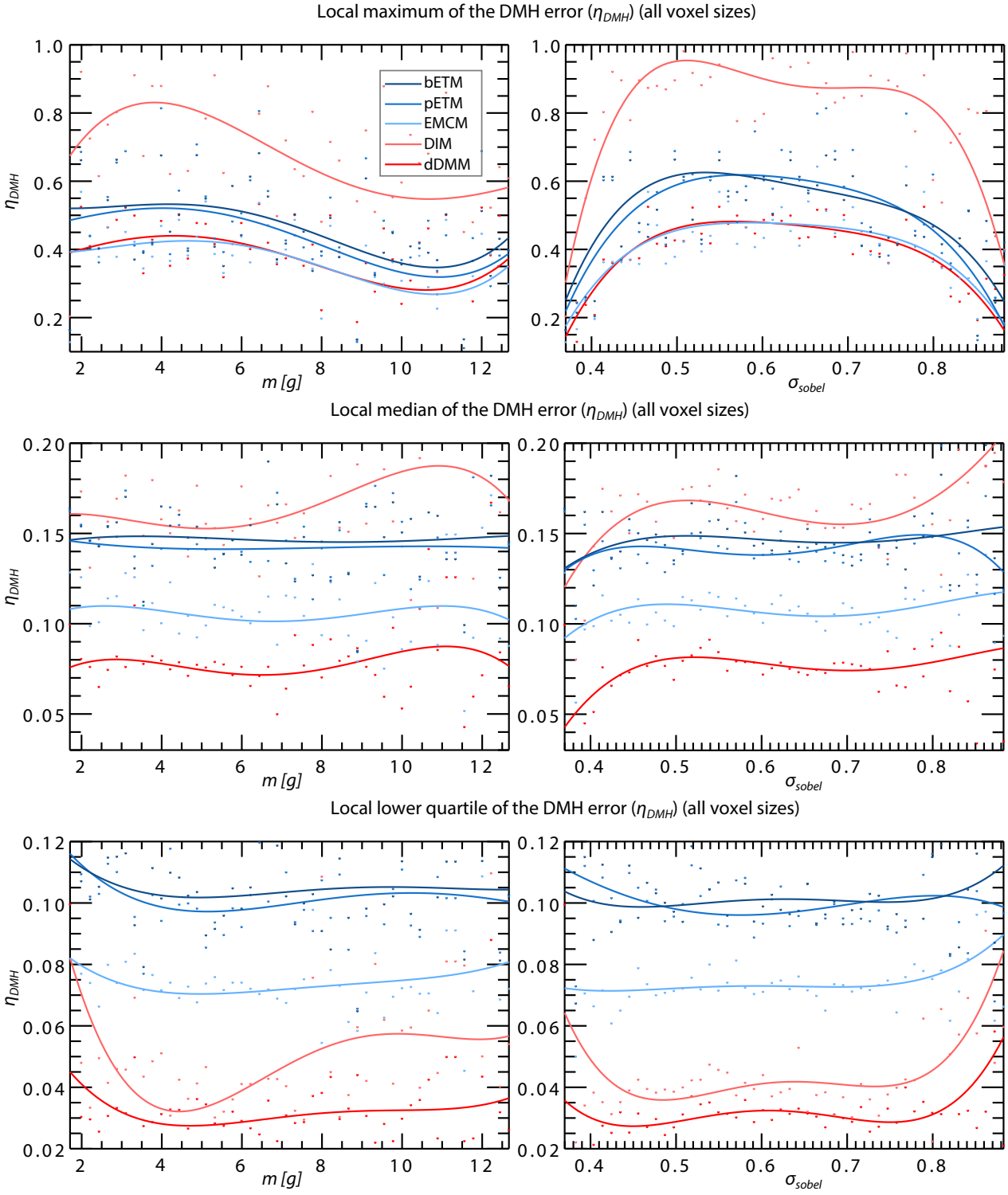

Figure 3.38 : The maximum, median and lower quartile DMH-error localized by the ELM: The ELM is splitted into single graphs regarding the mass index (left) and the homogeneity index (right). The results are grouped by certain transformation models (ETM: blue; DMM: red). The results inside a graph are based on the local scatter values and a fourth degree polynomial fit. A series uses sample ROIs of all breathing phases and all voxel sizes. Thus, every graph contains $32.4 \cdot 10^4$ samples.

their own graphs, whereas both serve as abscissa. The median, the lower quartile and the maximum of the DMH-error are scattered (ordinate value) in dependence of the respective mass or homogeneity index. For dependency analysis, the scattered data is fitted with a fourth degree polynomial function. Fig. 3.38 illustrates the results[30]. The first column of graphs (left) shows the mass dependency and the second column (right) describes the homogeneity influence. The procedure is performed for the maximum error (first row), median error (second row) and the lower quartile error (third row). It is clearly evident that the maximum error is larger for low mass regions, observable for all models. Secondly, the maximum error is shifted towards higher inhomogeneities. This is explainable by the maximum fits, which are all skewed to the left. However, the mentioned dependency is not observable for the median or the lower quartile. This means the true distribution points out a less strong spatial dependency in contrast to the maximum error. This is consistent to results of test three. Small fluctuations within the shape of the curves are explainable with the fitting approach. Further, this visualization confirms all previous conclusions again. dDMM yields the highest accuracy. Here, the differences between several models are even larger due to using samples of all voxel sizes. The median error of dDMM is about 4 % better then the same for any other model as well as the lower quartile. Again, the test confirms figuratively the power of dDMM.

Test 5: Global DMH-error regarding different breathing phases

This test is an investigation of mapping errors in relation to single breathing phases. The presumption is a large error for huge tissue movements, which is equivalent to a large breathing amplitude compared to the reference set. Fig. 3.39 illustrates the breathing selected results for η_{DMH} with the aid of a box-plot visualization. Every sample group is quite small (ca. 160 ROIs[31]), because the data derives from a fixed voxel size (2 mm) and the special destination area *homogeneous lung* (see Fig. 3.39) inside the geometry. There are only ROIs considered which are located in an area of homogeneous density inside the lung. The homogeneous area ensures only moving ROIs for testing. The supposed dependency in relation to the breathing amplitude is observable for bETM and pETM. The large displacement is associated with a large error. The maximum error for bETM is located at the maximal amplitude 60 %. Both models have a high deformation grid dependency. A large displacement leads to more defective grids in the vector field. This increases the probability of energy mass displacements (η_{MED}, see section 3.3.2). In contrast to bETM, pETM decreases the maximum values, but the overall outcome shows no improvement. EMCM, DIM and dDMM achieve constant error results for the full breathing cycle. They are resistant to large energy mass displacements. Indeed, there are small fluctuations visible for dDMM in the first third of the breathing cycle, but these results are may be explained by the small sample groups of this test. In summary, the test shows that dDMM is well suitable for dose transformation with median values up to 5 % better than EMCM or other solutions.

Test 6: Investigation of mean dose errors

Previous tests disclosed deficiencies of DIM, pETM and bETM, but the effect of energy mass displacement (η_{MED}, see section 3.3.2) was barely demonstrable. This could be explained with too small masses which were affected. Those fractions have a low influence on the DMH error due to the low mass weighting. In contrast, the fractions are normally processed with $\eta_{<D>}$. Hence, test six investigates such results with the aid of $\eta_{<D>}$. The findings are illustrated in Fig. 3.40 and distinguished by different voxel sizes.
The main effect is already apparent in the summarized view (all voxel sizes). The mean value of bETM is quite large. As intended, pETM decreases this value. The large mean error is caused by the great probability

[30] Scatter values are local unions. Hence, not all $32.4 \cdot 10^4$ samples are plotted.
[31] The exact value of considered ROIs may vary little with different breathing phases. Due to the deformation of the geometry, not exactly the same number of samples transforms to defined destination area *homogeneous lung*.

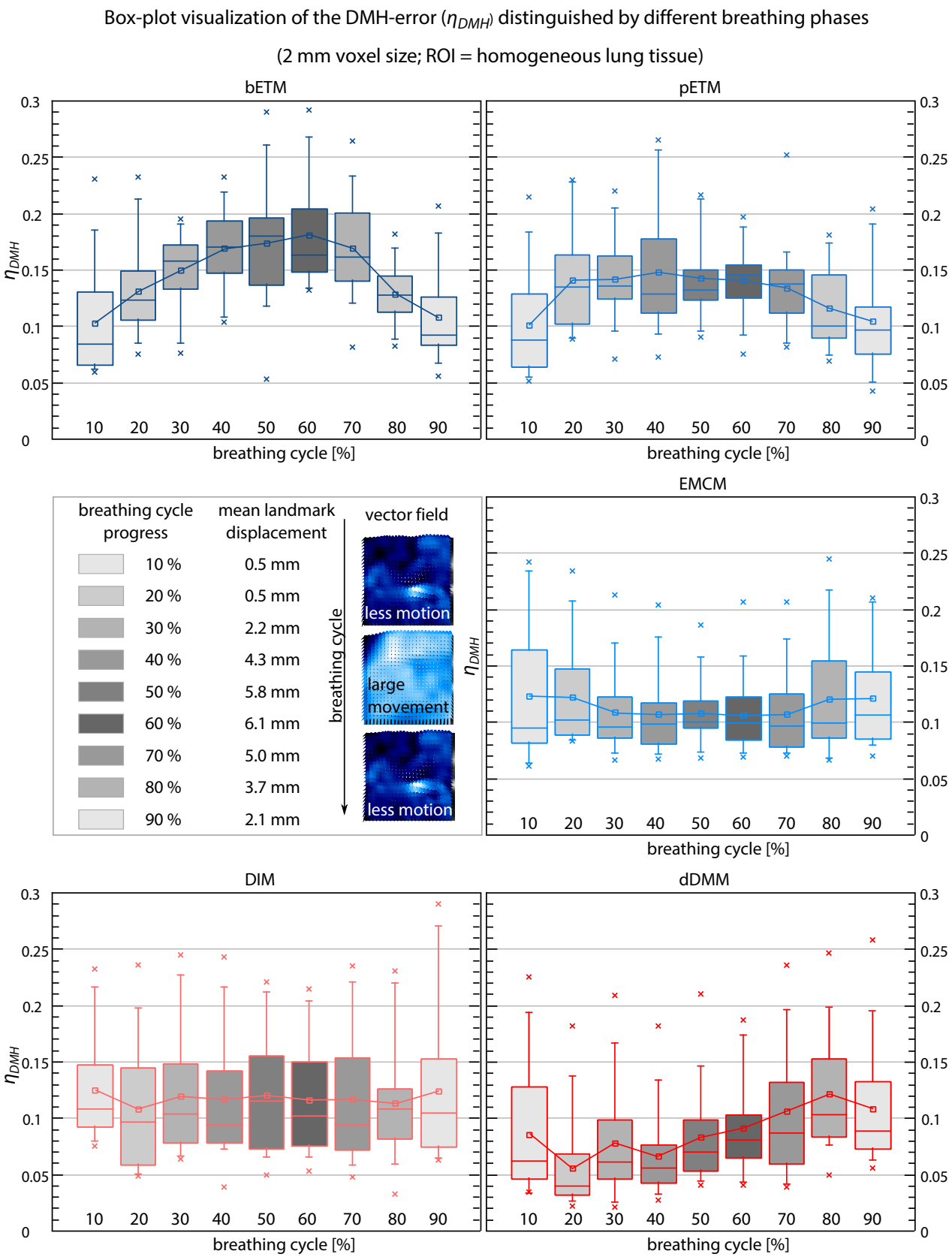

Figure 3.39 : DMH-error distinguished by different breathing phases: The graph visualizes the box-plot of η_{DMH}. The results are grouped by certain transformation models (ETM: blue; DMM: red). The breathing phases are marked with different gray scale values. The strength of the mean displacement is proportional to the darkness of the plot (legend in the middle). The results inside a single error distribution include sample ROIs of a fixed breathing phase, a fixed voxel size and a special destination area (*homogeneous lung*). Thus, every distribution contains about only 160 samples.

Box-plot visualization of the mean-dose-error ($\eta_{<D>}$) distinguished by different voxel sizes

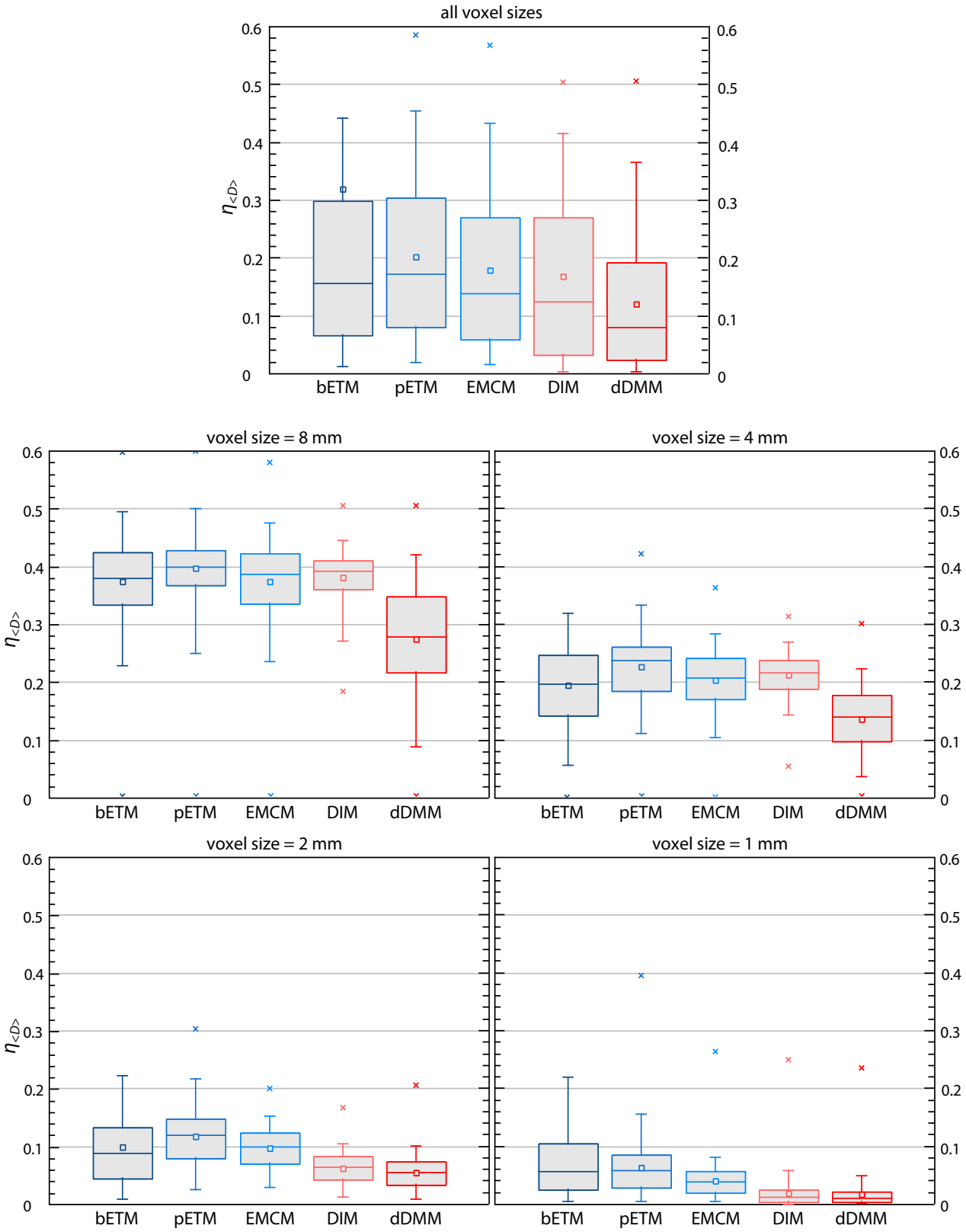

Figure 3.40 : Mean dose error regarding different voxel sizes: The graphs visualize the box-plot of $\eta_{<D>}$. The results are grouped by certain transformation models (DMM: red, ETM: blue). Several voxel sizes are distinguished by different plots. The results of each error distribution include sample ROIs of all breathing phases. The summarized group contains $24 \cdot 10^4$ samples and the voxel size groups contain $8.1 \cdot 10^3$ samples for each mapping model.

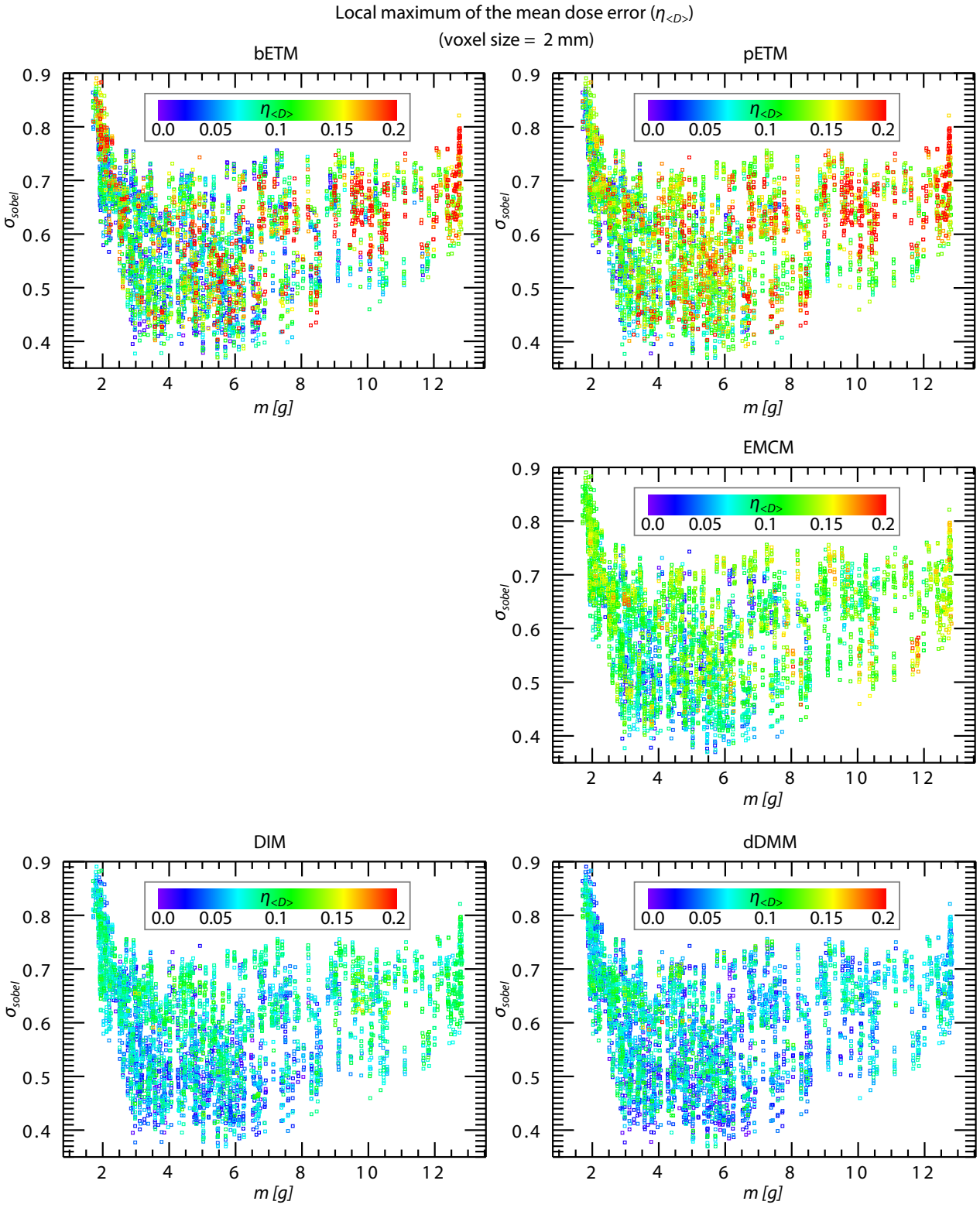

Figure 3.41 : The mean dose error distinguished by ELM: The results are separated with single graphs by certain transformation models. The graph describes the local maximum of $\eta_{<D>}$. The data is color scaled to identify the strength of the maximum error. The results inside a graph include sample ROIs of all breathing phases and a fixed voxel size of 2 mm. Thus, every graph contains $8.1 \cdot 10^3$ samples.

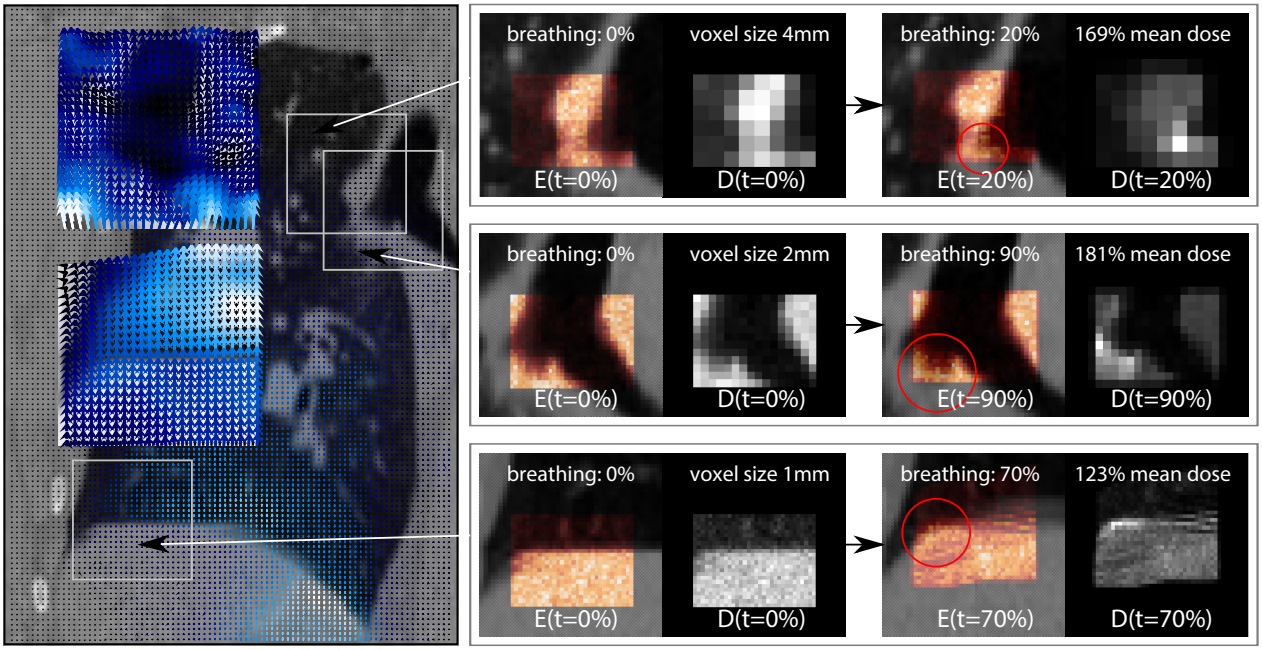

Figure 3.42 : Examples for energy mass displacements: bETM leads to large dose errors due to defective deformation grids. This could be confirmed with three examples for different voxel sizes, which transform selective doses from $t = 0$ % to different target geometries. An energy displacement from high masses (in the source) to low values (red circle in the target) results in extreme dose peaks after dose transformation. The auto-scaling of the grey dose distributions (before and after transformation) represents the effect.

for energy mass displacements with a high voxel resolution (2 mm, 1 mm). The maximum values are also larger for bETM in comparison to any other model (not visible in Fig. 3.32). The test confirms the main intention of pETM, because it compensates all outliers and maximum values of bETM dictated by energy mass displacements. However, why does pETM lead to bad results in the field of DMH error investigations? While maximum values are attenuated, low error values are deteriorated. This is observable for the lower quartile, the median, the variances such as the upper quartile for all voxel sizes. The effect is also visible in the ELM (see Fig. 3.41). Contrary to bETM, pETM leads to a smaller number of maximum values (red scatter values), but low error samples often occur in a higher error channel (bETM → large value of blue channels; pETM → large value of green channels). This suggests the conclusion that pETM merely works in the scenario when strong energy mass displacements occurs. Otherwise, in case of common transformation, pETM has deficiencies. The energy weighting leads to a change in the statistical number of events and this causes a change of the dose. For explanation, the effect of energy mass displacement is illustrated in Fig. 3.42 with the aid of three transformation examples. The figure describes how energy mass displacements appear. Single dose peaks often occur point wise at strong mass gradients. A strong dose overestimation arises, if the mass is much heavier in the source voxel in comparison to the target voxel.

Test six reveals the same global conclusion as all previous tests. dDMM yields the best results for all voxel sizes (about 5 % better median for the summarized view). This is also visible in the ELM of Fig. 3.41. A large number of maximum values is located in the low error channel (blue). A spatial dependency is not visible for all models. As expected, numerical effects are associated with lower resolutions. However, there is a reordering in the model related sequence of quality. For example, many samples of bETM achieve better results than the same for EMCM. Because of this, test six should not be used for general assessment. It mainly serves for investigation of energy mass displacements.

Test 7: Investigation of energy rearrangement

The approach to measure the energy rearrangement (see section 3.4.2) is the base of test seven. The resulting data is illustrated in Fig. 3.43. Again, the findings are distinguished by different voxel sizes. The results show an interesting effect. For low resolutions (8 mm, 4 mm), dDMM achieves the best results, which is not associated with the expectations. Since the I_E method is a inverse calculation of EMCM, better results for all energy models at low resolutions were expected. This inverse calculation of the error value is also the reason for very good results of all energy models (bETM, pETM, EMCM) for high resolutions. This should not be overrated. Moreover, the energy rearrangement is a numerical effect and it occurs primarily for low resolutions. With the aid of these results, we can demonstrate the minor effect of energy rearrangement. In contrast to extensive expectations and proposals [93, 32], it has not a large influence on DMM. Furthermore, energy models do not achieve better results in this test. The problem shows no real influence. Anyway, the DMH-error is much more significant. Hence, the importance of this problem can be reduced.
The results describe common numerical dependencies for all models. Obviously, at 1 mm voxel size, EMCM performs the inverse calculation of the error value which leads to a perfect result. Furthermore, the energy rearrangement shows a significant spatial dependency. Large errors occur often for low masses and high inhomogeneities. This confirms the ELM of I_E in Fig. 3.43 for a fixed voxel size of 2 mm. This strong spatial dependency is explainable with large tissue movements. They occur often inside the lung (e.g. *homogeneous lung*, see Fig. 3.36) due to the breathing motion. Since energy rearrangement depends on strong acting vector fields, a large number of small errors appear exactly in the mentioned region.

3.5 Discussion

Chapter 3 explains the basic procedure of 4D dose accumulation. The applications numerical strategy (section 3.1.3) discloses a major problem, because the deformation effect (sec. 3.1.2) is significant during calculation. The most important goal associated with dose transformation is the numerical unification of inhomogeneous dose distributions. This is exactly explained by section 3.1. A solution for numerical dose unification is offered by the mass weighted dose average derived from the basic dose definition for inhomogeneous irradiated objects in formula (3.8). The assumption is a good approximation to describe an inhomogeneous object dose in the context of numerical dose transformations. The suitability of the mentioned approach is confirmed by theoretical and biological considerations using the dose response analysis in section 3.2.
There exist different models that realize the considerations of the discrete dose definition for IIOs (3.8) more or less for numerical dose transformations (section 3.3.1 and 3.3.2). DIM is pursuing a rather unsuitable approach. The energy models (bETM, pETM, EMCM) fulfill the requirements in an indirect way due to dissection of the dose in masses and energy shares. This leads to undesirable effects. Additionally, it needs a high technical effort. This thesis introduces the new method dDMM that directly implements the dose definition for IIOs, almost without numerical restrictions due to the high resolution of the sub-voxel grid. The theoretical considerations are confirmed by empiric tests. The most meaningful assessment parameter for dose transformation is the DMH-error η_{DMH} (section 3.4.1). In all tests dDMM yields best results in comparison to any other model (see Fig. 3.32 - Fig. 3.39). Here, the error values are typically 3 % −5 % better than the findings of the energy models. The problems of DIM are disclosed by the measurements for low voxel resolutions with negative values up to 100 %. A practical use of DIM is only recommended for high resolutions (1 mm voxel size), but this is very restrictive.
bETM's susceptibility to errors based on energy mass displacements (section 3.3.2), is especially visible for tests with the mean dose value $\eta_{<D>}$ (section 3.4.2). pETM solves this dose peak problem. However, most of the other sample regions are not better or even worse. Generally, pETM does not improve bETM. Both

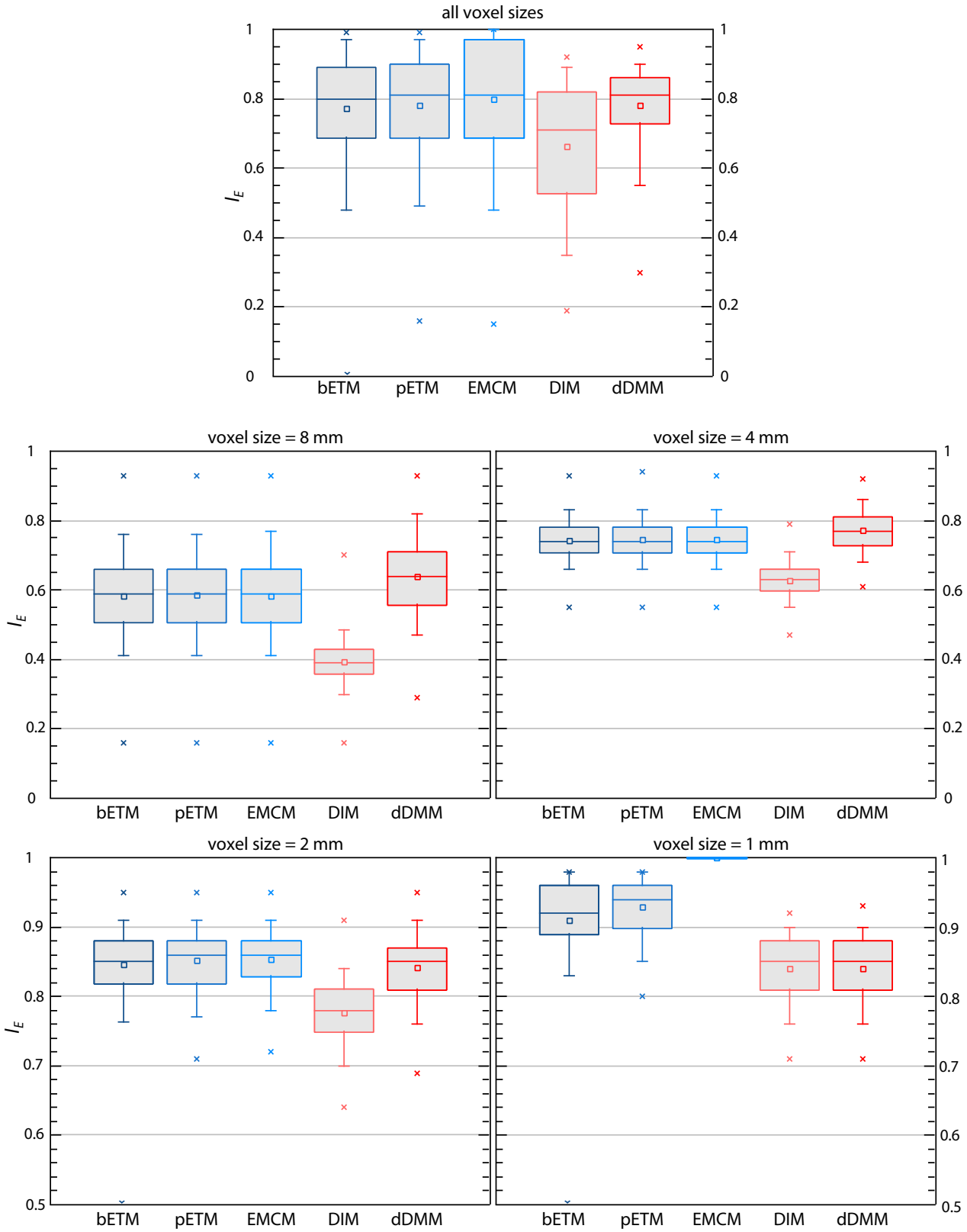

Figure 3.43 : Mutual information error regarding different voxel sizes: The graphs visualize the box-plot of I_E. The results are grouped by certain transformation models (ETM: blue; DMM: red). The several voxel sizes are distinguished by different plots. The results inside a single group include sample ROIs of all breathing phases. Thus, the summarized group contains $32.4 \cdot 10^4$ samples and the voxel size groups contain $8.1 \cdot 10^3$ samples.

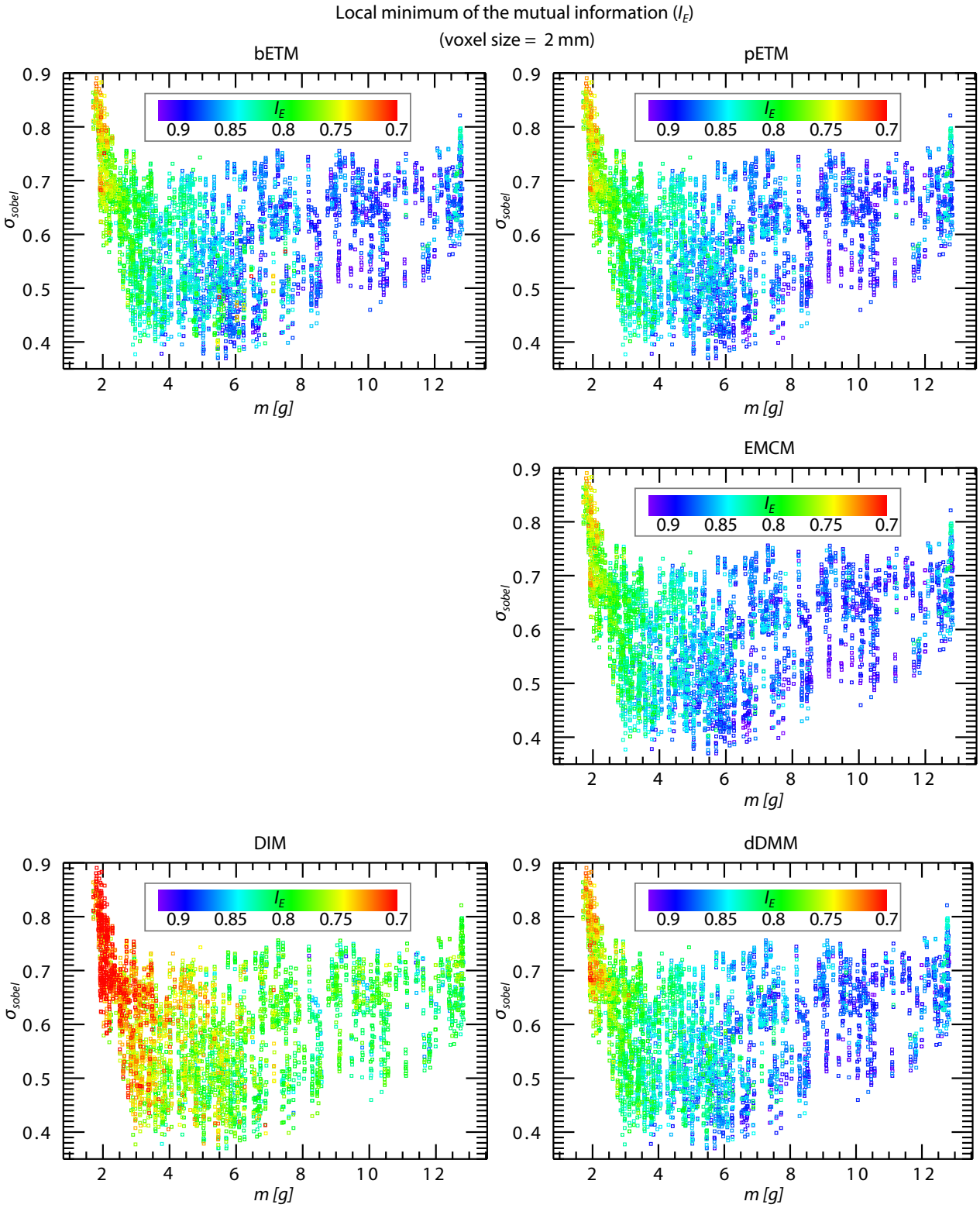

Figure 3.44 : The mutual information error distinguished by ELM: The results are separated with single graphs by certain transformation models. The graph describes always the local maximum of I_E. The data is color scaled (see legend) to identify the strength of the maximum error. The results inside a graph include sample ROIs of all breathing phases and a fixed voxel size of 2 mm. Thus, every group contains $8.1 \cdot 10^3$ samples.

models (bETM, pETM) are rather unsuitable for practical use. Beside dDMM, only EMCM presents very practical findings. However, the clinical application gets complicated due to the complex implementation strategies. Furthermore, the practicality of any energy model should be carefully analyzed. The tests of this study were performed with a simplified dose algorithm that realizes coordinate based energy deposition points (section 3.4.3). For example, a full Monte Carlo algorithm typically performs primary energy depositions along discrete path lengths. This discrepancy and a reduction of path lengths to single coordinates, which are needed for ETM, could cause additional errors. These influences are not considered yet and have to be investigated in further studies.

This study presented several tests to investigate the capabilities of certain dose transformation models for dose accumulations based on different breathing phases for lung cancer patients. DIM and pETM implement a rather unsuitable approach for practical implementations. bETM is prone to errors especially for energy mass displacements on high voxel resolutions with heterogeneous mass distributions. In contrast, dDMM as well as EMCM are best suited for practical applications. Their algorithm structure is consistent with the dose definition (3.10) and empirical tests (η_{DMH}, $\eta_{<D>}$, I_E) confirmed its practicality. EMCM is associated with a high technical effort, while dDMM is more straightforward and also more efficient.

4 Evaluation of the 4D treatment planning concepts

The 4D dose planning approach is associated with two major topics, the elastic image fusion and the 4D dose accumulation. The quality of a sufficient 4D planning approach directly depends on the accuracy of the mentioned applications. For this purposes, chapter 2 and chapter 3 gave a detailed description for their implementations with an comprehensive risk analysis. So far, 4D dose accumulation as well as the preceding elastic image fusion were analyzed individually. For example, the quality of image fusion is measured by mathematical landmarks, the accuracy of dose transformation is proven by physical error values based on the dose mass histogram, the mean dose and the energy rearrangement. These evaluations are very important to ensure the precision of the used algorithms. However, a clinical assessment study under consideration of a full 4D treatment plan is missing. The following chapter closes this gap. The aim is a verification of the explained algorithms with regard to important clinical criteria. This chapter describes the full integration of elastic image fusion and 4D dose accumulation into a software framework that is able to generate an entire 4D dose calculation. The integration is based on the findings of the chapters 2 and 3. The following evaluation study describes the clinical point of view, i.e. the clinical analysis of the 4D dose distributions for the tumor or the OARs quantified by the DVH. The final aim of this study is the comparison of the developed 4D planning approach with established static strategies of clinical practice to evaluate the benefit of the new 4D model. Therefore, different treatment modalities are used.

4.1 4D treatment planning

The treatment planning includes the entire 4D approach considering the elastic image fusion, the dose accumulation, the dose delivery process and a defined treatment modality for dose application. All aspects are important to complete a 4D treatment plan. The 4D planning module describes the software framework that realizes the mentioned algorithms for simulation. The treatment modalities regard to clinical and technical aspects. In context to the progress of the dose delivering machines, clinical studies and established strategies, different treatment modalities were developed for lung SBRT. This could be a static beam, a dynamic tumor tracking machine or a tumor gating system as well as intensity modulated beams or arcs. In principle, the integration of all modalities into the 4D treatment planning is feasible, because all deliver dose on a deforming patient geometry. However, the use of complex modalities accompanied with the 4D approach is considerably more difficult.

4.1.1 A software prototype for 4D dose delivery

The used software planning module for 4D dose delivery is a special prototype of the *iPlan™ RT* (*Brainlab AG*) framework. The prototype for 4D planning was developed as a part of this thesis.[1] The software package is used

[1] The prototype was developed by the author using the programming language C++ and using the software framework of *iPlan™ RT*.

for all studies of this chapter. The planning module includes all technical features that are already integrated in the commercial treatment planning system (e.g. different dose algorithms, visualization tools, features for plan evaluation). Based on the findings of this thesis, this prototype contains a set of extensions that enable a sufficient 4D treatment plan in comparison to the pure *iPlan™ RT* system. The most important changes are explained in the following outline.

Four dimensional Tissue-Model (4DTM)

In Brainlab's *iPlan™ RT Dose* the tissue model (TM) is a software construct, which forms the basis for every dose calculation. The TM allows access to the full 3D patient geometry with the density values respectively the HU-values. Furthermore, the software construct provides many methods and functions for dose calculations and other operations. However, the actual TM is a static three dimensional construct. Indeed, the software framework is already able to load full 4DCT patient data, but the TM is static and inherits even one defined 3D geometry. Generally, the dose calculation process has merely access to one static geometry. The four dimensional TM (4DTM) of this thesis extends the basic TM with all breathing phase geometries of the 4DCT. Thus, every dose calculation is performable on a specific data set of the breathing cycle. At any time, access to time dependent 4D geometry data (HU) with all accompanied functions is possible. To ensure the procedure of the basic 4D planning approach, one data set must be defined as reference set for dose accumulation. The 4DTM work flow is illustrated in Fig. 4.1. The TM may be combined with different dose algorithms (MC, PB), but with respect to this work and the large density deviations inside thorax geometries, only MC calculations are considered with dose-to-medium for further evaluations. The prototype uses the XVMC framework of *Fippel et al.* [21] for dose calculations.

4D dose delivery

The easiest way to define a conventional static treatment plan is use of particular static beams. These beams are also a software construct that receive a number of properties, which determine the treatment. For example, the isocenter coordinate, the shape of the multileaf collimator (MLC), the beam angle and the number of monitor units define the final dose delivery. The 4D prototype divides a static beams into sub-beams. Hence, the creation a 4D beam generates a whole set of time dependent static sub-beams which cover the full breathing cycle, because every sub-beam is assigned to a single breathing phase geometry of the 4DTM. Furthermore, every sub-beam receives its own properties (beam angle, monitor units) for the treatment definition. This enables a dynamic dose delivery like tumor tracking (see section 4.1.2), which apply time varying doses during breathing. Every time slice creates an own dose distribution based on a specific geometry with a particular sub-beam. The process is illustrated in Fig. 4.1. The disadvantage of the concept is the large number of static sub-beams. For example, if three different 4D beams were created in the reference set, the software automatically creates a series of three different sub-beams for every breathing geometry. On top of that, the concept needs a large number of monitor units per 4D beam, because the value has to be divided on all sub-beams of the respiratory cycle. Small dose fractions with a low value of monitor units are also difficult to implement. However, lung SBRT, which is the field of application, follows the approach of high doses accompanied with a low value of fractions, i.e. a large value of monitor units per treatment. Furthermore, the 4D prototype has not yet the functionality of temporal synchronization between dose delivery time and breathing time. Therefore, the full requirements for IMRT or arcs are not yet met. Indeed it is possible to adjust the monitor units of single time dependent sub-beams, but a real intensity modulation requires an advanced time synchronization, which could be a goal for future prototypes. However, this software fulfills a first major aim, the full simulation of dynamic tumor tracking or the simulation of static free breathing techniques.

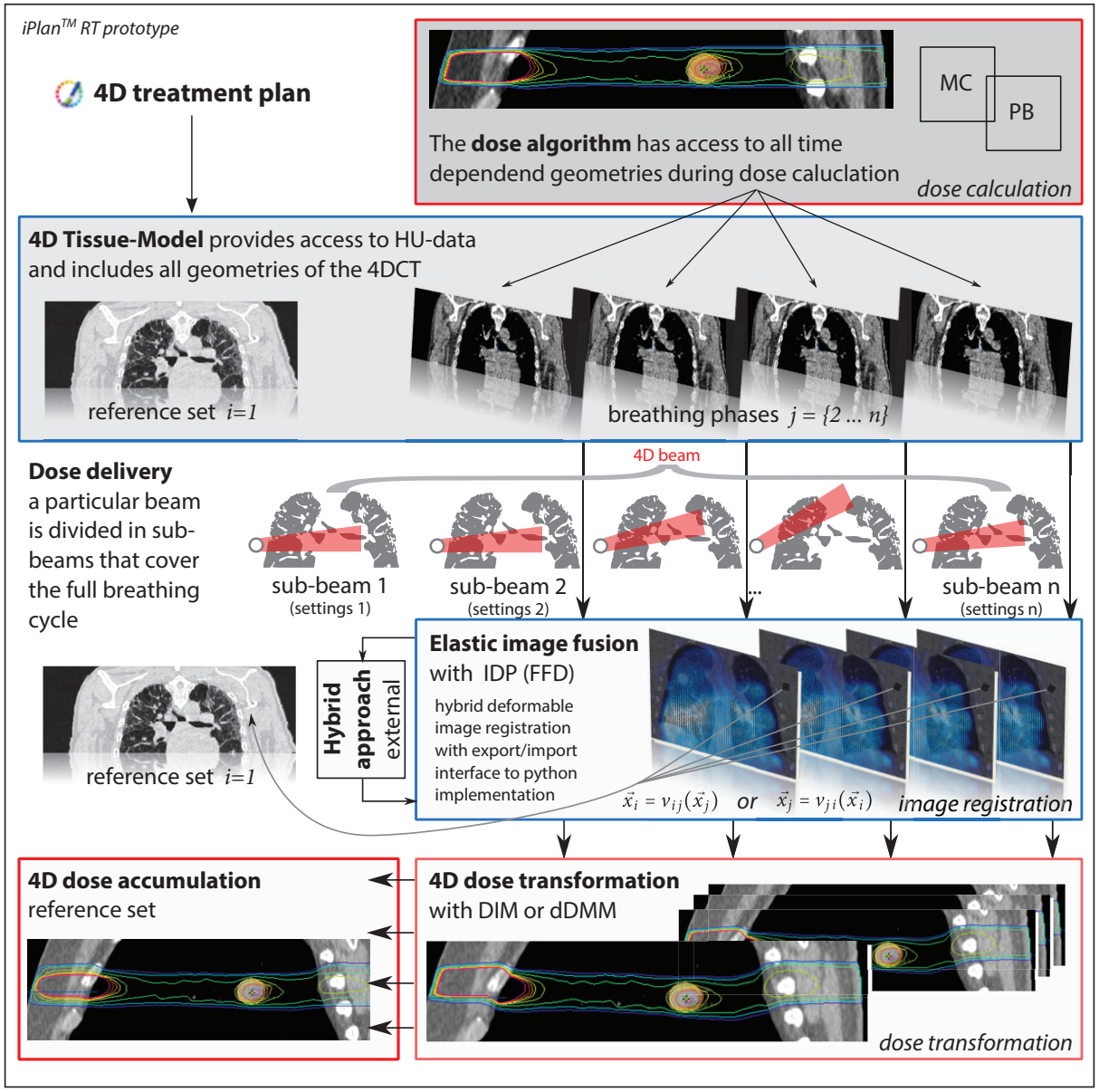

Figure 4.1 : Software prototype for 4D dose planning: The figure illustrates the schematic work flow inside the 4D *iPlan™ RT Dose* prototype of this thesis. The 4DTM provides all CT data, which are used by single beams for dose delivery. The dose calculation is performed separately. Finally, dose accumulation is based on the dose transformation accompanied with the elastic image fusion. The prototype is able to calculate accurate inverse vector fields based on the Newton-Raphson approximation.

Elastic image fusion

The concepts of elastic image fusion are explained in chapter 2. The 4DTM generates an image fusion vector field $v_{ij}(\vec{x}_j)$ for every breathing geometry j to connect coordinates $\vec{x}_j$ to the reference set i. The used algorithm for IDP image fusion is based on *iPlan™ RT Dose*. The method is described with all parameter settings in section 2.2.1. The algorithm regards to the FFD registration based on *Rueckert et al.* [81]. The software package is able to perform the new hybrid approach (section 2.2.3) based on IDP and PEM. For this purpose, the pro-

totype includes an interface that links to a python software package[2], which enables the physical deformation simulation of PEM. The resulting vector field is re-importable to the prototype. The software prototype is able to calculate an accurate inverse vector field based on a Newton-Raphson approximation [109], which is part of the *iPlan™ RT Dose* framework. The inverse vector field is necessary for different dose mapping models. A test measurement with the prototype revealed mean deviations between the original and the inverse vector field of 0.003 mm and an maximum deviation of 0.31 mm. This is acceptable, momentous effects of the inverse vector field can be neglected. The image fusion process within the prototype is explained by Fig. 4.1.

4D dose transformation and accumulation

Chapter 3 evaluates different dose transformation algorithms. The study revealed the highest accuracy for the dDMM method. All energy transfer models did not achieve similar results, even not the precise EMCM approach. Due to the minor improvement and the large technical effort of all ETM methods, this software prototype waives the implementation of any ETM approach. During dose accumulation, the software allows dose transformation either with the fast DIM approach or with the accurate dDMM model. The dDMM implementation uses a sub-voxel resolution of $3\times3\times3$ sub-voxels per voxel. Dose accumulation is performable with dose distribution weighting based on formula (3.2) and the PDF function described in section 3.2. Hence, the accumulation module takes the dwelling time of every breathing phase into account.

4.1.2 Design of 4D treatment modalities

As already mentioned, the 4D dose planning approach does not depend on the final treatment modality. However, the treatment modality completes the 4D treatment plan. Hence, a modality must be defined for every treatment. The approaches of established modalities for dose application depend on the clinical experience, the clinical infrastructure in the respective institute and on the existing technical solutions. For example, dynamic tumor tracking needs a dose delivering machine that is able to follow the target. Additionally, a lot of other technical solutions also are needed, e.g. tumor targeting methods of image guided radiotherapy (IGRT). Various treatment concepts considering the 4DCT as planning base have been reported recently [117]. The following outline presents three elementary treatment modalities for lung SBRT based on 4DCT with respect to clinical evaluation. It must be noted that complex intensity modulated treatment modalities (IMRT, dynamic arcs) are not considered for this evaluation due to the advanced software requirements on time synchronization (see *4D dose delivery*).

Concept of the internal target volume

The concept of the internal target volume (ITV) is based on a static beam associated with free breathing [43, 122, 2, 101, 95, 117, 11, 74, 29, 112, 28, 38, 17]. It is a widely used concept for lung cancer treatments, because of its low technical requirements. It uses conventional rules for treatment planning. The respiration-induced tumor motion is compensated through the definition of the target volume. Hence, this approach takes the tumor motion as uncertainty during object and target definition into account. For this, the target volume concept of radiotherapy must be clarified. The ITV-concept used by this thesis is based on the proposals of *Admiraal et al.* [2]. Generally, static treatment planning considers three different target volumes for plan assessment [14]. The basic volume describes the macroscopic position and the extent of the primary tumor. It is known as the gross tumor volume (GTV). The second volume, so called clinical target volume (CTV), surrounds the GTV considering a microscopic spread of tumor cells that are not visible in the image modality.

[2] The python software for PEM simulation is also part of this thesis. All hybrid approach simulations (IDP+PEM) of this work are based on this software.

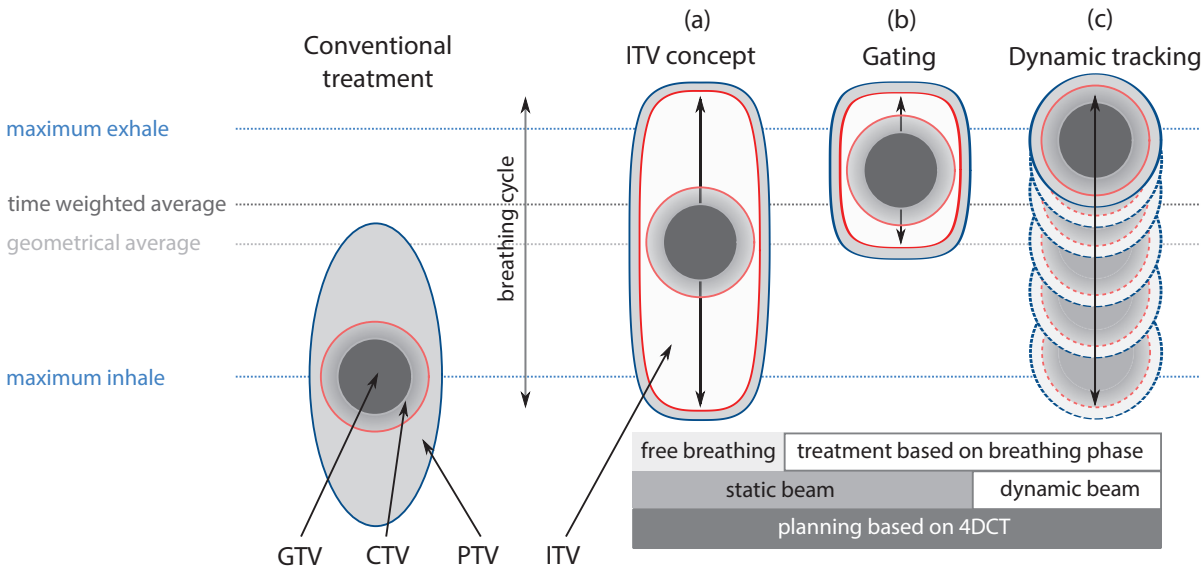

Figure 4.2 : Design of 4D treatment planning target volumes: The figure illustrates three concepts for 4D treatment planning. The sketch on the left explains the basic target volume for conventional radiotherapy. The right outlines possible treatment modalities for lung SBRT based on 4DCT data. (a) The ITV concept is intended for static treatments with free breathing. The tumor motion is considered within the ITV. (b) The gating technique reduces ITV margins based on the motion uncertainty reduction. The model assumes a static beam that delivers dose merely for a specific tumor position within a defined time frame of the breathing cycle. (c) Tumor tracking delivers dynamic doses on dynamic patient geometries. The system is able to track the delivering beam in relation to the tumor position with respect to requirements of real-time systems. All methods (a)-(c) are applicable with static planning approaches as well as with the 4D treatment planning concepts of this work. However, the 4D approach is always more precise. The figure is inspired by *Wolthaus et al.* [117].

The definition of both enables the determination of the planning target volume (PTV). The PTV considers uncertainties of dose planning and delivering. Normal tissue is assumed in the vicinity of the CTV. The aim of the PTV is to ensure an adequate treatment of the CTV. It is a geometrical concept. For treatment planning based on 4DCT, the conventional concept is extended by the ITV [28, 117, 89]. The ITV encompasses all CTVs of the single breathing phases. It is the unification of all time dependent CTVs to ensure the coverage of the full tumor movement during the breathing cycle. Hence, the ITV is also a geometrical concept that considers uncertainties of tumor movement.[3] Fig. 4.2.a illustrates the ITV concept.

The basic ITV concept is intended for a static dose planning. This could be a static beam that consequently delivers the PTV considering the total breathing induced ITV. Hence, the concept does not need a 4D dose calculation. Additionally, the concept does not need any dynamic treatment machine. As a result, it is much more important to achieve an accurate ITV that ensures the full coverage of the moving target. Different methods are established to define the ITV. The determination is based on the 4DCT considering all static CT data sets. The most trivial method is definition of the CTV_j for each breathing phase $j = \{1 \ldots n\}$ of the 4DTC [102]. The resulting $ITV_{\text{all phases}}$ is the geometrical unification of them:

$$ITV_{\text{all phases}} = \bigcup_{j=1}^{n} CTV_j \tag{4.1}$$

The mentioned model is very time consuming related to treatment planning. Usually, an equal outcome is

[3] In clinical practice, different margin definitions are established for ITV and PTV determination [117].

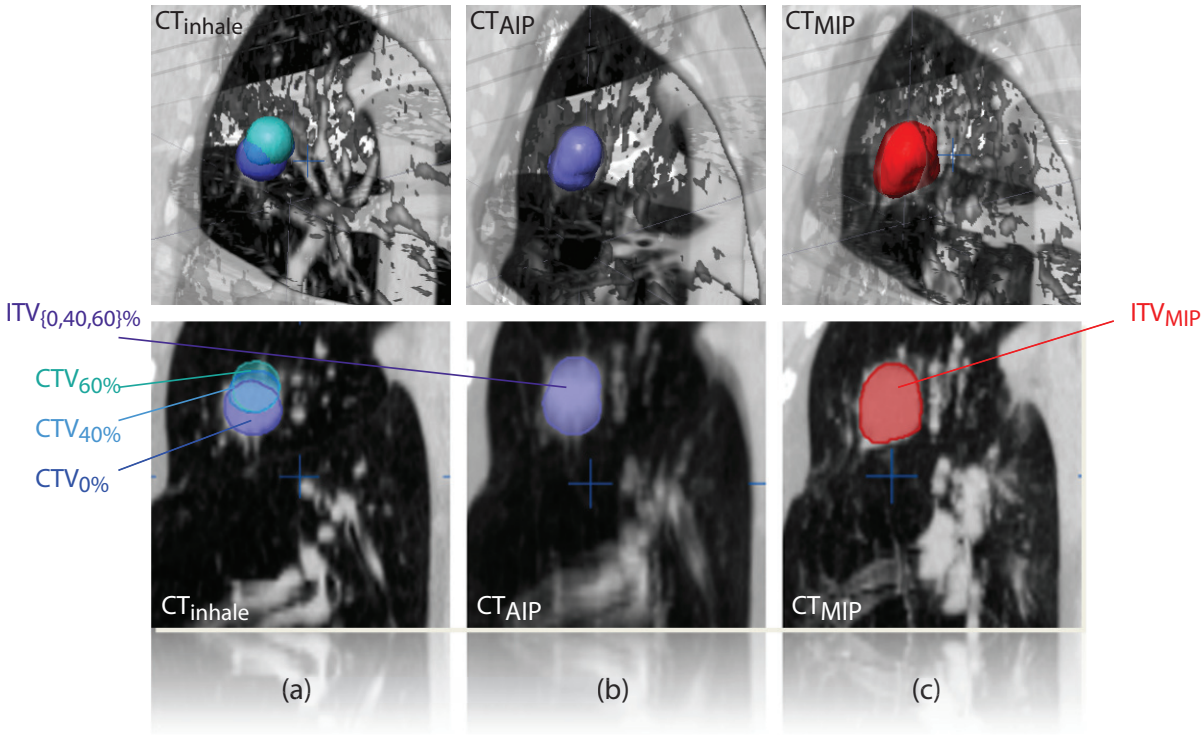

Figure 4.3 : ITV contour-techniques: The figures describes different contour strategies shown on various CT data sets retrieved from the POPI-model [105]. (a) CTVs of three different breathing phases (0 %, 40 %, 60 %) are located in the inhale geometry (0 % of the breathing cycle). (b) The ITV based on the unification (4.1) of the three phases is shown inside the AIP (all phases) geometry. (c) The ITV_{MIP} is shown in the MIP geometry.

given by the CTV contour of the maximum intensity projection (MIP) CT data set. The MIP CT is a static CT derived from the total 4DCT. Every voxel value $HU(x)$ represents the maximum HU value of all breathing based CTs at this voxel coordinate with $HU_{MIP}(x) = max[\{HU_1(x)...HU_n(x)\}]$. Based on the high density of a lung tumor located in a low density lung area, the MIP CT enables a good possibility to contour the ITV directly as CTV [102]. Here, the ITV_{MIP} is defined by:

$$ITV_{MIP} = CTV_{MIP} \tag{4.2}$$

For some indications, it is necessary to go the other way around. Here, only geometrical regions are important that exist in all breathing phases. For this purpose, the minimum intensity projection (MinIP) is used, with: $HU_{MinIP}(x) = min[\{HU_1(x)...HU_n(x)\}]$ [102]. The ITV is statically defined in the same manner:

$$ITV_{MinIP} = CTV_{MinIP} \tag{4.3}$$

The ITV_{MinIP} is secondary for lung SBRT. Usually, ITV_{MIP} is used. The final ITV assumes a static geometry accompanied with a static treatment. During dose delivery the patient performs free breathing, because all tumor positions are already considered in the ITV. However, the approximately accurate dose calculation should also consider the tumor movement. In common, the static dose calculation is performed on the average intensity projection (AIP) CT. Its data is based on the mean voxel values of the 4DCT with: $HU_{AIP}(x) = 1/n \cdot \sum_{j=1}^{n} HU_j(x)$. This approach shall compensate the effect that the real CTV is moving inside the ITV during treatment. The average density should represent the time varying densities, but the dose calculation concept for the ITV region is not totally explored. Experts disagree, MIP, AIP or water equivalent tissue can

be used for the ITV target area. For example, *Wiant et al.*[113] measured the highest accuracy for an artificial phantom by overriding all electron densities within the ITV to water. However, the most widely used method for dose calculation is the AIP for the full geometry as well as the ITV. The contour-strategies and the intensity projection procedures are illustrated in Fig. 4.3. A detailed ITV evaluation is given by section 4.4.2.

Gating

The concept of gating is also based on a static beam. A detailed explanation can be found in: [101, 38, 53, 68, 43, 118, 72, 58, 47]. Basically, the method tries to reduce geometrical target margins with a more accurate treatment due to a time dependent dose delivery. During treatment, the tumor location and the accompanied breathing amplitude are observed. Dose is delivered by a static beam only for a small time frame in relation to a defined tumor location (e.g. exhale state). No dose is applied within the rest of the breathing cycle. In this way, the approach ensures a defined tumor position for treatment planning. The disadvantage is a time consuming treatment, because dose is even applied repetitive short time frames. In general, the approach was developed to use a static dose calculation due to the supposedly small tumor motion. However, the ITV concept is generally used to plan a gated treatment scenario. Only a small set of the 4DCT data is considered for ITV determination, e.g. three exhale phases (50 %, 60 %, 70 %). Hence, the shape of the ITV is clearly reduced (see Fig. 4.2). Dose calculation and treatment planning are typically inspired by the basic ITV model for static beams. A full 4D planning approach is also conceivable (see section 4.4.4), because of the slightly moving tumor within the time frame.

Dynamic tumor tracking

The concept of tumor tracking is applicable, since suitable technologies were available. The approach considers a real-time tumor tracking that delivers a dynamic dose. For this, a suitable image guidance and a real-time beam movement machine are necessary [91, 51, 123]. Different systems were established, one of these application systems is the VERO™ SBRT (Brainlab AG). The machine is able to move the beam in real-time with regard to the tumor position. The application system is based on moveable gimbals [4, 45] that deliver a dynamic dose to the dynamic patient geometry [60]. Also other tumor tracking systems are available, e.g. the Cyberknife™ [16] or dynamic MLC tracking machines [51]. The basic idea of tumor tracking is the compensation of motion uncertainty by following the tumor. Therefore, the ITV concept is obsolete for this modality and the target volume margins are reduced (see Fig. 4.2.c). Disadvantages of the approach are high technical requirements. The most accurate planning approach for real-time tumor tracking is the 4D planning model based on the concepts of this work. A detailed description for tumor tracking is given by section 4.4.1. However, even static planning approaches are used in clinical practice. A detailed comparison is illustrated in section 4.4.2.

4.2 Clinical impact of the elastic image fusion model

The previous section described in detail the requirements and the properties of a 4D planning software prototype with respect to a practical treatment. Additionally, chapter 2 explains the importance of an accurate elastic image fusion model. The improvement of the new hybrid approach (section 2.3) was quantified using advanced landmark tests. Furthermore, the physiological plausibility of vector motion fields was analyzed. However, a direct influence on radiotherapy with clinical parameters is missing. Hence, this section analyzes transformed dose distributions for a 4D treatment plan with respect to different image fusion models. The study is based on the software module shown in section 4.1.1. The patient geometry (4DCT) is given by the POPI-model (see section 2.2.1 and 3.4.3). In general, one plan performs dose transformation with the pure

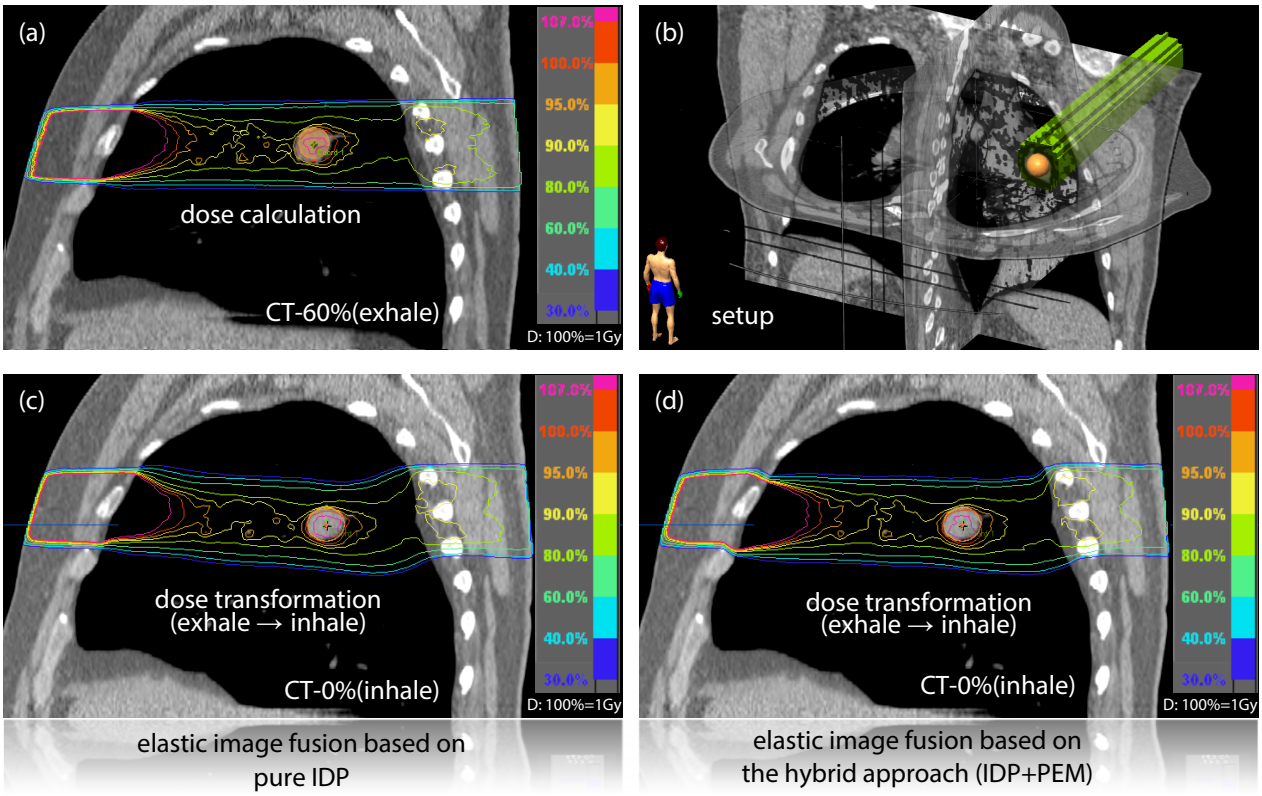

Figure 4.4 : Single dose transformations with different elastic image fusion models: The figure illustrates the setup (b) of the dose application to the exhale geometry with the resulting static dose distribution in (a). A dose transformation of (a) to the inhale geometry leads to different dose distributions, if different elastic image fusion models are used. (c) explains the transformed dose with the pure IDP model, (d) illustrates the contrary result of the hybrid approach (IDP+PEM). Dose calculations are based on MC (2 mm voxel size).

IDP algorithm (see section 2.2.1), the contrary plan is based on the new hybrid approach (IDP+PEM, see section 2.2.3). The DVH of the CTV and the DVH of the right lung (OAR) as well as gamma tests and dose line profiles serve for plan assessment and physical comparisons. The used dose transformation model (dDMM) is similar for both elastic image fusion tests to eliminate the influence of the dose transformation algorithm.

4.2.1 Results

Test 1: Investigation of a single dose transformation

To clarify the direct impact of the elastic image fusion model, the following test merely analyzes the result of one dose transformation. For this purpose, the CTV is delivered by one conformal beam (table: 0°, gantry: 0°, see Fig. 4.4.b). For a better dose transformation investigation, a large volume is treated by using a MLC-margin of 10 mm surrounding the CTV. This test delivers the dose merely to the exhale geometry. The assessment is performed in inhale position after dose transformation with the respective image fusion model. Hence, the study provides three different dose distributions: one untransformed dose distribution in exhale (Fig. 4.4.a); one dose transformation with the pure IDP solution in inhale (Fig. 4.4.c); one dose transformation with the hybrid approach (IDP+PEM) in inhale (Fig. 4.4.d).
Fig. 4.4 explains the resulting dose distributions. A clear spatial difference of the transformed doses is visible at the lung border area where the beam enters the organ. The additional motion of the hybrid approach results in a caudal displacement of the dose compared to the pure IDP model. To point out the clinical effect, the DVHs

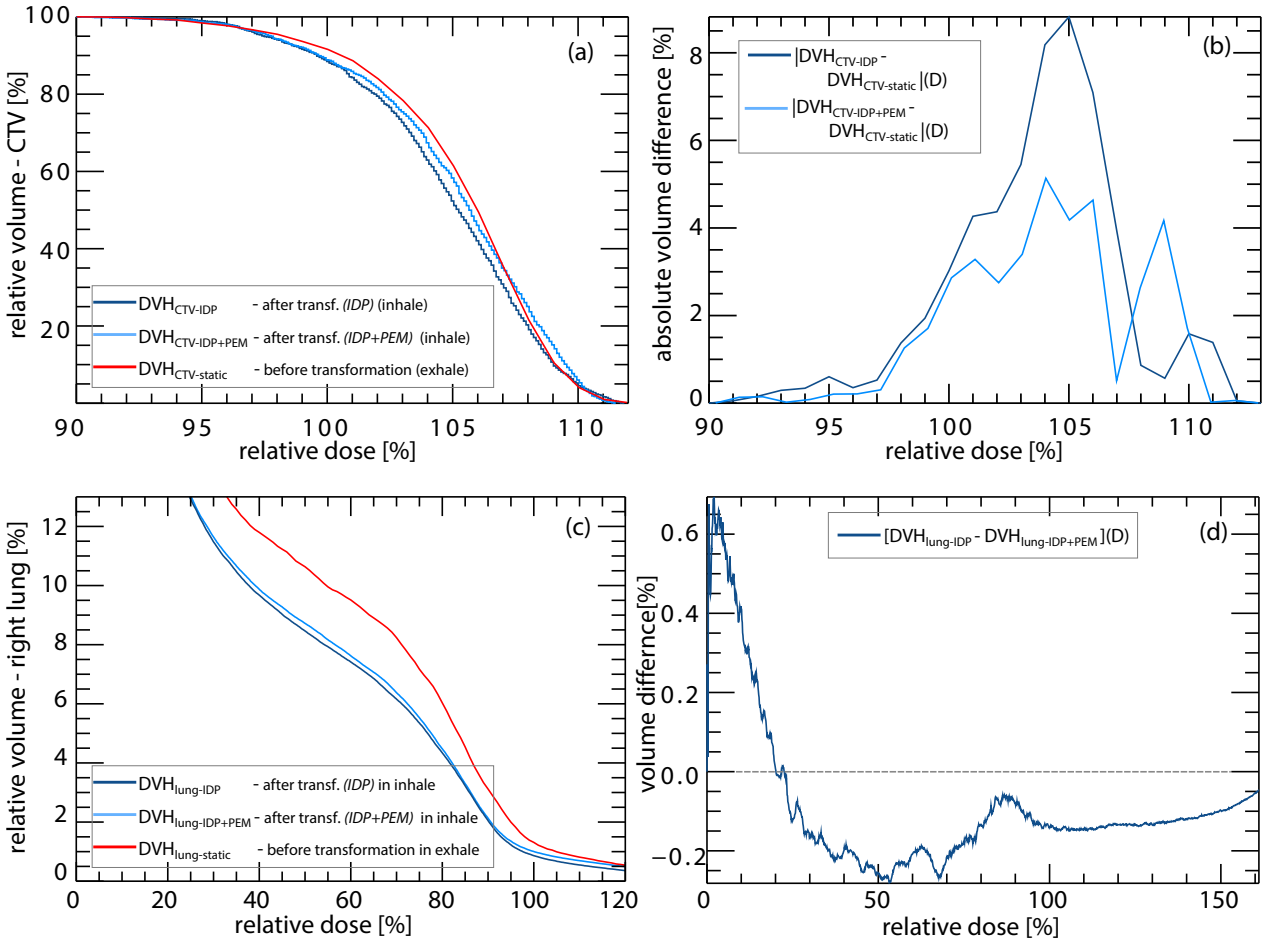

Figure 4.5 : Comparison of clinical DVHs based on different elastic image fusion models: The plot in (a) compares the DVHs of the CTV before and after dose transformation with the IDP approach and the hybrid solution (IDP+PEM). The difference plot in (b) describes the absolute deviation of the transformed dose distribution compared to the dose without transformation. The DVHs in (c) and (d) compare the results for the right lung. In (d) the lung DVH difference for both image fusion models is illustrated. The relative dose of 100 % refers to 1 Gy (see Fig. 4.4).

of the CTV and the right lung were investigated before and after dose transformation. The results are illustrated in Fig. 4.5. The cumulative DVH of the CTV is shown in Fig. 4.5.a. The plot distinguishes between the CTV of the static dose in exhale and the two transformed doses in inhale. A comparison of the DVH before and after transformation is reasonable merely for the CTV, because a strong deformation can be neglected for the moving tumor. There are no momentous differences observable for all three DVHs. However, it is well known (see section 2.2.1) that both image fusion approaches are very precise for the tumor area. This is confirmed by the test. Thus, it can be said that both models conserve the dose information for the CTV sufficiently accurate, whereas the hybrid approach is slightly superior. This can be proven by the graph in Fig. 4.5.b, which compares the absolute difference in relation to untransformed DVH.

The cumulative DVH of the right lung is shown in Fig. 4.5.c. Again, the DVHs of both solutions do not vary characteristically. However, it is clearly illustrated that the lungs DVH physiologically changes during dose transformation. The shapes are completely different due to the different lung (right) volumes for exhale ($2889\,cm^3$) and inhale ($3025\,cm^3$). Hence, this test confirms implicitly the DMH error concept, investigated in section 3.4.[4] Based on the spatial difference, a deviation of the two DVHs is estimated, but due to the small

[4]The volume values for the right lung of the POPI-model are based on measurements within *iPlan™ RT Dose*.

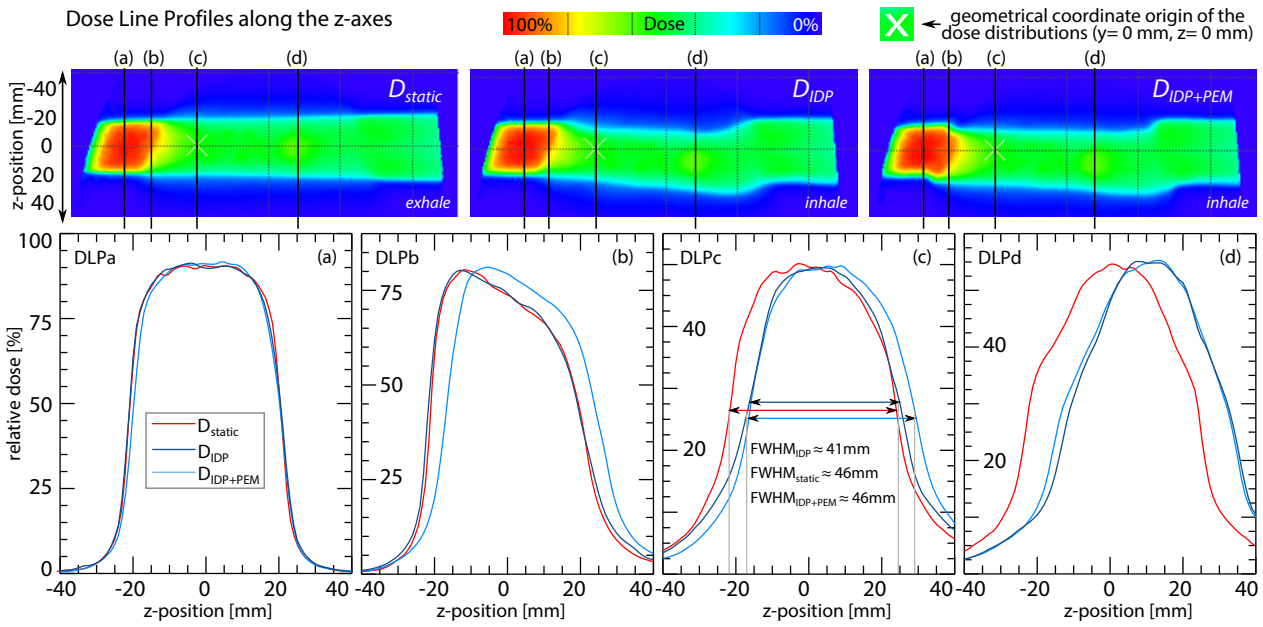

Figure 4.6 : Comparison of dose line profiles based on different elastic image fusion models: The figure shows the selected 2D dose distributions (sagital view) before and after dose transformation with the IDP approach and the hybrid solution (IDP+PEM). Similar located DLPs (a-d) in z-direction are compared for all dose distributions. The DLPs cover the entire beam path: (a) → thorax region at rib cage (outside lung, no deformation), (b) → lung border area (strong deformation gradient), (c) → area near lung surface (smooth deformation gradient), (d) → tumor area (homogenous displacement); The graphs of the four DLPs compare the shapes of the dose lines for all three cases (static, IDP, IDP+PEM). The dose distributions above are individually scaled to the maximum values (100 %) of their absolute dose values. For example, the individual maximums are: D_{static} = 1.844 Gy; D_{IDP} = 1.842 Gy; $D_{IDP+PEM}$ = 1.843 Gy; The DLPs are normalized to 1.845 Gy = 100 %. Hence, the DLPs compare the absolute dose values.

ratio of the treated volume compared to full lung organ, the variation is getting negligibly small. There exists even a small difference shown by the scaled DVH plot in Fig. 4.5.c. The difference plot in Fig. 4.5.d describes a maximum deviation of ca. 0.7 %. This is clinically irrelevant. Hence, considering a trivial setup (one beam) and a single dose transformation, both elastic image fusion models do have the same impact on the final DVH. However, a small spatial difference is shown in Fig. 4.5.d. For low dose areas the IDP concept affects a larger volume as the hybrid approach. The reverse behavior is observable for higher doses. This implies a larger dose blurring of IDP and a more conformal dose application for the hybrid dose transformation. This may be attributed to spatial effects. An appropriate investigation of spatial effects is the analysis of the global dose distribution. For this purpose, 2D dose distributions of both dose transformations are compared. Fig. 4.6 illustrates the selected dose distributions. The spatial difference is confirmed by four dose line profiles (DLP, a-d) along the z-direction. DLPa shows no difference for all plots due to the static tissue area outside the lung. DLPb offers differences directly at the lung border. Whereas the hybrid approach displaces the dose distribution based on the realistic lung slipping effect, the IDP concept enforces no dose displacement. The more medial located DLPc describes also more displacement for the hybrid approach. Here, the dose blurring of IDP occurs. The DLP of the hybrid approach looks like a realistic caudal shift of the untransformed DLP. Both (IDP+PEM, static) DLPs have the same full width at half maximum (FWHM) and a similar shape. However, the DLP of the IDP solution shows a different shape with smoother penumbras and a smaller FWHM. This is quite unrealistic concerning a lung expansion of about 150 cm^3 from exhale to inhale. The dose blurring effect of IDP is based on a less precise image fusion compared to the hybrid approach in this area. As expected, DLPd shows an accurate dose displacement for both elastic fusion solutions within the tumor area.

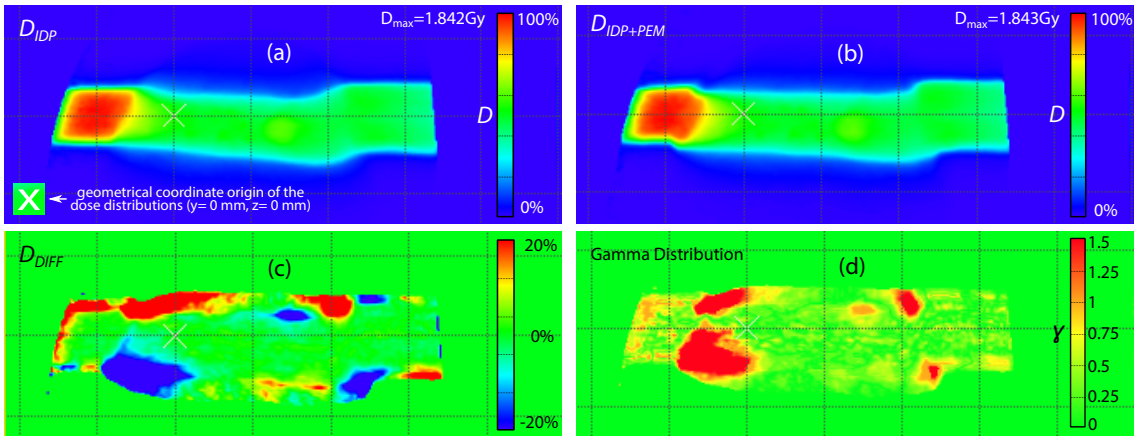

Figure 4.7 : Comparison of 2D dose distributions based on different elastic image fusion models: The test compares the dose transformation related to the IDP approach (a) and to the hybrid solution (b) (IDP+PEM). The local percentage difference in (c) compares directly the difference of both results. A single value inside the distribution is given by: $D_{\text{Diff}}(x) = \frac{D_{IDP}(x) - D_{IDP+PEM}(x)}{D_{IDP+PEM}(x)}$. Doses below 5 % of the maximum dose are suppressed. The gamma distribution in (d) offers the result of a 2D gamma test with 2 mm distance to agreement (DTA) and 2 % dose difference (DD). Only 89.5 % of the analyzed points passed the criterion ($\gamma < 1$). The gamma tests suppresses also doses below 5 % of the maximum dose. Hence, the dose distributions are different. The 2D gamma test used in this work is based on the approach of *Low et al.* [57]. Both tests use the absolute dose values of the respective dose distributions.

The strong spatial difference of both dose transformations along the surface of the lung organ, is also illustrated by Fig. 4.7. The figure explains the results of a more dimensional comparative study. Both dose distributions are analyzed with the local percentage spatial difference (Fig. 4.7.c) and with a 2D gamma test (Fig. 4.7.d). The percentage difference in the figure shows the local displacement of both distributions. A characteristic change is visible at both lateral lung border areas. The hybrid approach transforms more dose in caudal direction. The 2D gamma test based on *Low et al.* [57] revealed that only 89.5 % of all analyzed points passed the criterion ($\gamma < 1$) with 2 mm distance to agreement (DTA) and 2 % dose difference (DD). This confirms the momentous difference of the dose transformations. The gamma distribution shows large deviations with values up to 1.5 notably for lung slipping zones at the lung border area.

Test 2: Impact on an accumulated dose distribution

Test 1 revealed a characteristic dose difference using the mentioned DIR methods. However, for a single dose transformation with a trivial beam setup the clinical impact may be negligible. Test 2 analyzes a simplified accumulated dose. For this purpose, two dose distributions (exhale, inhale) were accumulated within the inhale geometry. The dose distribution of exhale was transformed with both image fusion models. The exhale and inhale dose distributions were accumulated with the same weight. The setup simulates a tumor tracking scenario (see section 4.1.2), where the beam follows the center of CTV with a MLC-margin of 0 mm. The different accumulated doses are illustrated in Fig. 4.8. Again, there exists a strong spatial difference inside the lung border area (red volume in Fig. 4.8). However, spatial differences of the clinical DVHs regarding the CTV or the right lung were negligibly small also for this accumulated dose. These DVH results for both image fusion models are approximately the same.

Therefore, one can assume that the lung slipping just affects clinical DVHs, if a large lung volume is irradiated. In that case, the treated volume at the lung border area has a momentous ratio in relation to the total volume of the lung. Another, impact scenario is a CTV that is located very close to the surface of the lung. To investigate these reflections, a small conceptional volume (no anatomical structure → red area in Fig. 4.8) close to the

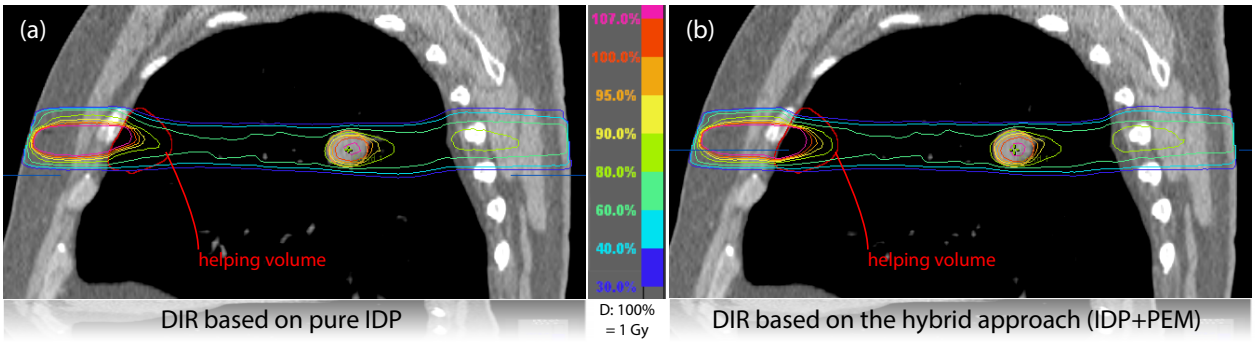

Figure 4.8 : Accumulated dose distributions with different elastic image fusion models: The figure illustrates the accumulated doses based on two dose distributions (exhale, inhale) within the inhale geometry. The results of the IDP solution and the hybrid approach (IDP+PEM) are distinguished by (a) and (b). Spatial differences are particularly visibly for the lung border area (red conceptional volume).

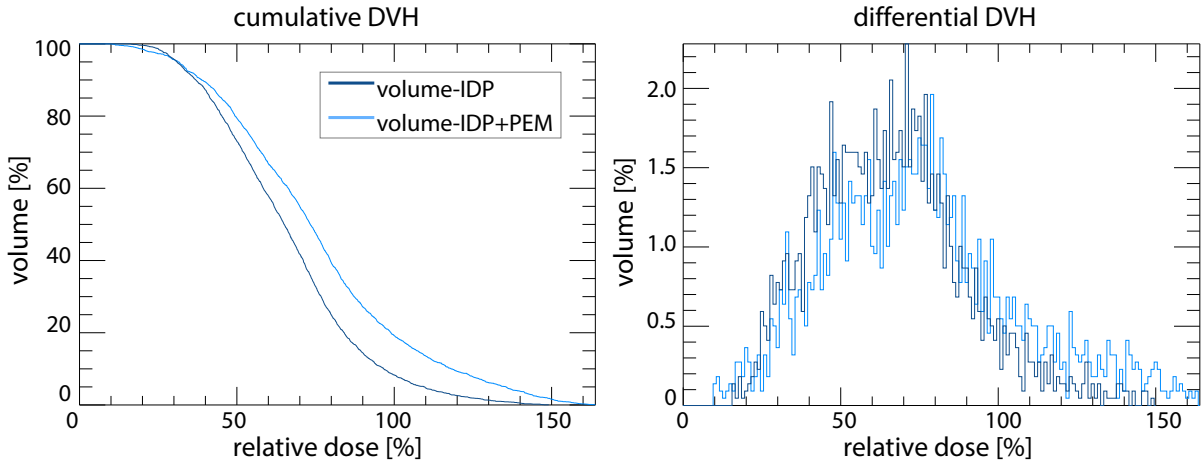

Figure 4.9 : Comparing the DVH of a lung border volume with different elastic image fusion models: The figure illustrates the cumulative DVH as well as the differential DVH for a conceptional lung border volume (see red ROI in Fig. 4.8). The DVHs are based on the simplified accumulated dose of test 2. The DVHs distinguish between image solutions of the IDP and the hybrid approach (IDP+PEM). The relative dose of 100 % refers to 1 Gy (see Fig. 4.8).

surface of the lung is analyzed. Here, the full volume is irradiated. As expected, the DVH for this conceptional volume strongly varies (see Fig. 4.9), if different image fusion models are used. This is particularly visible for the cumulative DVH with differences up to 15 % (e.g. at 100 % relative dose). Additionally, the differential DVHs have characteristic deviations of their peaks. A clear maximum peak displacement could be observable due to different spatial dose transformations.

4.2.2 Conclusion

The analysis has shown, that dose distributions that are based on transformations with various image fusion models are characteristically different. The new hybrid approach offers a more realistic dose transformation compared to the pure IDP solution. The differences a clearly visible at lung border areas, where the lung slipping effect occurs. Those differences are proven by DLP tests (see Fig. 4.6), 2D dose percentage difference tests as well as 2D gamma tests (see Fig. 4.7). The spatial investigations revealed a expressive difference for single dose transformations (test 1) such as simplified dose accumulations (test 2). However, the effective clinical impact is relatively small for trivial irradiation setups. DVHs for the CTV and the right lung are very

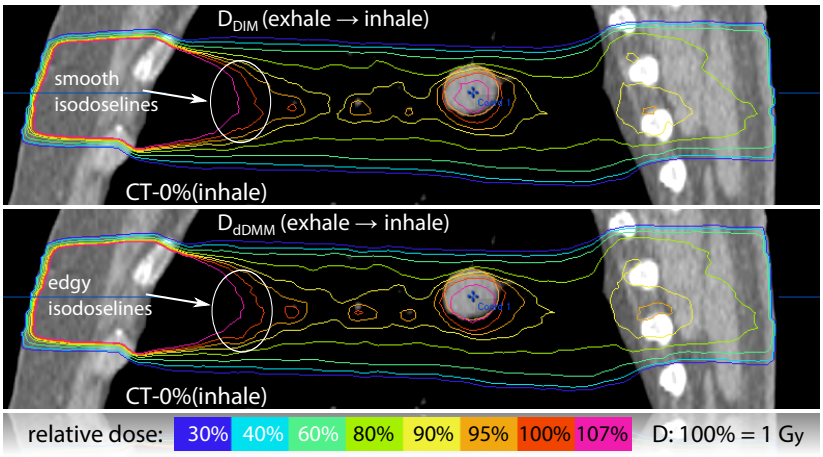

Figure 4.10 : Single dose transformations with DIM and dDMM: The figure illustrates the transformed dose distributions based on a single beam setup with a MLC-margin of 10 mm. The dose transformations lead to different dose distributions (DIM, dDMM). The dose is based on MC (2 mm voxel size, 2 % variance).

similar. Explanations for this is: The target volume is located in a medial lung area, where both solutions offer a precise motion prediction. Moreover, the treated lung border area is very small in relation to total lung volume. For simple treatments which fulfill the mentioned explanations, both solutions offer a sufficient and acceptable clinical outcome. However, if complex treatment strategies are used, where large lung volume are affected or if the CTV is located closed to the border of the lung, the clinical impact may become important. This significance was proven by the DVH investigations (see Fig. 4.9) of the conceptional lung border volume.

4.3 Clinical impact of the dose transformation model

This analysis is a clinical continuation of chapter 3. Based on the developed 4D software module, this section investigates the clinical impact of various dose transformation models. Only dDMM and DIM are compared due to the physical conclusions of chapter 3. Energy models are neglected. Beside the already discovered physical conclusions about dose transformation algorithms, this study investigates additionally the important clinical effects measured by clinical parameters such as DVHs or gamma distributions. Once again, the POPI-thorax model is used for assessment. All deformations are based on the hybrid image fusion model to eliminate the influence of different DIR algorithms. Moreover, the study uses a dose grid of 2 mm with MC dose calculations (2 % variance, dose-to-medium), because this resolution offers acceptable results (see Fig. 3.33) for both transformation models.

4.3.1 Results

Test 1: Investigation of a single dose transformation

This analysis investigates also a single dose transformation based on a trivial beam setup with a large MLC-margin (10 mm) for the CTV. Here, the dose distributions are calculated inside the exhale geometry, the doses are transformed to the inhale geometry. Here, the setup generates a dose gradient inside the target, because the isocenter of the static beam is focused on the center of the CTV at inhale position. The tumor slightly moves away from the beam's isocenter during dose application at exhale position. The transformed dose distributions are illustrated in Fig. 4.10. Both results appear to be similar, but a detailed analysis reveals that the dose distribution for DIM is smoother and dDMM offers more edgier isodoselines. The isodoselines of the pure MC dose calculation before dose transformation are also very edgy. Hence, DIM discards dose information in areas of dose gradients. This has no characteristic spatial influence, but it has a direct impact on the DVH of the CTV (see Fig. 4.11), because a dose gradient crosses the target. The variations of the isodoselines result

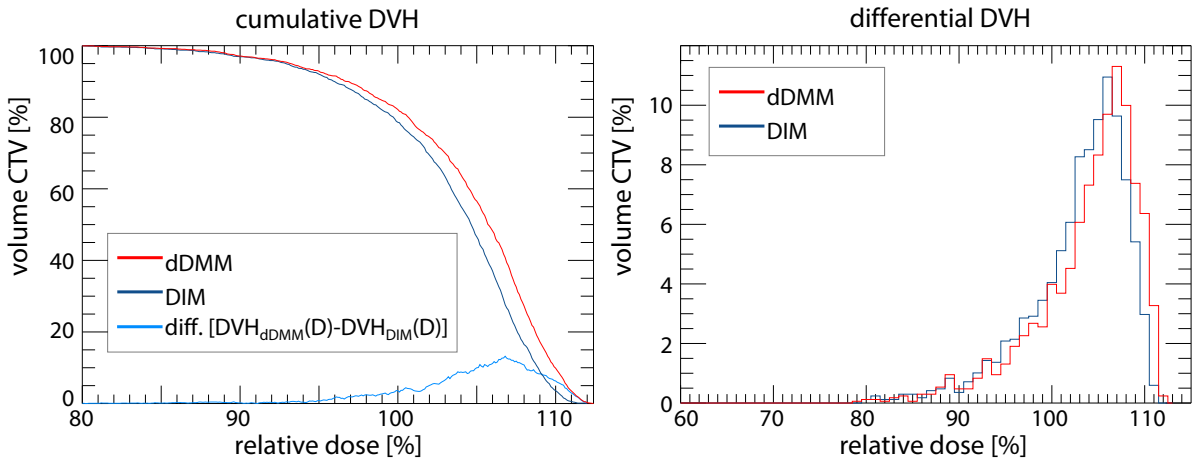

Figure 4.11 : Comparing the DVH of the CTV using DIM and dDMM: The plots show the cumulative and the differential DVHs (CTV) for the dose transformations based on dDMM and DIM (Fig. 4.10). The difference scatter within the cumulative graph shows deviations up to 12 % (at 107 % relative dose). The relative dose of 100 % refers to 1 Gy (see Fig. 4.10). The dose binning for the graph visualization of the differential DVH is 1 % per bin. However, the internal resolution of the doses is higher. Hence, the difference in the plot is not even a numerical shift of 1 %.

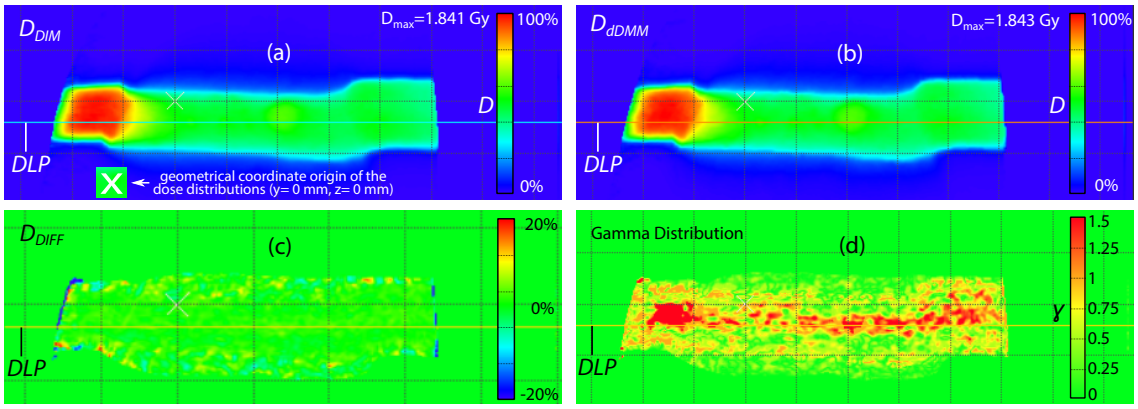

Figure 4.12 : Comparison of 2D dose transformations based on DIM and dDMM: The test compares the dose transformation of the DIM approach (a) and the dDMM model (b). The local percentage difference in (c) compares directly the difference of both results. A single value inside the distribution is given by: $D_{\text{Diff}}(x) = \frac{D_{DIM}(x) - D_{dDMM}(x)}{D_{dDMM}(x)}$. Doses below 10 % of the maximum dose are suppressed. The gamma distribution in (d) offers the result of a 2D gamma test with 1.5 mm distance to agreement (DTA) and 1.5 % dose difference (DD). 92 % of the analyzed points passed the criterion ($\gamma < 1$). Hence, the dose distributions are different. The gamma tests suppresses doses below 5 % of the maximum dose. A specific dose line profile along the y-axes is marked in every dose distribution.

in an underestimation using DIM compared to dDMM. The cumulative DVH for the CTV shows differences up to 12 % (e.g. at 107 % relative dose). The differential DVHs show characteristic variations with a shift of the dose peak and a modified DVH shape. The deviations of using DIM or dDMM are clinically meaningful. However, the DVHs of the right lung are approximately the same with maximum differences of only 0.4 %. Again, the treated lung volume is too small in relation to the full organ to measure momentous effects.
Both dose transformations are also compared by the 2D dose percentage difference test and the 2D gamma test [57]. The result of the percentage difference test is illustrated in Fig. 4.12.c. The result shows two approximately similar dose distributions without spatial deviations, shifts or displacements. However, the results of

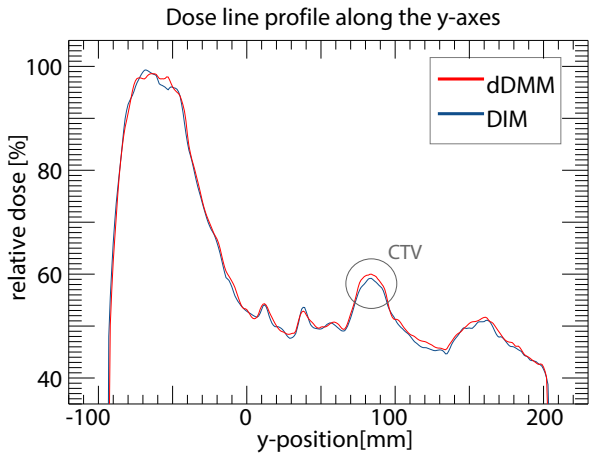

Figure 4.13 : Comparison of y-DLPs based on different dose transformations: This dose profile regards to the DLP (y-axes) mentioned in Fig. 4.12. The graph shows the DLP based on the DIM dose transformation (blue) in comparison to the dDMM dose transformation (red). For instance, substantial differences are visible for the tumor region, which is marked as CTV area (gray). The mass effect applies here, which is not considered by the DIM. Hence, DIM shapes the dose slope more smooth and underestimates the dose for the target area.

the gamma tests (1.5 % DTA, 1.5 % DD)[5] show characteristic differences with 92 % acceptable points ($\gamma < 1$). This numerical effect is directly based on the transformation algorithm, because the dose percentage difference test yielded no geometrical differences. Hence, the impact of the image fusion model or setup variations are negligible for the results. Large gamma scores are located in the center of the beam path (red), especially at regions, where the beam enters the lung. Here, the deformation effect (see section 3.1.2) applies, because the maximum motion vector gradient is present. This results in a maximum influence of the transformation model. Consequently, the mentioned numerical effects of the transformation model lead to deviations of the cumulative DVH for CTV (Fig. 4.11). This effect is also proven by a specific DLP along the y-axes, which intersects the tumor region in the center of the beam path. Fig. 4.13 illustrates a distinction of the mentioned DLP for both transformation results. Globally, both methods show the same macroscopic dose shape and similar gradients at large dose slopes. However, a detailed investigation reveals, that the differences are observable for small dose fluctuations based on density deviations around the target. DLP_{DIM} looks more smooth in comparison to the DLP_{dDMM}. An explanation for this is: DIM interpolates primitively between dose grid points within the dose gradient area. However, dDMM weights large doses within the tumor area (large masses) higher the dose in the low density tissue. The result is a smoother dose slope for dDMM and a hard, more realistic dose profile for dDMM. The mass effect mentioned in chapter 3 applies here. The effect leads to the shown clinical impact for the DHV (CTV). The underestimation of the DIM model is visible for the CTV.

Test 2: Investigation of a complex dose distribution

Test 2 investigates a single dose transformation based on a more complex dose distribution. Thereby, the overall irradiated lung volume is larger with more affected deformation regions at lung border areas. A setup containing three different static beams with a sharp MLC-margin (0 mm) surrounding the CTV and an equal beam weighting (monitor units) is assumed. All three beam axes are placed in the same sagital plane with different angles around the isocenter. This test investigates the dose transformation from exhale to inhale. The results are illustrated in Fig. 4.15.a-b. In similarity to test 1, a static treatment accompanied with free breathing is assumed. The beam setup (isocenter) is based on the inhale geometry. Hence, the CTV is not irradiated conformal in the shown dose transformation, because the target moves out of the beams isocenter during irradiation at exhale position. This generates again a strong dose gradient inside the target.
The analysis of the dose distributions inside the target shows a slight underestimation using DIM in contrast to dDMM. This can be proven by DVH of the CTV (Fig 4.14). The DVH graph of DIM is a bit higher than the

[5] A more strict gamma criterion as seen in the previous section is used for this evaluation, because dose deviations related to different transformation algorithms describe less spatial variations as more dose gradient effects.

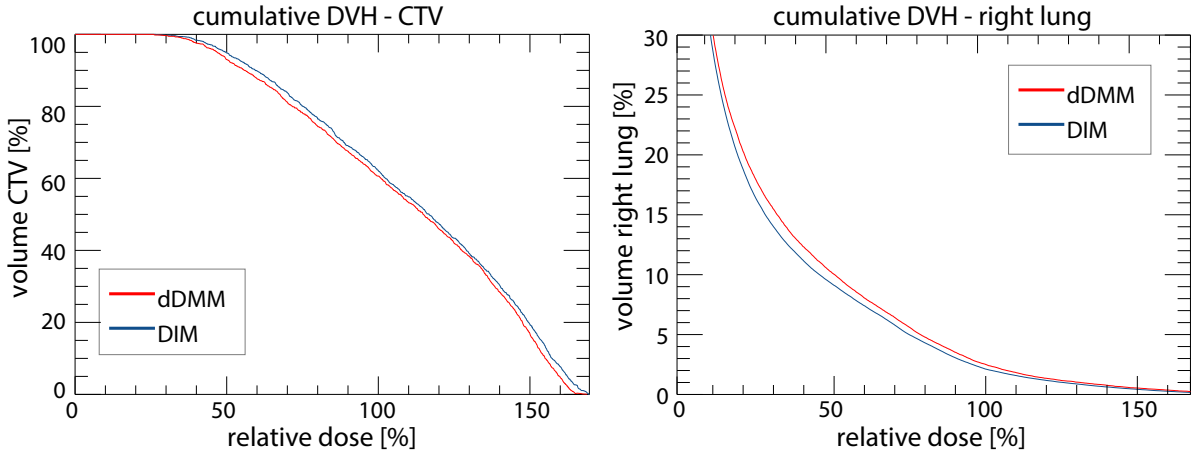

Figure 4.14 : Clinical DVHs using DIM and dDMM based on a complex dose distribution: The plots show the cumulative DVHs (CTV, right lung) for the dose transformations based on dDMM and DIM. The transformation regards to the beam setup described by Fig. 4.15. The DVHs of the CTV show deviations up to 4 % with a constant overestimation for DIM. The DVHs of the lung show differences up to 3 % due to the large irradiated lung volume.

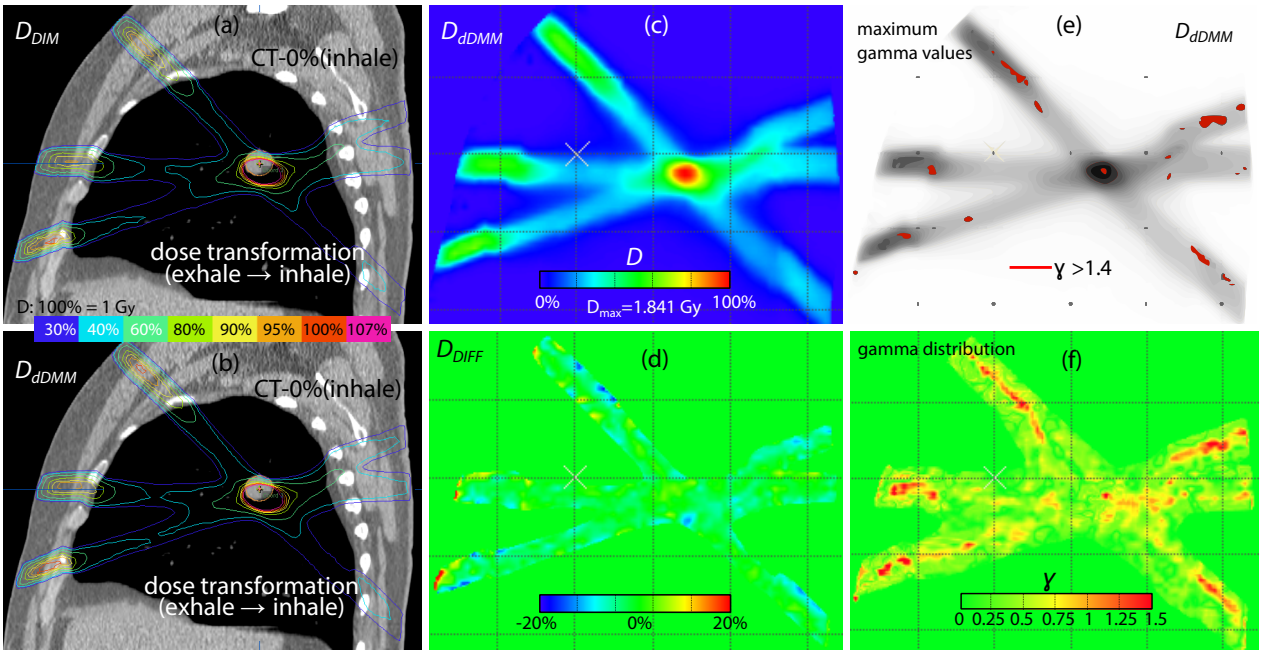

Figure 4.15 : Single dose transformation based on a complex dose distribution: The figure illustrates the setup and the resulting dose transformations (a-c) of test 2. A dose transformation (exhale → inhale) leads to different dose distributions, if different dose transformation algorithms fusion models are used (DIM, dDMM). The differences are proven by the local percentage difference (d) and the 2D gamma test (e,f) with 1.5 % DTA and 1.5 % DD. 96 % of the analyzed points passed the criterion ($\gamma < 1$). Hence, the dose distributions are substantial different. The gamma tests suppresses also doses below 5 % of the maximum dose. The largest gamma values (e) are particularly located at lung border areas where a strong motion gradient exists. Also a large density gradient applies. Hence, the mass effect applies additionally. Both tests use the absolute dose values of the respective dose distributions.

graph for dDMM with a maximum deviation of 4 %. This is contrary to test 1, but the behavior is explainable, because this test uses small MLC-shapes. DIM tends to simulate smoother dose gradients as dDMM, because it neglects the density variations within the border area of the tumor. Due to the strong dose gradient in the center of the CTV with a homogeneously mass, the calculation applies more dose to the DVH of DIM as for the DVH of dDMM. Hence, DIM shifts the dose gradient and dDMM accurately conserves the dose gradient due to the consideration of density variations. Also the DVHs of the lung show substantial differences with maximum deviations of 2 – 3 % (e.g. at 40 % relative dose). This is more important as in the results of test 1 (maximum: 0.4 %). The deviation increase is explainable with the expanded irradiated lung volume. This confirms the hypothesis that an inaccurate dose transformation algorithm affects the DVH of the lung, if a large volume is irradiated. Again, spatial deviations are proven by the 2D dose percentage difference test and the gamma test [57]. The results are shown in Fig. 4.15.c-f. The dose percentage test shows no characteristic variations. Hence, geometrical influences are negligible. The results of the gamma tests (1.5 % DTA, 1.5 % DD) show meaningful differences with 96 % passing points ($\gamma < 1$). This confirms again, the numerical influence of the transformation model. It should be noted, that particular large gamma values ($\gamma > 1.4$, Fig. 4.15.e) are especially located at lung border areas. Those volumes are affected by the deformation effect (section 3.1.2) due to the strong gradient in the motion vector field. Also large density variations at this lung border areas lead to different dose transformations, because the mass effect is neglected by DIM and considered by dDMM.

4.3.2 Conclusion

The study confirmed the clinical impact using different dose transformation models. Based on the findings of chapter 3 it could be said, that DIM shows worse results for the DVH of the CTV (Fig. 4.11 and Fig. 4.14) with errors up to 12 % compared to dDMM. This could be a constant overestimation (test 2; sharp MLC-shape for CTV) or a constant underestimation (test 1; large MLC-shape for the CTV). The impact depends on the setup as DIM typically displays smoother dose gradient regions. Theses smoother dose gradients are typically located at tumor border regions, where strong density variations occur. However, the important mass effect for dose transformations (derived by the findings of chapter 3) is not considered in the DIM approach. In contrast, dDMM takes the density variations and the voxel masses during transformation into account and determines more accurate dose distributions. The effect is clearly confirmed by the DLP comparisons along the y-axes (Fig. 4.13), which show characteristic differences particularly for the CTV.
The influence on the DVH of the lung is negligible for many setups. However, the effect becomes meaningful, if a complex irradiation strategy with a large irradiated lung volume is used. This volume effect is proven by test 2. Spatial deviations based on numerical issues are demonstrated by the gamma tests of all studies (Fig. 4.12, 4.15). Those results are clearly related to the transformation model, because the dose percentage tests eliminate other influences like geometrical displacements. Particularly noteworthy is the fact, that large gamma values often occur at lung border areas (see Fig. 4.15.e). Hence, the quality of the selected dose transformation model is superior for such areas. This is consistent with the findings of chapter 3. Hence, it confirms the impact of the theoretical deformation effect (section 3.1.2) and it also confirms the concept of the mass weighted dose average for dose transformations at these areas (section 3.2).
Beside, this study used a dose grid size of 2 mm per voxel, which is acceptable for dose accumulations. The strong voxel size dependency of DIM should always be taken into account for practical implementations. This means, that the shown variations are even larger for coarser resolutions. However, dDMM offers a precise dose transformation algorithm with a minor voxel size dependency.

4.4 4D planning in comparison to conventional strategies

The aim of this section is to investigate the significance of the clinical benefit of the full 4D treatment planning approach. Therefore, conventional static planning strategies are compared to the 4D approach based on all findings of this work using the new hybrid deformation model accompanied with the new dDMM for dose accumulation. For this purpose, different treatment modalities are evaluated. Section 4.1.2 explains the theoretical basics of dynamic tracking, gating and the ITV concept, which are utilized for comparison. All approaches are applied to the scientific 4D patient geometry (POPI-model, [105]) based on MC dose calculations (dose-to-medium) with a voxel resolution of 2 mm and a variance of 2 %.

4.4.1 4D planning for dynamic tracking

This sections illustrates a detailed explanation of the 4D planning approach to show the workflow of the 4D software prototype exemplary for dynamic tracking. The POPI-model includes ten breathing phases based on a respiratory correlated 4DCT [95]. For this example, the dynamic tracking approach applies a single beam that follows the moving target orthogonal to its major displacement direction (z-axes). The tracking starts with a conventional setup (table: 0°, gantry: 0°, 0 mm MLC-margin surrounding the moving CTV). The beam moves in parallel to the y-axes of the patient geometry. The investigated example defines the breathing inhale position (0 %) as reference geometry. In contrast, nine different breathing phases are covering the remaining respiratory cycle. Every CT geometry serves for a single dose calculation that simulates a specific moment during respiration. The motion of the beam is determined by the shift the CTV (center coordinate). The MLC-shape is fixed during tracking. In conclusion, the dose distributions of all breathing phases are mapped to the reference geometry. The final dose accumulation is determined for the reference set. The full experiment is illustrated in Fig. 4.16. The figure explains all time dependent dose distributions (ten breathing phases) before and after dose transformation for the sagital plane that intersects the isocenter. For a better distinction the untransformed dose distributions are black and white images, the transformed doses are colored. Important for a realistic dose accumulation is the beam weighting (see section 3.1.1, formula (3.2)). The dwelling time of every CT geometry could be different, because the common respiratory correlated CT acquires the time dependent data with respect to their breathing amplitude. Hence, the weighting of every single dose distribution is different for dose accumulation, because the irradiation at every time phase varies. Here, respiratory correlated breathing amplitudes are not accessible for the POPI-model [105]. Hence, the PDF model is not applicable for this solution. Therefore, the following evaluation do all use an equal weighting of the dose distributions related to the respective breathing phases.

4.4.2 Dynamic tracking: 4D planning vs. static planning

The previous section explained in the detail the accurate generation of an 4D dose accumulation for the dynamic tracking modality. Many degrees of freedom (here: hybrid image fusion model, dDMM dose transformation, MC with 2 mm voxel resolution and 2 % variance, breathing correlated time weighting) are necessary to calculate exact results. The good motion compensation of dynamic tracking leads to the presumption that a static plan fulfills the same clinical requirements (DVH for CTV and OARs) as an accurate 4D planning approach with a 4D dose distribution. Static dose planning in the context of dynamic tumor tracking is a dose calculation merely planned on one sample phase of the respiratory cycle. For example, the full dose delivery is planned on the reference set in a static way. The real dose application is done by dynamic tumor tracking. The idea of this static approach is a negligible small deviation of the static and the real applied dose due to the good motion compensation of the tracking dose delivery itself. For evaluation of this hypothesis, the following outline compares two 4D dynamic tracking plans (0 mm and 3 mm MLC-margin surrounding the CTV) with

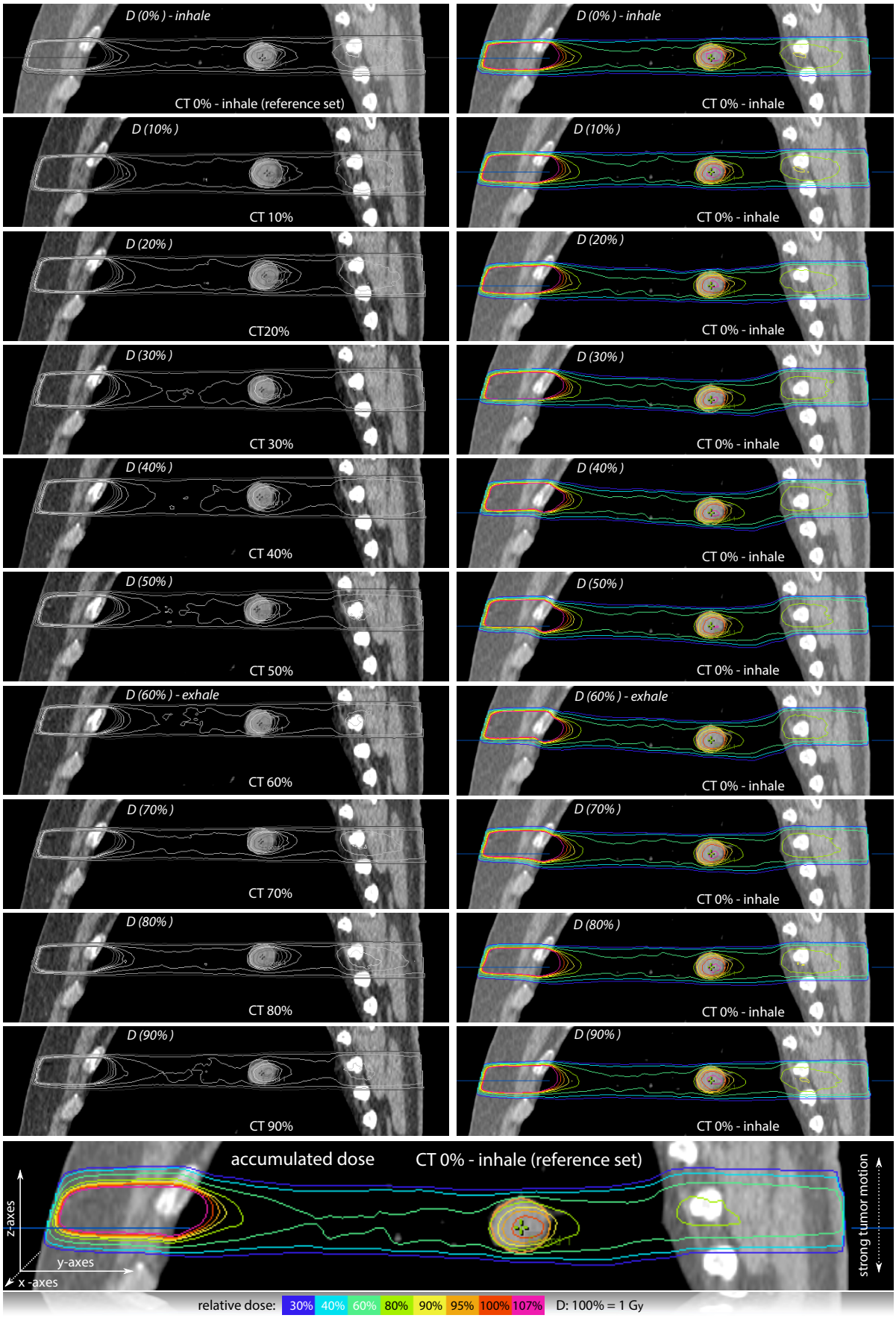

Figure 4.16 : The illustration of a 4D dose accumulation for dynamic tumor tracking: The dynamic beam follows the tumor in z-direction. This is illustrated with spatial displacements of the dose distributions at different breathing phases. All single dose calculations are performed inside the respective breathing geometry (left). For dose accumulation (bottom) all dose distributions are mapped (IDP+PEM, dDMM) to the reference geometry (right).

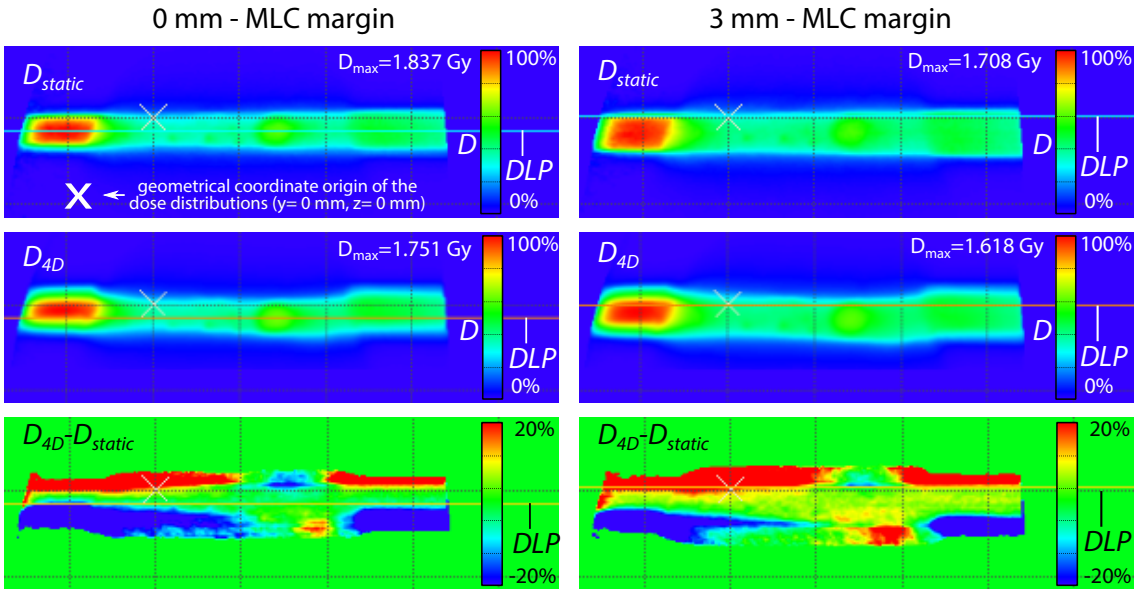

Figure 4.17 : Comparing static and accumulated dose distributions for dynamic tracking: The test compares the dose distributions based on the full 4D dose accumulation process and a static dose distribution planned on the reference set. Equal monitor units and the same reference set are required. The test distinguishes between two setups: left → 0 mm MLC-margin; 3 mm MLC-margin surrounding the CTV. The local percentage difference compares directly the difference of the 4D and the static solution. A single value inside the distribution is given by: $D_{\mathrm{Diff}}(x) = \frac{D_{4D}(x) - D_{static}(x)}{D_{static}(x)}$. Deviations are distributed over the full beam path. Both tests use the absolute dose values of the respective dose distributions.

their respective static solutions merely planned on the static geometry. To enable a comparative study, both plans (4D, static) apply the same value of monitor units. Furthermore, they use the same reference set. As suspected, the dose distributions are characteristically different (see Fig. 4.17). This is confirmed by the dose percentage difference tests for the 0 mm MLC-margin setup and for the 3 mm MLC-margin.
Clinical differences are observable. This is confirmed by Fig. 4.18. The DVH of the CTV shows a slight overestimation using the static solution. For example (at 105 % relative dose), the DVH is about 8 % (0 mm margin) or 5 % (3 mm margin) percent higher compared to 4D approach. This is an important clinical effect, as the static plan does not fulfill the assumed goal (e.g. TCP). Admittedly, the expansion of the margin reduces the effect, but the deviations remain meaningful. Reasons for the varying graphs are trivial. The path of tumor motion is not exactly parallel to the z-axes[6]. The vectorial motion has also fractions in y or x-directions during breathing. For this example, the CTV moves slightly away (y-direction) from the source of radiation. Based on the inverse square law, the CTV receives a lower dose at exhale position. Furthermore, density variations between single breathing phases could cause slight differences for CTV at varying time stamps. Here, a part of the rib cage with a higher density moves into the beam (in front of the tumor) due to the tracking process. This leads to lower 4D doses. In general, the overestimation of the static approach is not universal. An underestimation is also possible. The effect depends on the location, the motion direction and the dimension of tumor as well as the density variations in areas surrounding the CTV. However, the differences for the DVHs regarding the right lung or the total normal tissue are negligible for this example. Again, this could be explained with the large volumes of the investigated DVHs compared to their small irradiated fractions. The good motion compensation of the tracking approach wipes out all deviations for the lung (Fig. 4.18, DVH for the right lung). Spatial differences of the dose distributions outside the moving tissue lead to small variations for the normal tissue. An advanced scaling (Fig. 4.18, DVHs for the normal tissue) shows varying graphs. However, those

[6]The coordinate system (x,y,z) of the patient geometry is explained in Fig. 4.16

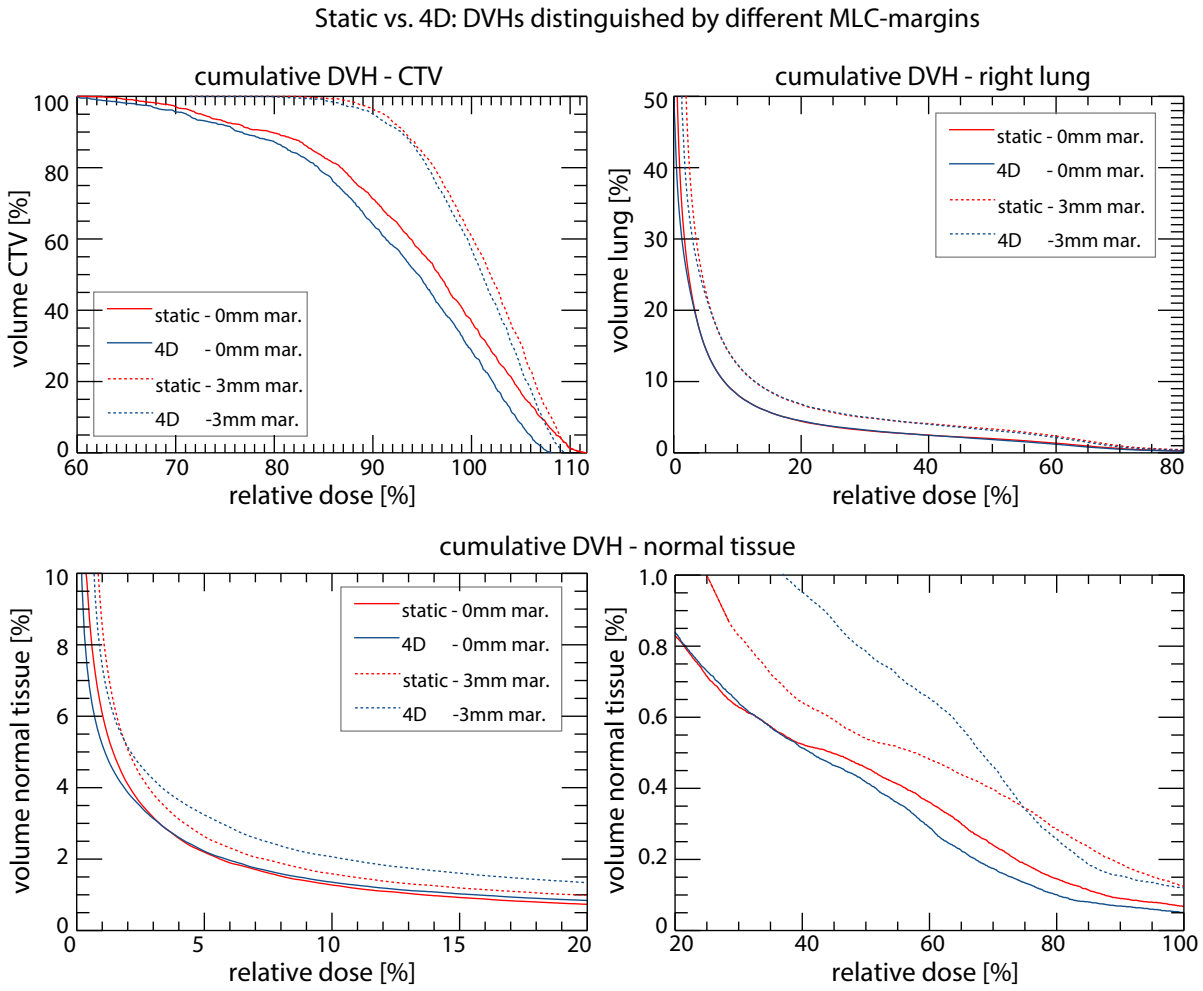

Figure 4.18 : Comparing clinical DVHs for dynamic tracking using 4D and static approaches: The plots show the cumulative DVHs for CTV, the right lung and the normal tissue (two axes scalings). The results are based on Fig. 4.14. Every graph distinguishes between the 4D approach (blue) and the static method (red) as well as two irradiation setups (0 mm MLC-margin surrounding the CTV → solid line; 3 mm MLC-margin → dotted line). Especially the CTV shows characteristic differences for both setups. The relative dose of 100 % refers to 1 Gy (see Fig. 4.16). The dose binning for the graph visualization of the differential DVH is 1 % per bin.

variations are clinically irrelevant, the may become important if larger volumes or other OARs are treated. Such an investigation could be a goal for further studies.

The obtained differences of the CTV and the normal tissue can be proven by particular DLPs illustrated in Fig. 4.19. The DLPs refer to the dose distributions of Fig. 4.17. In (a) the profile intersects the center of the CTV at inhale position (0 mm MLC-margin). Due to the tracked beam outside the moving tissue, a clear overestimation of the static approach is observable. The motion compensation starts when the beam enters the lung. Hence, both DLPs in (a) correlates for lung and CTV regions. The contrary DLP in (b) is located at the edge of the CTV. Based on the dose variations of the different breathing phases, the CTV receives a lower dose (4D) for this profile as estimated by the static method. Finally, the test has shown that the 4D approach is more precise. It can be recommended to use the 4D solution for dynamic tracking.

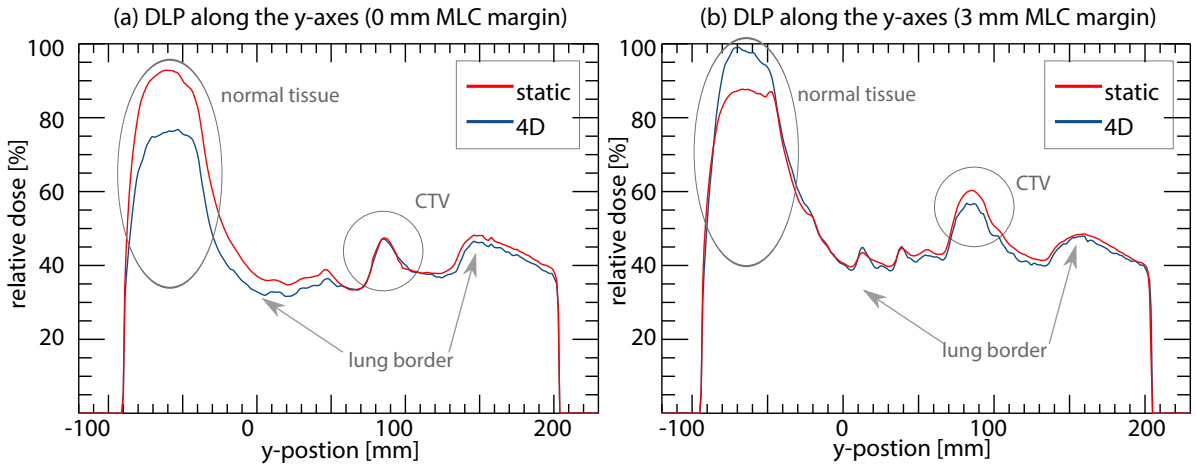

Figure 4.19 : y-DLPs based on different planning approaches (4D vs. static) for dynamic tracking: The dose profiles relate to the DLPs (y-axes) mentioned in Fig. 4.17. The graph in (a) shows the DLPs based on the 0 mm MLC-margin setup, the graph in (b) shows the DLP based on the 3 mm MLC-margin setup. Both plots distinguish between the 4D approach (blue) and the static method (red). Due to the location of the DLPs, substantial differences in (a) are visible for the normal tissue. The plot in (b) illustrates target specific variations.

4.4.3 Internal target volume: 4D planning vs. static planning

The ITV approach (see section 4.1.2) is a concept for static treatment planning with a free breathing technique for lung tumor treatments. Motion uncertainties are minimized with an appropriate target definition (ITV contouring, see Fig. 4.3). There is no dynamic motion compensation. Hence, the beam is fixed during irradiation. The dose application process is illustrated in Fig. 4.20. The figure shows the full 4D dose accumulation for an ITV based irradiation. Again, the POPI-models serves for investigations. As already shown in the previous outline, the 4D concept generates important differences compared to the static approaches. However, the static ITV concept is designed to compensate clinical motion effects.

The following test verifies the static concept with an accurate 4D dose accumulation calculation. For this purpose, the DVHs of the ITV (based on a single definition within the CT_{MIP}, see section 4.1.2) and the CTV inside reference set are compared. The static ITV dose calculations are based on the average CT (AIP). However, the assessment of the 4D dose accumulation is performed in the reference set. The test was calculated twice, for two MLC-margins surrounding the ITV. The results are illustrated in Fig. 4.21 with cumulative and differential DVHs. The measurements clearly reveal the robustness of the ITV concept. The DVH for the CTV (4D) is much more conformal as the DVH for the ITV (static) for both MLC setups. This can be proven by the cumulative and the differential DVH. The static ITV concept achieves the prescribed (static plan) doses with high probability. The validation results for the CTV (4D) are more conformal than prescribed for the ITV. However, the disadvantage of the static approach is observable for the DVHs of the right lung (Fig. 4.21). Here, a constant underestimation occurs (both margins) for the static solution with differences up to 4 – 5 % per dose. Side effects or OAR complications may not be taken into account, if a static simulation is used. It should be noted, that the comparison of the lung is more difficult, because the volume of the lung expanses during respiration. Here, the lung object at mid ventilation (static) is compared to lung object located in the reference set (4D). In summary, the results of the experiment confirmed the robustness of the ITV concept. The ITV method ensures the intended irradiation of the target in a static way. However, the 4D dose accumulation process could be used to improve the ITV dose planning to optimize the planning quality for the OARs in future.

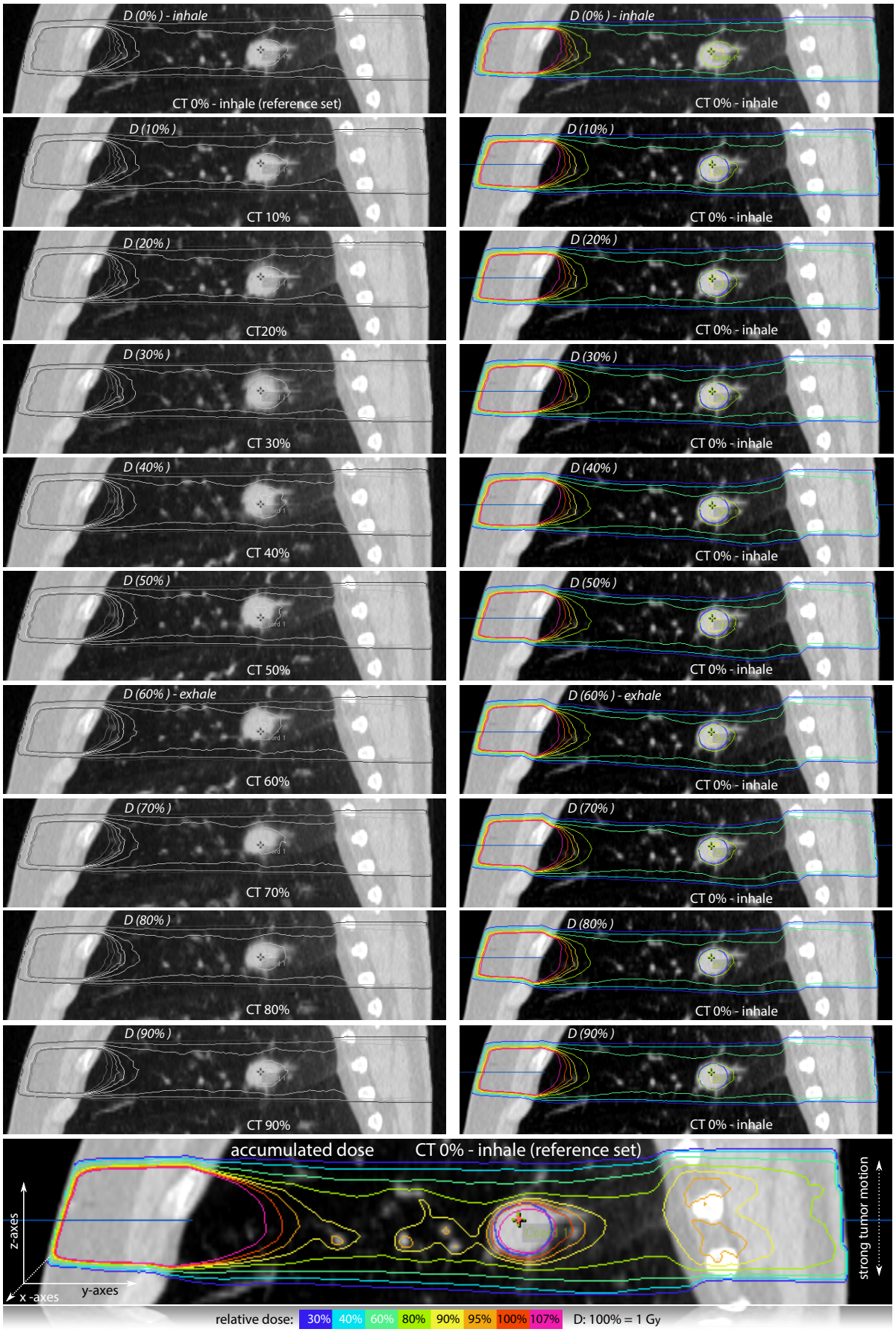

Figure 4.20 : The illustration of a 4D dose accumulation for the ITV dose application concept: The static beam compensates tumor motion with a large target definition (here: ITV + 3 mm MLC-margin). During irradiation the tumor is moving within the irradiated area. All single dose calculations are performed inside the respective breathing geometry (left). All dose distributions are mapped (IDP+PEM, dDMM) to the reference geometry (right) for dose accumulation (bottom).

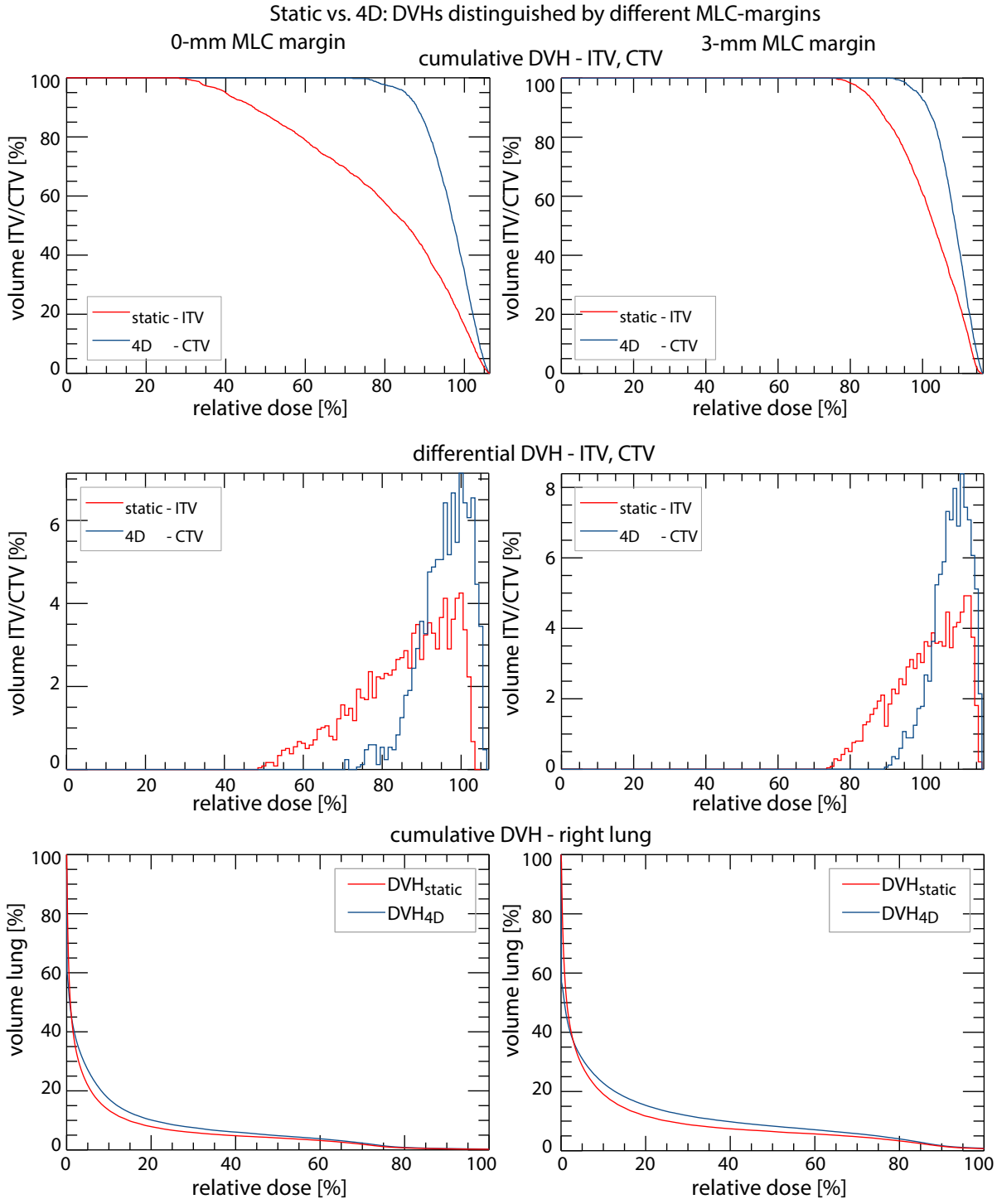

Figure 4.21 : Comparing clinical DVHs for the ITV concept using 4D and static approaches: The plots show the cumulative and the differential DVHs for the ITV (static solution, red) and the CTV (4D approach, blue). Also cumulative DVHs for the right lung are shown. The plots distinguish between two irradiation setups (0 mm MLC-margin surrounding the ITV → left; 3 mm MLC-margin → right). The static ITV concept ensures a safe irradiation of the CTV (4D), but the DVHs of the lung show a characteristic underestimation. The relative dose of 100 % refers to 1 Gy (see Fig. 4.20). The dose binning for the graph visualization of the differential DVH is 1 % per bin

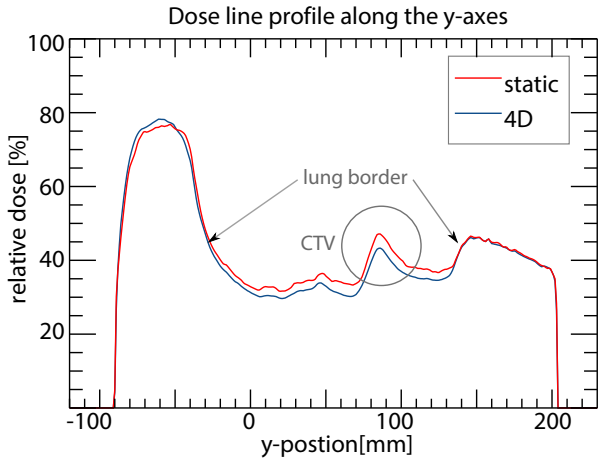

Figure 4.22 : y-DLP based on different planning approaches (4D vs. static) for gating: The shown dose profile regards to the DLP (y-axes) mentioned in Fig. 4.24. The graph shows a constant overestimation of the static approach compared to the 4D method. Especially for the region of moving tissue (lung border → lung border) the overestimation is meaningful. The small tissue motion within the gating time frame leads to a important effects.

4.4.4 Gating: 4D planning vs. static planning

The previous section confirmed the robustness of the ITV concept. The ITV concept is also intended for the gating modality due to small motion uncertainties. The following test proves the effect of those small motion uncertainties. In principle, gating compensates the tumor motion during irradiation with a simple time depending concept. The tumor is merely irradiated for a specific breathing phase (inhale). Thereby, a specific tumor location is assumed. However, even within the small time frame the tumor is moving. Hence, an adequate planning approach (ITV or 4D dose accumulation) is also necessary for gating. Fig. 4.23 illustrates the gated dose application with the aid of a full 4D dose accumulation approach. For this purpose, four breathing phases (0 %, 10 %, 20 %, 90 %) closed to the inhale position are used for irradiation. The mentioned phases are used for dose accumulation, whereas 0 % serves as reference set.
The following test investigates the motion uncertainty of gating. Therefore, the gated 4D dose accumulation plan is compared to a static dose calculation based on the reference set. The results are shown in Fig. 4.24. The illustration compares the dose distributions (static, 4D) planned on the reference set with a 3 mm MLC-margin around the CTV. Both dose distributions seem to be equal, but the dose percentage difference test and the 2D gamma test revealed important deviations at the upper and the lower beam penumbra. Indeed, the gamma test (2 % DD, 2 mm DTA) is positive, because 97 % of the analyzed points passed the criterion, but even these small differences could lead to important clinical effects. This can be shown comparing DVH for the CTV and the right lung in Fig. 4.25. The static approach shows a constant overestimation for CTV for both analyzed setups (0 mm,3 mm MLC-margin around the CTV). The effect is stronger for the sharp margin, but even the large margin does not remove the overestimation. The differential DVHs of the CTV show the shift of the dose-volume ratio figuratively. With the aid of a certain y-DLP marked in Fig. 4.23 and evaluated in Fig. 4.25 it is possible to explain the dose overestimation. Especially at the border of the CTV (location of the DLP), the small tissue movements lead to a reduction of dose within the 4D approach. This is confirmed by the DLP plot. The dose reduction is not considered in the static method. Hence, the DVH is shifted to larger doses, but this is not correct. However, the DVHs of the lung do not show any differences. The volume of the organ is too large in relation to mentioned dose shifts. It may become important for larger treatment areas. In conclusion, the gating approach is a good method to compensate tumor motion. However, the tumor is even moving within the small time frame. Such movements could have a clinical effect, especially for the CTV. It should be recommended to use an adequate approach for planning (static ITV or 4D dose accumulation), because the small movement during gating is not negligible.

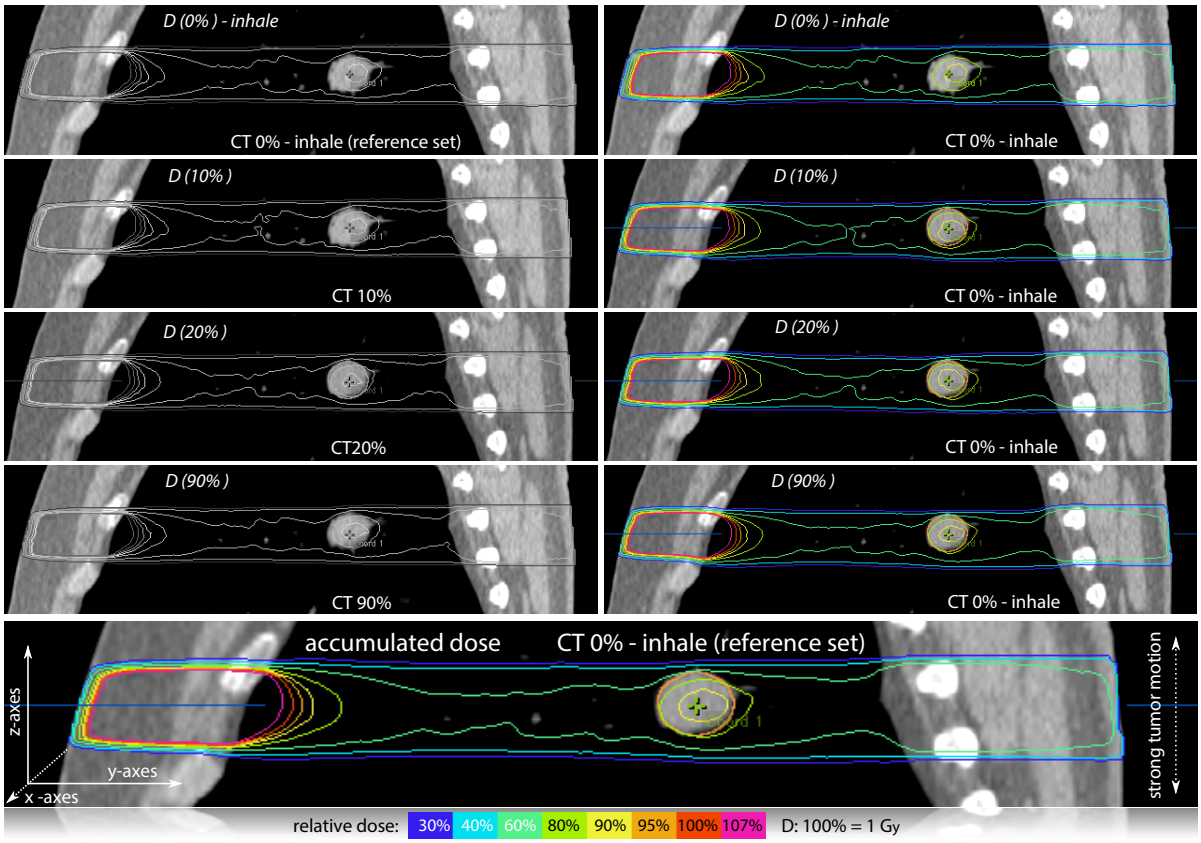

Figure 4.23 : The illustration of a 4D dose accumulation for gating: The static beam (3 mm MLC-margin surrounding the CTV) compensates tumor motion with time dependent irradiation. Hence, the treatment occurs merely for a specific time frame to ensure a defined tumor position during dose delivery. For this purpose, only time phases closed to the inhale geometry are used for dose accumulation (0 %, 10 %, 20 %, 90 %). During irradiation the tumor is slightly moving. All single dose calculations are performed inside the respective breathing geometry (left). All dose distributions are mapped (IDP+PEM, dDMM) to the reference geometry (right) for dose accumulation (bottom).

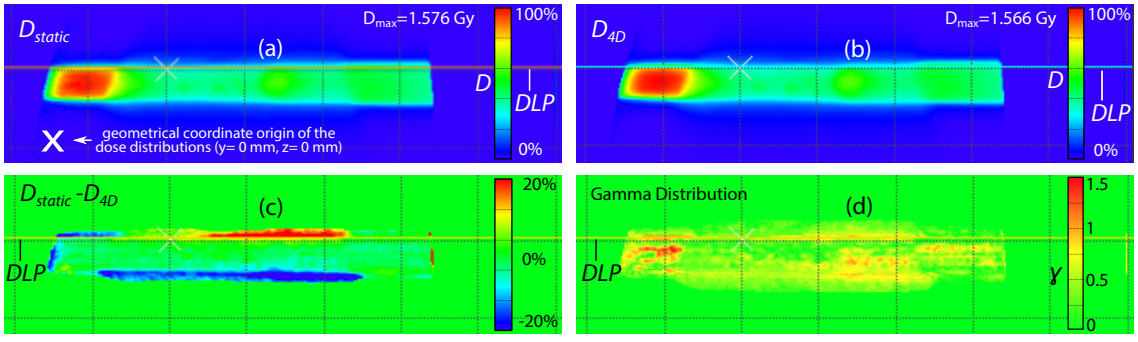

Figure 4.24 : Comparing static and accumulated dose distributions for gating: The figure illustrates the static (a) and the accumulated dose distribution (b) based on the setup shown in Fig. 4.23. The differences are proven by the local percentage dose difference test in (c) (parameters similar to Fig. 4.17) and by the 2D gamma test in (d) using a DTA of 2 mm and a DD of 2 %. 97 % of the analyzed points passed the criterion ($\gamma < 1$). For difference investigation, a y-DLP is located in a specific border region of the CTV. Both tests use the absolute dose values of the respective dose distributions.

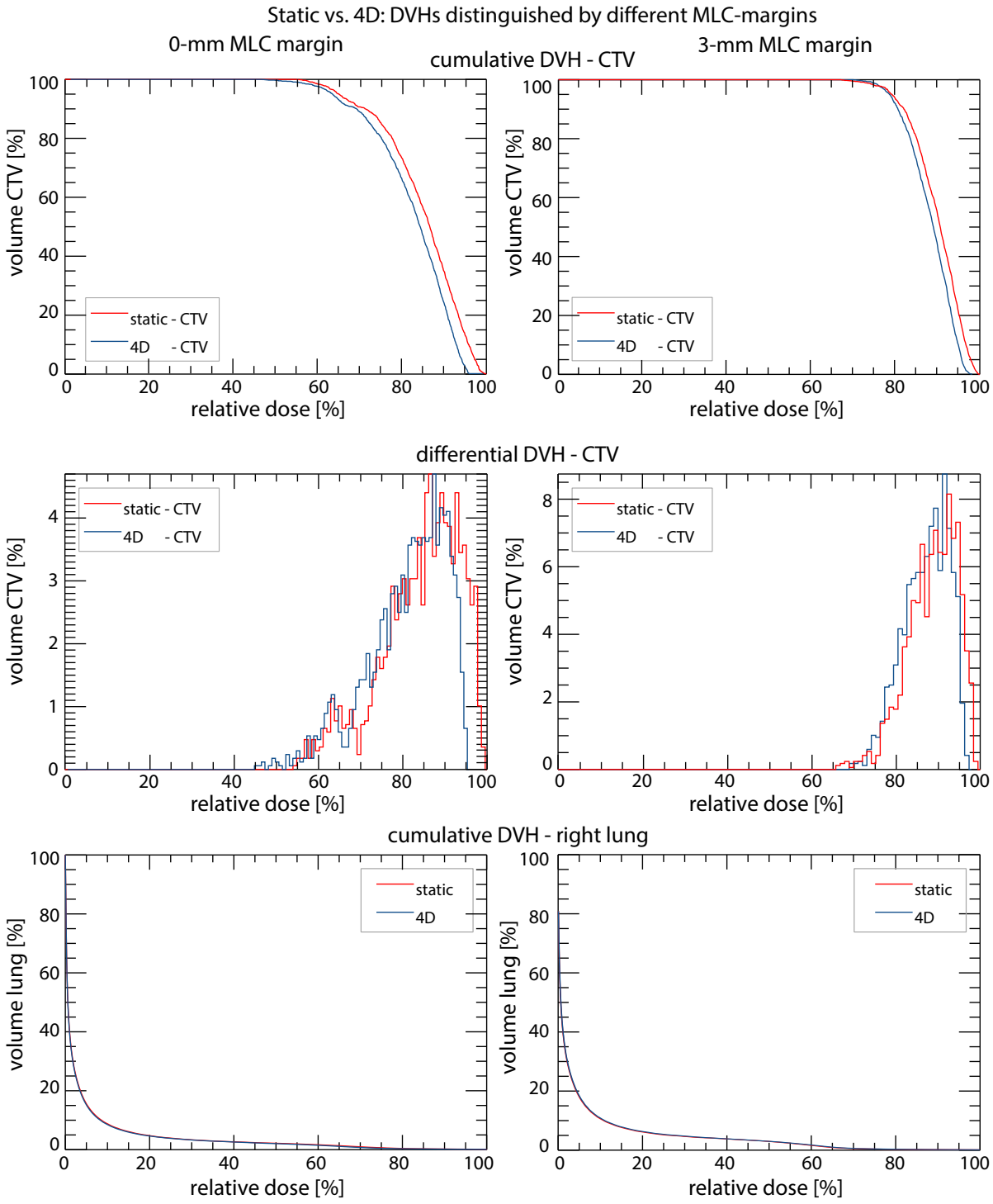

Figure 4.25 : Comparing clinical DVHs for the gating concept using 4D and static approaches: The plots show the cumulative and the differential DVHs for the CTV (static solution → red; 4D approach → blue). Also the cumulative DVHs for the right lung are shown. The plots distinguish between two irradiation setups (0 mm MLC-margin surrounding the CTV → left; 3 mm MLC-margin → right). Especially the CTV shows characteristic differences with deviations up to 4 – 5 % and a constant overestimation using the static approach. The DVHs of the right lung are equal. The relative dose of 100 % refers to 1 Gy (see Fig. 4.23). The dose binning for the graph visualization of the differential DVH is 1 % per bin.[7]

[7] Comparing the absolute dose of the static test for gating and the respective static dose for tumor tracking in Fig. 4.18 reveals that a lower value of monitor units is used for gating as for dynamic tracking. However, for this comparison study it is important to use the same value of monitor units within one test (4D vs. static). The different test series are comparable due to their relative results. The monitor units of several test series could vary due to different sizes of the MLC-margins, different number of CT geometries used for accumulation and an adequate adjustment of the value of monitor units to divide the value on different dose calculations for different breathing phases.

4.4.5 Conclusions

The previous tests confirmed the clinical requirement of an adequate 4D planning approach for SBRT of lung cancer treatments. In conclusion, it can be said that the 4D approach offers the most accurate method to explore and simulate applied doses on the deforming tissue. Independent from the treatment modality (here: dynamic tumor tracking, ITV concept, gating), all tests describe a momentous difference of the physical dose distributions, if a static or the 4D approach is used. Those variations are confirmed by local percentage dose tests and 2D gamma tests (Fig. 4.17, Fig. 4.24) and individually investigated by dose line profiles. The deviations have even a clinical effect. The 4D approach generated more accurate DVHs for the CTV either for dynamic tracking or for tumor gating compared to the static method (Fig. 4.18, Fig. 4.25). DVH-differences for the lung are negligible for gating and tracking due to the small irradiated lung volume compared to the full organ. The 4D investigation of the ITV concept revealed the robustness of the static ITV approach. The 4D DVHs for the CTV confirmed the prescriptions estimated for the static ITV (Fig. 4.21). For example, the 4D CTV was treated with higher conformity as statistically simulated for the ITV. However, the lung dose was characteristically underestimated in this case, which could cause unplanned side effects.
In conclusion, it should be recommended to use the 4D approach for tumor tracking, because the motion uncertainties are important for dose application. Tumor gating also requires an adequate planning approach for dose calculation, because even the small tissue motion is not negligible. The ITV concept is a robust approach to ensure the treatment prescriptions in a static way. Thus, it is also well suited for gating. However, the 4D planning approach is very useful to verify the ITV concept, especially for the minimization of side effects and for plan optimization. The comparisons 4D vs. static of all modalities revealed differences that are not negligible. This confirms the compelling need of a sufficient 4D dose planning model for lung SBRT.
Since all conclusions of this study were based on one patient data set (POPI-model), further evaluation studies should repeat the investigation for a large number of patients. In many cases tumor location, tumor motion path, tumor dimension and other properties affect the planning outcome. A comprehensive future study would be helpful to generalize the mentioned hypotheses.

4.5 Discovering possibilities for future developments

The explained 4D software planning module and the inherent functions enable many possibilities for future developments. Such applications may improve the full treatment planning process.

4.5.1 Simplified data acquisition

On one side, there is the new hybrid image fusion model. A further development of the approach could be an 4DCT merely containing the inhale and the exhale breathing phase. Due to the iterative design of the hybrid approach, it would be possible to estimate every time step between the contrary amplitudes. This results in a simplified data acquisition and offers time savings for an accurate 4D dose accumulation approach (see Fig. 4.26). The final improvement could be an 4D dose accumulation approach without any 4DCT. A static CT is used for deformation, whereas the vector field is extracted from an external modality (see Fig. 4.27). Maybe a fluoroscopy or another motion tracking system is used to approximate sufficient motion vector fields to deform the lung object which is based on a static CT. Another solution could be an atlas with generic motion vector fields, which are applicable for every lung indicated by specified patient properties. Furthermore, the hybrid deformation inherit the advantage of real-time deformation calculations. This results in many other possibilities, like a real-time dose verification. This could be helpful, if the simulated breathing amplitude and the real breathing amplitude during irradiation differ strongly. Such a system would be able to calculate

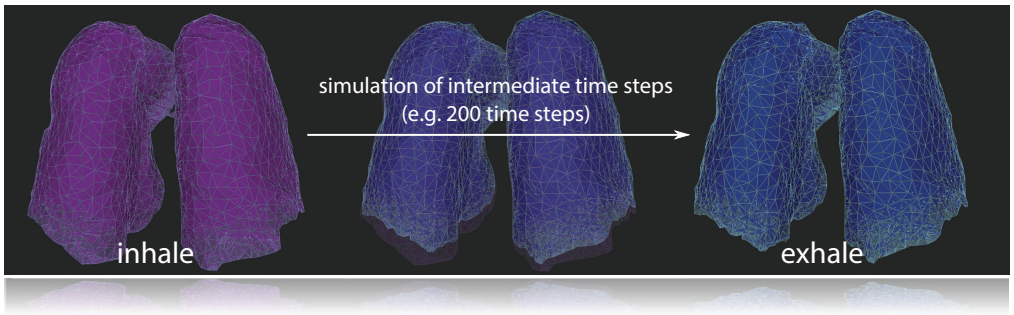

Figure 4.26 : Full breathing cycle simulation with two time states: The hybrid elastic image fusion approach (see section 2.2.1) introduced by this thesis enables the possibility to simulate a set of time states between the discrete defined CT states (e.g. inhale and exhale). In future, this may characteristically reduce the expenditure for 4DCT data acquisition. To simulate the full breathing cycle merely two breathing phases (exhale, inhale) have to be acquired.

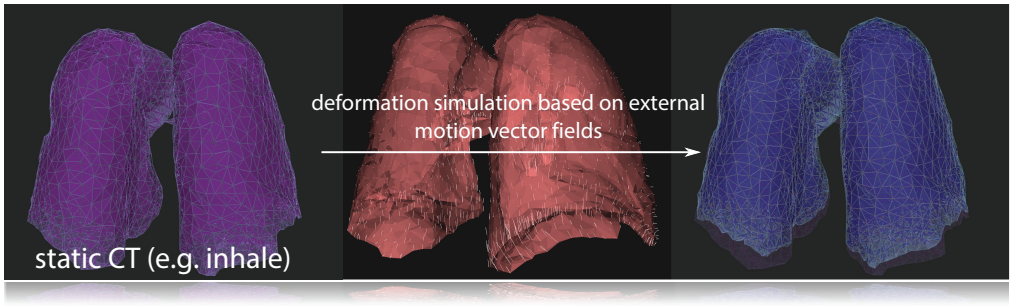

Figure 4.27 : Deformation simulation without 4DCT: The hybrid elastic image fusion approach (see section 2.2.1) may be able to simulate the deformation of the lung merely based on a static CT data set. This could be achieved if the motion vector field is externally applied. Such external motion vector fields may be extracted from a generic data atlas or from an another modality (e.g. fluoroscopy). The elastic deformation could be calculated in real-time in parallel to motion vector acquisition.

this discrepancy in order to react with a sufficient dose correction during irradiation or for the next dose application session (fraction). All the mentioned ideas regarding hybrid DIR for 4D dose accumulation should be discussed carefully in future studies and developments.

4.5.2 Four dimensional IMRT

Furthermore, the 4D dose accumulation concept enables specific possibilities for certain dose application techniques. 4D IMRT is one of those concepts. First proposals were made by *Li et al.* [56] and *Unkelbach et al.* [103]. The idea is to consider the individual dose distributions of the breathing cycle during IMRT optimization. For this purpose, the total scope of functions included in the developed 4D software planning module of this work is necessary. This mainly includes the accurate DIR, the dose accumulation and the time dependent application of individual dose distributions. The following outline shows a basic approach to implement a possible 4D IMRT. The basis of IMRT is the optimization of a cost function f_{cost} controlled by constraints [114]. Usually, the cost function is controlled by the difference of an optimal prescribed dose $D_p(x)$ and the delivered dose with a specific beamlet setup $D(x)$. Hence, f_{cost} can be written as:

$$f_{cost} = \sum_{V} I(\vec{x}) \cdot \left[D(\vec{x}) - D_p(\vec{x}) \right]^2 \tag{4.4}$$

with $\vec{x}$ being a voxel of the entire volume. $I(\vec{x})$ represents the importance of the respective voxel, i.e. $I(\vec{x})$ weights specific voxel differences to achieve clinical constraints. The optimization tries to find the best solution for the parametrization of the cost function. A 4D IMRT approach of such an optimization has to calculate precisely the 4D accumulated dose to obtain the applied dose of the object. For this purpose, $D(\vec{x})$ represents even the accumulated dose. It must be calculated for the reference set i. The necessary dose operator $D_{i\sum}$ is derived by formula (3.12). Hence, (4.4) can be written as:

$$f_{cost} = \sum_{V} I(\vec{x}) \cdot \left[D_{i\sum}(\vec{x}) - D_p(\vec{x})\right]^2; \quad D_{i\sum} = \sum_{j=1}^{n} W_{ji}(v_{ji}) * D_j \tag{4.5}$$

The formula illustrates the dependency of 4D IMRT on the dose transformation algorithm (W_{ji}) and on the motion vector field v_{ji} (DIR) calculated for all breathing phases n. The disadvantage of the 4D method is also shown: The entire dose accumulation $D_{i\sum}(\vec{x})$ must be calculated before optimization, because single dose points could influence entire dose regions through deformation. Due to dose accumulation, the number of parameters of freedom increases significantly comparing 4D IMRT with static IMRT. Another disadvantage is the selection of time depending dose applications. The 4D concept, which considers beamlets that have to be applied for a specific breathing phase j, require a precise respiratory patient monitoring system (real-time). Furthermore, the dose delivery time increases enormous due to repetition time (breathing cycle) of certain geometric tissue states. A further problem of the approach is the penalization of single voxel values during IMRT. The influence of certain voxels to whole neighborhood areas (set of different voxels) during dose accumulation impedes the weighting of single voxel differences $D(\vec{x}) - D_p(\vec{x})$. Therefore, *Li et al.* [56] offers a practical solution that combines the static ITV concept with 4D dose accumulation for a robust implementation of 4D IMRT. The short outline demonstrates many new possibilities for 4D dose calculations. However, the power of the 4D concept is always accompanied with a large number of free parameters, which could lead to inflexible solutions. Therefore, all future implementations need a sufficient and comprehensive verification study.

5 Summary and Outlook

The aim of this thesis is to analyze the potential benefits of four dimensional (4D) dose planning for stereotactic body radiation therapy (SBRT) of lung cancer. Static concepts like the internal target volume (ITV) fulfill not longer the requirements of accurate dose planning. Due to the continuous development of the dose application machines (e.g. tumor tracking), the delivery of temporally varying dose distributions on deforming anatomies became possible. In order to fulfill the requirements of dose planning, an accurate 4D solution needs to be developed which is also suitable for clinical practice. This is the goal for this thesis.
For this purpose, a detailed investigation of the universal 4D dose planning work-flow is necessary. The general steps are well known and widely used for clinical research, but a detailed analysis shows large potential for improvement. The present thesis discovers two major problems during 4D dose planning: the deformable image registration (DIR) of 4DCT data and the 4D dose transformation during dose accumulation (section 1, Fig. 1.1). These major topics are investigated separately. Due to the sequential concept of 4D dose planning, the present thesis is divided in three chronological chapters:

1. *Elastic image fusion for respiration induced deforming patient models:*
   → compares and analyzes the accuracy of DIR algorithms for 4DCT data (lung)
2. *4D dose calculation based on accumulation of time dependent dose distributions:*
   → defines the requirements for 4D dose accumulations
   → compares the accuracy of dose accumulation algorithms with regard to the defined goals
3. *Evaluation of the 4D treatment planning concepts:*
   → offers a practical 4D prototype planning solution
   → proves the clinical impact of the findings derived by 1 and 2
   → proves the clinical benefit of the 4D planning approach compared to established static methods

1. Elastic image fusion for respiration induced deforming patient models: The beginning of the process is an adequate imaging that records temporally sufficiently resolved image data. Therefore, section 2.1 gives an overview of proper respiratory correlated 4DCT image acquisition. There exist typical temporal requirements (section 2.1.2). The next step is the tissue motion calculation generated by DIR algorithms (section 2.2). There exist a large number of algorithms. At least, two major groups are established for 4DCT image fusion.
The first group contains signal and image processing methods (section 2.2.1), so called information driven patterns (IDP). The Free-Form-Deformation (FFD) by *Rueckert et al.* is the best known algorithm. This work has proven the accuracy of two different FFD implementations. On the one hand, an implementation developed in this thesis based on the *iPlan™ RT* framework and on the other hand, the results of an implementation provided by the scientific POPI-model [105]. This model offers also a respiratory correlated 4DCT data set and 40 landmarks defined by medical experts. These anatomic coordinates are suitable to verify tissue displacements. They are distributed over the full 4DCT geometry and located in every breathing phase. The experiment of

this work used the landmarks to verify the two FFD implementations. The test reveals an acceptable accuracy for the IDP concept with similar results for both implementations (mean deviation about 1 mm). Facing global registration of 4DCT data, IDP has proven to be a very robust method. However, a further analysis of IDP has shown that motion estimation at lung borders is error prone. Here, the lung slipping effect occurs. For this purpose, 20 new landmarks are introduced that especially cover those areas. The second experiment achieved deviations up to 15 mm (*iPlan™ RT*) or 10 mm (POPI-model). Indeed, these results affect only a small part of the lung, but they are not acceptable.

The second group of deformation algorithms, so called physical elasticity models (PEM), is based on methods that simulate mechanic laws. They calculate the physics of lung tissue motion and deformation (section 2.2.2). This work uses a specific implementation of PEM combining finite element methods (FEM) and mass spring models (MSM). However, the complexity of such algorithms currently allows only the simulation of single organ deformations. Motion estimation for the entire 4DCT requires too many parameter definitions for the interaction of various tissue types.

For this purpose, the present thesis introduced a third method for DIR of respiratory correlated 4DCT, the hybrid approach. The aim of the hybrid approach is the combination of IDP and PEM using advantages of both to achieve a higher accuracy. The hybrid approach is a sequential series of algorithms. The robustness of IDP is used to achieve at first an accurate vector motion field. In a second step, the motion estimation inside the lung is getting optimized with PEM. The idea is, to use highly precise vectors (filter) of IDP to deform the full 3D lung object (Fig. 2.23). The filter vector set of IDP drives the elastic PEM simulation to calculate remaining vectors more realistically. The biggest challenge of IDP is the determination of a sufficient filter. Poorly chosen filters deteriorate the overall accuracy (section 2.3.1). For this reason, the hybrid approach was used for DIR to prove the general accuracy with global landmarks. The experiment achieved a slightly better results as the IDP concept. Therefore, the test confirmed the main suitability of the hybrid approach for DIR of 4DCT. To prove the benefit of the new method (section 2.3.1) the lung-slipping landmark test was repeated. The experiment achieved an important improvement. The hybrid approach signifcantly minimizes the maximum landmark error (Fig. 2.35): 15 mm → 9 mm (*iPlan™ RT*) and 10 mm → 5 mm (POPI-model); as well as the median landmark error: 7.5 mm → 4.5 mm (*iPlan™ RT*) and 5 mm → 2 mm (POPI-model); In conclusion, the hybrid approach offers the possibility for more precise DIR deformations accompanied with the robustness of the IDP solution. It should be noted, that also the hybrid approach has a small weakness. This is the effect of false positive lung slipping (Fig. 2.36). In such cases, the method predicts motion for non-deforming tissue. A better filter may improves these influences.

In summary, the analysis presented accurate methods for DIR of respiratory correlated 4DCTs. IDP offers a robust solution for global thorax registration, but the new hybrid approach is able to simulate the lung slipping effect more accurately. The validation has shown that both approaches are suitable for 4D dose calculations. Furthermore, the hybrid approach offers a lot of new future possibilities (section 2.4), e.g. the simulation of motion between defined breathing phases (inter-phase motion simulation).

Conclusions:

1. IDP offers a robust solution for global DIR of respiratory correlated 4DCT data.
2. IDP is weak at lung border areas (lung slipping effect).
3. The new hybrid approach significantly improves the accuracy for lung border areas.
4. The hybrid approach offers new possibilities (e.g. inter-phase motion simulation).
5. 4D planning using IDP or the hybrid approach must be decided individually with regard to the present influence of lung slipping and the technical effort.

2. 4D dose calculation based on accumulation of time dependent dose distributions: The second independent part of this thesis deals with the topic of 4D dose accumulation. For this purpose, general numerical approaches that are necessary for dose transformation are being introduced (section 3.1). The main concept is the calculation of several dose distributions that respectively depend on temporal CT geometries. With the aid of motion vector fields (result of DIR) all dose distributions are transformed to a reference geometry, which serves for clinical assessment (section 3.1.1). An important problem that occurs during dose transformation is the deformation effect (section 3.1.1). The numerical effect describes the unification of inhomogeneous dose distributions based on inhomogeneous densities. The question is: How to calculate a transformed voxel dose, if different deforming voxels with varying doses and varying masses are involved? The problem is currently not fully explored. For a better understanding, section 3.2 gives a detailed overview of biological dose dependencies that exist during dose transformation. It is proven that the tissue response directly depends on a combination of dose and mass (section 3.2.2), so called mass effect. Finally, the outline leads to the mass weighted dose average for final voxel dose calculations.

A list of algorithms for 4D dose transformation is described in section 3.3. For example, the dose interpolation model (DIM) neglects the mass effect. This thesis introduces a new algorithm, so called divergent dose mapping model (dDMM), that directly implements the mass weighted dose average (section 3.3.1). In contrast, several energy algorithms apply the indirect equation due to the determination of all mapped energies in relation to their masses (section 3.3.2). To find an accurate solution, the thesis presents a comprehensive 4D transformation error evaluation study (section 3.4). The study analyzes dose distributions in specific regions of interest (ROIs) before and after dose transformation. For comparison, the dose transformations are performed with all mentioned algorithms. To assess the quality of a certain ROI transformation, a new error metric is introduced (section 3.4.1). This metric is based on the analysis of the dose mass histogram (DMH). A good mapping approach, should not change the DMH during transformation, because the DMH inherits all dose-mass relations of the applied dose. The DMH error metric calculates the integral difference of the DMH before and after dose transformation. Other proposed metrics either consider average dose values (section 3.4.2) or integral energy mass ratios for the entire ROI. Therefore, coordinate specific dose mass relations are neglected in such cases. The DMH approach represents a real improvement for verification of the 4D dose transformations.

The 4D evaluation study of this work compared 900 small ROIs distributed in the dynamic thorax geometry of the POPI-model. All transformations are repeated for different algorithms, for different breathing phases, for different fluence distributions and for different voxel sizes (section 3.4.3). Evaluated by the DMH metric, all results revealed the highest accuracy for the dDMM model (section 3.4.4). Most significant is the comparison of the voxel size error dependency (Fig. 3.33). For example, dDMM received a median DMH error of 0.6 for a voxel size of 2 mm. The second best algorithm yielded only 1.2, achieved by the energy mass congruent mapping (EMCM). Any method except of DIM generated a reasonable voxel size dependency. However, DIM yielded especially for large voxel sizes bad results up to mean errors of 45 % (8 mm), in contrast to dDMM with only 19 %. This supports the correctness of the biological investigations of this thesis, since DIM neglects the mass effect. Further evaluations of this study investigated the 4D dose error and its spatial dependency, the behavior of dose gradients induced by inhomogeneous fluences and the influence of different breathing amplitudes. In general, dose transformations are more error prone for lung tissue areas due to their large density deviations and due to the more often occurring deformation effect. This conclusion was confirmed by a new method of error identification, the error localization map. Furthermore, it can be concluded that the dose transformation error is mainly driven by dose gradients. However, it does not matter whether these gradients are induced by density deviations or fluence manipulations, because different artificial fluences of this study yielded no significant change on the results, because the geometry includes already strong density

deviations. The investigation of the breathing amplitude revealed that some energy models are more error prone in case of large displacements. This was observable for the basic energy transformation models (bETM, pETM) (Fig. 3.39). For large amplitudes, more vector field artifacts are present. The mass energy discrepancy (MED) error is introduced whenever masses between source and target of the mapping strongly. For example, many energy deposition events are located in voxels with a high mass during dose calculation. Despite the high energy values, the voxel-result is an adjusted dose, because of the high voxel mass. However, if large energy values are mapped to voxels with a significant lower mass, the result is a very large unrealistic dose. Since there is never an optimal vector motion field, such cases were directly proven in this study. In general, the MED error occurs only for energy models, dDMM and DIM are not affected. The MED error for the precise EMCM method is much smaller, because the model uses the similar mass values for energy and dose calculation. The results of EMCM are also acceptable. However, the numerical MED effect can not be completely excluded for EMCM.

This study presented several tests to investigate the capabilities of specific dose transformation models for dose accumulations based on different breathing phases for lung cancer patients (section 3.5). DIM implements a rather unsuitable approach. The basic energy models are prone to errors especially for energy mass displacements on high voxel resolutions with heterogeneous mass distributions. In contrast, dDMM as well as EMCM are best suited for practical applications. Their algorithm structure is consistent with the biological mass effect. EMCM is associated with a high technical effort and it implements the numerical MED error. However, dDMM is more straightforward, immune to MED errors and also more efficient.

Conclusions:

1. The mass weighted dose average is a precise formula for dose transformations.
2. The new DMH metric improves the investigation of the transformation quality.
3. DIM implements an error prone approach due to the neglection of the mass effect.
4. The MED error prevents precise results for basic energy models (bETM, pETM).
5. dDMM and EMCM are well suited for accurate dose transformations.
6. The new dDMM is the most efficient algorithm of this study.

3. Evaluation of the 4D treatment planning concepts: The fourth chapter presents an overall assessment of the entire 4D approach. For this purpose, an individual 4D planning prototype is developed in this work (section 4.1.1, Fig. 4.1). The software is an individual implementation of *iPlan™ RT*. Based on the findings of chapter two and chapter three, the prototype contains two different DIR algorithms (IDP, hybrid approach) and two dose transformation models (DIM, dDMM). The aim of this chapter is the investigation of clinical effects. Due to the scope of this study, all tests were simulated for one patient geometry derived by the POPI-model.

The first investigation (section 4.2) explains the influence of the DIR algorithm. For this purpose, 4D doses were generated using IDP or the hybrid approach with the same irradiation setup. The study shows (section 4.2.1) that these dose distributions are characteristically different. The new hybrid approach offers more realistic dose transformations. The differences are clearly visible at lung border areas, where the lung slipping effect occurs. This is confirmed by specific 2D gamma tests and demonstrated with the comparison of different dose line profiles (Fig. 4.6). However, the clinical effect of the differences is negligible small. The dose volume histograms (DVHs) for the clinical target volume (CTV) and the right lung are approximately the same. Motion optimization of the hybrid approach especially occurs at lung border areas, where the CTV is not located in the investigated patient geometry. Furthermore, the irradiated lung border area is very small in relation to the entire organ. Hence, no effect is measured for DVH of the lung. However, if a larger volume is treated, the effect becomes important. This is proven with a helping volume that only includes the irradiated lung border area. Here, significant different DVHs are generated (Fig. 4.9). The benefit of the hybrid approach

in relation to its technical effort must be estimated individually. Nonetheless, the hybrid approach calculates more realistic dose transformations.

The second part investigates the clinical influence of using different dose transformation models (section 4.3). For this purpose, the same dose transformations are repeatedly calculated using either DIM or dDMM. A dose grid size of 2 mm is used to ensure comparable results for DIM and dDMM (section 4.3.1). The experiment shows characteristic differences for the DVH of the CTV with deviations up to 12 %. The results confirm the importance of the mass effect which is neglected by DIM. The deviations are either demonstrated for a single beam dose transformation or for a complex does distribution. Meaningful differences are also observable for single dose line profiles or 2D gamma distributions. The DVHs for the lung are approximately the same, which is explainable with the small volume ratio. In conclusion, it is highly recommendable to use an efficient dose transformation model (e.g. the new dDMM approach) for clinical 4D treatment planning, since the resulting deviations of inaccurate methods are clinically not negligible.

The third investigation compares established static planning methods with the advanced 4D dose planning approach of this work considering the new hybrid approach for DIR and the new dDMM for dose accumulation. For this purpose, three different treatment modalities for lung cancer SBRT are explained (section 4.1.2): dynamic tracking, free-breathing accompanied with the internal target volume (ITV) and gating. In detail, the dose accumulation process using the dynamic tracking procedure (4.4.1) generated meaningful deviations compared to the static method. This is proven with several 2D gamma tests and dose line profile comparisons. The DVHs for the CTV show a characteristic overestimation when using static calculations. Hence deviations up to 9 % are observable. Those results clearly confirm that static methods are not capable of simulating all temporal effects. Deforming geometries and adapting dose distribution during dynamic tracking require 4D methods for clinical precision.

In contrast to motion adaption, the concept of the ITV is an established approach that statically considers the motion uncertainty. The method is widely used for lung SBRT. The comparison of the ITV concept and the 4D approach serves for verification (section 4.4.2). The test compares the prescribed static dose of an ITV with a verification dose for the CTV generated by a full 4D dose accumulation. The results clearly show the robustness of the ITV concept. The prescribed dose for the target is delivered with a higher conformity (CTV) as simulated (ITV). However, the analysis of the lungs DVH reveals an underestimation up to 5 % using the static method. Side effects may not be taken into account during static dose planning. Therefore, it should be recommended to use the 4D approach for verification of the ITV-concept.

The last test compares static planning and 4D dose accumulation for tumor gating (section. 4.4.4). Assumed is an entire motion compensation due to the temporal dose delivery in a short time frame. However, the results show characteristic differences confirmed by a gamma test, by different dose line profiles and by the comparison of the DVHs of the CTV with deviations up to 5 %. The conclusion is that also small tissue movements, as they occur during gating, can have important clinical effects. Therefore, an adequate planning approach like the ITV or the full 4D dose accumulation approach should also be used for gating. Conventional static planning is not sufficient for tumor gating.

Conclusions:

1. The thesis presents a comprehensive prototype for 4D dose planning (*iPlan™ RT*).
2. The new hybrid approach optimizes the final 4D dose at lung borders.
3. The new dDMM improves the quality of 4D dose accumulations.
4. The full 4D planning approach is clinical more accurate than static methods.
   This is shown for tumor tracking, gating and free breathing with the ITV concept.

In summary, this thesis presents new algorithms and techniques to optimize the entire 4D dose planning concept. The final concept achieves a significant benefit for the dose planning process. All comparisons of static and dynamic 4D dose calculations revealed characteristic differences measured by clinical criteria. The variations are clinically significant. Hence, this thesis confirms the need of a comprehensive 4D dose planning approach, due to the uncertainties of static methods. Furthermore, the thesis shows that the quality of the 4D outcome directly depends on its sub-steps: the elastic image fusion and the 4D dose accumulation model. This thesis has shown that a new hybrid approach for DIR has a final impact on the 4D dose distribution with a more accurate dose simulation at lung border areas. Furthermore, the new dDMM method significantly improves the quality of the 4D dose distributions. Further improvements are, however, possible. New possibilities are shown, e.g. the simplified data acquisition or the 4D IMRT concept (section 4.5). Since this work uses only one patient data set, future comparison studies should investigate a large set of patients for general conclusions. The future will show if the mentioned algorithms will be used for clinical treatment planning. The continuous improvement of treatment application machines does, however, require at least a part of the demonstrated concept.

Acknowledgments

At this point I would like to take the chance to thank all the people who contribute to this work. Without their support the work would not have been possible.
First and foremost, I want to thank my supervisor and first referee Prof. Dr. Jan J. Wilkens. He was always available for advice and consultation and his guidance was very important for the outcome and the shape of this work. I am grateful for his enduring patience and his enthusiasm for medical physics, which was always a motivation for me. He deserves my gratitude for spending so many time in the research and the improvement of my work. You gave this thesis the decisive direction and the right impulse. It was a pleasure to work with you! I am also very thankful to Prof. Dr. Franz Pfeiffer for being the second referee.
This work was realized in cooperation with the Brainlab AG, where I had the great opportunity to work as postgraduate and software-engineer in the field of medical physics. That gave me the possibility to collaborate with many other researchers and colleagues to investigate the problems of four dimensional dose calculations.
Special thanks go to Dr. Wolfgang Ullrich for being a great mentor, supervisor and colleague. You taught me to work hard, to question what I am doing, to be exact and many other important things. Thank you for sharing your experiences and knowledge of medical physics with me, although you had a tough time schedule.
Furthermore, I am very thankful to share my office with Dr. Bernhard Fischer for being my first supporter solving many challenges that occur as part of this work. Thank you for so many purposeful discussions and for the careful proofreading of the manuscript.
Additionally, I would like to thank Johannes Flake for being a very helpful colleague and friend. Without your support and the comprehensive software implementations for the hybrid elastic image fusion model the results of this work would not have been possible. Furthermore, I would like to thank Cecilia Hung, Linda Ahnen and Claus Promberger for the intensive proofreading of the manuscript and for a lot of meaningful discussions for 4D dose calculations. I am also very grateful to work with so many researchers and colleagues who are always available for discussions about medical physics and software engineering. Therefore, special thanks go to: Dr. Matthias Fippel, Dr. Stefan Schell, Dr. Thorsten Bschorr, Stefan Popp, Ullrich Haberhauer and all my other colleagues that supported this work. Working at Brainlab was always a pleasure.
And last but not least, I would like to thank my parents Kerstin and Thomas, my brother Sebastian, my grandparents Marianne, Renate and Ewald as well as all of my friends for their continuous support and inspiration that motivated me for this work.
Finally, I am so grateful to my fiancee Julia for her love and for always supporting me, regardless of what I am doing. This thesis is devoted to you. Thank you!

List of Publications

Publications

- Milz S., J.J. Wilkens and W. Ullrich: "A dose error evaluation study for 4D dose calculations", in preparation, planned for 2014 (paper).

- Milz S., J.J. Wilkens, W. Ullrich and J. Flake: "A new elastic image fusion model for lung deformation simulation in 4D dose calculations", Radiother Oncol, ICTR-PHE 2014, Geneva, accepted, planned for 2014 (conference proceeding).

- Milz S., J.J. Wilkens and W. Ullrich: "Ein massen-gewichtetes Dosistransformationsmodell für 4D Dosisberechnungen", in: Abstractband der 44. Jahrestagung der Deutschen Gesellschaft für Medizinische Physik, Cologne, p.143-145, ISBN-978-3-9816002-1-6, 2013 (conference proceeding).

- Milz S., J.J. Wilkens and W. Ullrich: "A mass-weighted dose mapping model for 4D dose calculations", Medical Physics International Journal, vol. 1, No. 2, p.336, ICMP-2013 The International Conference on Medical Physics, Brighton, 2013 (conference proceeding).

- Hietschold V., S. Milz, N. Abolmaali, R. von Kummer, M. Laniado: "Segmentation of cranial MR images : retrospective signal intensity correction concerning inhomogeneous B 1 intensity", European Congress of Radiology, Vienna, 2011 (poster and e-paper).

Patent

- Milz S., and J. Flake: "Method and Device for Determining a Transformation between Two Images of an Anatomical Structure", PCT application number: EP2013075277, December 2^{th} of 2013

List of Figures

List of Tables

List of Abbreviations

4DCT ..... Four Dimensional Computer Tomography
4DTM ..... Four Dimensional Tissue Model
AIP ..... Average Intensity Projection
bETM ..... Basic Energy Transfer Model
CC ..... Cross Correlation
CG ..... Conjugated Gradient
CT ..... Computer Tomography
CTV ..... Clinical Target Volume
DD ..... Dose Difference
dDMM ..... Divergent Dose Mapping Model
DIM ..... Dose Interpolation Method
DIM ..... Dose Interpolation Method
DIR ..... Deformable Image Registration
DLP ..... Dose Line Profile
DMM ..... Dose Mapping Model
DP ..... Distance Preservation
DTA ..... Distance To Agreement
DVH ..... Dose Volume Histogram
ELM ..... Error Localization Map
EMCM ..... Energy Mass Congruent Mapping
FEM ..... Finite Element Method
FFD ..... Free Form Deformation
FWHM ..... Full Width at Half Maximum
GD ..... Gradient Descent
GTV ..... Gross Tumor Volume
HU ..... Hounsfield-Units
IDP ..... Information Driven Pattern
IGRT ..... Image Guided Radiotherapy
IIO ..... Inhomogeneous Irradiated Object
ITV ..... Internal Target Volume
LC ..... Local Correlation
LQ ..... Linear Quadratic
MC ..... Monte Carlo
MED ..... Mass Energy Discrepancy
MI ..... Mutual Information

MinIP ..... Minimum Intensity Projection
MIP ..... Maximum Intensity Projection
MLC ..... Multileaf Collimator
MSM ..... Mass Spring models
NTCP ..... Normal Tissue Complication Probability
OAR ..... Organs At Risk
OHM ..... One Hit Model
PB ..... Pencil Beam
PDF ..... Probability Density Function
PEM ..... Physical Elasticity Models
pETM ..... Probabilistic Energy Transfer Model
PSF ..... Point Spread Function
PTV ..... Planning Target Volume
ROI ..... Region of Interest
SAP ..... Surface Area Preservation
SBRT ..... Stereotactic Body Radiation Therapy
SSD ..... Sum of Squared grey value Differences
TCP ..... Tumor Control Probability
TM ..... Tissue Model
TRE ..... Target Registration Error
VP ..... Volume Preservation

Bibliography

[1] Adamus-Górka, M. *Improved dose response modeling for normal tissue damage and therapy optimization*. PhD thesis, Stockholm University & Karolinska Institute, 2008.

[2] Admiraal, M., Schuring, D., and Hurkmans, C. W. Dose calculations accounting for breathing motion in stereotactic lung radiotherapy based on 4D-CT and the internal target volume. *Radiotherapy and Oncology 86*, 1 (Jan. 2008), 55–60.

[3] Ahnen, L. *Phantom Development for the Validation of 4D Dose Calculation Models for Lung Tumors*. Diploma thesis, Technische Universität München, Brainlab AG, 2012.

[4] Akimoto, M., Nakamura, M., Mukumoto, N., Yamada, M., Ueki, N., Matsuo, Y., Sawada, A., Mizowaki, T., Kokubo, M., and Hiraoka, M. Optimization of the x-ray monitoring angle for creating a correlation model between internal and external respiratory signals. *Medical Physics 39*, 10 (Oct. 2012), 6309–15.

[5] Amrani, M., Jaillet, F., and Shariat, B. Deformable Objects Modeling and Animation: Application to Organs' Interactions Simulation. *Journal for Geometry and Graphics 4*, 2 (2000), 181–88.

[6] Bergou, M., Wardetzky, M., Harmon, D., Zorin, D., and Grinspun, E. Discrete quadratic curvature energies. *Computer Aided Geometric Design 24*, 8 (2006), 499–518.

[7] Bethesda, M. Tissue Substitutes in Radiation Dosimetry and Measurement, Report 44 of the International Commission on Radiation Units and Measurements. *ICRU Report 44* (1989).

[8] Brahme, A. Dosimetric precision requirements in radiation therapy. *Acta Radiologica Oncology 23*, 5 (Jan. 1984), 379–91.

[9] Bro-Nielsen, M. Finite element modeling in surgery simulation. *Proceedings of the IEEE 86*, 3 (Mar. 1998), 490–503.

[10] Brock, K. K., McShan, D. L., Ten Haken, R. K., Hollister, S. J., Dawson, L. a., and Balter, J. M. Inclusion of organ deformation in dose calculations. *Medical Physics 30*, 3 (2003), 290–95.

[11] Brock, K. K., Sharpe, M. B., Dawson, L. a., Kim, S. M., and Jaffray, D. a. Accuracy of finite element model-based multi-organ deformable image registration. *Medical Physics 32*, 6 (2005), 1647–59.

[12] Brock, K. M., Balter, J. M., Dawson, L. a., Kessler, M. L., and Meyer, C. R. Automated generation of a four-dimensional model of the liver using warping and mutual information. *Medical Physics 30*, 6 (2003), 1128–33.

[13] Broeker, F. Diskrete Mischverteilungen. In *Statistik III: Statistik und Ökonometrie*. Universitaet Goettingen "http://www.statoek.wiso.uni-goettingen.de/veranstaltungen/statistik3alt/", Goettingen, 1999, pp. 160–85.

[14] Burnet, N. G., Thomas, S. J., Burton, K. E., and Jefferies, S. J. Defining the tumour and target volumes for radiotherapy. *Cancer Imaging 4*, 2 (Jan. 2004), 153–61.

[15] Buzug, T. Zweidimensionale Rekosntruktionstechniken. In *Einführung in die Computertomographie*, no. 1. Springer, Berlin, 2004, pp. 107–87, ISBN–9783540208082.

[16] Cavedon, C., Francescon, P., Cora, S., Moschini, G., Rossi, P., McDaniel, F. D., and Doyle, B. L. Performance of a Motion Tracking System During Cyberknife Robotic Radiosurgery. *AIP Conference Proceedings 464* (2009), 464–67.

[17] Chan, M. K. H., Kwong, D. L. W., Ng, S. C. Y., Tam, E. K. W., and Tong, A. S. M. Investigation of four-dimensional (4D) Monte Carlo dose calculation in real-time tumor tracking stereotatic body radiotherapy for lung cancers. *Medical Physics 39*, 9 (Sept. 2012), 5479–87.

[18] Desbrun, M., Schröder, P., and Barr, A. Interactive animation of structured deformable objects. In *Proceedings of the 1999 conference on Graphics interface '99*. Morgan Kaufmann Publishers Inc., 1999, pp. 1–8, ISBN–1–55860–632–7.

[19] Endo, M., Tsunoo, T., Kandatsu, S., Tanada, S., Aradate, H., and Saito, Y. Four-dimensional computed tomography (4D CT)-concepts and preliminary development. *Radiation Medicine 21*, 1 (2003), 17–22.

[20] Erdi, Y., Nehmeh, S., and Pan, T. The CT motion quantitation of lung lesions and its impact on PET-measured SUVs. *Journal of Nuclear Medicine 45*, 8 (2004), 1–9.

[21] Fippel, M. Fast Monte Carlo dose calculation for photon beams based on the VMC electron algorithm. *Medical Physics 26*, 8 (Aug. 1999), 1466–75.

[22] Fippel, M., and Nüsslin, F. Bestimmung der Wechselwirkungsparameter des menschlichen Gewebes für Monte-Carlo-Dosisberechnungen in der Strahlentherapie. *Strahlentherapie und Onkologie 117*, 4 (2001), 206–211.

[23] Ford, E. C., Mageras, G. S., Yorke, E., and Ling, C. C. Respiration-correlated spiral CT: A method of measuring respiratory-induced anatomic motion for radiation treatment planning. *Medical Physics 30*, 1 (2003), 88–97.

[24] Frisken-Gibson, S. Using linked volumes to model object collisions, deformation, cutting, carving, and joining. *IEEE Transactions on Visualization and Computer Graphics 5*, 4 (1999), 333–48.

[25] Glide-Hurst, C. K., Hugo, G. D., Liang, J., and Yan, D. A simplified method of four-dimensional dose accumulation using the mean patient density representation. *Medical Physics 35*, 12 (2008), 5269–77.

[26] Goitein, M. The utility of computed tomography in radiation therapy: An estimate of outcome. *International Journal of Radiation Oncology, Biology, Physics 5*, 10 (1979), 1799–00.

[27] Goldman, L. W. Principles of CT: multislice CT. *Journal of Nuclear Medicine 36*, 2 (June 2008), 57–68.

[28] Guckenberger, M., Wilbert, J., Krieger, T., Richter, A., Baier, K., Meyer, J., and Flentje, M. Four-dimensional treatment planning for stereotactic body radiotherapy. *International Journal of Radiation Oncology, Biology, Physics 69*, 1 (Sept. 2007), 276–85.

[29] Guckenberger, M., Wilbert, J., Meyer, J., Baier, K., Richter, A., and Flentje, M. Is a single respiratory correlated 4D-CT study sufficient for evaluation of breathing motion? *International Journal of Radiation Oncology, Biology, Physics 67*, 5 (Apr. 2007), 1352–59.

[30] Haken, R. T., and Jee, K. TU-A-M100F-01: Biological/Clinical Outcome Models in RT Planning. *Medical Physics 34* (2002), 2537.

[31] Harbrecht, H. Nichtlineare Optimierung. In *Angewandte Mathematik: Optimierung*. Universitaet Stuttgart "http://www.ians.uni-stuttgart.de/SimTech/Harbrecht/teaching/optimierung/", 2011.

[32] Heath, E., and Seuntjens, J. A direct voxel tracking method for four-dimensional Monte Carlo dose calculations in deforming anatomy. *Medical Physics 33*, 2 (2006), 434–45.

[33] Heath, E., Tessier, F., and Kawrakow, I. Investigation of voxel warping and energy mapping approaches for fast 4D Monte Carlo dose calculations in deformed geometries using VMC++. *Physics in Medicine and Biology 56*, 16 (Aug. 2011), 5187–202.

[34] Henríquez, F. C., and Castrillón, S. V. A quality index for equivalent uniform dose. *Journal of Medical Physics 36*, 3 (July 2011), 126–32.

[35] Herrmann, T., Baumann, M., and Dörr, W. Biologische Modelle. In *Klinische Strahlenbiologie 3*. Elsevier, 2005, pp. 17–19, ISBN–9783437239601.

[36] Hietschold, V. Tomographische Techniken. Tech. rep., Technische Universität Dresden, Oncoray - Zentrum für Strahlenforschung in der Onkologie, Lecture - Course: Medical radiation sciences, Dresden, 2010.

[37] Hubbell, J., and Seltzer, S. Tables of x-ray mass attenuation coefficients and mass energy-absorption coefficients 1 keV to 20 MeV for elements Z = 1 to 92 and 48 additional substances of dosimetric interest. Tech. rep., Radiation and Biomolecular Physics Division, PML, NIST, "http://www.nist.gov/pml/data/xraycoef/", 1995.

[38] Hugo, G. D., Yan, D., and Liang, J. Population and patient-specific target margins for 4D adaptive radiotherapy to account for intra- and inter-fraction variation in lung tumour position. *Physics in Medicine and Biology 52*, 1 (Jan. 2007), 257–74.

[39] International Commission on Radiological Protection. 2007 Recommendations of the International Commission on Radiological Protection. *Annals of the ICRP 37*, (2-4) (2007).

[40] Jaffray, D. A., Lindsay, P. E., Brock, K. K., Deasy, J. O., and Tomé, W. A. Accurate accumulation of dose for improved understanding of radiation effects in normal tissue. *International Journal of Radiation Oncology, Biology, Physics 76*, 3 (Mar. 2010), 135–39.

[41] Janssens, G., Orban de Xivry, J., Fekkes, S., Dekker, A., Macq, B., Lambin, P., and van Elmpt, W. Evaluation of nonrigid registration models for interfraction dose accumulation in radiotherapy. *Medical Physics 36*, 9 (2009), 4268–76.

[42] Jiang, S. B., Ph, D., Keall, P., Chen, G., Low, D., Mageras, G., and Foster, K. 4D Scanning. Tech. rep., Department of Radiation Oncology, Harvard - University, "http://www.aapm.org/meetings/amos2/pdf/26%20-4449-58255-447.pdf", 2007.

[43] Jin, J.-Y., Ajlouni, M., Chen, Q., Yin, F.-F., and Movsas, B. A technique of using gated-CT images to determine internal target volume (ITV) for fractionated stereotactic lung radiotherapy. *Radiotherapy and Oncology 78*, 2 (Feb. 2006), 177–84.

[44] Kaatsch, P., Spix, C., and Katalinic, A. *Krebs in Deutschland 2007/2008*. Gesellschaft der epidemiologischen Krebsregister e. V. (GEKID), Zentrum für Krebsregisterdaten (ZfKD), Robert Koch Institut, "http://www.rki.de/Krebs/DE/Content/Publikationen/Krebs_in_Deutschland/kid_2012/krebs_in_deutschland_2012.pdf", 2013.

[45] Kamino, Y., Takayama, K., Kokubo, M., Narita, Y., Hirai, E., Kawawda, N., Mizowaki, T., Nagata, Y., Nishidai, T., and Hiraoka, M. Development of a four-dimensional image-guided radiotherapy system with a gimbaled X-ray head. *International Journal of Radiation Oncology, Biology, Physics 66*, 1 (Sept. 2006), 271–80.

[46] Karlis, D., and Xekalaki, E. Mixed poisson distributions. *International Statistical Review 73*, 1 (2005), 35–58.

[47] KAUS, M., and BROCK, K. Deformable image registration for radiation therapy planning: algorithms and applications. In *Biomechanical Systems Technology: Computational Methods*, vol. 1. World Scientific Pub Co Inc, Singapore, 2007, pp. 1–28, ISBN–978–982–370–982–3.

[48] Kawrakow, I., and Fippel, M. 3D electron dose calculation using a Voxel based Monte Carlo algorithm (VMC). *Medical Physics 23*, 4 (1996), 445–57.

[49] Keall, P. Acquiring a four-dimensional computed tomography dataset using an external respiratory signal. *Physics in Medicine and Biology 48*, 1 (2003), 45–65.

[50] Keall, P., Langer, U., and Suh, Y. 4D CT Scanning: Imaging and Planning. Tech. rep., Stanford University, "http://www.aapm.org/meetings/amos2/pdf/29-7914-12669-520.pdf", 2012.

[51] Keall, P. J., Joshi, S., Vedam, S. S., Siebers, J. V., Kini, V. R., and Mohan, R. Four-dimensional radiotherapy planning for DMLC-based respiratory motion tracking. *Medical Physics 32*, 4 (2005), 942–51.

[52] Keall, P. J., Siebers, J. V., Joshi, S., and Mohan, R. Monte Carlo as a four-dimensional radiotherapy treatment-planning tool to account for respiratory motion. *Physics in Medicine and Biology 49*, 16 (Aug. 2004), 3639–48.

[53] Keall, P. J., Vedam, S. S., George, R., and Williamson, J. F. Respiratory regularity gated 4D CT acquisition: concepts and proof of principle. *Australasian Physical and Engineering Sciences in Medicine 30*, 3 (Sept. 2007), 211–20.

[54] Klein, S., Staring, M., and Pluim, J. P. W. Comparison of gradient approximation techniques for optimisation of mutual information in nonrigid registration. *Medical Imaging 5747*, 2 (Apr. 2005), 192–203.

[55] Krieger, H. Strahlenschutzbegriffe und Dossigrößen. In *Grundlagen der Strahlungsphysik und des Strahlenschutzes*. Teubner, Wiesbaden, 2007, ch. 9, pp. 305–30, ISBN–978–3834808011.

[56] Li, X., Wang, X., Li, Y., and Zhang, X. A 4D IMRT planning method using deformable image registration to improve normal tissue sparing with contemporary delivery techniques. *Radiation Oncology 6*, 2 (Jan. 2011), 83–97.

[57] Low, D. a., and Dempsey, J. F. Evaluation of the gamma dose distribution comparison method. *Medical Physics 30*, 9 (2003), 2455–64.

[58] Low, D. a., Nystrom, M., Kalinin, E., Parikh, P., Dempsey, J. F., Bradley, J. D., Mutic, S., Wahab, S. H., Islam, T., Christensen, G., Politte, D. G., and Whiting, B. R. A method for the reconstruction of four-dimensional synchronized CT scans acquired during free breathing. *Medical Physics 30*, 6 (2003), 1254–53.

[59] Luxton, G., Keall, P. J., and King, C. R. A new formula for normal tissue complication probability (NTCP) as a function of equivalent uniform dose (EUD). *Physics in Medicine and Biology 53*, 1 (Jan. 2008), 23–36.

[60] Mao, W., Kearney, V., Jiang, L., Yordy, J., and Solberg, T. SU-C-103-04: 3D Tumor Tracking On Vero. *Medical Physics 40* (2013), 94.

[61] Mavroidis, P., and Plataniotis, G. SU-GG-T-429: Dose-mass-histogram (DMH) vs. dose-volume histogram (DVH) in predicting lung complications. *Medical Physics 35* (2008), 2823.

[62] McClelland, J. R., Blackall, J. M., Tarte, S., Chandler, A. C., Hughes, S., Ahmad, S., Landau, D. B., and Hawkes, D. J. A continuous 4D motion model from multiple respiratory cycles for use in lung radiotherapy. *Medical Physics 33*, 9 (2006), 3348–58.

[63] McInerney, T., and Terzopoulos, D. Deformable Models in Medical Image Analysis: A Survey. *Medical Image Analysis 1*, 2 (June 1996), 91–108.

[64] Meier, U., López, O., Monserrat, C., Juan, M. C., and Alcañiz, M. Real-time deformable models for surgery simulation: a survey. *Computer Methods and Programs in Biomedicine 77*, 3 (Mar. 2005), 183–97.

[65] Moerland, M. The influence of respiration induced motion of the kidneys on the accuracy of radiotherapy treatment planning, a magnetic resonance imaging study. *Radiotherapy and Oncology 30*, 2 (1994), 150–54.

[66] Mosegaard, J. *Cardiac Surgery Simulation Graphics Hardware meets Congenital Heart Disease*. PhD thesis, University of Aarhus, Aarhus, 2006.

[67] Narayanan, C. S. Dose prescription dilemma. *International Journal of Radiation Oncology, Biology, Physics 15*, 4 (Oct. 1988), 595–96.

[68] Neicu, T., Shirato, H., Seppenwoolde, Y., and Jiang, S. B. Synchronized moving aperture radiation therapy (SMART): average tumour trajectory for lung patients. *Physics in Medicine and Biology 48*, 5 (Mar. 2003), 587–98.

[69] Niemierko, a. Reporting and analyzing dose distributions: a concept of equivalent uniform dose. *Medical Physics 24*, 1 (Jan. 1997), 103–10.

[70] Nolting, W. Lagrange-Mechanik. In *Analytische Mechanik - Grundkurs Theoretische Physik 2*. Springer, Berlin, 2011, pp. 3–9, ISBN–978–3642129490.

[71] Owen, M. R., and Lewis, M. A. The mechanics of lung tissue under high-frequency ventilation. *Journal on Applied Mathematics 61*, 5 (2001), 1731–61.

[72] Pan, T., Lee, T.-Y., Rietzel, E., and Chen, G. T. Y. 4D-CT imaging of a volume influenced by respiratory motion on multi-slice CT. *Medical Physics 31*, 2 (2004), 333–40.

[73] Pennec, X., Cachier, P., and Ayache, N. Understanding the Demons Algorithm: 3D Non-rigid Registration by Gradient Descent. *In 2nd int. conf. on medical image computing and computer-assisted intervention (MICCAI'99) LNSC 1679* (1999), 597–605.

[74] Podgorsak, E. B., and Kainz, K. Dosimetric principles, quantities and units. In *Radiation Oncology Physics: A Handbook for Teachers and Students*, vol. 33. IAEA, 2006, pp. 45–70, ISBN–92–0–107304–6.

[75] Richter, C. *Der Einfluss der Atembewegung auf die PET/CT-Schwächungskorrektur*. Diploma thesis, Technische Universität Dresden, 2007.

[76] Rietzel, E., Chen, G. T. Y., Choi, N. C., and Willet, C. G. Four-dimensional image-based treatment planning: Target volume segmentation and dose calculation in the presence of respiratory motion. *International Journal of Radiation Oncology, Biology, Physics 61*, 5 (Apr. 2005), 1535–50.

[77] Rietzel, E., Liu, A. K., Doppke, K. P., Wolfgang, J. a., Chen, A. B., Chen, G. T. Y., and Choi, N. C. Design of 4D treatment planning target volumes. *International Journal of Radiation Oncology, Biology, Physics 66*, 1 (Sept. 2006), 287–95.

[78] Rosu, M., Chetty, I. J., Balter, J. M., Kessler, M. L., McShan, D. L., and Ten Haken, R. K. Dose reconstruction in deforming lung anatomy: Dose grid size effects and clinical implications. *Medical Physics 32*, 8 (2005), 2487–95.

[79] Rosu, M., Chetty, I. J., Kessler, M. L., and Ten Haken, R. K. Monte Carlo non-adaptive 4-D treatment planning in conformal radiation therapy: Why, how, and what to look for. In *Medical Physics Monograph* (2006), vol. 32, Medical Physics Publishing, Madison, pp. 293–310.

[80] Rosu, M., and Hugo, G. Advances in 4D Radiation Therapy for Managing Respiration: Part II 4D Treatment Planning. *Zeitschrift für Medizinische Physik 22(4)* (2012), 272–80.

[81] Rueckert, D., Sonoda, L. I., Hayes, C., Hill, D. L., Leach, M. O., and Hawkes, D. J. Nonrigid registration using free-form deformations: application to breast MR images. *IEEE Transactions on Visualization and Computer Graphics 18*, 8 (Aug. 1999), 712–21.

[82] Saini, S. Multi-detector row CT: principles and practice for abdominal applications. *Radiotherapy and Oncology 233*, 2 (Nov. 2004), 323–30.

[83] Schaly, B., Kempe, J. a., Bauman, G. S., Battista, J. J., and Van Dyk, J. Tracking the dose distribution in radiation therapy by accounting for variable anatomy. *Physics in Medicine and Biology 49*, 5 (Mar. 2004), 791–805.

[84] Scharr, H. *Optimale Operatoren in der digitalen Bildverarbeitung*. PhD thesis, Ruprecht-Karls-Universität Heidelberg, 2000.

[85] Schlegel, W. Medizinische Strahlenphysik. In *Medizinische Physik 2*. Springer, Heidelberg, 2002, pp. 3–5, ISBN–9783540652540.

[86] Schultheiss, T., Orton, C., and Peck, R. Models in radiotherapy: Volume effects. *Medical Physics 10* (1983), 410–15.

[87] Sederberg, T., and Parry, S. Free-form deformation of solid geometric models. *ACM SIGGRAPH Computer Graphics 20*, 4 (1986), 151–60.

[88] Shen, J., Matuszewski, B., Shark, L., and Moore, C. Deformable Image Registration using Spring Mass System. In *BMVC*. British Machine Vision Association, 2006, pp. 1199–208, ISBN–1–904410–14–6.

[89] Shih, H. a., Jiang, S. B., Aljarrah, K. M., Doppke, K. P., and Choi, N. C. Internal target volume determined with expansion margins beyond composite gross tumor volume in three-dimensional conformal radiotherapy for lung cancer. *International Journal of Radiation Oncology, Biology, Physics 60*, 2 (Oct. 2004), 613–22.

[90] Shimizu, S., Shirato, H., Kagei, K., Nishioka, T., Bo, X., Dosaka-Akita, H., Hashimoto, S., Aoyama, H., Tsuchiya, K., and Miyasaka, K. Impact of respiratory movement on the computed tomographic images of small lung tumors in three-dimensional (3D) radiotherapy. *International Journal of Radiation Oncology, Biology, Physics 46*, 5 (Mar. 2000), 1127–33.

[91] Shirato, H., Suzuki, K., Sharp, G. C., Fujita, K., Onimaru, R., Fujino, M., Kato, N., Osaka, Y., Kinoshita, R., Taguchi, H., Onodera, S., and Miyasaka, K. Speed and amplitude of lung tumor motion precisely detected in four-dimensional setup and in real-time tumor-tracking radiotherapy. *International Journal of Radiation Oncology, Biology, Physics 64*, 4 (Mar. 2006), 1229–36.

[92] Si, H. TetGen, a quality tetrahedral mesh generator and three-dimensional delaunay triangulator. *"http://tetgen. berlios. de" Berlin* (2006), Weierstrass Institute for Applied Analys.

[93] Siebers, J. V., and Zhong, H. An energy transfer method for 4D Monte Carlo dose calculation. *Medical Physics 35*, 9 (2008), 4096–05.

[94] Söhn, M., Birkner, M., Chi, Y., Wang, J., Yan, D., Berger, B., and Alber, M. Model-independent, multimodality deformable image registration by local matching of anatomical features and minimization of elastic energy. *Medical Physics 35*, 3 (2008), 866–78.

[95] Söhn, M., Weinmann, M., and Alber, M. Intensity-modulated radiotherapy optimization in a quasi-periodically deforming patient model. *International Journal of Radiation Oncology, Biology, Physics 75*, 3 (Nov. 2009), 906–14.

[96] Sonke, J.-J., Lebesque, J., and van Herk, M. Variability of four-dimensional computed tomography patient models. *International Journal of Radiation Oncology, Biology, Physics 70*, 2 (Feb. 2008), 590–98.

[97] Taguchi, K. Temporal resolution and the evaluation of candidate algorithms for four-dimensional CT. *Medical Physics 30*, 4 (2003), 640–50.

[98] Terzopoulos, D., Platt, J., Barr, A., and Fleischer, K. Elastically deformable models. *ACM SIGGRAPH Computer Graphics 21*, 4 (Aug. 1987), 205–214.

[99] Teschner, M., and Heidelberger, B. A versatile and robust model for geometrically complex deformable solids. In *CGI '04 Proceedings of the Computer Graphics International*. IEEE Computer Society Washington, 2004, pp. 312–19, ISBN–0–7695–2171–1.

[100] Thirion, J. Image matching as a diffusion process: an analogy with Maxwell's demons. *Medical Image Analysis 2*, 3 (1998), 243–60.

[101] Trofimov, A., Rietzel, E., Lu, H.-M., Martin, B., Jiang, S., Chen, G. T. Y., and Bortfeld, T. Temporo-spatial IMRT optimization: concepts, implementation and initial results. *Physics in Medicine and Biology 50*, 12 (June 2005), 2779–98.

[102] Underberg, R. W. M., Lagerwaard, F. J., Slotman, B. J., Cuijpers, J. P., and Senan, S. Use of maximum intensity projections (MIP) for target volume generation in 4DCT scans for lung cancer. *International Journal of Radiation Oncology, Biology, Physics 63*, 1 (Sept. 2005), 253–60.

[103] Unkelbach, J. *Inclusion of organ motion in IMRT optimization using probabilistic treatment planning*. PhD thesis, University of Heidelberg, 2006.

[104] Unkelbach, J., and Oelfke, U. Incorporating organ movements in IMRT treatment planning for prostate cancer: Minimizing uncertainties in the inverse planning process. *Medical Physics 32*, 8 (2005), 2471–83.

[105] Vandemeulebroucke, J. The POPI-model, a pointvalidated pixel-based breathing thorax model. In *Proceedings of the XVth ICCR Conference*. ICCR, Toronto, Canada, 2007.

[106] Villard, P., Baudet, V., Beuve, M., Shariat, B., Jaillet, F., and LIRIS, V. Resolution of Non-Linear Problems In Realistic-Lung-Inflating Simulation with Finite Element Method. In *10th workshop on Heavy Charged Particles in Biology and Medicine* (Oropa, 2005), pp. 184–87.

[107] Villard, P., Beuve, M., and Shariat, B. Lung mesh generation to simulate breathing motion with a finite element method. In *Eighth International Conference on Information Visualisation (IV'04)*. IEEE, 2004, pp. ISBN–0–7695–2177–0.

[108] Villard, P., Bourne, W., and Bello, F. Modelling organ deformation using mass-springs and tensional integrity. In *Biomedical Simulation: 4th International Symposium*. Springer, 2008, pp. 221–26, ISBN–978–3–540–70520–8.

[109] Villard, P.-F., Beuve, M., Shariat, B., and Baudet, V. Simulation of lung behaviour with finite elements: Influence of bio-mechanical parameters. In *MEDIVIS '05 Proceedings of the Third International Conference on Medical Information* (2005), vol. c, IEEE, pp. 9–14, ISBN–0–7695–2393–5.

[110] Villard, P.-f., Bourne, W., and Bello, F. Interactive Simulation of Diaphragm Motion Through Muscle and Rib Kinematics. In *Recent Advances in the 3D Physiological Human*. Springer, 2009, pp. 1–13, ISBN–978–1–84882–565–9.

[111] Webb, E., and Nioutsikou, S. Reconsidering the definition of a dose volume histogram. *Physics in Medicine and Biology 51*, 21 (2005), 43–50.

[112] Wei, X. SU-FF-T-380: Dose Mass Histogram and Its Application for 4D Treatment Planning. *Medical Physics 32*, 6 (2005), 2038.

[113] Wiant, D., Terrell, J., and Sintay, B. SU-E-T-889: Target Definition in TomoTherapy Lung SBRT Treatment Plans. *Medical Physics 38* (2011), 3696.

[114] Wilkens, J. J., Alaly, J. R., Zakarian, K., Thorstad, W. L., and Deasy, J. O. IMRT treatment planning based on prioritizing prescription goals. *Physics in Medicine and Biology 52*, 6 (Mar. 2007), 1675–92.

[115] Wilkens, J. J., and Oelfke, U. Direct comparison of biologically optimized spread-out bragg peaks for protons and carbon ions. *International Journal of Radiation Oncology, Biology, Physics 70*, 1 (Jan. 2008), 262–66.

[116] Wolberg, G. Image metamorphosis with scattered feature constraints. *IEEE Transactions on Visualization and Computer Graphics 2*, 4 (1996), 337–54.

[117] Wolthaus, J. W. H., Sonke, J.-J., van Herk, M., Belderbos, J. S. a., Rossi, M. M. G., Lebesque, J. V., and Damen, E. M. F. Comparison of different strategies to use four-dimensional computed tomography in treatment planning for lung cancer patients. *International Journal of Radiation Oncology, Biology, Physics 70*, 4 (Mar. 2008), 1229–38.

[118] Yaegashi, Y., Tateoka, K., Nakazawa, T., Fujimoto, K., Shima, K., Suzuki, J., Nakata, A., Saito, Y., Abe, T., Sakata, K., and Hareyama, M. Analysis of the optimum internal margin for respiratory-gated radiotherapy using end-expiratory phase assessments using a motion phantom. *Journal of Applied Clinical Medical Physics 13*, 2 (Jan. 2012), 3715–26.

[119] Yan, C., Hugo, G., Salguero, F. J., Saleh-Sayah, N., Weiss, E., Sleeman, W. C., and Siebers, J. V. A method to evaluate dose errors introduced by dose mapping processes for mass conserving deformations. *Medical Physics 39*, 4 (Apr. 2012), 2119–28.

[120] Yan, D., Jaffray, D. a., and Wong, J. W. A model to accumulate fractionated dose in a deforming organ. *International Journal of Radiation Oncology, Biology, Physics 44*, 3 (June 1999), 665–75.

[121] Yin, Y., Hoffman, E. a., and Lin, C.-L. Mass preserving nonrigid registration of CT lung images using cubic B-spline. *Medical Physics 36*, 9 (2009), 4213–22.

[122] Zhang, G., Feygelman, V., Huang, T.-C., Stevens, C., Li, W., and Dilling, T. Motion-weighted target volume and dose-volume histogram: A practical approximation of four-dimensional planning and evaluation. *Radiotherapy and Oncology 99*, 1 (Mar. 2011), 67–72.

[123] Zhang, P., Hugo, G. D., and Yan, D. Planning study comparison of real-time target tracking and four-dimensional inverse planning for managing patient respiratory motion. *International Journal of Radiation Oncology, Biology, Physics 72*, 4 (Nov. 2008), 1221–27.

[124] Zhong, H., and Siebers, J. V. Monte Carlo dose mapping on deforming anatomy. *Physics in Medicine and Biology 54*, 19 (2009), 5815–30.

[125] Zhou, S.-M., Das, S., Wang, Z., and Marks, L. B. Relationship between the generalized equivalent uniform dose formulation and the Poisson statistics-based tumor control probability model. *Medical Physics 31*, 9 (2004), 2606–09.

[126] Zink, K. Einführung in die Strahlentherapie und Therapie mit offenen Nukliden. Tech. rep., Fachhochschule Gießen, "http://homepages.thm.de/~hg11956/Lehrveranstaltungen/AMP01/", 2004.